

Causes of along- and across-arc
geochemical variations in the Southern
Volcanic Zone (33°-43°S) in Chile and
Argentina

DISSERTATION

Zur Erlangung des Doktorgrades
an der Mathematisch-Naturwissenschaftlichen
Fakultät der Christian-Albrechts-Universität Kiel

Vorgelegt von

Guillaume JACQUES

Kiel, Freitag den 31. Mai 2013

Ersten Gutachter:

Professor Dr. Kaj Hoernle

Zweiten Gutachter:

Professor Dr. James Gill

Tag der mündlichen Prüfung:

Freitag den 21. Juni 2013

Zum druck genehmigt:

.....

.....

Der Dekan

Hiermit erkläre ich, dass ich die vorliegende Doktorarbeit selbständig und ohne Zuhilfenahme unerlaubter Hilfsmittel erstellt habe. Weder diese noch eine ähnliche Arbeit wurde an einer anderen Hochschule im Rahmen eines Prüfungsverfahrens vorgelegt, veröffentlicht oder zur Veröffentlichung vorgelegt. Ferner versichere ich, dass die Arbeit unter Einhaltung der Regeln guter wissenschaftlicher Praxis der Deutschen Forschungsgemeinschaft entstanden ist.

Kiel, den

Guillaume JACQUES

Contents

Abstract	v
Zusammenfassung	viii
1 General introduction	001
1.1 Introduction	002
1.1.1 Subduction zone tectonic	002
1.1.2 Subdction zone magmatism	003
1.2 Studied area and dissertation outline	004
1.2.1 The Andes	004
1.2.2 The Southern Volcanic Zone	005
1.2.3 Thesis outline	007
2 Across-arc geochemical variations in the Southern Volcanic Zone, Chile (34.5-38°S): Constraints on mantle wedge and slab input composition	010
Chapter overview	011
2.1 Introduction	012
2.2 Geological setting	013
2.3 Sample collection, preparation and analytical methods	017
2.4 Results	030
2.5 Discussion	039
2.5.1 Crustal assimilation	040
2.5.2 The mantle wedge and subcontinental lithosphere	043
2.5.3 The slab component	048
2.5.3.1 Sources of slab component	048
2.5.3.2 Nature of the slab component: solid, fluid or melt?	050

2.5.4 Quantitative flux melting model	052
2.5.5 Regional and global comparison	058
2.6 Conclusions	059
3 Geochemical variations in the Central Southern Volcanic Zone, Chile (38-43°S): The role of fluids in generating arc magmas	062
Chapter overview	063
3.1 Introduction	064
3.2 Geological setting and previous geochemical studies	065
3.2.1 Geological background	065
3.2.2 Previous geochemical studies	068
3.3 Material and analytical methods	069
3.4 Results and descriptive comparison with the TSVZ	071
3.4.1 Major elements	071
3.4.2 Trace elements	076
3.4.3 Isotopes	078
3.5 Discussion	084
3.5.1 Is crustal assimilation occurring during fractional crystallization in the CSVZ VA?	085
3.5.2 CSVZ VA stratovolcanoes compared to CSVZ VA cinder cones and TSVZ VA: Differences in the mass fraction of the slab component	090
3.5.3 Comparison of CSVZ and TSVZ BA: Differences in mantle source composition	091
3.5.4 Differences in the composition of subduction inputs: the mantle wedge, subducting oceanic crust, and subducting sediments	092

3.5.4.1 <i>The mantle wedge</i>	092
3.5.4.2 <i>Subducting altered oceanic crust (AOC)</i>	093
3.5.4.3 <i>Subducting sediment</i>	094
3.5.5 Differences in slab surface temperature beneath the Volcanic Front	094
3.5.6 Differences in the amount of slab serpentinization	095
3.5.7 Quantitative flux melting model	096
3.6 Conclusions	102
Appendix	104
4 Origin of the enriched isotopic signature in the Northern Southern Volcanic Zone (33-34.5S), Chile	108
Chapter overview	109
4.1 Introduction	110
4.2 Geological setting	110
4.3 Sampling and analytical methods	114
4.4 Results	122
4.4.1 Major elements	124
4.4.2 Trace elements	124
4.4.3 Isotopes	124
4.4.4 Basement samples	127
4.5 Discussion	133
4.5.1 Variations of the slab input compositions and mantle wedge	133
4.5.1.1 <i>The oceanic crust</i>	133
4.5.1.2 <i>The sediments</i>	135
4.5.1.3 <i>The mantle wedge</i>	135
4.5.1.4 <i>Summary</i>	136

4.5.2 Crustal effects: Crystal fractionation, assimilation and subduction erosion	136
4.5.2.1 <i>The effect of fractional crystallization (FC)</i>	138
4.5.2.2 <i>Assimilation plus Fractional Crystallisation (AFC) of the upper crust</i>	139
4.5.2.3 <i>Subduction erosion of the upper crust</i>	142
4.5.2.4 <i>Lower crust influence</i>	143
4.5.2.4 <i>Summary</i>	145
4.5.3 Mantle effects: enriched mantle in the NSVZ?	145
4.5.3.1 <i>Enriched lithospheric mantle</i>	146
4.5.3.2 <i>Enriched asthenosphere</i>	147
4.5.4 General comparison: NSVZ-TSVZ-CSVZ	148
4.6 Conclusions	149
References	151
Acknowledgements	172
Curriculum Vitae	174

Abstract

The Southern Volcanic Zone (SVZ) in Chile is a 1,200 km long subduction zone. Along-arc variation in the magma geochemistry is a common characteristic of such long subduction zones. Many factors can control the magma composition. First, the slab input can vary in composition. The subducted sediments composition can vary, as they are a function of climate and therefore erosion and material supply in the trench, whereas the composition of the oceanic crust can vary in age (and consequently in slab surface temperature) and depends also at which mid-ocean ridge it has formed. The local tectonic settings of the incoming plate (e.g. the presence or absence of major fracture zones or bend faults) will affect the degree of alteration and hydration of the lower oceanic crust and the lithospheric upper mantle, increasing the potential for serpentinization. The slab geometry can also vary. A deeper slab will be hotter and could possibly melt, which will increase the potential of carrying incompatible but fluid-immobile elements. On the upper plate, the tectonic will also play an important role. Increasing crustal thickness may increase the potential for crustal assimilation or fractional crystallization.

In order to evaluate the effect of these factors on magmatic geochemistry, this PhD thesis presents a comprehensive geochemical data set (major and trace elements and O-Sr-Nd-Hf-Pb isotopes) from Holocene primarily olivine-bearing volcanic arc rocks, Chilean trench sediments and Andean crustal basement from 33°S to 43°S and extending to 300 km into the backarc in Argentina.

All the volcanic arc samples show typical subduction zone trace element enrichment in highly incompatible and fluid-mobile elements and depletions in High Field Strength Elements and Heavy Rare Earth Elements. The backarc show the least enrichments and depletions, consistent with less of a slab-derived component, and consequently lower degrees of melting. The Transitional (T) SVZ (34.5-38°S) overlap the backarc samples in Sr and Nd isotopic composition, whereas the Northern (N) SVZ (33-34.5°S) extends to higher Sr and lower Nd and Hf isotope ratios. The Central (C) SVZ (38-43°S) stratovolcano samples are slightly shifted to higher Sr and/or Nd isotope ratios, whereas the monogenetic cinder cones between them are similar to the TSVZ samples. All samples form a tight correlation on the Pb isotopes diagrams. The volcanic arc samples plot at the radiogenic end of the array formed by the backarc samples.

And largely overlap the trench sediments. This correlation indicates mixing between a South Atlantic Mid-Ocean Ridge Basalt (MORB) source and a slab component derived from subducted trench sediments and altered oceanic crust. The difference in ratios of more- to less-incompatible fluid-immobile element ratios between the volcanic arc, backarc and trench sediments indicate that the slab component is a hydrous melt. The lack of correlations between MgO (or SiO₂) and isotopes and the tight correlations of the Pb isotopes preclude significant assimilation of the old sialic crust in the TSVZ and CSVZ. Hf-Nd isotope ratios define separate linear arrays for the volcanic arc and backarc, neither of which trend toward subducting sediment, possibly reflecting a primarily asthenospheric mantle array for the volcanic arc and involvement of enriched Proterozoic lithospheric mantle in the backarc. Some backarc samples show an extra-enriched component with slightly higher Sr but lower Nd and Hf isotope ratios, and elevated $\delta^{7/4}$ and $\delta^{8/4}$, which are interpreted to be a different enriched mantle component, possibly subcontinental lithospheric mantle, than found in the other backarc samples.

Although the CSVZ monogenetic cones are similar to the TSVZ stratovolcano samples, the CSVZ stratovolcanoes have higher fluid-mobile to fluid-immobile element ratios and lower more- to less-incompatible fluid-immobile element ratios, consistent with an overall higher fluid flux and higher degrees of melting for the CSVZ. The higher Hf-Nd isotope ratios of the stratovolcanoes suggest a greater contribution from a more depleted source. Combined with geomorphologic data and geophysical data, this indicates derivation of a slab component carrying a combined signature of trench sediments and seawater altered oceanic crust and possibly serpentinized upper mantle, due to the larger hydration of the incoming plate caused by the more prominent and numerous fracture zones and bend faults in this segment.

$\delta^{18}\text{O}(\text{melt})$ from groundmass or converted from olivine (by adding 0.6‰) yields values that extend below and above the MORB mantle range (see Bindeman, 2008 and references therein). The TSVZ, CSVZ monogenetic cone and backarc samples largely overlap the MORB mantle range and extend slightly above, but remain within the Island arc range. In contrast, the CSVZ stratovolcano samples fall below the MORB mantle range, indicating the possible influence from a depleted source such as serpentinites. The NSVZ samples, surprisingly, fall

within the MORB range and show no correlation with parameters of differentiation (e.g. SiO₂ or MgO) or isotopes precluding significant upper crustal assimilation.

A quantitative mixing model between a mixed-source (slab-derived melt and a heterogeneous mantle beneath the volcanic arc) is consistent with local geodynamic parameters, assuming water-saturated conditions within the slab. This model predicts melting of the top several km of the slab (including sediments and oceanic crust) in both TSVZ and CSVZ. The SED:AOC ratio differs in the TSVZ (60:30) and in the CSVZ (30:70), whereas the amount of slab-derived melt added to the mantle wedge is higher in the CSVZ than in the TSVZ, consistent with the observed geochemical variations.

The NSVZ samples are shifted to higher Sr isotope ratios and delta 8/4, and lower ²⁰⁶Pb/²⁰⁴Pb and Nd isotope ratios, but have similar delta 7/4 than the other volcanic arc samples. This is inconsistent with the pre-existing models of crustal assimilation or subduction erosion of the old sialic upper crust. Looking at a larger scale, there is evidence that both Southern and Northern American plates shared a common history since the Proterozoic (Ramos, 2010). The lower crust in Arizona for example has Sr, Nd and Pb isotope ratios appropriate to explain the NSVZ geochemical isotopic variations. Therefore the lower crust beneath the NSVZ may be similar to the one in Arizona.

Another plausible scenario would be the flow of enriched asthenosphere derived from a plume component (Gough-type) that has been dragged into the Andes by convection of the South Atlantic mantle and then pushed southward via trench-parallel flow, consequently to the slab flattening and eastward arc migration during the Miocene.

Finally, at least three mantle components have been identified in the SVZ: 1) depleted South Atlantic MORB (SAM-D) and 2) enriched South Atlantic MORB (SAM-E), which both were inferred from the normal backarc array in Sr-Nd isotopes, 3) an extra-enriched component in some CSVZ backarc, with high ⁸⁷Sr/⁸⁶Sr, delta 7/4 and delta 8/4, possibly reflecting enriched plums in the lithosphere. There may be an additional component that reached the NSVZ segment through flow of enriched (OIB-type) asthenospheric mantle, with higher ⁸⁷Sr/⁸⁶Sr and delta 8/4, lower ¹⁴³Nd/¹⁴⁴Nd and ²⁰⁶Pb/²⁰⁴Pb and similar delta 7/4 than the TSVZ.

Zusammenfassung

Die Vulkankette im Süden Chiles (im Englischen „Southern Volcanic Zone“, SVZ) hat eine Länge von 1200 km und wird durch Subduktion der Nazcaplatte unter die Südamerikanische Platte angetrieben. An solch langen Subduktionszonen variiert meist die Magmenzusammensetzung entlang des vulkanischen Bogens (im Englischen „volcanic arc“). Diese Änderung der chemischen Zusammensetzung wird durch zahlreiche Faktoren beeinflusst. Der wichtigste Faktor ist die Zusammensetzung des Materials, welches in die Subduktionszone eingetragen wird. Das sind zum einen marine Sedimente, die variieren können in Abhängigkeit vom Klima, welches wiederum die terrestrische Erosion und demnach die Art und die Menge an abgelagertem Material beeinflusst. Zum anderen variiert die Zusammensetzung der abtauchenden ozeanischen Kruste in Abhängigkeit von dem Bereich am Mittelozeanischen Rücken (MOR), an dem sie gebildet wurde. Über die unterschiedliche chemische Zusammensetzung hinaus steigt mit zunehmendem Abstand vom Spreizungszentrum das Alter der ozeanischen Kruste, und damit sinkt ihre Oberflächentemperatur. Dies wirkt sich auf Prozesse der Stofffreisetzung in der Tiefe der Subduktionszone aus. Desweiteren spielen die tektonischen Gegebenheiten der abtauchenden Platte (im Englischen „slab“) eine entscheidende Rolle. Sind z. B. große Bruchzonen oder Störungen vorhanden, so kann Wasser tief in die untere ozeanische Kruste und den oberen Erdmantel eindringen, wodurch sich der Grad der Krustenalteration und möglicherweise auch der der Serpentinisierung des Erdmantels erhöht. Ein weiterer Faktor ist die Subduktionszonengeometrie. Eine tiefer abtauchende Platte wird wärmer, könnte möglicherweise schmelzen und damit den Anteil an inkompatiblen, aber fluid-mobilen Spurenelementen in einer neu entstehenden Schmelze erhöhen. Bei der oberen Platte steigt mit zunehmender Krustenmächtigkeit das Potenzial, dass Krustenmaterial von der aufsteigenden Schmelze assimiliert wird und dass die Schmelze auf ihrem längeren Weg durch die Kruste eine stärkere fraktionierte Kristallisation durchläuft.

Ziel dieser Dissertation ist es, anhand eines umfassenden Datensatzes (Haupt- und Spurenelemente und O-Sr-Nd-Hf-Pb-Isotopen) die Wirkung dieser Faktoren auf die geochemische Zusammensetzung junger basaltischer Gesteine der Vulkankette zu evaluieren. Dafür wurden meist Holozäne, Olivin enthaltenden Gesteine aus der Südchilenischen

Vulkankette zwischen 33°S and 43°S analysiert. Die Ergebnisse werden mit Pleistozänen bis Holozänen Vulkangesteinen des Argentinischen Backarc-Bereiches bis zu einer Distanz von 300 km von der Vulkankette, mit marinen Sedimenten aus dem Tiefseegraben vor Chile und mit Proben vom Grundgebirge der Anden verglichen und in geologischen Zusammenhang gebracht.

Die Proben des Vulkanbogens zeigen eine für Subduktionszonen typische Anreicherung an sehr inkompatiblen und fluid-mobilen Elementen und eine Verarmung in Elementen mit hohen Ionen-Wertigkeiten („High field strength elements“, HFSE) und den schweren Seltenen Erden. Bei den Proben aus dem Backarc-Bereich ist diese Anreicherung und Verarmung generell geringer ausgeprägt, was im Einklang mit einem reduzierten Einfluss durch die abtauchende Platte und folglich mit einem niedrigeren Aufschmelzgrad steht. Die Proben aus dem Übergangsbereich der SVZ („Transitional Southern Volcanic Zone“, TSVZ), zwischen 34.5–38°S, überlappen mit den Backarc-Proben in der Sr und Nd Isotopenzusammensetzung, während die Proben der nördlichen SVZ (NSVZ), zwischen 33–34.5°S, höhere Sr und niedrigere Nd und Hf Isotopenverhältnisse zeigen. Die Proben der Stratovulkane im zentralen Bereich der SVZ (CSVZ), zwischen 38–43°S, sind leicht zu höheren Sr und/oder Nd Isotopenverhältnisse verschoben, während die kleineren monogenetischen Schlackekegel, die sich zwischen den Schichtvulkanen befinden, ähnlich der Proben der TSVZ sind. Alle Proben bilden eine enge Korrelation in den Pb-Isotopendiagrammen. Die Proben des „volcanic arc“ liegen am radiogenen Ende des durch die Backarc-Proben definierten Datenfeldes und überlappen weitgehend die marinen Sedimenten vom Tiefseegraben. Diese Korrelation deutet auf darauf hin, dass diese durch eine Mischung zwischen Südatlantischem mittelozeanischen Rückenbasalt (MORB), subduzierten Grabensedimenten und alterierter Ozeankruste entstanden sind. Basierend auf den Unterschieden im Verhältnis von hoch- zu gering inkompatiblen, fluid-immobilien Elementverhältnissen zwischen den Proben der Vulkankette, den Backarc-Proben und den Grabensedimenten lässt sich die Art der Slabkomponente charakterisieren. In diesem Fall handelt es sich bei der beteiligten Komponente der abtauchenden Platte nicht um eine reine Fluidphase, sondern um eine wässrige Schmelze. Die fehlende Korrelationen von MgO (oder SiO₂) mit radiogenen Isotopenverhältnissen und die deutliche Korrelation der Pb-Isotopenverhältnisse schließen eine signifikante Assimilation der alten sialischen Kruste im

Bereich der TSVZ und CSVZ aus. Hf-Nd Isotopenverhältnisse definieren jeweils eine eigene lineare Korrelation für den „volcanic arc“ und Backarc-Bereich, wobei keiner linear zu den subduzierten Sedimenten liegt, was möglicherweise die Beteiligung von asthenosphärischem Mantel für die Vulkankette und angereicherter proterozoischer Lithosphäre im Backarc-Bereich widerspiegelt. Zusätzlich zeigen einige Backarc-Proben eine angereicherte Komponente mit etwas höheren Sr aber niedrigeren Nd und Hf Isotopenverhältnissen und erhöhtem, $\delta^{7/4}$ und $\delta^{8/4}$ was auf die Beteiligung einer anderen angereicherten Mantelkomponente, möglicherweise subkontinentale Lithosphäre, hindeutet.

Obwohl die kleinen monogenetischen Schlackekegel der CSVZ den Schichtvulkane der TSVZ geochemisch ähneln, haben die Schichtvulkane der CSVZ höhere fluid-mobil / fluid-immobil Elementverhältnisse und geringere höher / weniger-inkompatible fluid-immobile Elementverhältnisse, was im Einklang mit einem insgesamt höheren Fluidanteil und höherem Schmelzgrad im Bereich der CSVZ steht. Die höheren Hf-Nd Isotopenverhältnisse der Stratovulkane deuten darauf hin, dass die Mantelquelle unter der CSVZ stärker verarmt ist. Zusammen mit geomorphologischen und geophysikalischen Beobachtungen lassen die geochemischen Charakteristika darauf schließen, dass die abtauchende Platte unter der CSVZ erhöhte Mengen an Fluiden sowie die Signatur von Tiefseesedimenten in das System speist. Die Hydratisierung der abtauchenden Platte ist wahrscheinlich auf starke Interaktion mit Seewasser aufgrund der zahlreichen Bruchzonen und Störungen in diesem Bereich zurückzuführen, wodurch die Ozeankruste alteriert und möglicherweise auch der oberer Erdmantel serpentinisiert.

Die $\delta^{18}\text{O}$ -Werte der Schmelze, gemessen in der Grundmasse oder konvertiert von Olivine durch Hinzufügen von 0.6‰, befinden sich innerhalb der durch MORB definierten Bereiche. Proben aus der TSVZ, der monogenetischen Schlackekegel der CSVZ, und dem Backarc sind immer innerhalb der Ozeanbögen, weitestgehend überlappend mit dem MORB Bereich. Hingegen sind die CSVZ Stratovulkanproben unterhalb dieses Bereiches. Sie zeigen möglicherweise einen Einfluss von der hydratisierten Platte. Unerwarteterweise befinden sich die NSVZ Proben innerhalb des MORB Bereichs. Da sie weder mit Differenzierungsparametern

wie zum Beispiel SiO_2 oder MgO noch mit Isotopen korrelieren, kann eine Krustenassimilation ausgeschlossen werden.

Ein quantitatives Mischungsmodell einer gemischten Quelle (von einer Platte stammenden Schmelze und einem heterogenen Mantel unter dem Vulkanbogen) steht im Einklang mit den lokalen geodynamischen Parametern, vorausgesetzt, es bestehen wassergesättigte Bedingungen innerhalb der abtauchenden Platte. Dieses Modell zeigt, dass es zum Schmelzen der oberen Kilometer der Platte (einschließlich der Sedimente (SED) und der alterierten ozeanischen Kruste (AOC), sowohl im Bereich der TSVZ als auch im Bereich der CSVZ, kommt. Das SED:AOC Verhältnis der TSVZ (60:30) unterscheidet sich von dem der CSVZ (30:70), wobei die Menge der Schmelze, die durch die abtauchende Platte entstanden ist und dem Mantelkeil hinzugefügt wird, in der CSVZ höher ist als in der TSVZ. Dies ist im Einklang mit den beobachteten geochemischen Variationen.

Die NSVZ Proben sind zu höheren Sr-Isotopenverhältnissen und $\delta^{87}\text{Sr}/^{86}\text{Sr}$, und niedrigeren $^{206}\text{Pb}/^{204}\text{Pb}$ und Nd Isotopenverhältnissen verschoben, haben aber ähnliche $\delta^{143}\text{Nd}/^{142}\text{Nd}$ wie andere „volcanic arc“-Proben. Dies ist nicht mit den bereits in der Literatur bestehenden Modellen der Krustenassimilation oder subduktionsinduzierter Erosion der alten sialischen oberen Kruste in Einklang zu bringen. Großräumig gibt es Nachweise, dass die Süd- und Nordamerikanischen Platten seit der Proterozoischen Zeit eine gemeinsame Geschichte haben (Ramos, 2010). Beispielweise könnte die untere Kruste von Arizona vergleichbar sein mit der unteren Kruste unter der NSVZ. Die untere Kruste von Arizona hat Sr, Nd und Pb-Isotopenverhältnisse, mit denen die geochemischen Variationen der NSVZ erklärt werden können. Somit könnte die untere Kruste der NSVZ derjenigen von Arizona sehr ähnlich sein.

Ein weiteres mögliches Szenario schließt den Transport einer angereicherten Plumekomponente ein (EM-1, ähnlich der Zusammensetzung der Gough Ozeaninsel im Südatlantik). Diese Plumekomponente konnte dadurch in das System gelangen, dass sich die abtauchende Platte während des Miozäns abflachte und sich weiter nach Osten verschob. Mantelkonvektion im Südatlantik führte dann zu einem Materialfluss parallel zum Tiefseegraben, und in der Folge dazu, dass dieses Material in den Andinischen Vulkanismus eingetragen werden konnte.

Zusammenfassend konnten mindestens drei Mantelkomponenten in der SVZ identifiziert werden: 1) verarmter südatlantischer mittelozeanischer Rückenbasalt (SAM-D), 2) angereicherter südatlantischer mittelozeanischer Rückenbasalt (SAM-E), beide ergeben sich aus dem Backarc-Datenfeld in den Sr- und Nd-Isotopenverhältnissen, 3) eine zusätzlich angereicherte Komponente in einigen CSVZ Backarc-Proben mit hohem $^{87}\text{Sr}/^{86}\text{Sr}$, $\delta 7/4$ und $\delta 8/4$, was möglicherweise das Vorkommen von angereicherten Arealen in der Lithosphäre widerspiegelt. Darüber hinaus könnte durch Mantelfluss eine weitere Komponente unter die NSVZ gelangt sein, die aus angereichertem (OIB-Typ) astenosphärischen Mantel mit höheren $^{87}\text{Sr}/^{86}\text{Sr}$ und $\delta 8/4$, niedrigeren $^{143}\text{Nd}/^{144}\text{Nd}$ und $^{206}\text{Pb}/^{204}\text{Pb}$ und ähnlichem $\delta 7/4$ wie im Bereich der TSVZ besteht.

Chapter 1

General Introduction and Thesis outline

1.1 Introduction

1.1.1 Subduction zone tectonic

In contrast to other planets of our Solar System, Earth is still an active planet where Plate Tectonics is a fundamental process. Plates can move apart at Mid-Ocean Ridges (e.g. the Mid-Atlantic Ridge), move along transform faults (e.g. the San Andreas Fault in California) or converge with each other. Subduction zones are the result of the convergence between an oceanic plate (oceanic crust and lithospheric mantle) and another oceanic or a continental plate (continental crust and subcontinental lithospheric mantle) (Stern, 2002). The colder oceanic (and therefore denser) plate will dive beneath the less dense oceanic or continental plate. Therefore, excess density is the force that drives plate tectonics, and the going-down slab induces mantle convection (Stern, 2002). Subduction zones are also the place where most of the continental crust is created.

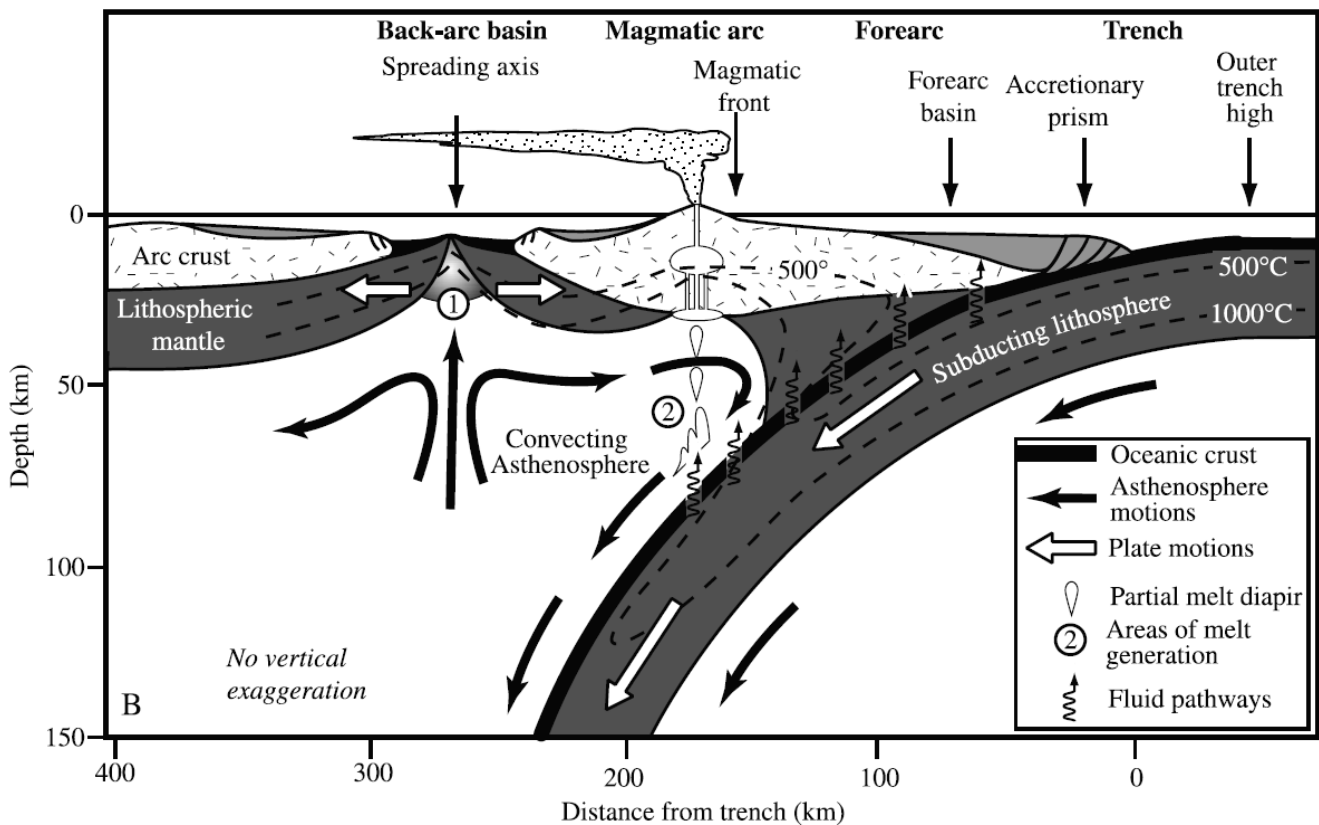


Figure 1.1 (Previous page) Schematic profile view of a subduction zone (Stern, 2002). The subducting lithosphere (including sediments, the oceanic crust and the lithospheric mantle) dives beneath the continental lithosphere and will be subject to different dehydration and melting processes as the slab goes down. The volcanic front magmatism results from the incorporation of these fluids/melts into the convecting mantle wedge (2). The backarc magmatism results from decompression melting (1).

Subduction zones are where most great earthquakes and important and dangerous explosive volcanic activities occur (e.g. the Ring of Fire around the Pacific Ocean). Millions of people live within the range of earthquakes and volcanic eruptions (e.g. Japan, Chile, Central America etc.).

1.1.2 Subduction zone magmatism

The subducting oceanic plate includes pelagic and continent-derived trench sediments, hydrothermally Altered Oceanic Crust (AOC), and lithospheric mantle that together are known as the “slab”. The overriding plate includes the crust (oceanic or continental), the lithospheric mantle, and the underlying asthenospheric mantle wedge.

The oceanic crust becomes progressively hydrated from its formation at the Mid-Ocean Ridge to its subduction at the trench. Hydration also occurs at fracture zones and bend-faults as the plate flexes on approach to the trench. The slab, while moving downward, undergoes increasing temperature and pressure, which causes compaction and dehydration during metamorphic reactions (greenschist > blueschist > eclogite). Dehydration releases volatiles (e.g. H₂O) and fluid-mobile elements (e.g. Pb, U, K) from the sediments, the oceanic crust, and the lithospheric mantle (e.g. Schmidt and Poli, 1998). The fluids released will infiltrate the mantle wedge, lowering the solidus of the mantle and causing partial melting (Stern, 2002). While most of the sediment dewatering occurs at <20 km depth beneath the forearc, at greater depth (> 100 km), serpentine will break down and consequently release an important source of water (Peacock, 2001). In some cases, the temperature is high enough to provoke melting of the sediments (e.g. Elliot et al., 1997, Plank, 2005) and/or of the AOC (e.g. Johnson and Plank, 1999, Tollstrup et al., 2010). Therefore, melting will release less-fluid mobile but incompatible elements such as Th (Elliot et al., 1997). Material recycling is an important process that occurs

at subduction zones (e.g. Plank and Langmuir, 1993, Elliot et al., 1997). The elements that are not recycled will be stored deep in the Earth, waiting to be heated up again and to form mantle plumes (Hofmann, 1997).

Therefore, arc volcanic rocks carry important information about the magma sources and the processes that affect the magma during its ascent. Typical subduction zone volcanic rocks display enrichment in fluid-mobile elements such as Rb, Ba, U, Pb, K, as explained above. Depletion in High Field Strength Elements (HFSE) such as Nb, Ta and Heavy Rare Earth Elements (HREE) is explained by high degrees of mantle partial melting of more depleted mantle sources. The retention of these elements in refractory minerals during dehydration causes also depletion. Ratios of more- to less-fluid-mobile to fluid-immobile elements (e.g. Pb/Ce, Ba/Nb, U/Th) can assess the fluid fluxes while ratios of incompatible to compatible elements (e.g. Nb/Yb, La/Yb) provide information about the degree of mantle partial melting and depletion. Trace elements are sensitive to physical processes, such as magma differentiation. Radiogenic isotopes (e.g. Sr, Nd, Hf, Pb) are not fractionated at magmatic temperature and provide good information about the source components and/or the shallow-level processes that affect the magma such as assimilation of the continental crust.

1.2 Studied area and dissertation outline

1.2.1 The Andes

The Andean Cordillera is a 7,500 km long volcanic chain in South America, extending from Colombia to south Chile. The cordillera is divided into four active segments (e.g. see Stern, 2004): the Northern Volcanic Zone (NVZ; 5°N-2°S) in Colombia and Ecuador, the Central Volcanic Zone (CVZ; 16-28°S) in Peru and northern Chile, the Southern Volcanic Zone (SVZ, 33-46°S) in Central Chile, and the Austral Volcanic Zone (AVZ; 49-54°S) in southern Chile. Volcanism occurs when the slab dip angle is greater than 25°. Volcanic gaps divide the segments where dip

angles are less than 10°. This dissertation focuses on the SVZ in Chile and the associated backarc in Argentina.

1.2.2 The Southern Volcanic Zone

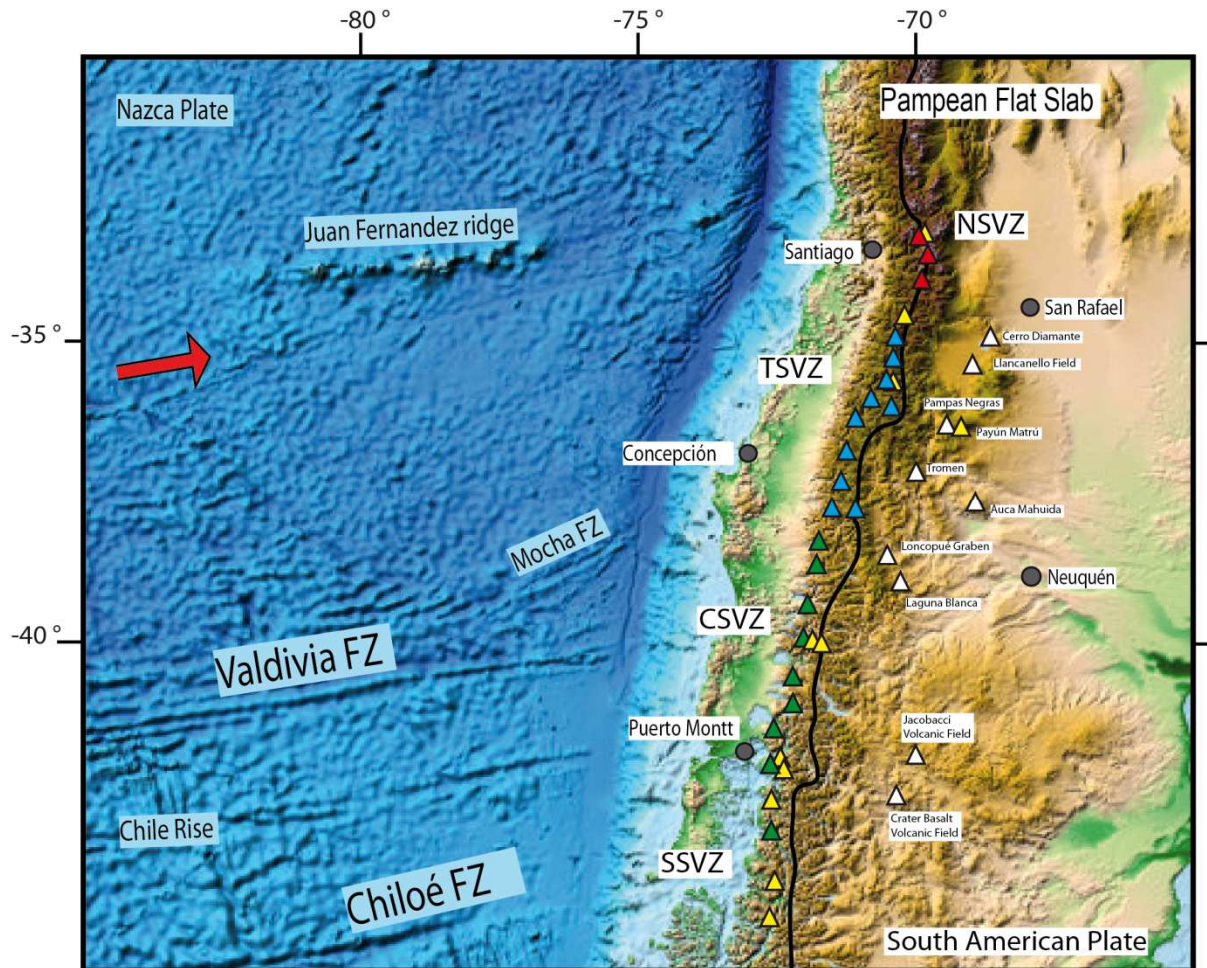


Figure 1.2 Overview map of the Southern Volcanic in Zone (SVZ) in Chile between 30°S and 45°S and the backarc in Argentina. Red, blue and green triangles = studied Northern SVZ, Transitional SVZ and Central SVZ volcanic arc centers, respectively. White triangles = major sampling sites in the backarc in Argentina. Yellow triangles = other non-studied volcanoes. The red, blue and green boxes includes the three segments of the Northern SVZ, Transitional SVZ and Central SVZ, respectively, delimited in this dissertation. The general movement of the Nazca Plate beneath the South American Plate is indicated by the red arrow. The thick black line shows the schematic border between Chile and Argentina. Grey circles = major cities. The ETOPO1 map source is from NOAA, modified (Amante and Eakins, 2009).

Volcanism in the SVZ results from the oblique convergence of the Nazca Plate (7-9 cm/year) beneath the South American Plate. It consists of more than 60 Cenozoic to Quaternary active volcanoes, three silicic caldera systems, and numerous minor eruptive centers (Stern, 2004). It has been divided into different segments based on the geochemistry of the erupted rocks (e.g. López-Escobar et al., 1995). These segments are: the Northern Southern Volcanic Zone (NSVZ; 33°-34.5°S; e.g. Hildreth and Moorbath, 1988), the Transitional Southern Volcanic Zone (TSVZ; 34.5-37°S; e.g. Tormey et al., 1991), the Central Southern Volcanic Zone (CSVZ; 37.0-41.5°S; e.g. Hickey-Vargas et al., 1984, 1986, 1989) and the Southern Southern Volcanic Zone (SSVZ; 41.5-46°S; e.g. Naranjo and Stern, 2004). Other authors have divided the SVZ differently (e.g. Dungan et al., 2001): the Tupungato-Maipo Segment (TMS, 33°-34.2°S), the Palomo-Tatara Segment (PTS, 34.7°-36°S), and the Longaví-Osorno Segment (LOS, 36.2°-42°S) (e.g. Sellés et al., 2004).

The age of the Nazca Plate along-strike of the arc varies from 0 Ma at 46°S at the triple Junction between the Nazca, Antarctic and South American Plates, to 36 Ma at 33°S where the Juan Fernández Ridge subducts. The Nazca Plate currently subducting north of the Valdivia Fracture Zone (40°S) formed at the East Pacific Rise and at the Chilean Ridge further south (Herron et al., 1981; Tebbens and Cande, 1997; Tebbens et al., 1997). Offshore of the CSVZ, more bend-faults and major fracture zones can be observed (e.g. Contreras-Reyes, 2007). The Chilean Trench is flooded with sediments, mostly-continent-derived turbidites (e.g. Völker et al., 2008). The pelagic section at the base of the sediment is not well-known, but is estimated to be 100-150 m thick. The continental character of the sediments increases southward, where the climate favours greater erosion of the Andean basement (Plank, 2011).

The continental crustal thickness beneath the SVZ reaches a maximum of 60 km in the northern segment (at 33°S), and decreases to 30 km in the southern segment (at 43°S) (Völker et al., 2011). The depth of the slab varies from 100 km beneath the NSVZ and CSVZ, to 140 km beneath the TSVZ (Tassara et al., 2006). As a result, the asthenospheric mantle wedge thickness varies from 40 to 100 km.

The Andean basement consists primarily of Mesozoic and Cenozoic volcanic and sedimentary rocks intruded by Miocene to Pliocene plutons. The central valley west of the

volcanic arc is covered the same Mesozoic and Cenozoic volcano-sedimentary units, intruded by Mesozoic plutons. The Meso-Cenozoic volcano-sedimentary cover may be underlain by Paleozoic metamorphic rocks which outcrop east of the volcanic arc in the cordillera frontal (Hildreth and Moorbath, 1988). On the coast, metamorphic meta-sedimentary rocks are intruded by Carboniferous to Permian batholiths (e.g. Stern, 2004; Lucassen et al., 2004; Cembrano and Lara, 2009).

1.2.3 Thesis outline

I conducted an along- and across-arc geochemical characterization (major and trace elements, and Sr-Nd-Hf-Pb-O isotopes) of the magmatic output, from the volcanic front volcanoes to the isolated cinder cones in the backarc, in order to identify the different sources and components that affect Andean volcanism. The major goal of this PhD thesis is to constrain the spatial variations of material cycling and its interaction with the mantle wedge through the subduction zone.

I analyzed mostly young, mafic olivine-bearing volcanic rocks. Trench sediments and Andean basement samples also were collected and analyzed in order to better constrain the influence of these sources.

My Ph.D is divided into three inter-dependant chapters, each of them focusing on one key segment of the SVZ.

Chapter two focuses on the TSVZ volcanic arc (34.5-38°S) and extending up to 300 km into the backarc. This chapter constrains the role of the slab inputs (sediments and oceanic crust) in generating arc lavas, whereas the backarc samples help to constrain the mantle heterogeneity in trace elements and isotopes prior to being metasomatized by fluids and melts from the slab. This segment is used as a “baseline” for the subduction input, and is compared to the other segments in the next chapters. This chapter has been accepted for publication in *Geochimica et Cosmochimica Acta*.

Chapter three focuses on the CSVZ (38-43°S). It investigates the role of slab-derived fluids in generating arc magmas. The more prominent and numerous fracture zones and bend faults in this segment provide pathways for seawater alteration of the oceanic crust and serpentinization of the underlying lithospheric mantle. Although the slab inputs are similar to the TSVZ, the geochemistry of the CSVZ statovolcanoes differs from the adjacent cinder cones and the TSVZ statovolcanoes because of differences in the amount and nature of slab fluid. Whereas most of the CSVZ backarc basalts are similar in composition to those in the TSVZ backarc, an extra-enriched component derived from the lithospheric mantle, is observed. This chapter was submitted to *Chemical Geology*.

Chapter four focuses on the NSVZ (33-34.5°S). Two models – assimilation and subduction erosion of the continental crust – have been proposed for this segment where the crust is thick and obvious enrichment in radiogenic isotopes occurs. Subduction erosion of the lower crust may cause the isotopic enrichment. Alternatively, I propose that these traits reflect an enriched asthenospheric mantle derived from a Plume-type component, flowing beneath the NSVZ via trench parallel flow. Taken together, the SVZ volcanic and backarc data constrain the different mantle component present in the lithosphere and asthenosphere. This chapter is in preparation for submission to *Earth and Planetary Science Letters*.

Chapter 2

Across-arc geochemical variations in the Southern Volcanic Zone, Chile (34.5- 38.0°S): Constraints on Mantle Wedge and Slab Input Compositions

This chapter was accepted for publication in *Geochimica et Cosmochimica Acta* in May 13Th 2013

Co-authors: Kaj Hoernle, James Gill, Folkmar Hauff, Heidi Wehrmann, Dieter Garbe-Schönberg, Paul van den Bogaard, Ilya Bindeman, Luis E. Lara

DOI: <http://dx.doi.org/10.1016/j.gca.2013.05.016>

Chapter overview

Crustal assimilation (e.g. Hildreth and Moorbath, 1988) and/or subduction erosion (e.g. Stern, 1991; Kay et al., 2005) are believed to control the geochemical variations along the northern portion of the Chilean Southern Volcanic Zone. In order to evaluate these hypotheses, we present a comprehensive geochemical data set (major and trace elements and O-Sr-Nd-Hf-Pb isotopes) from Holocene primarily olivine-bearing volcanic rocks across the arc between 34.5-38.0°S, including volcanic front centers from Tinguiririca to Callaqui, the rear arc centers of Infernillo Volcanic Field, Laguna del Maule and Copahue, and extending 300 km into the backarc. We also present an equivalent data set for Chile Trench sediments outboard of this profile. The volcanic arc (including volcanic front and rear arc) samples primarily range from basalt to andesite/trachyandesite, whereas the backarc rocks are low-silica alkali basalts and trachybasalts. All samples show some characteristic subduction zone trace element enrichments and depletions, but the backarc samples show the least. Backarc basalts have higher Ce/Pb, Nb/U, Nb/Zr, and Ta/Hf, and lower Ba/Nb and Ba/La, consistent with less of a slab-derived component in the backarc and, consequently, lower degrees of mantle melting. The mantle-like $\delta^{18}\text{O}$ in olivine and plagioclase phenocrysts (volcanic arc = 4.9-5.6 and backarc = 5.0-5.4 per mil) and lack of correlation between $\delta^{18}\text{O}$ and indices of differentiation and other isotope ratios, argue against significant crustal assimilation. Volcanic arc and backarc samples almost completely overlap in Sr and Nd isotopic composition. High precision (double-spike) Pb isotope ratios are tightly correlated, precluding significant assimilation of older sialic crust but indicating mixing between a South Atlantic Mid Ocean-Ridge Basalt (MORB) source and a slab component derived from subducted sediments and altered oceanic crust. Hf-Nd isotope ratios define separate linear arrays for the volcanic arc and backarc, neither of which trend toward subducting sediment, possibly reflecting a primarily asthenospheric mantle array for the volcanic arc and involvement of enriched Proterozoic lithospheric mantle in the backarc. We propose a quantitative mixing model between a mixed-source, slab-derived melt and a heterogeneous mantle beneath the volcanic arc. The model is consistent with local geodynamic parameters, assuming water-saturated conditions within the slab.

2.1 Introduction

The Chilean Southern Volcanic Zone (SVZ) extends from 33°S, just south of where the Juan Fernandez ridge is subducting and the crust of the overriding plate is ~60 km thick, to 46°S where the Chile Ridge is subducting and the crust is ~30 km thick. About 70% of the Chilean population live close to some of the most active volcanoes in the Andes along the SVZ (Stern, 2004). In this paper we report data for an across-arc profile between 34.5-38.0°S that overlaps and extends slightly further south than the Transitional Southern Volcanic Zone (TSVZ), 34.5-37.0°S, of Tormey et al. (1991). We also report data for trench sediments being subducted outboard of this region. The 1932 eruption at Quizapu volcano, one of the largest Plinian eruptions of an Andean volcano in historical time and older highly explosive silicic ignimbrite-forming eruptions that formed giant calderas, such as the Diamante caldera, took place in this part of the SVZ.

There are several potential sources for arc magmas in continental margin subduction zones: the subducting slab (including pelagic and continentally-derived trench sediments, seawater-altered upper oceanic crust, lower oceanic crust and possibly serpentinites in the subducting lithospheric mantle), the overlying mantle wedge, and the overriding lithosphere (including both continental crust and lithospheric mantle). In order to evaluate the relative role of these potential sources in generating the volcanism in the TSVZ, we present a new and comprehensive geochemical data set, including major and trace elements and Sr, Nd, Hf, O and high resolution Pb double spike isotope ratios, for primarily olivine-bearing Holocene and Late Pleistocene lavas and trench sediments from the region. Our igneous samples are from both the volcanic arc (VA), which includes the volcanic front in Chile and the rear arc up to 70 km behind the volcanic front in Chile/Argentina, and backarc (BA) volcanic centers in Argentina that are 100 to 300 km behind the volcanic front.

2.2 Geological setting

Andean volcanism results from the subduction of the Nazca (7-9 cm/year towards the northeast) and Antarctic plates (2 cm/year) beneath the South American Plate (Norabuena et al., 1998; Angermann et al., 1999). The Andean cordillera is more than 7,500 km long, extending from Colombia to southern Chile. There are four active segments divided by volcanic gaps. They have been termed the Northern Volcanic Zone (NVZ; 5°N-2°S) in Colombia and Ecuador, the Central Volcanic Zone (CVZ; 14-27°S) in Peru and northern Chile, the Southern Volcanic Zone (SVZ, 33-46°S) in central Chile, and the Austral Volcanic Zone (AVZ; 49-55°S) in southern Chile. Volcanism occurs when the slab dip angle is steep ($>25^\circ$), whereas volcanic gaps occur where subduction dip angles are shallow ($<10^\circ$) (Stern, 2004).

The SVZ consists of over 60 Quaternary volcanoes in Chile and Argentina, three silicic caldera systems and numerous minor eruptive centers (Stern, 2004). The SVZ has been divided into the Northern Southern Volcanic Zone (NSVZ; 33°-34.5°S; e.g. Hildreth and Moorbath, 1988), the Transitional Southern Volcanic Zone (TSVZ; 34.5-37°S; e.g. Tormey et al., 1991), the Central Southern Volcanic Zone (CSVZ; 37.0-41.5°S; e.g. Hickey-Vargas et al., 1984, 1986, 1989) and the Southern Southern Volcanic Zone (SSVZ; 41.5-46°S; e.g. Naranjo and Stern, 2004), based on the geochemical characteristics of the erupted rocks (see also López-Escobar et al., 1995) (Figure 1a). Other authors have divided the SVZ differently (e.g. Dungan et al., 2001): the Tupungato-Maipo Segment (TMS, 33°-34.2°S), located entirely on thick crust; the Palomo-Tatara Segment (PTS, 34.7°-36°S), where the frontal arc centers lie west of the continental divide; and the Longaví-Osorno Segment (LOS, 36.2°-42°S), where the southernmost chain lies near the topographic front of the Cordillera (see also Sellés et al., 2004 for further discussion of SVZ segmentation).

The TSVZ and related backarc centers, which provide information on the mantle wedge composition, are the focus of this study (Figure 1b). Our volcanic arc (VA) samples are from nine Quaternary centers at the volcanic front that are denoted by blue circles in Figure 1b for centers north of 36°S (Tinguiririca, Planchón-Peteroa, and the Los Hornitos and the Resolana cones in the area of Cerro Azul), referred to as the northern volcanic arc, and blue diamonds for

centers south of 36°S (San Pedro and its nearby cones, Nevado del Longaví, Chillán and its nearby cones, Antuco and Callaqui), referred to as the southern volcanic arc.

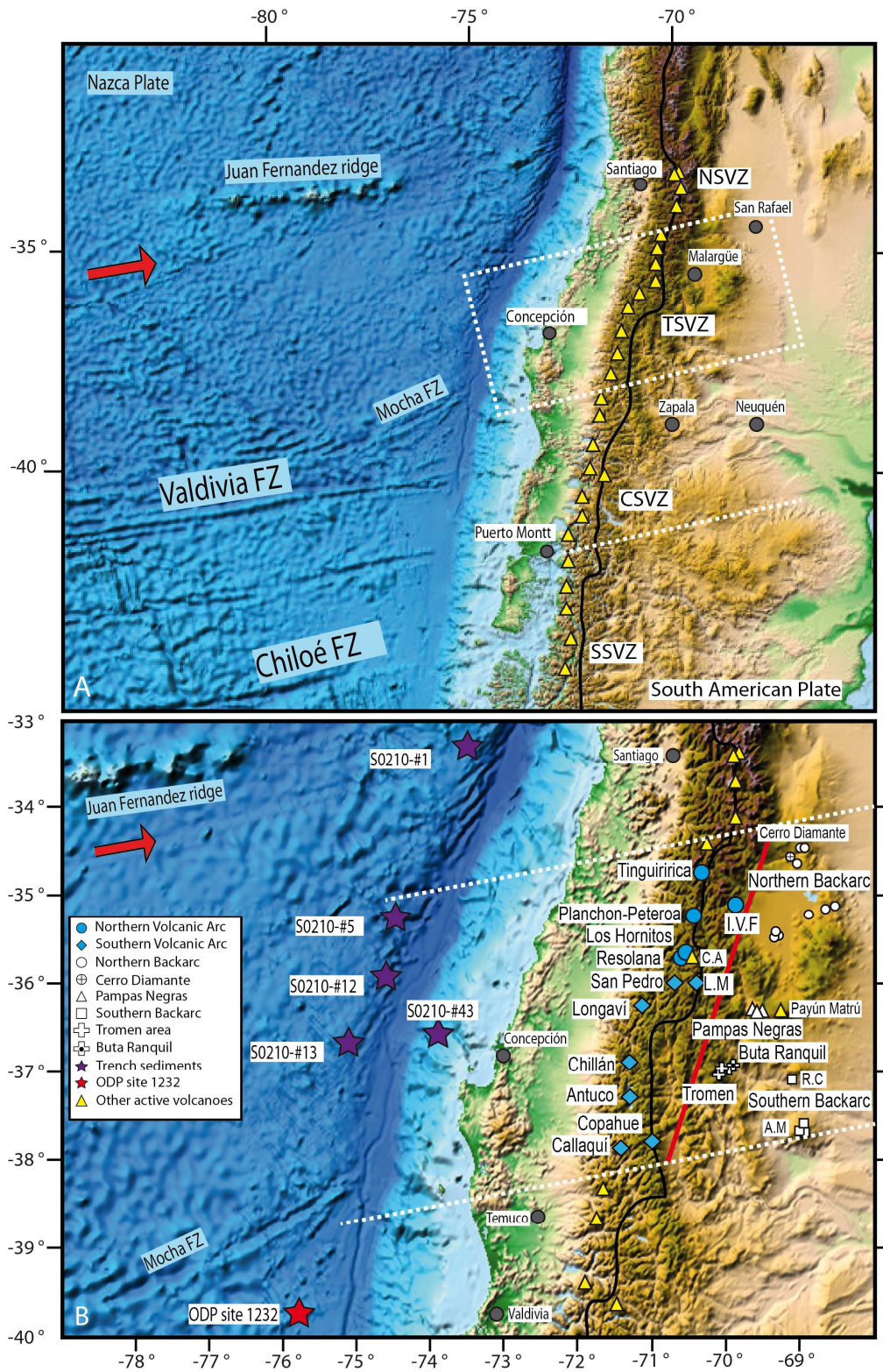


Figure 2.1 (Previous page) (a) Map of the Southern Volcanic Zone (SVZ) in Chile and Argentina between 30° and 45°S. Yellow triangles = Quaternary active volcanic front volcanoes. (b) Map of the Transitional Southern Volcanic Zone (TSVZ) between 34.5°S and 38°S. Red line = separates the Volcanic Arc (VA) and rear arc centers from the Backarc (BA). Blue circles and diamonds = northern and southern VA centers, respectively. Open circles = cinder cones from the Northern Backarc (NBA). Open circle with a cross = the Cerro Diamante stratovolcano that was an active arc center in the Miocene. Open triangles = central BA Pampas Negras volcanic field. Open = Southern Backarc (SBA; Auca Mahuida and Rio Colorado volcanic fields). Open crosses = Tromen stratovolcano area. Open cross with a dot = Buta Ranquil monogenetic center at the foot of Tromen. Yellow triangles = other Quaternary active VA volcanoes. Grey filled circles = major cities. Purple stars = the location of the SO210 cruise sediments. Red star = location of ODP site 1232. The white dashed lines bracket the TSVZ transect. The thick black line represents the border between Chile and Argentina. C.A. = Cerro Azul, L.M. = Laguna del Maule, I.V.F. = Infernillo Volcanic Field, R.C. = Rio Colorado, A.M. = Auca Mahuida. The ETOPO1 map source is from NOAA, modified (Amante and Eakins, 2009).

It also includes three areas in the rear arc, located up to 70 km behind the front. From north to south they are the Infernillo Volcanic Field (Folguera et al., 2009, Gudnason et al., 2012), the Laguna del Maule volcanic complex (Hildreth et al., 2010), and the Copahue stratovolcano. They are grouped together as rear arc volcanism in the tables but included in the appropriate VA group in the figures.

The backarc (BA) domain, from 100 km to 300 km behind the volcanic front is known as the Payenia volcanic field (Munoz and Stern, 1988, Stern, 1989) and volcanic centers are denoted by open symbols in Figure 1b. Some authors include the Payenia field in the larger Patagonian mafic volcanic province (Kay et al, 2004, Bertotto et al., 2009), while others keep it separate for geological and tectonic reasons (Ramos and Folguera, 2011). The Payenia volcanic field covers more than 40,000 km² between 34°S-38°S with an estimated volume of 8400 km³ erupted from more than 800 centers in the last 2 Ma. The K-Ar ages of the volcanic centers between 34.5° and 35.5° range from 1.8 to <0.01 Ma (Folguera et al., 2009; Ramos and Folguera, 2011 and references therein). Eruptions were episodic with distinct spatial and temporal patterns. Eruptions near San Rafael in the north took place between 1.8-0.7 Ma, whereas those near Malargüe were younger, 0.1-0.01 Ma. The Pampas Negras volcanic field erupted from 320 ka to recent, and the Auca Mahuida field (including Auca Mahuida Volcano and cinder cones to the north along the Rio Colorado) erupted between 2.1-0.34 Ma (Gudnason et al., 2012). We have divided the Payenia volcanic field into three segments: northern, central and southern. Our samples from the northern BA segment (NBA between 34.5-35.5°S; open circles in the figures), behind the northern volcanic front, are from the monogenetic cones near San Rafael and Malargüe, and the Cerro Diamante stratovolcano and nearby cones. Samples

from the Cerro Diamante stratovolcano are denoted with a circle enclosing a cross, because it may be affected by processes related to the Miocene volcanic front (Kay et al., 2004, 2005, Kay and Copeland, 2006, Kay et al. 2006a,b and references therein). The central segment samples are from the Late Pleistocene to Holocene Pampas Negras cones (36.0-36.5°S; open triangles in the figures) at the western end of a rift system extending from the Payún Matrú caldera. The southern BA segment (SBA between 37.0-38.0°S; open squares in the figures) includes the Auca Mahuida shield volcano that is farthest from the VA, the Rio Colorado volcanic field, and the Tromen stratovolcano (open crosses). The Buta Ranquil sample (open cross with a dot inside) is from a monogenetic cone at the foot of Tromen. The Tromen samples may have been affected by the same processes as at Cerro Diamante. Most samples are Late Pleistocene to Holocene in age (Table 1).

The subducted Nazca Plate formed at the East Pacific Rise north of the Valdivia Fracture Zone (40°S) and at the Chilean Rise further south (Herron et al., 1981; Tebbens et al., 1997 a,b). Its age increases towards the north, from ~30 Ma at 38°S to ~35 Ma at 34.5°S. Only one fracture zone appears to be subducting beneath the TSVZ - an extension of the Mocha Fracture Zone at 38°S that might project beneath the area near Longaví (Sellés et al., 2004; Contreras-Reyes et al., 2008). This fracture zone, however, is not nearly as prominent as the Valdivia and other fracture zones further south (Figure 1a).

The trench contains 1.0 km of sediments (Plank, 2011). Chilean trench sediments are mostly continentally-derived turbidites eroded from the Andean arc (Völker et al., 2008). Their trace element and Sr-Nd-Pb isotope compositions are similar to those of the Cretaceous to Holocene magmatic arc (Lucassen et al., 2010). ODP site 1232 is located at 39.9°S, 75.9°W in the Chile basin on the Nazca Plate ~50 km outboard of the trench (Figure 1b). Its sediments are mostly continentally-derived turbidites (Mix et al., 2003; Lucassen et al., 2010).

The crust beneath the VA, especially from San Pedro to Tinguiririca where the volcanic front steps eastward onto the Cordillera, is believed to be relatively thick based on interpretations of regional gravity data (~35-45 km, Hildreth and Moorbath, 1988; Völker et al., 2011), but thinner than in the NSVZ where it reaches a maximum thickness of 60 km. The exposed basement of the volcanic arc consists primarily of Mesozoic and Cenozoic volcanic and

sedimentary rocks intruded by Miocene to Pliocene plutons. Near the coast, metamorphic meta-sedimentary rocks are intruded by Carboniferous to Permian batholiths (e.g. Stern, 2004; Lucassen et al., 2004; Cembrano and Lara, 2009). In the backarc, the San Rafael block consists of Paleozoic rocks that were uplifted during the late Miocene. There is evidence of extensional deformation in the areas where crustal attenuation occurred (Gilbert et al., 2006, Yuan et al., 2006). The depth of the slab beneath the TSVZ volcanic front is relatively uniform in this part of Chile and lies between 120 and 140 km (Tassara et al., 2006). Due to relatively uniform crustal thicknesses and depths to the slab, the thickness of the intervening asthenospheric wedge beneath the VA is also relatively uniform and ranges from 60 to 80 km (Tassara et al., 2006; Völker et al., 2011). Magnetotelluric data indicate the presence of a low resistivity plume-like zone beneath the Payenia volcanic field, presently concentrated under the Payún Matrú caldera. This region of low resistivity is rooted deeper than 200 km, just above the projected Nazca Plate (Burd et al., 2008, Ramos and Folguera, 2011).

2.3 Sample collection, preparation, and analytical methods

The youngest and freshest, mostly olivine-bearing volcanic rocks (lava and tephra) were collected from each volcanic area along the volcanic front from Tinguiririca to Callaqui volcanoes and in the adjacent BA from 34.5°S to 38°S. During fieldwork, units containing xenolithic or xenocrystic material were avoided or only sampled where there was no obvious foreign material present, in an attempt to minimize crustal contamination. Their GPS-based locations, the presence or absence of olivine phenocrysts, and age estimates are presented in Table 1. We also collected sediment samples during the October 2010 RV SONNE SO210 cruise. They come from gravity cores taken from the incoming Nazca Plate (12 m length) and from the Biobio Canyon in the trench (6 m length) (33.20°-36.63°S, Figure 1b). Descriptions of the cores are available in the SO210 cruise report (Linke et al., 2011, [www.dfg-ozean.de/fileadmin/DFG/Berichte METEOR/Fahrtbericht Sonne 210.pdf](http://www.dfg-ozean.de/fileadmin/DFG/Berichte_METEOR/Fahrtbericht_Sonne_210.pdf)). The cores were relatively homogeneous, consisting mostly of clay, silt, and sand derived mostly from the

volcanic arc (Lucassen et al., 2010). We avoided ash layers in order to minimize the direct input of arc products. Two representative samples per core were analyzed.

Hardrock samples were crushed, sieved, and washed in distilled water in an ultrasonic bath. In order to minimize the effects of alteration and crustal contamination, 5-10 g of 1-2 mm size chips were carefully handpicked under a binocular microscope to ensure selection of the freshest part of the rock and to avoid xenocrystic and xenolithic material and tephra or lava pieces with vesicle fill. Handpicked chips were powdered in an agate mill to obtain homogenous powders for XRF and ICPMS analysis. Chips were used for isotope analysis. Fresh olivine and plagioclase phenocrysts were carefully selected for oxygen isotope analysis to avoid inclusions and attached matrix.

Major element compositions were obtained at GEOMAR and at the Institute of Geosciences at the University of Kiel, both on a Phillips X'Unique PW 1480 XRF. Several reference materials (JB-2, JB-3, JA-2, BHVO-2, HTB-1, OU) were also analyzed, and yielded deviations of <5% from the published reference values (Govindaraju, 1994; Potts and Kane, 2005; Webb et al., 2009). The sediments were analysed at the University of Hamburg on a MagixPro PW 2540 XRF.

Matrix glass compositions of Planchón-Peteroa, Los Hornitos and Antuco samples were determined by electron microprobe with a Jeol JXA 8200 at GEOMAR, using polished glass shard mounts and petrographic thin sections. An accelerating voltage of 15 kV and current of 10 mA was applied; the beam was set to 10 μm in diameter with a count time of 20 seconds per major element. Na was analyzed first to minimize element loss. The instrument was calibrated and monitored using natural reference materials VG-2 (USNM 111240/52), VGA-99 (USNM113498), ALV-981 (R23-5), and CFA-47. The reported composition is an average of 20-50 measurements.

Thirty-seven trace elements (Li, Sc, V, Cr, Co, Ni, Cu, Zn, Ga, Rb, Sr, Y, Zr, Nb, Sn, Cs, Ba, rare earth elements (REE), Hf, Ta, Pb, Th, U) were determined by ICP-MS using an Agilent 7500cs at the University of Kiel. Analytical procedures are described by Garbe-Schönberg (1993). The sediments were digested using PARR bombs in an oven in order to maximize zircon dissolution. Accuracy of analytical results was assessed with rock reference materials BHVO-2

and JA-2 analyzed as unknowns (Table 1). Average accuracy of the results (in % deviation from GeoReM's recommended values)) was better than 4% for all elements except Sc, Cr and Th in BHVO-2, and Cr, Zr, Nb and Hf in JA-2, being better than 10% for these elements. The average instrumental precision of the measurements as estimated from multiple analyses distributed over 5 to 6 hours is typically better than 1% for almost all elements. The average reproducibility of the digest procedure was monitored by duplicate preparation of at least every tenth sample and found to be better than 1%.

Sr, Nd and Pb isotope ratios were determined on ThermoFinnigan TRITON (Sr, Nd) and Finnigan MAT 262-RPQ2+ (Pb) thermal ionization mass spectrometers at GEOMAR. Pb analyses were carried out using a double spike method. A detailed description of the chemical and TIMS analytical procedures can be found in Hoernle et al. (2008, 2011). 100-150 mg of 0.5-2 mm sized, fresh rock chips were first leached in 2N HCl at 70°C for 1-2 hours and then triple-rinsed with ELGA water to remove possible surface contamination. Sr and Nd isotope ratios were mass-bias corrected within run to $^{86}\text{Sr}/^{88}\text{Sr} = 0.1194$ and $^{146}\text{Nd}/^{144}\text{Nd} = 0.7219$ and all errors are reported at the 2σ confidence level. NBS987 and our in-house Nd SPEX reference material were measured every 4th to 5th sample to obtain a normalization value for each turret relative to our preferred values of $^{87}\text{Sr}/^{86}\text{Sr} = 0.710250$ for NBS987 and $^{143}\text{Nd}/^{144}\text{Nd} = 0.511715$ for SPEX (corresponding to $^{143}\text{Nd}/^{144}\text{Nd} = 0.511850$ for La Jolla, Krolikowska-Ciaglo et al., 2005). The normalization value was then applied to the sample data for each turret. This procedure compensates for machine drift over the course of the project (2009-2012) and therefore allows maximum data comparability. External 2σ uncertainties are ± 0.000011 (n= 25) for NBS987 and ± 0.000005 for SPEX. Long term machine drift for $^{143}\text{Nd}/^{144}\text{Nd}$ and $^{87}\text{Sr}/^{86}\text{Sr}$ between 2008 and 2012 is within 0.000030. The double spike corrected NBS981 values measured along with the samples are $^{206}\text{Pb}/^{204}\text{Pb} = 16.9413 \pm 21$, $^{207}\text{Pb}/^{204}\text{Pb} = 15.4994 \pm 20$, $^{208}\text{Pb}/^{204}\text{Pb} = 36.7241 \pm 56$, $^{207}\text{Pb}/^{206}\text{Pb} = 0.914889 \pm 37$, $^{208}\text{Pb}/^{206}\text{Pb} = 2.16773 \pm 13$ (n=38), and compare well with published double and triple spike data for NBS981 (see Hoernle et al., 2011). Total Pb chemistry blanks were determined for each sample batch and were below 25 pg, with the exception of a single Pb blank of 200 pg. Sr-Nd chemistry blanks are typically below 100 pg and 50 pg, respectively. These blank levels are negligible even relative to the amount loaded on the

filaments (60-80 ng Pb and 500-1000 ng Sr and Nd). Replicate analyses by means of separate digestions are within the external 2σ reproducibility of the Sr-Nd-Pb reference materials stated above.

Hf isotopes were determined on a NU Plasma HR MC-ICPMS at GEOMAR. 200-500 mg of 0.5-2 mm sized fresh rock chips were digested for 60 hours at 130°C in a HF-HNO₃ mixture. Details of the chemical separation procedures are reported in Blichert-Toft et al. (1997) and Geldmacher and Hoernle (2006). Prior to analysis, samples were diluted to 80-100 ppb Hf to obtain a total Hf beam of 12-14 V. Hf isotope ratios were measured using static multi-collection and were mass-bias corrected to $^{179}\text{Hf}/^{177}\text{Hf} = 0.7325$ assuming exponential mass fractionation. Our in-house Hf reference material solution SPEX was measured every 3 to 5 samples to obtain a normalization value for each sample sequence. Over the course of the project (2010-2012), our in-house SPEX reference material solution had $^{176}\text{Hf}/^{177}\text{Hf} = 0.282170 \pm 6$ (2σ , $n = 45$), which corresponds to $^{176}\text{Hf}/^{177}\text{Hf} = 0.282163$ for JMC-475 (Blichert-Toft et al., 1997).

Oxygen isotope analyses were performed at the University of Oregon using CO₂-laser fluorination (e.g. Bindeman, 2008) and a Newwave 35W CO₂ laser. Single and bulk phenocryst grains, ranging in weight from 0.6-2 mg, were reacted in the presence of BrF₅ to liberate oxygen gas (protocol #1 in Table 2). The gas generated in the laser chamber was purified through a series of cryogenic traps held at liquid nitrogen temperature, and a mercury diffusion pump was used to remove traces of fluorine gas. Oxygen was converted to CO₂ gas in a small platinum graphite converter, the yield was measured, and then CO₂ gas was analyzed on a MAT 253 mass spectrometer. Four to seven aliquots of internal garnet reference material (UOG1, $\delta^{18}\text{O} = 6.56\text{‰}$, calibrated against the Gore Mt. Garnet ($\delta^{18}\text{O}_{\text{olivine}} = 5.8\text{‰}$ VSMOW, Valley et al., 1995)), as well as aliquots of reference materials (mantle olivine from San Carlos with $\delta^{18}\text{O}_{\text{olivine}} = 5.25\text{‰}$, Bindeman, 2008) were analyzed together with the unknowns during each analytical session. Between-run variability of the measured $\delta^{18}\text{O}_{\text{olivine}}$ values of the reference materials ranged from 0.1 to 0.25‰ less than their accepted value, and samples values were adjusted to correct for this small day-to-day variability. The average precision of reference materials and duplicates of single grains and bulk analyses was in the range ± 0.02 to $\pm 0.08\text{‰}$ (1σ).

For oxygen isotope analysis of bulk sediment, powdered sediments were heated at 150°C in a vacuum oven overnight to remove any loosely absorbed environmental water. Then one of two protocols was used: 1) minimal BrF₅ pretreatment of multiple samples hard-pressed into holes in a holder in a laser fluorination chamber (protocol #2 in Table 2); or 2) one-by-one analysis in a regular chamber or an air-lock sample chamber (protocol #3). As demonstrated with other clay-rich sediments, there is systematic ~1‰ difference between these two methods because of rapid BrF₅ stripping of loosely-bound H₂O in clays. Although it remains unclear which protocol is more appropriate for subducted sediment, we favor results from protocol #2.

Table 2.1

Major (wt. %) and trace elements ($\mu\text{g/g}$) for volcanic front, rear arc, backarc and sediment samples. Major element compositions recalculated to 100%, Total Fe expressed as FeO. N.d. = not determined. (+) No olivine observed on thin sections. (*) Original total retained.

Sample number	Sample Location	Country	Sample type	Lat (S)	Long (W)	Distance from VF (Km)	Group	ages		Age references
Volcanic Front										
CL 721D	Tinguiririca	Chile	lava	-34.8253	-70.3699	0	VA	Quaternary-Holocene	estimate	Stern (2004)
CL 725	Tinguiririca	Chile	lava	-34.8253	-70.3699	0	VA	Quaternary-Holocene	estimate	Stern (2004)
CL 726(+)	Tinguiririca	Chile	lava	-34.8253	-70.3699	0	VA	Quaternary-Holocene	estimate	Stern (2004)
CL 207	Planchón-Peteroa	Chile	lava	-35.2126	-70.5251	0	VA	Quaternary-Holocene	estimate	Stern (2004)
CL 736	Resolana (small cone near Cerro Azul)	Chile	lava	-35.6708	-70.8364	0	VA	Quaternary-Holocene	estimate	Stern (2004)
CL 741	Resolana	Chile	bomb	-35.6566	-70.8379	0	VA	Quaternary-Holocene	estimate	Stern (2004)
CL 745	Resolana	Chile	bomb	-35.6392	-70.8351	0	VA	Quaternary-Holocene	estimate	Stern (2004)
CL 196	Los Hornitos (small cone near Cerro Azul)	Chile	tephra	-35.7266	-70.7861	0	VA	Quaternary-Holocene	estimate	Stern (2004)
CL 565(+)	San Pedro	Chile	lava	-36.0122	-70.8371	0	VA	Holocene to 235 ka	estimate	Dungan et al. (2001)
CL 568	San Pedro	Chile	lava	-36.0114	-70.8330	0	VA	Holocene to 235 ka	estimate	Dungan et al. (2001)
CL 570	San Pedro	Chile	lava	-36.0133	-70.8218	0	VA	Holocene to 235 ka	estimate	Dungan et al. (2001)
CL 571	San Pedro	Chile	lava	-36.0182	-70.8121	0	VA	Holocene to 235 ka	estimate	Dungan et al. (2001)
CL 572	San Pedro (Satellite cones)	Chile	bomb	-36.1025	-70.5995	0	VA	Probably Holocene	estimate	Dungan et al. (2001)
CL 575b	San Pedro (Satellite cones)	Chile	bomb	-36.0858	-70.5954	0	VA	Probably Holocene	estimate	Stern (2004)
CL 576	San Pedro (Satellite cones)	Chile	lava	-36.1025	-70.5995	0	VA	Probably Holocene	estimate	Stern (2004)
CL 577	San Pedro (Satellite cones)	Chile	lava	-36.0993	-70.7033	0	VA	Probably Holocene	estimate	Stern (2004)
CL 447(+)	Longaví	Chile	lava	-36.1231	-71.2228	0	VA	Quaternary-Holocene	estimate	Stern (2004)
CL 449	Longaví	Chile	lava	-36.1735	-71.1661	0	VA	Quaternary-Holocene	estimate	Stern (2004)
CL 520	Longaví	Chile	lava	-36.1735	-71.1661	0	VA	Quaternary-Holocene	estimate	Stern (2004)
CL 530	Longaví	Chile	lava	-36.1849	-71.1609	0	VA	Quaternary-Holocene	estimate	Stern (2004)
CL 531	Longaví	Chile	lava	-36.1896	-71.1615	0	VA	Quaternary-Holocene	estimate	Stern (2004)
CL 555	Paranor (Chillán Satellite cone)	Chile	bomb	-36.8767	-71.4291	0	VA	Quaternary-Holocene	estimate	Stern (2004)
CL 071	Antuco	Chile	lava	-37.3971	-71.4321	0	VA	Quaternary-Holocene	estimate	Stern (2004)
CL 080	Antuco	Chile	tephra	-37.4132	-71.2924	0	VA	Quaternary-Holocene	estimate	Stern (2004)
CL 085	Antuco	Chile	lava	-37.3711	-71.3524	0	VA	Quaternary-Holocene	estimate	Stern (2004)
CL 557	Callaqui (Satellite cones)	Chile	lava	-37.9077	-71.3989	0	VA	Quaternary-Holocene	estimate	Stern (2004)
CL 559	Callaqui (Satellite cones)	Chile	lava	-37.9090	-71.3951	0	VA	Quaternary-Holocene	estimate	Stern (2004)
CL 560	Callaqui (Satellite cones)	Chile	lava	-37.9090	-71.3951	0	VA	Quaternary-Holocene	estimate	Stern (2004)
Rear arc										
CL 323	Laguna de la Niña Encantada	Argentina	lava	-35.1623	-69.8716	70	VA	< 1 Ma	K-Ar from the area	Folguera et al. (2009), Gudnason et al. (2012)
CL 325	Infernillo	Argentina	lava	-35.1750	-69.7960	70	VA	< 1 Ma	K-Ar from the area	Gudnason et al. (2012)
CL 220	Laguna del Maule	Chile	lava	-35.9971	-70.5613	20	VA	Quaternary-Holocene	estimate	Stern (2004)
CL 221	Laguna del Maule	Chile	lava	-35.9694	-70.5687	20	VA	Quaternary-Holocene	estimate	Stern (2004)
CL 563	Copahue	Chile	bomb	-37.8604	-71.1635	20	VA	Quaternary-Holocene	estimate	Stern (2004)

Table 2.1 (continued)
Sample number

Sample number	Sample Location	Country	Sample type	Lat (S)	Long (W)	Distance from VF (km)	Group	ages	Age references
Backarc									
CL 273	Cerro Chato	Argentina	lava	-34.4780	-68.8423	140	Northern Backarc	< 1 Ma	Folguera et al. (2009), Gudnason et al. (2012)
CL 274	Cerro Chato	Argentina	lava	-34.4718	-68.8730	140	Northern Backarc	< 1 Ma	Folguera et al. (2009), Gudnason et al. (2012)
CL 279	Cerro Diamante	Argentina	lava	-34.6328	-69.0891	130	Northern Backarc	Probably Miocene	Folguera et al. (2009), Gudnason et al. (2012)
CL 277	Cerro Diamante	Argentina	lava	-34.5919	-69.0351	130	Northern Backarc	Probably Holocene	Folguera et al. (2009), Gudnason et al. (2012)
CL 304	Diamante Chico	Argentina	lava	-34.6598	-69.0322	130	Northern Backarc	0.4-1.1 Ma	Folguera et al. (2009), Gudnason et al. (2012)
CL 308	Trintrica	Argentina	lava	-35.3737	-68.7379	190	Northern Backarc	0.8-1.7 Ma	Folguera et al. (2009), Gudnason et al. (2012)
CL 313	Llancanelo field	Argentina	lava	-35.2906	-68.2378	240	Northern Backarc	0.8-1.7 Ma	Folguera et al. (2009), Gudnason et al. (2012)
CL 318	Cones South-East of El Mihuil	Argentina	lava	-35.3255	-68.3877	225	Northern Backarc	0.8-1.7 Ma	Folguera et al. (2009), Gudnason et al. (2012)
CL 346	Cerro Malacara	Argentina	lava	-35.7102	-69.4606	120	Northern Backarc	< 1 Ma	Folguera et al. (2009), Gudnason et al. (2012)
CL 350	Eastern Cerro Malacara	Argentina	lava	-35.7922	-69.4632	120	Northern Backarc	< 1 Ma	Folguera et al. (2009), Gudnason et al. (2012)
CL 354	Cerro los Leones	Argentina	bomb	-35.4960	-69.4504	120	Northern Backarc	< 1 Ma	Folguera et al. (2009), Gudnason et al. (2012)
CL 360	Pampas Negras	Argentina	lava	-36.2892	-69.5751	150	Pampas Negras	< 320 ka	Gudnason et al. (2012)
CL 367	Pampas Negras	Argentina	lava	-36.3372	-69.4705	150	Pampas Negras	< 320 ka	Gudnason et al. (2012)
CL 371	Pampas Negras	Argentina	lava	-36.3745	-69.4016	150	Pampas Negras	< 320 ka	Gudnason et al. (2012)
CL 372	Pampas Negras	Argentina	lava	-36.3748	-69.4025	150	Pampas Negras	< 320 ka	Gudnason et al. (2012)
CL 387	Pampas Negras	Argentina	bomb	-36.3190	-69.6836	145	Pampas Negras	< 320 ka	Gudnason et al. (2012)
CL 472	Buta Rancuil	Argentina	bomb	-37.0071	-69.8230	140	Buta Rancuil	< 2 Ma	Kay et al. (2006a)
CL 406	Tromen	Argentina	bomb	-37.0342	-69.8503	140	Tromen area	< 2Ma	Kay et al. (2006a)
CL 410	Tromen	Argentina	lava	-36.9889	-69.9988	140	Tromen area	< 2Ma	Kay et al. (2006a)
CL 411	Tromen	Argentina	lava	-37.0671	-70.0638	140	Tromen area	< 200 ka	Kay et al. (2006a)
CL 412	Tromen	Argentina	lava	-36.9935	-70.0100	140	Tromen area	< 2Ma	Kay et al. (2006a)
CL 392	Auca Mahuida	Argentina	bomb	-37.7206	-68.9232	245	Southern Backarc	0.8-2 Ma	Kay et al. (2006a), Gudnason et al. (2012)
CL 394	Auca Mahuida	Argentina	lava	-37.7271	-68.8905	245	Southern Backarc	0.8-2 Ma	Kay et al. (2006a), Gudnason et al. (2012)
CL 401	Auca Mahuida	Argentina	bomb	-37.6061	-68.8147	245	Southern Backarc	0.8-2 Ma	Kay et al. (2006a), Gudnason et al. (2012)
CL 404	Auca Mahuida	Argentina	bomb	-37.3019	-68.9069	245	Southern Backarc	0.8-2 Ma	Kay et al. (2006a), Gudnason et al. (2012)
CL 455	Cerro Redondo, Rio Colorado	Argentina	bomb	-37.3019	-68.9069	280	Southern Backarc	0.3-1 Ma	Gudnason et al. (2012)
CL 459	Cerro Mendez, Rio Colorado	Argentina	bomb	-37.3401	-68.9641	280	Southern Backarc	0.3-1 Ma	Kay et al. (2006a), Gudnason et al. (2012)
Sediments									
SO210-#01_T	Incoming Plate	Chile	Trench sediment	-33.1995	-73.5713				
SO210-#01_B	Incoming Plate	Chile	Trench sediment	-33.1995	-73.5713				
SO210-#05_T	Incoming Plate	Chile	Trench sediment	-35.1667	-74.6666				
SO210-#05_B	Incoming Plate	Chile	Trench sediment	-35.1667	-74.6666				
SO210-#13_T	Incoming Plate	Chile	Trench sediment	-36.5000	-75.1665				
SO210-#13_B	Incoming Plate	Chile	Trench sediment	-36.5000	-75.1665				
SO210-#12_T	Incoming Plate	Chile	Trench sediment	-35.8334	-74.7051				
SO210-#12_B	Incoming Plate	Chile	Trench sediment	-35.8334	-74.7051				
SO210-#43_T	BioBio Slide	Chile	Trench sediment	-36.6341	-73.7627				
SO210-#43_B	BioBio Slide	Chile	Trench sediment	-36.6341	-73.7627				

Table 2.1 (continued)

Sample number	Method	SiO ₂ (wt. %)	TiO ₂ (wt. %)	Al ₂ O ₃ (wt. %)	FeOt (wt. %)	MnO (wt. %)	MgO (wt. %)	CaO (wt. %)	Na ₂ O (wt. %)	K ₂ O (wt. %)	P ₂ O ₅ (wt. %)	L.O.I	Sum*
Volcanic Front													
CL 721D	XRF	58.69	0.89	16.89	6.61	0.11	3.77	6.23	3.80	2.68	0.18	0.22	98.58
CL 725	XRF	57.21	0.86	15.97	6.50	0.11	4.02	6.19	3.63	2.45	0.18	0.32	98.61
CL 726(+)	XRF	59.41	0.91	17.00	6.48	0.11	3.22	6.07	3.84	2.66	0.18	0.20	100.38
CL 207	EMP	53.56	0.94	18.17	8.78	0.13	5.07	8.62	3.82	1.17	0.24		
CL 736	XRF	54.99	0.90	17.59	7.88	0.13	4.97	8.04	3.81	1.34	0.21	0.00	98.66
CL 741	XRF	54.07	0.85	17.23	8.38	0.14	5.75	8.87	3.40	1.00	0.19	0.00	98.85
CL 745	XRF	53.31	0.95	17.96	8.40	0.14	5.36	8.90	3.57	1.06	0.22	0.00	98.70
CL 196	EMP	53.16	0.85	15.13	8.71	0.16	8.50	9.67	2.78	0.86	0.14		
CL 565(+)	XRF	63.25	0.59	17.62	4.63	0.09	1.84	4.95	4.85	1.81	0.23	0.00	98.51
CL 568	XRF	53.31	1.24	17.78	9.35	0.14	4.64	8.09	3.78	1.25	0.27	0.00	99.42
CL 570	XRF	54.95	1.07	17.42	8.71	0.13	4.83	7.20	3.89	1.40	0.25	0.00	99.23
CL 571	XRF	53.05	1.18	17.79	9.37	0.14	4.95	8.19	3.72	1.22	0.26	0.00	99.20
CL 572	XRF	51.40	1.16	19.13	8.96	0.12	4.65	9.87	3.39	0.93	0.23	0.00	98.42
CL 575b	XRF	51.06	1.10	18.94	9.13	0.12	5.35	9.76	3.25	0.90	0.22	0.00	99.49
CL 576	XRF	61.07	0.89	16.72	5.88	0.10	2.81	5.37	4.39	2.37	0.23	0.00	98.65
CL 577	XRF	51.30	1.13	18.94	9.15	0.13	5.08	9.64	3.38	0.91	0.23	0.00	99.15
CL 447(+)	XRF	51.04	1.04	19.54	9.92	0.15	5.02	9.23	3.07	0.70	0.17	1.73	99.18
CL 449	XRF	52.00	1.03	18.42	9.02	0.13	5.70	8.90	3.61	0.83	0.22	0.42	99.49
CL 520	XRF	52.24	1.05	18.30	8.93	0.13	5.66	8.91	3.60	0.82	0.20	0.17	99.97
CL 530	XRF	59.09	0.79	17.73	6.36	0.10	3.66	6.42	4.53	0.97	0.20	0.04	100.02
CL 531	XRF	56.60	0.92	18.01	7.50	0.12	4.14	7.09	4.39	0.85	0.24	0.44	100.25
CL 555	XRF	55.58	1.03	17.35	8.14	0.13	4.58	7.86	3.95	1.04	0.22	0.00	98.98
CL 071	EMP	52.29	1.05	19.30	8.75	0.14	4.51	9.67	3.74	0.71	0.22		
CL 080	EMP	55.32	1.47	16.13	9.16	0.13	4.47	8.33	3.69	0.96	0.26		
CL 085	EMP	54.08	1.41	16.94	10.80	0.17	3.87	7.68	4.43	0.91	0.27		
CL 557	XRF	55.89	1.19	17.00	8.63	0.14	3.90	6.97	3.99	1.85	0.28	0.00	98.85
CL 559	XRF	53.99	1.04	17.66	8.69	0.13	5.52	7.51	3.73	1.30	0.28	0.54	98.73
CL 560	XRF	50.90	1.05	18.96	9.32	0.15	5.38	9.65	3.28	0.97	0.17	0.00	99.62
Rear arc													
CL 323	XRF	54.95	1.05	17.25	8.28	0.14	5.19	7.62	3.75	1.54	0.31	0.94	100.51
CL 325	XRF	54.62	1.04	17.45	8.36	0.14	5.18	7.91	3.87	1.54	0.30	0.24	100.33
CL 220	XRF	51.22	1.08	18.26	10.21	0.14	5.51	8.72	3.54	0.93	0.24	0.48	99.75
CL 221	XRF	52.24	1.21	18.91	9.81	0.13	3.67	8.70	3.82	1.08	0.26	0.34	99.77
CL 563	XRF	56.26	1.35	16.41	9.02	0.14	3.81	6.28	3.97	2.22	0.38	0.23	98.75

Table 2.1 (continued)

Sample number	Method	SiO ₂ (wt. %)	TiO ₂ (wt. %)	Al ₂ O ₃ (wt. %)	FeOt (wt. %)	MnO (wt. %)	MgO (wt. %)	CaO (wt. %)	Na ₂ O (wt. %)	K ₂ O (wt. %)	P ₂ O ₅ (wt. %)	L.O.I	Sum*
Backarc													
CL 273	XRF	45.26	1.32	15.10	11.64	0.19	10.78	10.88	2.81	1.16	0.56	0.42	99.21
CL 274	XRF	47.03	1.51	16.33	10.76	0.17	7.50	11.16	3.47	1.30	0.50	0.15	99.85
CL 279	XRF	54.41	1.09	17.15	8.25	0.15	4.25	8.15	3.95	1.91	0.45	0.08	99.84
CL 277	XRF	47.93	1.57	14.89	11.83	0.16	9.71	8.99	3.31	1.04	0.35	0.05	99.98
CL 304	XRF	46.37	1.26	14.81	11.06	0.17	10.95	10.65	2.78	1.21	0.44	0.64	98.70
CL 308	XRF	46.25	1.49	15.55	11.32	0.17	9.21	11.12	3.20	1.04	0.43	0.41	99.36
CL 313	XRF	47.90	1.52	15.51	11.66	0.16	8.62	9.87	3.39	0.82	0.35	0.58	99.00
CL 318	XRF	48.21	1.54	15.64	11.61	0.16	8.38	9.51	3.49	0.90	0.37	0.18	100.12
CL 346	XRF	46.34	1.63	15.56	10.83	0.16	8.53	9.98	3.26	1.05	0.43	0.00	98.88
CL 350	XRF	46.86	1.63	16.23	11.34	0.17	7.31	10.16	3.44	0.80	0.36	0.00	99.15
CL 354	XRF	47.87	1.65	15.82	12.31	0.17	7.88	9.27	3.46	0.77	0.30	0.50	100.03
CL 360	XRF	49.78	1.83	17.18	10.48	0.16	5.44	8.28	4.31	1.76	0.59	0.20	100.47
CL 367	XRF	47.36	2.27	18.30	11.62	0.16	4.70	8.04	4.88	1.74	0.73	0.11	100.67
CL 371	XRF	50.22	1.90	17.36	10.14	0.15	4.74	8.59	4.39	1.76	0.56	0.09	100.34
CL 372	XRF	46.26	2.17	17.53	11.49	0.15	6.01	10.50	3.75	1.34	0.60	0.43	98.68
CL 387	XRF	47.72	1.76	16.28	11.43	0.15	7.62	10.43	3.33	0.78	0.34	0.18	100.23
CL 472	XRF	46.71	1.13	17.06	10.81	0.16	7.67	12.29	2.52	1.14	0.34	0.65	100.36
CL 406	XRF	48.23	1.51	17.77	10.94	0.17	6.77	10.80	3.15	0.68	0.26	0.00	100.15
CL 410	XRF	51.52	1.41	17.58	9.37	0.15	4.53	8.33	3.65	1.44	0.41	0.00	99.20
CL 411	XRF	58.80	1.01	17.05	6.50	0.11	2.90	5.44	4.16	2.62	0.29	0.10	99.49
CL 412	XRF	58.33	1.41	16.67	7.10	0.17	2.26	4.87	4.81	2.32	0.62	0.50	99.56
CL 392	XRF	46.94	2.26	14.37	12.00	0.16	9.65	9.41	3.26	1.15	0.58	0.00	97.90
CL 394	XRF	53.87	1.66	17.90	8.64	0.15	2.49	5.31	5.86	3.18	0.75	0.00	99.00
CL 401	XRF	48.58	1.97	15.96	11.38	0.16	7.57	9.16	3.69	0.97	0.38	0.00	99.33
CL 404	XRF	48.24	1.97	15.46	10.80	0.15	8.04	8.89	3.70	1.87	0.64	0.67	98.06
CL 456	XRF	48.95	2.13	15.41	11.96	0.16	6.91	8.84	3.92	1.12	0.46	0.00	98.73
CL 459	XRF	49.68	2.04	17.07	9.58	0.15	5.55	7.96	4.60	2.53	0.62	0.58	99.49
Sediments													
SO210-#01_T	XRF	44.73	0.66	13.92	6.48	0.26	2.77	8.36	4.64	1.83	0.20	14.73	101.27
SO210-#01_B	XRF	52.93	0.76	16.10	6.79	0.09	3.23	2.63	4.58	2.46	0.17	8.49	100.70
SO210-#05_T	XRF	49.12	0.78	15.54	7.30	0.10	3.05	3.01	4.88	2.02	0.18	10.82	100.52
SO210-#05_B	XRF	52.28	0.75	15.35	6.96	0.10	2.86	2.59	4.85	2.11	0.17	9.31	100.82
SO210-#13_T	XRF	50.52	0.88	17.06	7.57	0.10	3.14	5.12	4.84	1.41	0.20	7.65	100.64
SO210-#13_B	XRF	51.97	0.78	15.25	7.04	0.08	2.74	4.30	4.72	1.95	0.17	9.59	101.39
SO210-#12_T	XRF	52.33	0.75	14.92	6.66	0.09	2.60	4.88	4.59	1.82	0.18	10.11	101.54
SO210-#12_B	XRF	50.31	0.81	15.84	6.99	0.07	2.82	3.00	4.95	1.81	0.19	10.60	100.36
SO210-#43_T	XRF	52.35	0.89	16.38	7.06	0.08	2.95	4.85	3.86	1.41	0.21	9.11	101.16
SO210-#43_B	XRF	53.04	0.90	18.61	7.47	0.10	3.70	7.55	3.95	1.19	0.18	3.66	100.74
Reference materials													
BHVO	XRF	49.95	2.76	13.63	12.25	0.17	7.41	11.46	2.31	0.51	0.26		100.71
JA-2	XRF	56.23	0.67	15.47	6.39	0.11	8.00	6.27	3.12	1.76	0.15		98.17

Table 2.1 (continued)

Sample number	Li	Sc	V	Cr	Co	Ni	Cu	Zn	Ga	Rb	Sr	Y	Zr	Nb	Sn	Cs	Ba	La	Ce	Pr	Nd	Sm	Eu	Gd	Tb	Dy	Ho	Er	Tm	Yb	Lu	Hf	Ta	Tl	Pb	Th	U			
	µg/g	µg/g	µg/g	µg/g	µg/g	µg/g	µg/g	µg/g	µg/g	µg/g	µg/g	µg/g	µg/g	µg/g	µg/g	µg/g	µg/g	µg/g	µg/g	µg/g	µg/g	µg/g	µg/g	µg/g	µg/g	µg/g	µg/g	µg/g	µg/g	µg/g	µg/g	µg/g	µg/g	µg/g	µg/g	µg/g	µg/g	µg/g		
Volcanic Front																																								
CL 721D	20.8	24.5	205	74.3	24.1	31.3	65.1	74.9	21.0	130	545	21.7	240	7.55	1.82	7.23	442	22.8	49.1	6.20	24.2	4.90	1.08	4.30	0.635	3.69	0.777	2.00	0.302	2.00	0.300	5.71	0.511	0.259	13.2	14.5	4.28			
CL 725	20.3	24.8	190	132	24.2	39.0	54.1	75.5	20.2	115	503	21.5	217	7.13	1.64	6.67	436	21.7	47.0	5.92	23.4	4.80	1.09	4.25	0.629	3.68	0.734	2.03	0.304	2.03	0.308	5.25	0.478	0.397	15.1	13.0	3.86			
CL 726(+)	21.5	23.5	203	48.8	21.7	21.2	132	545	22.0	240	7.69	1.80	7.38	455	23.3	50.2	6.28	24.8	5.03	1.10	4.37	0.644	3.73	0.739	2.03	0.303	2.01	0.299	5.70	0.520	0.317	13.5	14.7	4.35						
CL 207	10.5	26.1	230	130	28.7	56.1	88.7	79.1	18.5	27.1	517	17.5	122	3.82	1.04	0.935	332	14.1	31.7	4.19	17.9	3.98	1.12	3.72	0.561	3.32	0.656	1.80	0.264	1.76	0.263	3.03	0.231	n.d.	7.77	2.55	0.637			
CL 736	12.5	29.5	247	73.2	29.7	32.7	82.9	84.3	20.9	32.7	719	17.1	119	4.54	0.997	1.45	361	15.3	32.9	4.35	18.1	3.86	1.12	3.47	0.505	2.97	0.596	1.63	0.242	1.60	0.241	2.81	0.255	0.130	9.27	3.81	0.991			
CL 741	10.0	35.1	274	88.7	33.1	31.9	87.4	84.8	20.1	19.8	734	15.2	76.3	2.68	0.829	0.798	270	11.4	25.2	3.44	14.9	3.31	1.02	3.04	0.448	2.66	0.533	1.45	0.215	1.44	0.216	1.97	0.155	0.090	7.18	2.48	0.665			
CL 745	10.9	33.1	281	85.8	33.5	37.1	97.0	89.0	21.2	21.5	788	16.0	92.0	3.99	0.901	0.842	312	13.8	29.8	4.00	17.1	3.67	1.13	3.30	0.479	2.78	0.557	1.50	0.222	1.46	0.218	2.24	0.215	0.082	7.68	2.69	0.686			
CL 196	7.98	32.0	223	543	49.9	32.1	86.2	71.6	14.6	11.5	482	12.2	58.6	1.20	0.579	0.399	171	6.88	15.8	2.17	9.78	2.36	0.749	2.31	0.361	2.24	0.461	1.29	0.191	1.26	0.187	1.60	0.083	0.073	7.05	1.95	0.628			
CL 565(+)	19.3	9.99	88.0	22.2	11.5	9.85	36.9	65.9	19.9	43.6	622	13.7	159	4.27	0.927	2.59	488	15.5	33.5	4.23	16.9	3.42	0.935	3.04	0.442	2.49	0.490	1.35	0.203	1.36	0.213	3.78	0.295	0.207	11.8	3.95	0.991			
CL 568	11.0	27.7	268	56.5	29.3	30.9	43.1	97.8	20.8	28.0	545	22.5	146	4.53	1.22	0.913	312	15.2	35.0	4.84	21.4	4.93	1.35	4.76	0.730	4.26	0.844	2.25	0.331	2.16	0.318	3.72	0.302	0.071	8.83	3.33	0.927			
CL 570	13.9	22.6	217	77.5	29.7	44.3	62.2	84.7	19.9	38.7	543	17.7	134	4.57	1.08	1.93	371	15.9	35.1	4.63	19.4	4.21	1.23	3.92	0.585	3.34	0.651	1.75	0.257	1.66	0.250	3.26	0.320	0.150	9.27	3.79	0.977			
CL 571	12.2	29.4	285	71.4	32.8	39.8	61.2	92.1	21.6	30.7	585	22.1	145	4.47	1.22	0.786	310	14.8	34.1	4.68	20.6	4.77	1.34	4.61	0.710	4.14	0.817	2.20	0.315	2.06	0.310	3.56	0.289	0.082	8.10	3.23	0.885			
CL 572	7.96	25.5	271	91.2	30.4	38.2	56.8	74.4	20.1	22.8	622	13.8	101	4.23	0.851	0.798	273	13.4	29.5	3.93	16.7	3.61	1.14	3.31	0.488	2.72	0.518	1.35	0.193	1.27	0.187	2.41	0.277	0.095	5.20	2.93	0.705			
CL 575b	8.61	28.7	299	102	35.8	43.6	60.4	85.8	21.3	24.2	658	14.5	107	4.49	0.947	0.857	289	14.0	30.8	4.07	17.4	3.73	1.19	3.48	0.507	2.80	0.544	1.44	0.207	1.31	0.195	2.54	0.297	0.109	5.66	3.08	0.768			
CL 576	7.66	26.9	286	112	35.5	59.7	61.2	78.9	20.6	23.1	643	13.9	101	4.23	0.991	0.819	275	13.4	29.6	3.90	16.6	3.56	1.13	3.26	0.477	2.70	0.516	1.35	0.196	1.26	0.187	2.44	0.281	0.139	5.49	3.06	0.751			
CL 577	17.7	17.6	146	45.9	17.1	16.8	29.7	74.8	20.6	87.7	487	18.7	318	8.81	1.33	2.71	531	28.6	58.3	7.00	26.7	4.98	1.37	4.31	0.620	3.42	0.674	1.85	0.281	1.92	0.292	6.47	0.630	0.361	11.7	10.8	2.83			
CL 447(+)	12.0	24.8	240	16.0	31.1	19.5	47.8	81.8	19.0	14.3	557	15.9	n.d.	2.23	0.553	0.418	197	8.43	19.5	2.72	12.1	3.06	1.03	3.16	0.496	3.00	0.591	1.55	0.216	1.37	0.193	n.d.	0.148	0.105	4.76	1.17	0.217			
CL 449	8.66	24.1	230	96.8	30.4	52.1	58.9	81.5	20.3	15.2	766	14.8	75.2	2.06	0.834	1.60	217	10.5	23.5	3.24	14.5	3.39	1.10	3.20	0.477	2.79	0.549	1.45	0.212	1.37	0.202	2.00	0.130	0.097	11.5	3.58	1.04			
CL 520	9.17	25.0	246	108	32.0	57.4	63.8	85.1	21.3	13.4	796	15.0	81.3	2.22	0.896	1.30	234	11.4	25.5	3.45	15.4	3.54	1.14	3.33	0.490	2.86	0.550	1.45	0.211	1.37	0.202	2.15	0.143	0.074	10.9	4.50	1.22			
CL 530	17.4	15.7	157	61.2	20.4	31.7	24.5	74.5	20.0	18.7	602	11.2	103	2.90	0.720	0.408	343	11.3	24.9	3.26	13.8	2.90	0.915	2.59	0.372	2.10	0.402	1.08	0.158	1.02	0.155	2.52	0.209	0.090	6.78	1.52	0.412			
CL 531	16.4	18.5	193	64.3	23.6	37.3	52.6	85.2	20.4	15.2	656	13.2	98.8	2.93	0.797	1.26	296	12.1	28.2	3.34	14.8	3.32	1.04	3.08	0.444	2.54	0.482	1.28	0.186	1.21	0.181	2.52	0.181	0.081	7.62	1.22	0.343			
CL 555	14.0	26.4	227	72.3	26.8	36.8	70.1	86.0	19.9	29.0	528	17.6	118	3.20	1.03	2.11	282	12.1	27.5	3.71	16.2	3.71	1.11	3.62	0.553	3.29	0.656	1.80	0.263	1.74	0.260	2.98	0.218	0.169	10.4	3.31	0.960			
CL 071	10.8	27.4	239	95.0	25.7	31.8	75.4	72.4	19.4	13.5	548	16.9	82.8	2.58	0.955	0.562	203	9.47	22.6	3.15	14.1	3.44	1.12	3.46	0.534	3.23	0.649	1.79	0.264	1.75	0.259	2.24	0.171	n.d.	5.96	1.50	0.432			
CL 080	12.4	30.1	234	97.2	25.6	33.5	69.7	72.2	19.9	17.0	586	17.5	83.3	2.58	0.847	0.948	219	9.89	23.2	3.18	14.1	3.39	1.13	3.39	0.524	3.21	0.651	1.77	0.263	1.74	0.261	2.16	0.174	0.095	5.76	1.61	0.413			
CL 085	13.3	31.1	300	30.7	25.6	10.7	92.9	92.9	20.4	16.9	454	23.9	117	3.19	1.25	0.516	251	11.1	27.1	3.87	17.8	4.49	1.43	4.63	0.731	4.52	0.921	2.53	0.377	2.49	0.373	3.06	0.212	n.d.	5.78	1.65	0.495			
CL 557	18.0	26.1	219	48.9	24.1	20.5	70.3	90.6	20.6	56.5	530	27.7	207	5.36	1.87	3.96	419	21.6	49.2	6.63	28.4	6.31	1.44	5.87	0.881	5.11	1.02	2.78	0.413	2.72	0.411	5.24	0.357	0.254	16.0	8.55	2.25			
CL 559	11.4	22.2	200	186	31.4	79.7	62.1	86.4	20.2	27.3	623	18.6	132	3.86	1.24	2.06	328	16.0	35.5	4.90	21.2	4.61	1.30	4.26	0.617	3.46	0.669	1.81	0.259	1.69	0.250	3.25	0.247	0.214	10.1	3.42	0.881			
CL 560	9.81	31.8	303	65.5	32.1	33.3	82.1	89.4	22.2	17.0	835	18.8	87.3	2.06	1.07	1.58	277	12.9	28.9	4.00	17.9	4.17	1.27	3.99	0.602	3.55	0.710	1.93	0.283	1.84	0.275	2.38	0.147	0.100	14.2	5.98	1.77			
Rear arc																																								
CL 323	11.9	22.8	187	117	24.7	59.2	40.1	80.7	20.8	36.9	830	20.2	161	7.00	1.18	1.64	416	23.2	50.0	6.32	26.3	5.33	1.48	4.44	0.630	3.58	0.696	1.90	0.273	1.80	0.276	3.46	0.341	0.139	12.1	5.75	1.51			
CL 325	12.4	24.3	195	97.6	25.1	50.7	40.0	80.4	20.9	36.8	856	20.2	154	6.36	1.13	2.03	419	22.1	48.1	6.04	25.3	5.14	1.45	4.33	0.618	3.55	0.699	1.92	0.280	1.84	0.287	3.37	0.311	0.154	13.9	5.63	1.65			
CL 220	8.33	25.3	216	82.1	35.4	30.8	51.3	85.5	19.3	21.5	570	17.3	110	3.99	0.933	0.738	289	14.4	31.8	4.16	17.9	3.97	1.23	3.76	0.560	3.29	0.636	1.70	0.246	1.61	0.237	2.68	0.266	0.062	5.91	2.95	0.682			
CL 221	10.3	26.8	265	24.1	27.1	9.42	49.9	84.9	21.2	28.2	609	18.4	121	4.33	1.06	0.952	331	16.1	35.2	4.55	15.2	4.21	1.28	3.98	0.594	3.47	0.678	1.82	0.264	1.72	0.255	2.91	0.294	0.077	7.57	3.82	0.896			
CL 563	15.5	24.																																						

Table 2.2 Sr-Nd-Hf-Pb-O isotopic compositions for volcanic front, rear arc, backarc and sediment samples.
 $\delta^{18}\text{O}_{\text{melt}}$ is calculated after Bindeman et al. (2004).

Sample number	Sample Location	$^{87}\text{Sr}/^{86}\text{Sr}$	2σ	$^{143}\text{Nd}/^{144}\text{Nd}$	2σ	ϵNd	$^{176}\text{Hf}/^{177}\text{Hf}$	2σ	ϵHf
Volcanic Front									
CL 721D	Tinguiririca	0.703909	3	0.512752	2	2.22			
CL 725	Tinguiririca	0.704139	2	0.512751	3	2.21	0.282926	5	5.44
CL 726	Tinguiririca	0.703970	3	0.512745	2	2.08	0.282928	5	5.52
CL 207	Planchón-Peteroa	0.704108	3	0.512752	5	2.22	0.282978	4	7.27
CL 736	Resolana (small cone near Cerro Azul)	0.703769	3	0.512795	2	3.07			
CL 741	Resolana	0.703645	3	0.512833	3	3.81	0.283004	4	8.19
CL 745	Resolana	0.703747	3	0.512803	2	3.22	0.282979	3	7.33
CL 196	Los Hornitos (small cone near Cerro Azul)	0.703738	3	0.512828	3	3.70	0.283026	5	8.99
CL 196_rep							0.283015	4	8.60
CL 565	San Pedro	0.703928	3	0.512799	3	3.15			
CL 568	San Pedro	0.704016	3	0.512788	3	2.92	0.282970	6	7.01
CL 570	San Pedro	0.704065	3	0.512767	3	2.51			
CL 571	San Pedro	0.704023	3	0.512785	3	2.86	0.282981	6	7.39
CL 571_rep		0.704009	3	0.512780	2	2.76			
CL 572	San Pedro (Satellite cones)	0.704050	3	0.512752	3	2.23			
CL 575b	San Pedro (Satellite cones)	0.704046	3	0.512749	3	2.17	0.282943	6	6.06
CL 576	San Pedro (Satellite cones)	0.704053	3	0.512756	3	2.30			
CL 577	San Pedro (Satellite cones)	0.704161	3	0.512714	2	1.48			
CL 447	Longaví	0.703803	3	0.512869	2	4.51			
CL 449	Longaví	0.704105	3	0.512761	3	2.40	0.282964	6	6.79
CL 520	Longaví	0.703903	3	0.512844	3	4.02			
CL 530	Longaví	0.704029	3	0.512798	3	3.12	0.282994	5	7.83
CL 531	Longaví	0.703979	3	0.512806	3	3.27			
CL 555	Paranor (Chillán Satellite cone)	0.703915	3	0.512836	3	3.87			
CL 071	Antuco	0.703853	3	0.512839	3	3.91	0.283020	5	8.78
CL 080	Antuco	0.703863	3	0.512835	2	3.85			
CL 085	Antuco	0.703840	3	0.512847	2	4.07			
CL 557	Callaqui (Satellite cones)	0.703939	3	0.512814	3	3.44			
CL 559	Callaqui (Satellite cones)	0.703854	2	0.512807	3	3.30	0.283011	6	8.46
CL 560	Callaqui (Satellite cones)	0.703907	3	0.512814	3	3.43			
CL 560_rep		0.703853	3	0.512807	2	3.30			
Rear arc									
CL 323	Laguna de la Ninna Encantada	0.704150	3	0.512703	3	1.43	0.282882	5	3.89
CL 325	Infernillo	0.704228	3	0.512708	3	1.36	0.282880	5	3.81
CL 220	Laguna del Maule	0.704059	3	0.512760	3	2.39			
CL 221	Laguna del Maule	0.704074	3	0.512756	3	2.29	0.282954	7	6.44
CL 563	Copahue	0.703922	2	0.512780	3	2.77			
Backarc									
CL 273	Cerro Chato	0.703971	4	0.512816	2	3.48			
CL 274	Cerro Chato	0.704129	3	0.512767	2	2.51	0.282952	6	6.57
CL 279	Cerro Diamante	0.704246	3	0.512705	2	1.30			
CL 277	Cerro Diamante	0.704125	3	0.512766	2	2.50	0.282884	6	3.95
CL 304	Diamante Chico	0.704213	2	0.512764	2	2.46			
CL 308	Trintrica	0.703908	3	0.512822	2	3.59			
CL 313	Llancanelo field	0.704040	3	0.512781	2	2.78	0.282894	5	4.32
CL 318	Cones South-East of El Nihuil	0.704029	3	0.512792	3	3.00			
CL 346	Cerro Malacara	0.704074	3	0.512769	3	2.56			
CL 350	Eastern Cerro Malacara	0.704114	3	0.512737	3	1.92			
CL 354	Cerro los Leones	0.704009	3	0.512769	3	2.56			
CL 360	Pampas Negras	0.703904	3	0.512793	3	3.03	0.282901	5	4.58
CL 367	Pampas Negras	0.703890	3	0.512791	3	2.98	0.282915	6E-06	5.05
CL 367_rep		0.703902	3	0.512788	2	2.93			
CL 371	Pampas Negras	0.703946	3	0.512768	3	2.53			
CL 372	Pampas Negras	0.703915	3	0.512789	3	2.95	0.282894	6	4.33
CL 387	Pampas Negras	0.703999	3	0.512772	2	2.61			
CL 472	Buta Ranquil	0.704065	3	0.512877	3	4.66	0.283003	6	8.17
CL 412_rep		0.704038	3	0.512890	3	4.91			
CL 406	Tromen	0.703851	3	0.512833	3	3.81			
CL 410	Tromen	0.704096	3	0.512761	3	2.40			
CL 411	Tromen	0.703927	3	0.512791	3	2.98	0.282941	5	5.97
CL 412	Tromen	0.704329	3	0.512725	2	1.69	0.282877	4	3.72
CL 392	Auca Mahuida	0.703777	3	0.512809	2	3.34			
CL 394	Auca Mahuida	0.703727	3	0.512823	2	3.61			
CL 401	Auca Mahuida	0.703749	3	0.512805	2	3.25			
CL 404	Auca Mahuida	0.703881	3	0.512804	3	3.25			
CL 456	Cerro Redondo, Rio Colorado	0.703641	2	0.512840	2	3.94	0.282914	4	5.02
CL 456_rep		0.703620	3	0.512846	3	4.05			
CL 459	Cerro Mendez, Rio Colorado	0.703598	3	0.512857	2	4.27	0.282941	4	5.97
Sediments									
SO210-#01_T	Incoming Plate								
SO210-#01_B	Incoming Plate	0.705984	3	0.512690	3	1.01	0.282990	4	7.72
SO210-#05_T	Incoming Plate								
SO210-#05_B	Incoming Plate	0.705623	3	0.512699	3	1.19	0.282982	5	7.41
SO210-#13_T	Incoming Plate								
SO210-#13_B	Incoming Plate	0.705889	3	0.512701	2	1.22	0.282980	5	7.36
SO210-#12_T	Incoming Plate								
SO210-#12_B	Incoming Plate	0.705605	3	0.512700	1	1.21	0.282980	5	7.37
SO210-#43_T	BioBio Slide								
SO210-#43_B	BioBio Slide	0.704163	3	0.512815	1	3.45	0.283015	3	8.48

Table 2.2 (continued)

Sample number	$^{206}\text{Pb}/^{204}\text{Pb}$	2 σ	$^{207}\text{Pb}/^{204}\text{Pb}$	2 σ	$^{208}\text{Pb}/^{204}\text{Pb}$	2 σ	$\delta^{18}\text{O}$ olivine	1 σ	Protocol	$\delta^{18}\text{O}$ melt used
Volcanic Front										
CL 721D	18.6383	11	15.6166	14	38.5622	45				
CL 725	18.6493	14	15.6165	16	38.5678	52	5.07	0.10	plag.	#1 5.87
CL 726	18.6375	13	15.6155	12	38.5584	35	5.62	0.10	Plag.	#1 6.47
CL 207	18.5813	11	15.6111	14	38.5054	44				
CL 736	18.6028	13	15.6057	14	38.4935	44				
CL 741	18.6020	9	15.6024	9	38.4673	27				
CL 745	18.6057	10	15.6051	12	38.4881	38				
CL 196	18.6291	12	15.6119	14	38.5349	46	5.31	0.10		#1 6.42
<i>CL 196_rep</i>										
CL 565	18.5707	19	15.6049	22	38.4730	70				
CL 568	18.6074	14	15.6100	16	38.5043	54				
CL 570	18.5922	8	15.6075	10	38.4950	30				
CL 571	18.6042	10	15.6031	8	38.4808	21	5.24	0.05		#1 6.33
<i>CL 571_rep</i>										
CL 572	18.6093	9	15.6097	9	38.5202	30	5.09	0.10		#1 6.04
CL 575b	18.6123	11	15.6120	13	38.5274	40	5.28	0.05		#1 6.20
CL 576	18.6135	11	15.6111	11	38.5272	39	5.29	0.02		#1 7.09
CL 577	18.6205	22	15.6117	25	38.5349	79				
CL 447	18.5561	9	15.6019	11	38.4441	37				
CL 449	18.6444	11	15.6137	12	38.5410	38	5.52	0.03		#1 6.53
CL 520	18.5762	18	15.6077	21	38.4788	70				
CL 530	18.5860	112	15.6084	14	38.4894	45				
CL 531	18.5868	7	15.6073	8	38.4865	28	4.88	0.10		#1 6.29
CL 555	18.5981	24	15.6073	22	38.5015	62				
CL 071	18.5824	8	15.6068	8	38.4852	20				
CL 080	18.5724	10	15.6058	12	38.4766	38				
CL 085	18.5836	9	15.6013	7	38.4714	18				
CL 557	18.5866	13	15.6092	16	38.4964	53				
CL 559	18.5687	13	15.6066	12	38.4723	30	5.35	0.14		#1 6.53
CL 560	18.6306	10	15.6078	11	38.5185	35	5.20	0.10		#1
<i>CL 560_rep</i>										
CL 560_rep	18.6339	7	15.6100	6	38.5258	19				
Rear arc										
CL 323	18.6744	14	15.6178	13	38.5869	34				
CL 325	18.6870	9	15.6213	11	38.6112	35				
CL 220	18.6241	9	15.6122	10	38.5359	31	5.41	0.06		#1 6.35
CL 221	18.6251	12	15.6118	14	38.5358	46				
CL 563	18.5887	13	15.6110	5	38.5009	48				
Backarc										
CL 273	18.5626	8	15.5962	10	38.4737	32				
CL 274	18.6066	14	15.6000	15	38.4889	44	5.42	0.10		#1 5.99
CL 279	18.4662	17	15.5877	16	38.3714	44				
CL 277	18.5171	2	15.5882	15	38.3879	46	5.42	0.08		#1 6.07
CL 304	18.5908	11	15.6039	12	38.5022	39				
CL 308	18.5405	7	15.5955	7	38.4159	20				
CL 313	18.5136	13	15.5900	15	38.3501	48	5.42	0.10		#1 6.07
CL 318	18.5191	9	15.5903	10	38.3570	33				
CL 346	18.4954	12	15.5911	4	38.3968	44				
CL 350	18.4589	27	15.5836	25	38.3649	67				
CL 354	18.4737	24	15.5973	29	38.4054	92				
CL 360	18.3755	9	15.5748	10	38.2600	30	5.02	0.02		#1 5.83
CL 367	18.2966	6	15.5634	7	38.1741	22				
<i>CL 367_rep</i>										
CL 367_rep	18.2955	9	15.5633	10	38.1726	28				
CL 371	18.3264	5	15.5703	5	38.2226	16				
CL 372	18.3326	15	15.5665	9	38.2053	58	5.06	0.10		#1 5.56
CL 387	18.4152	9	15.5833	8	38.3153	24				
CL 472	18.5278	11	15.5819	14	38.3287	43				
<i>CL 412_rep</i>										
CL 412_rep	18.5281	6	15.5823	5	38.3294	14				
CL 406	18.5299	9	15.5929	19	38.3809	59				
CL 410	18.5656	16	15.6044	19	38.4667	63				
CL 411	18.5455	8	15.6023	9	38.4175	28				
CL 412	18.5791	13	15.6038	11	38.4782	29				
CL 392	18.4113	12	15.5777	3	38.3011	43	5.17	0.19		#1 5.73
CL 394	18.3893	10	15.5804	11	38.2879	34				
CL 401	18.3959	19	15.5814	22	38.2891	71				
CL 404	18.4568	18	15.5869	21	38.3335	70				
CL 456	18.3811	18	15.5786	22	38.2741	69	5.09	0.10		#1 5.83
<i>CL 456_rep</i>										
CL 456_rep	18.3809	8	15.5781	7	38.2736	16				
CL 459	18.3620	14	15.5723	17	38.2440	56				
Sediments										
SO210-#01_T							8.83	0.10		#2
SO210-#01_B	18.6116	14	15.6199	15	38.5595	45				
SO210-#05_T							8.86	0.10		#2
SO210-#05_B	18.6252	12	15.6212	15	38.5715	48				
SO210-#13_T							8.49	0.10		#2
SO210-#13_B	18.6291	16	15.6226	19	38.5801	61				
SO210-#12_T							8.89	0.10		#2
SO210-#12_B	18.6310	9	15.6221	9	38.5849	27	14.12	0.10		#2
SO210-#43_T							7.76	0.10		#2
SO210-#43_B	18.5776	11	15.6093	14	38.4896	44	8.39	0.10		#2

2.4 Results

Sixty volcanic samples were analyzed for major elements, trace elements and Sr, Nd and Pb isotope compositions, twenty-three for Hf isotopes, and nineteen for O isotopes. Ten sediment samples were analyzed for major and trace elements, five for Sr-Nd-Pb isotopes, four for Hf isotopes, and seven for O isotopes. The data are presented in Table 1 (major and trace elements) and in Table 2 (Sr-Nd-Hf-Pb-O isotopes).

VA samples consist primarily of basalts to andesites/trachyandesites with $\text{SiO}_2 = 51\text{-}61$ wt. % and $\text{MgO} = 2.8\text{-}8.5$ wt. %, with the exception of one sample that plots on the andesite/dacite boundary (Figure 2). About half of our VA samples have $\text{MgO} > 5\%$ and $\text{SiO}_2 < 54\%$. They are mostly calc-alkalic (they lack Fe-enrichment). Three from Tinguiririca, one from San Pedro and one from Copahue plot in the high-K field of Gill (1981) (not shown). In MgO versus major element oxide diagrams (Figure 3), the VA samples have positive correlations of MgO versus FeO_t (total iron as FeO) and CaO (Figure 3a,b), and negative correlations of MgO versus Al_2O_3 , Na_2O (Figure 3c,d), SiO_2 , and K_2O (not shown).

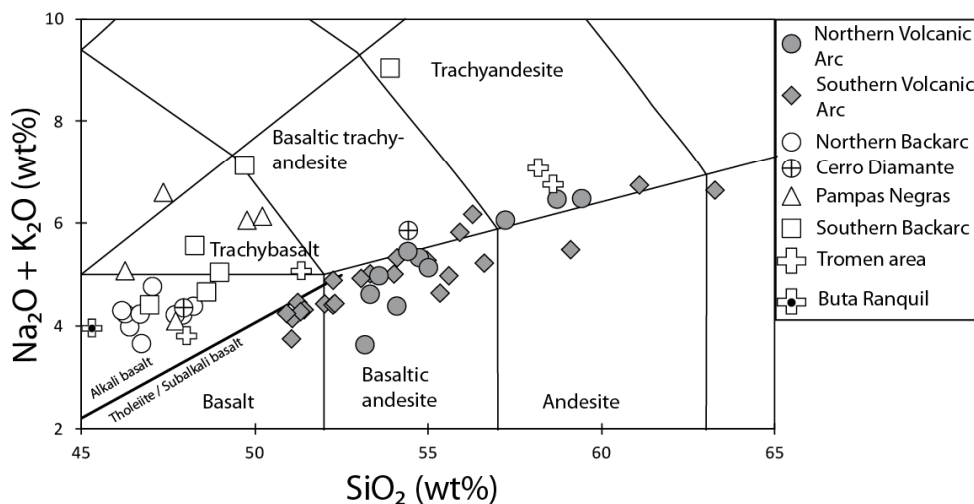


Figure 2.2 Total Alkali versus Silica [TAS] after Le Maitre et al. (1989). VA samples range from basalt to trachyandesite, BA samples are mostly alkali basalts and trachybasalts. BA samples are lower in silica than the VA samples except for one sample from Cerro Diamante stratovolcano.

BA samples are more mafic alkali basalts and trachybasalts with $\text{SiO}_2 = 45\text{-}50$ wt. % and $\text{MgO} = 4\text{-}11$ wt. %, except for three trachyandesite (Figures 2 and 3). Most Pampas Negras

samples are evolved with MgO = 4-6 wt. %. BA samples have similar correlations between MgO and the other oxides as observed for the VA samples. Relative to the VA, the BA trend is shifted to lower SiO₂ (Figure 2) but higher FeOt, Na₂O, TiO₂, P₂O₅ (Figure 3a,d,e,f), K₂O and MnO contents (not shown) and lower concentrations of most incompatible trace elements (e.g. Zr, Hf, Nb, Ta, REE and Ba). There is little or no overlap between VA (including rear arc) and BA samples for Ti, Na, and P, and the change occurs between 70 and 100 km behind the volcanic front.

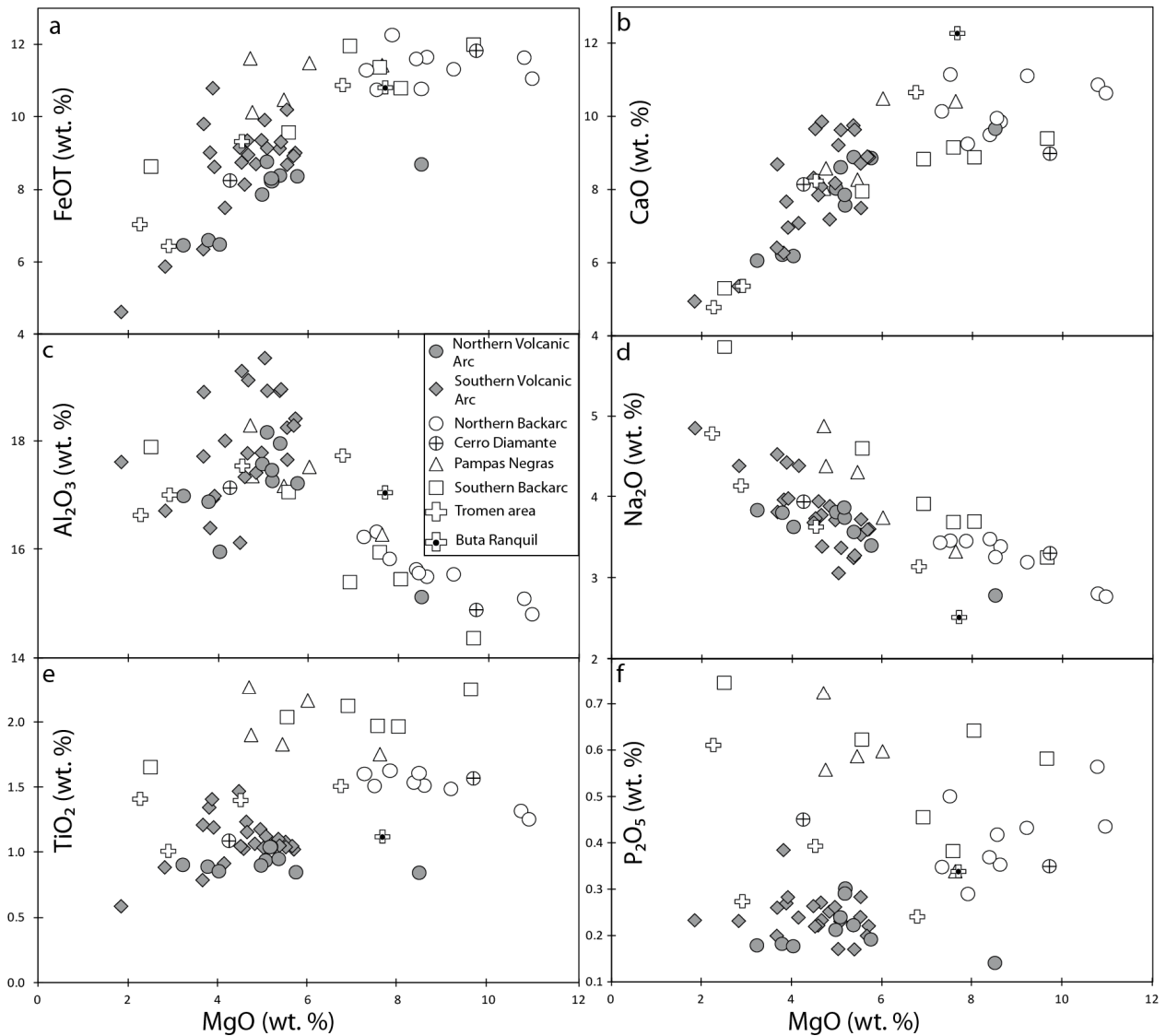


Figure 2.3 MgO versus (a) FeOt, (b) CaO (c) Al₂O₃, (d) Na₂O, (e) TiO₂ and (f) P₂O₅. The VA and the BA generally form two different petrogenetic trends, reflecting different magma formation and evolution processes.

All VA samples show typical subduction zone incompatible element signatures, characterized by enrichment in fluid-mobile Large Ion Lithophile Elements (LILE), such as Cs, Rb, Ba, U, K and Pb, and depletion in the High Field Strength Elements (HFSE) Nb and Ta, relative to light REE (Figure 4a). Differentiated VA samples show relative enrichment in Zr and Hf, and depletion in Ti. BA samples have similar patterns but overall greater enrichment in highly incompatible elements, steeper heavy REE patterns (Sm/Yb in VA = 1.48-2.25, in BA = 2.26-4.32), and less pronounced negative Nb and Ta troughs (Figure 4b). Consequently, the VA samples have higher fluid-mobile (e.g. LILE) to fluid-immobile (e.g. HFSE and REE) element ratios (e.g. higher Ba/La, Ba/Nb and Th/Nb and lower Ce/Pb, Nd/Pb, Nb/U), and lower ratios of more to less incompatible HFSE and REE ratios (e.g. lower Nb/Zr, Nb/Y, Ta/Hf, Zr/Hf, Nb/Yb, Ta/Yb, Gd/Yb, Tb/Yb, TiO₂/Yb) than the BA samples. In general, some NBA and Tromen samples show a more pronounced subduction zone signature than other BA groups. Sample CL 472 from Buta Ranquil near Tromen shows the most pronounced subduction zone signature in the BA.

Our ⁸⁷Sr/⁸⁶Sr and ¹⁴³Nd/¹⁴⁴Nd isotope data are similar to those of previous studies for the TSVZ (Hildreth and Moorbath, 1988; Tormey et al., 1995; Davidson et al., 1987, 1988; Hickey-Vargas et al., 1986; Harmon et al., 1984; Sigmarsson et al., 1990) and the BA (Kay and Copeland, 2006; Kay et al., 2006a,b; Varekamp et al., 2010). ⁸⁷Sr/⁸⁶Sr vs. ¹⁴³Nd/¹⁴⁴Nd isotopes are negatively correlated for both VA and BA samples, the VA and BA data almost completely overlap, and both lie within the South Atlantic Mid-Ocean Ridge Basalt (MORB) field (Figure 5). The Buta Ranquil sample is displaced to higher Nd and/or Sr isotope ratios and has the highest Nd isotope ratio of the samples we analyzed, while the other Tromen samples plot together with the other BA samples. The trench sediments largely overlap the volcanic rocks in Nd, but extend to higher Sr isotope ratios. Most of the sediments that we analysed lie at the enriched end of the Chilean trench sediment field in Figure 5 defined by data from Lucassen et al. (2010).

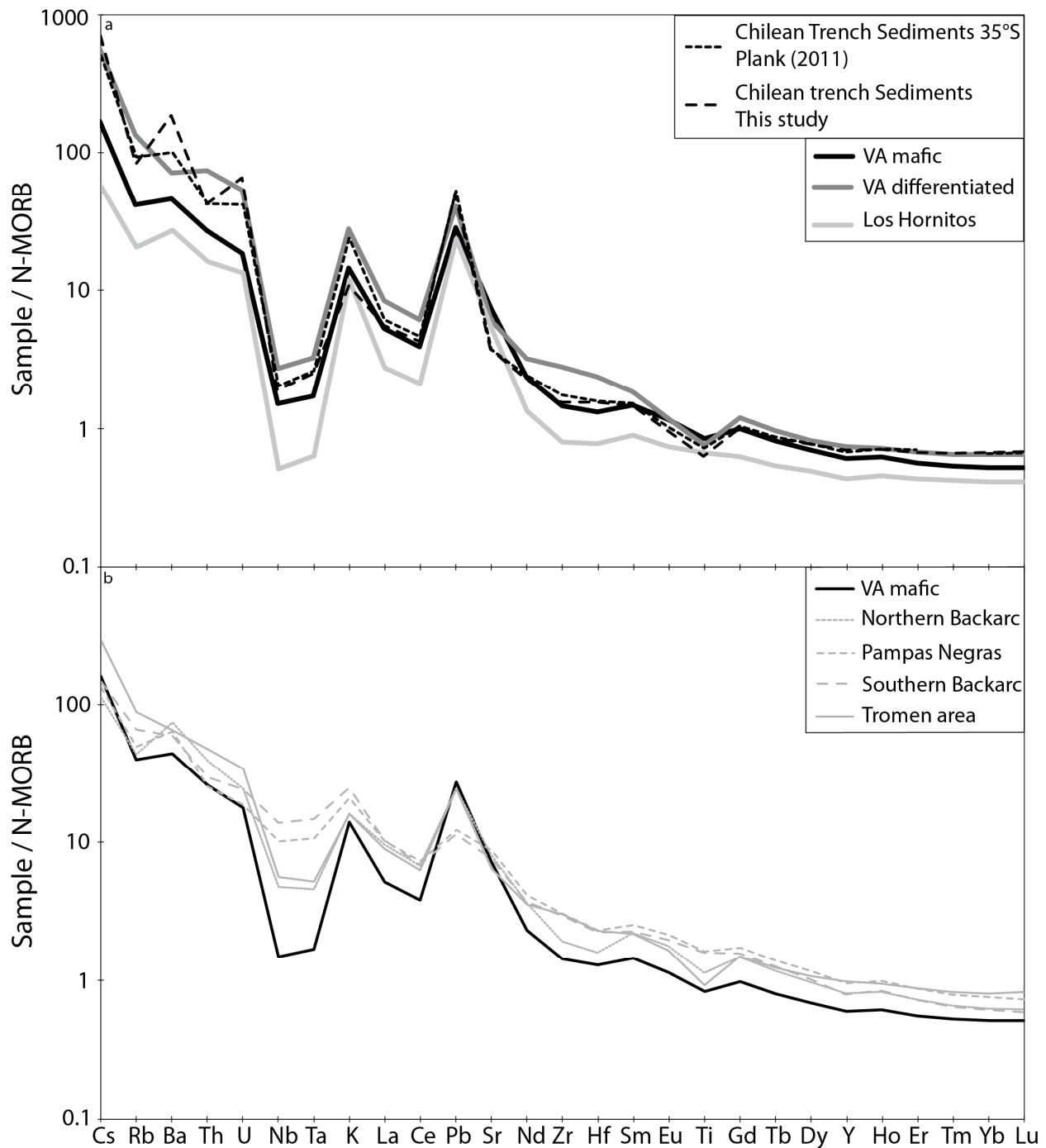


Figure 2.4 Multi-element diagram normalized to N-MORB after Sun and McDonough (1989), showing (a) the VA and trench sediments and (b) the BA. VA samples show typical subduction zone trace element signatures highlighted by Pb and K peaks and Nb and Ta troughs. More differentiated VA samples (with MgO < 5 wt. % and SiO₂ > 54 wt. %) show greater enrichment in Cs, Rb, Zr, and Hf, and depletion in Ti. BA samples from Pampas Negras and SBA show less pronounced peaks at Pb and K, and troughs at Nb and Ta, while NBA and Tromen samples have an intermediate subduction zone signature. Trench sediments from this study and Plank (2011) overlap the VA pattern.

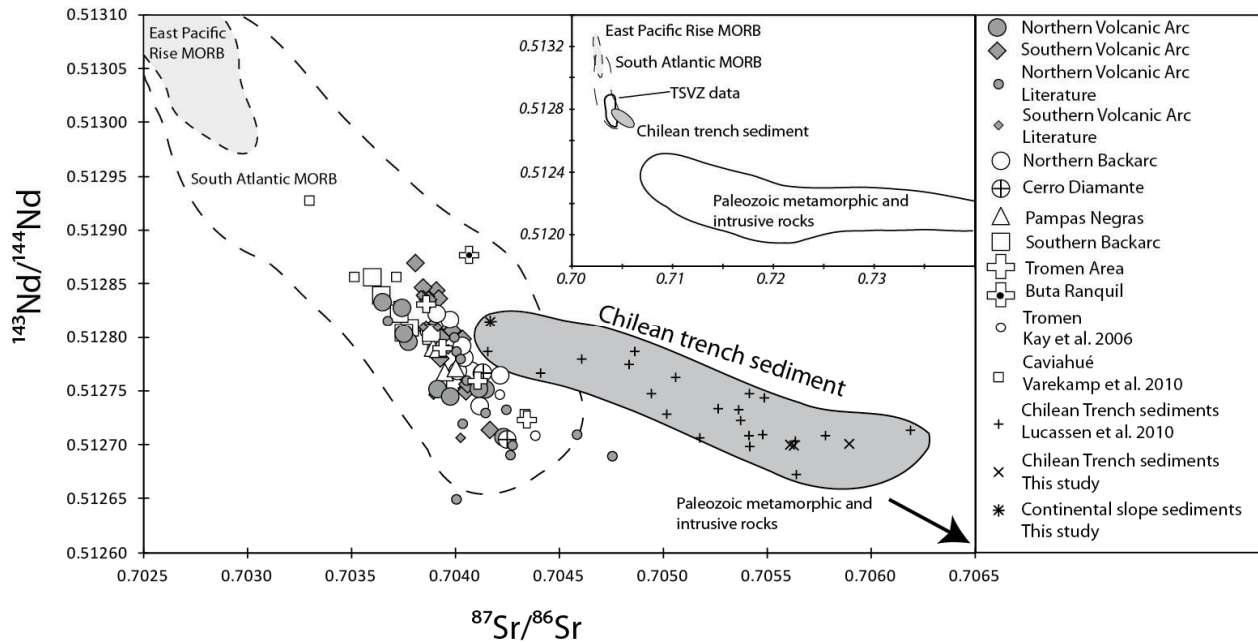


Figure 2.5 $^{87}\text{Sr}/^{86}\text{Sr}$ versus $^{143}\text{Nd}/^{144}\text{Nd}$. VA and BA samples form two similar negative arrays which overlap almost completely. All samples from this study lie within the South Atlantic MORB field. The BA samples from the three segments (north, central = Pampas Negras, and south = SBA, Tromen) have distinct compositions (also see Figure 12). Trench sediments have similar Nd isotopes ratios as the volcanic rocks but more radiogenic Sr isotopes. The inset shows the TSVZ data (VA and BA) in a larger scale, including the Paleozoic metamorphic and intrusive basement in Chile and Argentina. VA literature data are from Hildreth and Moorbath (1988), Tormey et al. (1995), Davidson et al. (1987, 1988), Hickey-Vargas et al. (1986), Harmon et al. (1984), and Sigmarsson et al. (1990). BA literature data are from Kay and Copeland (2006) and Kay et al. (2006a,b) and Varekamp et al. (2010). Trench sediment data are from this study and Lucassen et al. (2010). Basement data are from Lucassen et al. (2004). East Pacific Rise (20-34°S) MORB data are from Fontignie and Schilling (1991), Haase (2002), Hamelin et al. (1984), Hanan and Schilling (1989), Ito et al. (1980), Ito et al. (1987), Kingsley et al. (2007), MacDougall and Lugmair (1986), Mahoney et al. (1994), Newsom et al. (1986) and White et al. (1987). South Atlantic (30-50°S) MORB data are from Andres et al. (2002), Douglas et al. (1999), Fontignie and Schilling (1996), Hanan et al. (1986) and Roy-Barman et al. (1998).

The Pb isotope data for VA and BA samples have the same tight positive correlations on uraniumogenic Pb ($r^2 = 0.92$ or 0.94 excluding the Buta Ranquil sample) and thorogenic Pb ($r^2 = 0.96$ or 0.97) isotope diagrams (Figures 6a,b). This is a much tighter array than for older unspiked data (e.g. Hildreth and Moorbath, 1988; Tormey et al., 1995; Davidson et al., 1987, 1988, not shown). The VA samples (with $^{206}\text{Pb}/^{204}\text{Pb} = 18.56-18.65$) fall almost completely within the field for the Chilean trench sediments and cover nearly the full range in $^{206}\text{Pb}/^{204}\text{Pb}$ ratios of the sediments, whereas the backarc samples (with $^{206}\text{Pb}/^{204}\text{Pb} = 18.30-18.61$) extend to significantly less radiogenic Pb isotopic compositions, whereas the southern and central part of the BA have the least radiogenic Pb isotopic compositions, whereas the NBA, Tromen and Buta Ranquil have Pb isotope ratios intermediate between the VA and the southern BA and are shifted to slightly lower $^{207}\text{Pb}/^{204}\text{Pb}$ at a given $^{206}\text{Pb}/^{204}\text{Pb}$ isotope ratio (towards a Pacific MORB component). Pb isotope ratios (e.g.

$^{206}\text{Pb}/^{204}\text{Pb}$ correlate well with Nb/Zr ($r^2 = 0.70$), Nb/U ($r^2 = 0.84$), Ce/Pb ($r^2 = 0.81$) (Figure 7), if the BA samples from Buta Ranquil and the Cerro Diamante stratovolcano are excluded. The correlations within individual volcanic centers are slightly more scattered, especially for the VA samples which overlap the Chilean trench sediment field on these diagrams.

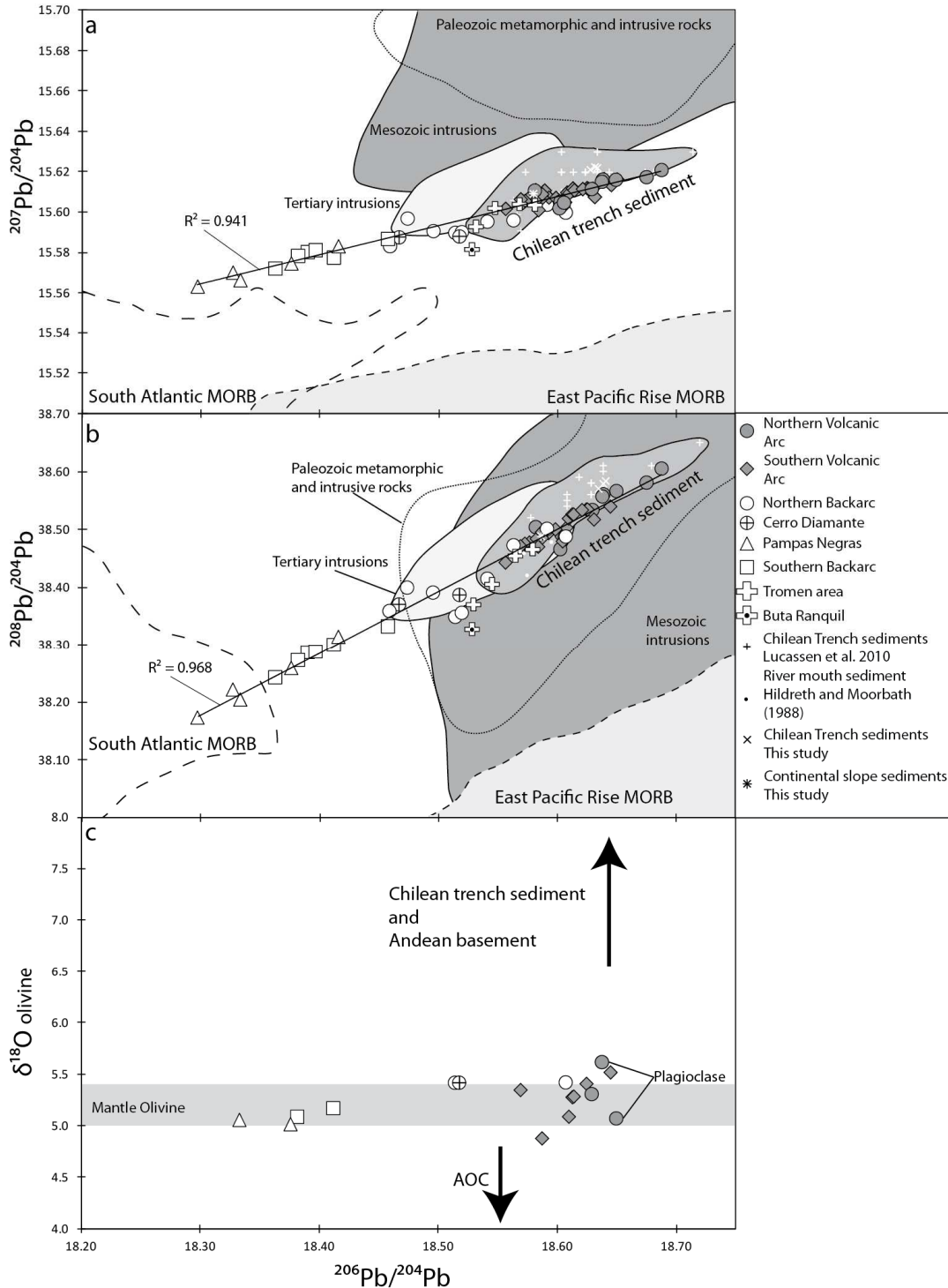


Figure 2.6 (Previous page) $^{206}\text{Pb}/^{204}\text{Pb}$ versus (a) $^{207}\text{Pb}/^{204}\text{Pb}$, (b) $^{208}\text{Pb}/^{204}\text{Pb}$ and (c) $\delta^{18}\text{O}_{\text{olivine}}$. The samples form positive arrays from the BA to the VA with good correlations represented by the thin black lines ($r^2 = 0.941$ and 0.968 if the Buta Ranquil sample is excluded). An extrapolation of the arrays intersects the South Atlantic MORB but not the East Pacific Rise MORB field. The trench sediments fall at the radiogenic end of the BA-VA arrays. The Cretaceous to Paleozoic basement fields overlap the data on the thorogenic Pb isotope diagram but have higher $^{207}\text{Pb}/^{204}\text{Pb}$ on the uraniumogenic Pb isotope diagram. The NBA samples are shifted to lower $^{207}\text{Pb}/^{204}\text{Pb}$ or more Pacific MORB-like compositions compared to the VA samples. There is no correlation between O isotopes and Pb isotopes. Data sources are the same as in Figure 5. Trench sediment field includes river mouth sediments from Hildreth and Moorbath (1988).

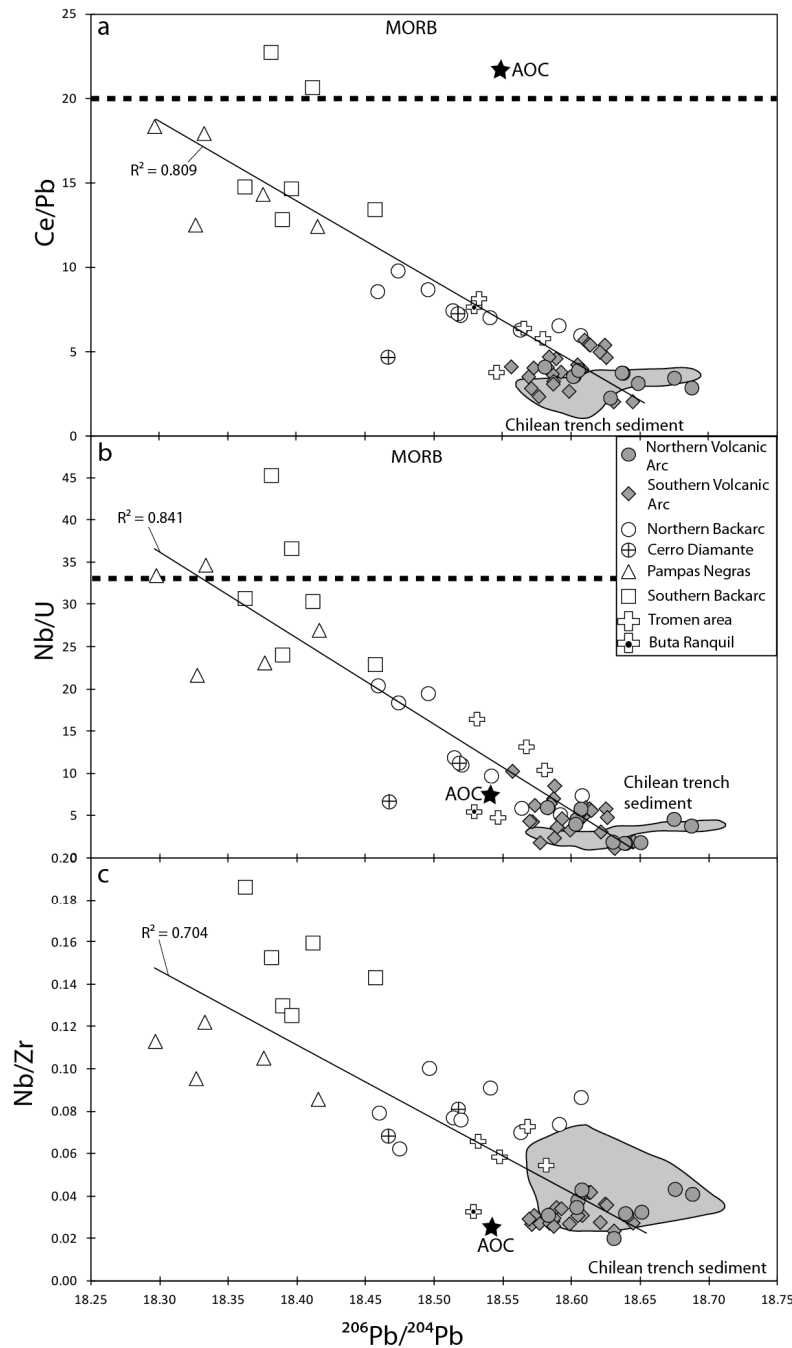


Figure 2.7 (Previous page) $^{206}\text{Pb}/^{204}\text{Pb}$ (a) versus Ce/Pb, (b) Nb/U, and (c) Nb/Zr. The data form good negative correlations for the BA to the VA data ($r^2 = 0.809, 0.841$ and 0.704 , respectively). Two-component mixing must form a straight line when the denominator is the same on both axis as in (a). The VA samples overlap the trench sediment field. The SBA samples extend to higher Ce/Pb, Nb/U and Nb/Zr than the Pampas Negras basalts which have similar Pb isotope ratios, which we believe reflects source heterogeneity. MORB field is represented by the dashed line box (range in average values for MORB and OIB from Hoffman et al., 1986). Trench sediments are from this study and Lucassen et al. (2010). AOC is from Tollstrup et al. (2010).

The samples form two subparallel positive arrays on a plot of Nd versus Hf isotope ratios with the VA samples ($r^2 = 0.87$) having higher ϵHf for a given ϵNd than the BA samples ($r^2 = 0.79$) (Figure 8). We know of no other arc like this (cf. Pearce et al., 1999, Woodhead et al., 2001, 2012, Tollstrup and Gill 2005, Yodozinski et al., 2010). The Chilean trench sediment outboard of the TSVZ is displaced above the VA field, which we attribute to the presence of a pelagic component, while sediments from the Peru/Chile trench >2000 km farther north have lower ϵNd than any of the TSVZ volcanic rocks (Vervoort et al., 1999, 2011). The most radiogenic Peru trench sediment with $\epsilon\text{Hf} = +4-5$ slightly overlaps the least radiogenic TSVZ VA samples in ϵHf . The sediment from the canyon on the continental slope has similar Hf-Nd isotopes to the VA.

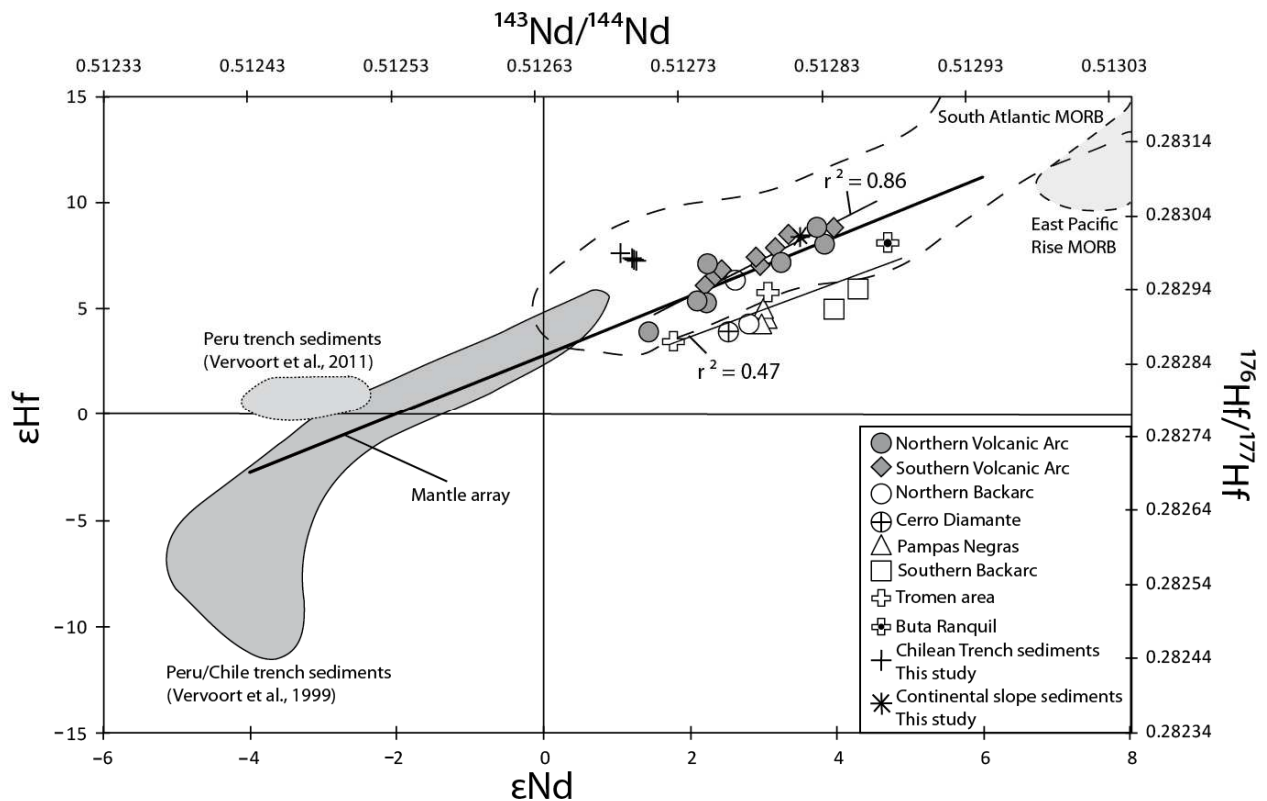


Figure 2.8 (Previous page) ϵNd versus ϵHf . The VA and BA samples form separate subparallel positive correlations with correlation coefficients (r^2) of 0.87 and 0.79, respectively. VA samples have higher ϵHf than the BA for a given ϵNd . The thick black line represents the mantle array (Geldmacher et al., 2006). Data sources are the same as in Figure 5. The Peru/Chile trench sediments are from Vervoort et al. (1999) and Vervoort et al. (2011).

Oxygen isotope analyses of olivine (and two plagioclase samples normalized to olivine) define narrow ranges for both the VA (4.88 to 5.62‰ or 5.52‰ if the plagioclase value from CL 726, the most evolved sample measured for oxygen isotopes, is excluded) and BA (5.02-5.42‰) (Figure 6c). The VA samples spread around canonical mantle olivine values (5.0-5.4‰; Matthey et al., 1994) and extend to both slightly lighter and heavier compositions. Excluding CL726, $\delta^{18}\text{O}$ for the other samples show no correlation with parameters of differentiation, such as SiO_2 (Figure 9a) or MgO content (not shown), or with incompatible elements or Sr, Nd, or Pb isotope ratios (e.g. Figure 6c).

The compositions of the SO210 trench sediments (major and trace elements and Sr-Nd-Pb isotopes) are comparable to those reported previously (Lucassen et al., 2010) and summarized by Plank (2011), except that our samples have higher Ba concentrations. Since our results for reference materials are close to expected values and the Ba data are reproducible, we exclude an analytical problem with our data. Our trench sediments are quite uniform in isotopic composition apart from the one from a canyon on the continental slope where the sediments are similar to Quaternary volcanic rocks and are likely to reflect eroded volcanic arc rocks. Our “typical” trench sediment composition in Table 3 is similar to that of Plank (2011) for 35°S and 40°S except for Ba. In order to use actual samples for representative values, we used our sample SO210-#5-B for trace elements and sample 75KD(1) from Lucassen et al. (2010) for isotopes. Sample 75KD(1) comes from a bit further south of the studied area but is similar to our sediment data (Table 1 and Table 2) and is the single best mixing end member to explain TSVZ VA volcanic rocks. Isotopically, our new sediment data and sample 75KD(1) enclose the values chosen by Plank (2011), although her values are more radiogenic than most of our samples. In general, the trench sediments and volcanic rocks are similar in composition, which is not unexpected because the trench sediments at 35°-40°S are dominated by turbidites from the Cenozoic magmatic arc delivered through canyons in the continental slope and also contain

ash from the volcanic arc. The chief isotopic differences are that the sediments have considerably higher $\delta^{18}\text{O}$, ranging from 7.8-14.1‰, and higher $^{87}\text{Sr}/^{86}\text{Sr}$ relative to $^{143}\text{Nd}/^{144}\text{Nd}$.

2.5 Discussion

Based on the major element data, two distinct magmatic series can be recognized in the TSVZ. The VA is subalkaline (calc-alkaline/medium-Fe) whereas the BA is alkaline with higher Ti, Na, and P (Figures 2 and 3). Compared to the BA samples, the VA samples have higher fluid mobile (LILE) and lower fluid immobile element (HFSE and heavy REE) contents, and lower ratios of more to less incompatible HFSE and REE (e.g. Nb/Zr, Nb/Y, Nb/Yb, Ta/Yb, Gd/Yb, Tb/Yb) (e.g. Figure 7c, not all ratios shown). Due to differences in bulk distribution coefficients, these ratios can be fractionated by differing degrees of mantle melting (e.g. Green et al., 2000). In contrast, some elements that cannot be easily fractionated by mantle melting can instead be fractionated by fluids or hydrous melts from the subducted slab. Ratios of fluid-mobile (e.g. LILE) to fluid-immobile (e.g. HFSE and REE) elements (e.g. Ba/Nb, U/Nb, Pb/Ce and Pb/Nd ratios) (e.g. Figure 7a,b, not all ratios shown) are higher in VA lavas. The variations in these ratios are consistent with a higher fluid flux beneath the VA than the BA, resulting in higher degrees of melting beneath the VA (e.g., Marianas arc, Elliot et al., 1997; Kelley et al., 2006) to produce the larger volume stratovolcanoes of the VA relative to the isolated fields of cinder cones in the BA, including those on older shield and stratovolcanoes. Although the VA and BA almost completely overlap in Sr, Nd and O isotopic composition, the VA samples have more radiogenic Pb isotopic compositions which overlap the field for Chilean Trench sediments, whereas the BA samples have less radiogenic Pb, projecting into the field for South Atlantic MORB. On the Nd versus Hf isotope diagram, the VA and BA form distinct positive linear arrays with the VA samples shifted towards more radiogenic Hf at a given Nd isotopic composition.

We will next discuss possible reasons for the differences between the VA and the BA: assimilation of the continental crust, heterogeneity of the mantle wedge, and the nature of the slab-derived component.

2.5.1 Crustal assimilation

Because the TSVZ overlies 35-45 km thick crust, crustal assimilation is a distinct possibility during magma ascent. In particular, Hildreth and Moorbath (1988) and Tormey et al. (1991) noted an increase in trace element concentrations and Sr-Nd isotopic enrichment of evolved rocks erupted north versus south of 37°S, correlating with an increase in crustal thickness to the north, and interpreted this to result from greater degrees of crustal assimilation in the north where the crust is thicker. Studies of single volcanoes north of 37°S also demonstrate that crustal contamination is possible in the more evolved magmas. Tormey et al. (1995) proposed that crustal assimilation played a role in dacitic and rhyodacitic rocks at the Azufre-Planchón-Peteroa complex at the volcanic front, as did Hildreth et al. (2010) for the Laguna del Maule area in the rear arc. Davidson et al. (1987, 1988) studied the Tatara-San Pedro-Pellado complex in detail. They suggested that although the sub-arc asthenospheric mantle was the principle source of basalts, and their LILE enrichments were largely from slab fluids, the more evolved rocks were affected by crustal assimilation during crystal fractionation. Dungan et al. (2001) and Dungan and Davidson (2004) proposed that assimilation of mafic plutonic roots occurs sometimes in San Pedro, primarily affecting the major and trace element contents of the magmas with little effect on the radiogenic isotopic composition. Therefore, it is essential to evaluate if these processes affected the geochemistry of our samples.

We analysed the most mafic of the youngest samples that we could find at each edifice, mostly with olivine phenocrysts, because most studies of the SVZ between 34.5-43°S have concluded that the olivine basalts in the SVZ were not significantly crustally contaminated (e.g. Hickey-Vargas et al., 1984, 1986, 1989, 2003; Futa and Stern, 1988; Sigmarsson et al., 1990, 2002). We also avoided xenocrystic and xenolithic material during sampling and sample preparation. Our VA samples can be divided into a mafic group with MgO > 5 wt. % and SiO₂ < 54 wt. %, and a differentiated group with lower MgO and higher SiO₂ content. The differentiated group consists of three samples from Tinguiririca, three from San Pedro, two from Longaví, two from Antuco, one from Callaqui and one from Copahue. There is no difference between the average of mafic and evolved groups in trace element ratios or in any

isotope ratio (Figure 9) and the most-evolved high-K calc-alkalic Tinguiririca samples do not have the highest Sr or lowest Nd isotope ratios (Figure 5, 9b,c). Neither the VA nor BA shows systematic variations with SiO₂ or MgO (not shown). Due to the high Pb concentrations in most crustal rocks, Pb isotopes are a very sensitive indicator of crustal assimilation. The end member VA samples, with the most radiogenic Pb isotope ratios, fall below (have lower ²⁰⁷Pb/²⁰⁴Pb than) all basement rocks with similar ²⁰⁶Pb/²⁰⁴Pb on the uraniumogenic Pb isotope diagram (Figure 6a; basement data from Lucassen et al., 2004; 36-41°S). Since neither the VA nor BA end member falls within the fields for the crustal basement rocks, the very tight correlations in our high-precision Pb isotope ratios preclude significant crustal assimilation having affected any of these samples. Furthermore, there is no correlation between any isotope ratio and δ¹⁸O (for example, Figures 6c and 13). Thus, radiogenic isotopes show no evidence of crustal assimilation of older basement rocks, even in the andesites.

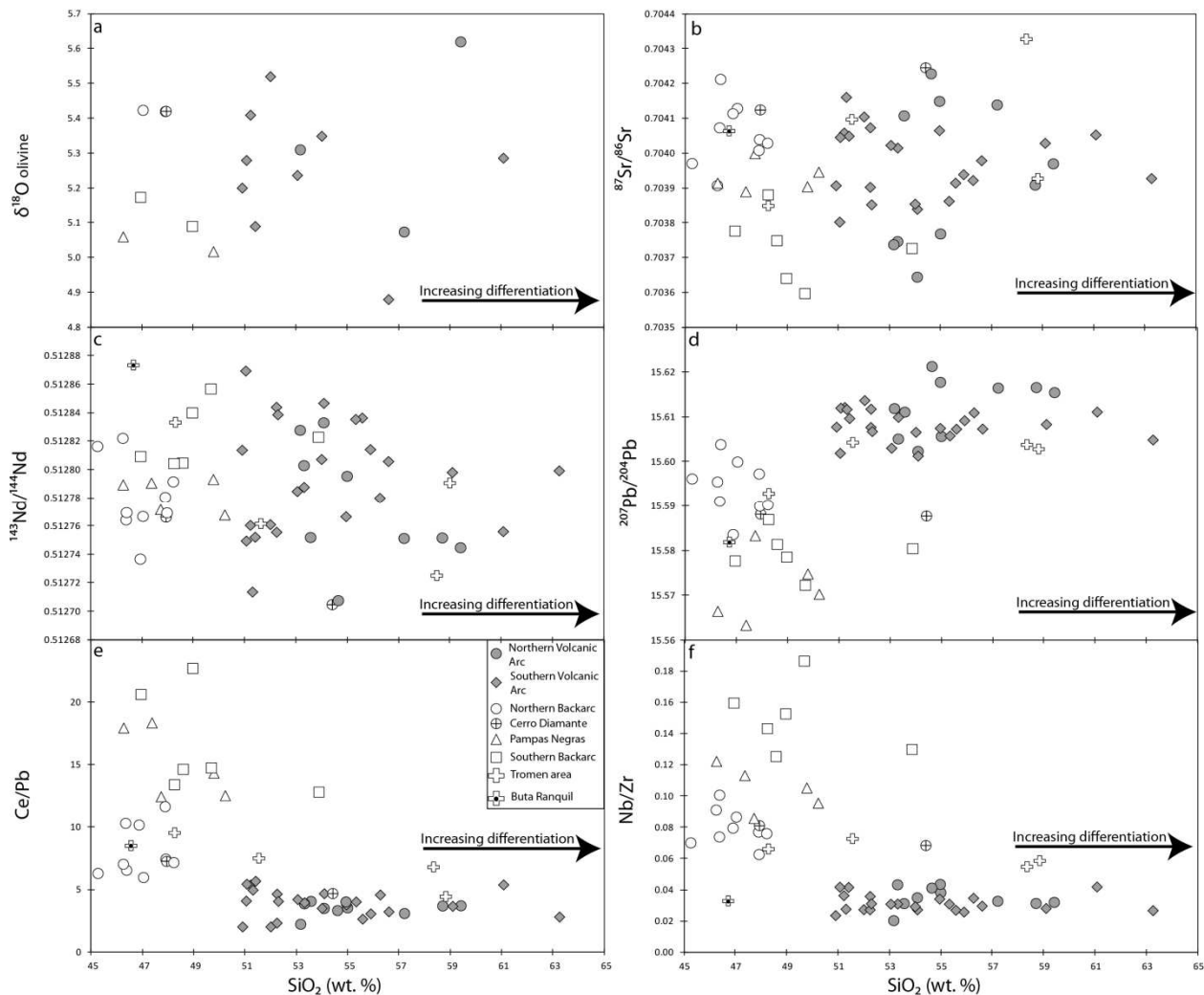


Figure 2.9 (Previous page) SiO₂ versus (a) Ce/Pb, (b) Nb/Zr, (c) ⁸⁷Sr/⁸⁶Sr, (d) ¹⁴³Nd/¹⁴⁴Nd, (e) ²⁰⁷Pb/²⁰⁴Pb and (f) δ¹⁸O_{olivine}. There is no clear correlation for the VA or BA samples between SiO₂ and isotopes or trace element ratios used in this paper indicating that assimilation of old sialic crust during differentiation does not significantly modify these isotopes and trace element ratios in our samples.

Variations in O isotope values in volcanic rocks can be used to constrain the amount of assimilation of isotopically diverse components (e.g. Bindeman, 2008). However, the δ¹⁸O_{olivine} in the volcanic rocks from the VA overlap the range of mantle olivine (5.0-5.4‰, Matthey et al., 1994) and extend to only slightly higher values (5.5‰ if the most evolved sample is excluded) and lower values (4.9‰) (Figure 6c), which could reflect slightly variable contributions from lower δ¹⁸O subduction fluids from the lower oceanic crust, or higher δ¹⁸O subduction melts from the seawater-altered upper crust (e.g. Bindeman et al., 2005; Martin et al., 2011). The BA samples (5.02-5.42‰) are within the mantle range. In both the VA or BA samples, δ¹⁸O do not correlate with indices of differentiation (for example SiO₂, Figure 9a) or other isotope ratios, such as ²⁰⁷Pb/²⁰⁴Pb (not shown), which are discriminantly higher in Andean basement rocks (Lucassen et al., 2004, Figures 6). Moreover, δ¹⁸O values are within the typical range for subduction zone volcanic rocks lacking other evidence for crustal assimilation (e.g. Central America: see Heydolph et al., 2012). They are also within the range for oceanic arcs where there is less potential for crustal assimilation. The Mariana arc has whole rock δ¹⁸O values between 5.5‰ and 6.6‰ (Wade et al., 2005), and Tonga arc values are between 5.6‰ and 6.8‰ (Ewart and Hawkesworth, 1987, Vallier et al., 1991, Turner et al., 2009). We corrected our VA phenocryst δ¹⁸O values to equilibrium melt following Bindeman et al. (2004) who calculate the Δ(min.-melt) based on the SiO₂ content of the whole rock. However this correction needs to be applied with caution, since the linear equation is based on the liquid-descent line of Kamchatka magmas. If the liquid line of descent of the Andean magmas is different, it can decrease or increase the Δ(min.-melt) and therefore change the range in δ¹⁸O(melt). Our corrected VA phenocryst δ¹⁸O values yield a similar range of 5.9-6.5‰ (excluding the most evolved sample CL 576 with δ¹⁸O melt of 7.1) (Table 2). It has been proposed that whole rock δ¹⁸O up to ~6.6‰ can be inherited from a slab component (Eiler et al., 2005) or metasomatized mantle containing pyroxenitic veins from earlier arc volcanism (Heydolph et al., 2012), or a preexisting subduction enrichment (Auer et al., 2009, Martin et al., 2011).

The low $\delta^{18}\text{O}$ value for CL 531 from Longaví (4.88‰) could be explained by assimilation of hydrothermally altered mafic rocks, such as in the lower crust (with $\delta^{18}\text{O} = 0\text{-}6\%$, Bindeman et al., 2005, and references therein), as proposed by Dungan and Davidson (2004) for San Pedro. Our samples from San Pedro do not have low $\delta^{18}\text{O}_{\text{olivine}}$, however. Alternatively, the low $\delta^{18}\text{O}$ at Longaví could possibly reflect the derivation of fluids from serpentinite associated with the Mocha Fracture Zone subducting beneath Longaví.

In summary, our isotope data show no clear evidence that assimilation of old sialic crust affected our TSVZ basalt to andesite samples. Even if there was assimilation of the mafic roots of the volcanoes in some of our more differentiated samples, it would only add potential for sampling greater Sr-Nd-Hf-Pb isotope mantle heterogeneity throughout the Cenozoic in the vicinity of the volcanoes, and would not affect our conclusion that the primary isotopic diversity comes from the mantle, not the sialic crust.

2.5.2 The mantle wedge and subcontinental lithosphere

BA basalts have less subducted component signature in their trace element abundance patterns (Figure 4b) than the VA samples and are displaced the most from sediment in their Pb isotopic compositions (Figures 6a,b). Indeed, those from the southern and central BA extend to MORB-OIB (Ocean Island Basalt) Ce/Pb, Nd/Pb, Nb/U, and Nb/Th ratios (Hofmann et al., 1986) with little if any evidence for slab-derived Pb, U or Th (Figures 7a,b and 10-11). Therefore, we propose that BA basalts in general, and the SBA and Pampas Negras basalts in particular, best represent the geochemical character of the TSVZ BA mantle source.

On the uranogenic Pb isotope diagram (Figure 6a), the BA array lies above the Pacific MORB field. An extension of the BA trend does not intersect the Pacific MORB field but does intersect the enriched part of the South Atlantic MORB field, which has elevated $^{207}\text{Pb}/^{204}\text{Pb}$ at $^{206}\text{Pb}/^{204}\text{Pb}$ between 17.6 and 18.2. Consequently, the BA mantle source has South Atlantic rather than East Pacific Rise affinity. This is in agreement with the work of Husson et al. (2012) that modeled the flow of South Atlantic mantle beneath South America. They modeled

westward mantle convection beneath South America as a counterflow above the subducting Nazca plate. Therefore, this convection brings South Atlantic Ridge mantle beneath the Andes.

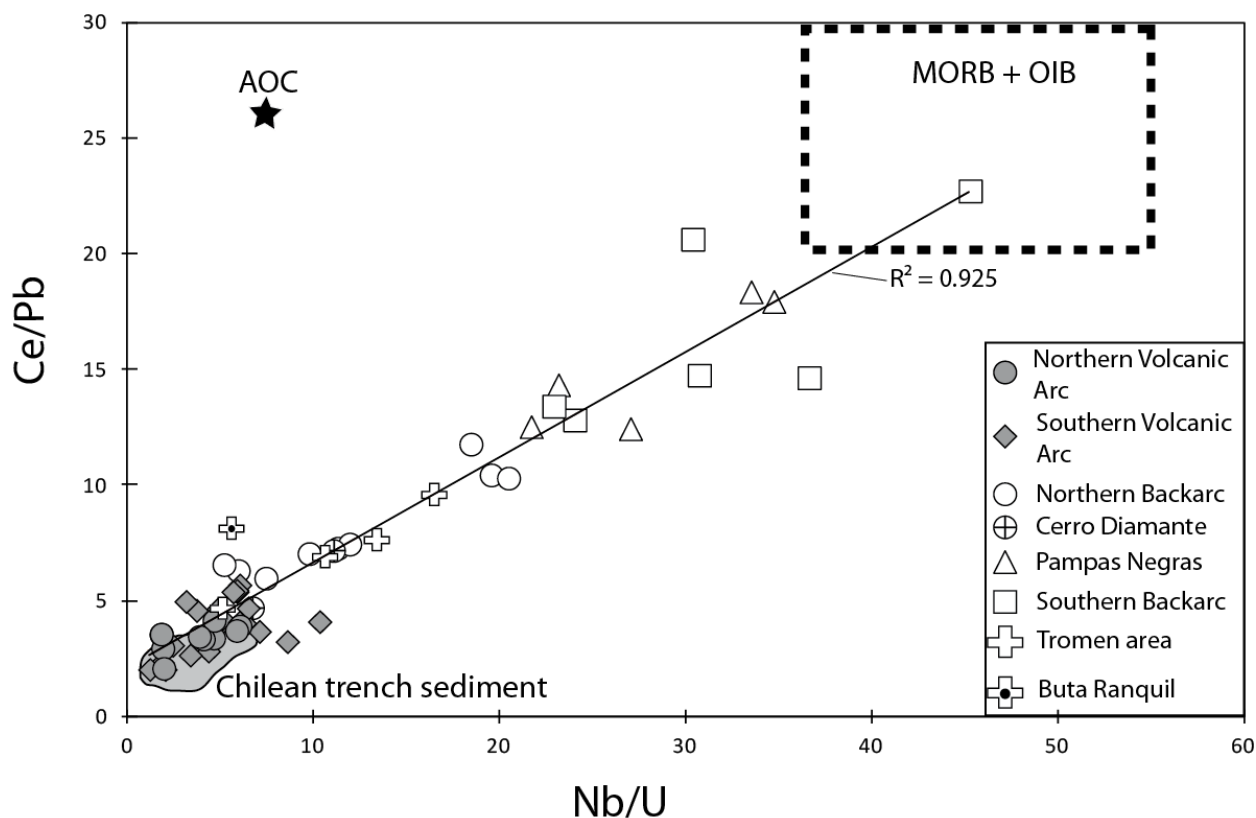


Figure 2.10 Nb/U versus Ce/Pb. The VA and BA samples form an array from the trench sediments field to the MORB-OIB mantle field represented by the dashed line box (range in average values for MORB and OIB from Hoffman et al., 1986). The correlation ($r^2 = 0.925$) indicates the presence of variable amounts of a uniform slab component in all samples, but least at the SBA and Pampas Negras. Trench sediments are from this study and Lucassen et al. (2010). AOC is from Tollstrup et al. (2010).

Many of our BA basalts, and especially those from the SBA and Pampas Negras, are enriched in HFSE with $Nb/Yb > 10$, like alkalic OIB (Figure 11), and plot beneath the field for South Atlantic MORB on the Hf versus Nd isotope ratio diagram (Figure 8). Therefore, the TSVZ BA mantle may contain OIB or EMORB-type components. In contrast, VA basalts have lower Nb/Yb (Figure 11) and Nb/Zr (Figure 7c) indicating that the VA mantle source is more depleted, or has experienced higher degrees of melting or both, than the BA source. Increasing source depletion closer to the VA may reflect progressive extraction of small degree melts as a result of corner flow in the mantle wedge (Hochstaedter et al., 2001). Increasing percent melting beneath the VA is consistent with a higher mass fraction of slab flux there.

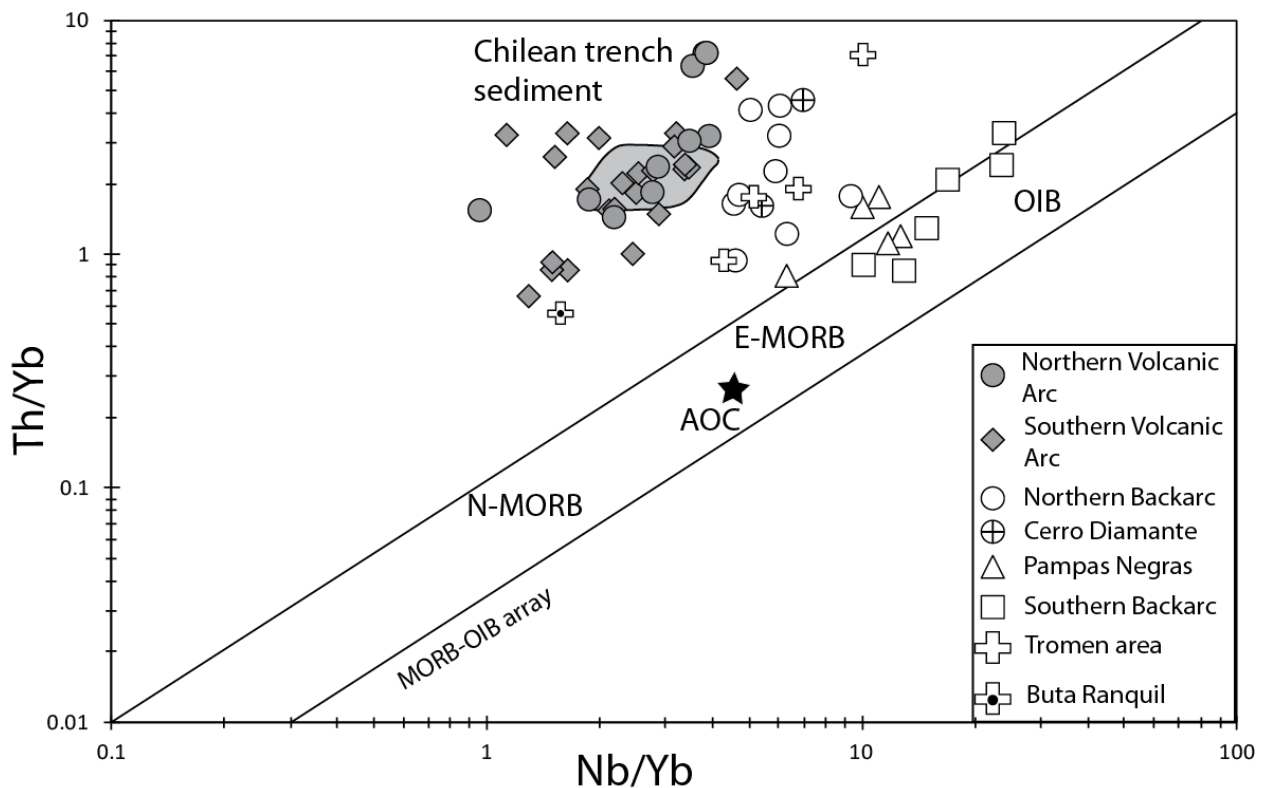


Figure 2.11 Nb/Yb versus Th/Yb, after Pearce (2008). MORB and OIB define the positive trend labeled MORB-OIB array, reflecting greater mantle enrichment at higher ratios. VA and NBA samples lie above this array due to the addition of a Th-bearing slab component whereas most BA samples from Pampas Negras and the SBA lie within the mantle array or straddle its boundary and therefore lack slab-derived Th. The VA samples overlap, but show a larger range, than the trench sediments (grey field). Data sources are the same as in Figure 10.

The Sr and Nd isotopes of most VA and BA basalts lie within the enriched portion of the South Atlantic MORB (SAM) field (Figure 5). In detail, those from the SBA and Pampas Negras (36–38°S), which show no evidence for the addition of slab-derived Th (Figure 11) and little addition of U and Pb (Figure 7a,b), span a range of Sr and Nd isotopes that we attribute to the mantle source. These rocks form a negative array on the Sr-Nd isotope diagram and plot at the left edge of the TSVZ VA field, having less radiogenic $^{87}\text{Sr}/^{86}\text{Sr}$ at a given $^{143}\text{Nd}/^{144}\text{Nd}$ isotope ratio. Basalts from the Resolana and Los Hornitos cones near Cerro Azul and from Tinguiririca in the northern VA (34.5–36°S) overlap the range for the southern BA lavas, excluding the Buta Ranquil sample. Therefore, the TSVZ mantle is heterogeneous in Sr and Nd, and contains both depleted (SAM-D) and enriched (SAM-E) components (Figure 12a).

Although VA and BA samples overlap almost completely on the Sr-Nd isotope diagram (Figure 5), the same is not true for Pb (Figures 6a,b) or Hf isotope ratios (Figure 8). This can be seen most easily by combining Sr and Pb isotope ratios (Figure 12b), where the northern and southern VA groups, the central and southern BA groups, and perhaps even NBA samples seem

to define different mixing trends between a slab component (trench sediment \pm Altered Oceanic Crust (AOC)) and variable mantle components. The northern and southern VA groups could be derived through mixing of the same end members (slab component + SAM-D) with different Pb/Sr ratios in one or both of the end members, or through mixing of slab and/or mantle components with slightly different compositions. The BA groups require a spatially heterogeneous mantle source with the addition of less slab component than at the VA. The SBA and Pampas Negras mantle end members most closely approximate the SAM-D and SAM-E components respectively.

This explanation, however, does not easily apply to the variation between Hf and Nd isotopes. The VA and BA groups define subparallel and offset positive correlations between Hf and Nd isotopes (Figure 8). Within the VA, the depleted end (with highest Nd and Hf ratios) consists of the Resolana/Los Hornitos cones that have the least radiogenic Sr and most radiogenic Nd isotope ratios and are the closest to the depleted mantle component (SAM-D in Figure 12). The more enriched VA samples do not lie on a mixing line between the depleted end and trench sediment as is the case on the $^{87}\text{Sr}/^{86}\text{Sr}$ vs. $^{206}\text{Pb}/^{204}\text{Pb}$ isotope diagram (Figure 12b). Instead they define a mixing array slightly steeper than the mantle Hf-Nd array (Geldmacher et al., 2006) such as observed in South Pacific backarc basalts (Todd et al., 2011). This mixing array is most easily explained by mantle heterogeneity. The completely offset BA Hf-Nd array is without precedent in subduction zones to our knowledge. Apart from Central America where some BA samples also plot beneath the VA array (Heydolph et al., 2012), in no other arc do VA and BA samples define separate subparallel trends. All of these BA basalts have typical mantle Hf/Nd concentration ratios. The more depleted end of the BA Hf-Nd isotope array (SBA) also extends to the lowest Sr and Pb isotope ratios. The more enriched end of the BA array (NBA) is not offset toward subducting sediment in Nd and Hf isotopes. We think that the BA Hf-Nd trend also reflects mixing between depleted and enriched mantle components. Because the BA array is without precedent in oceanic arcs and lies below the field of South Atlantic MORB, we believe that both of its mantle components may lie within South American Proterozoic subcontinental lithosphere. Similarly low Hf with respect to Nd isotopes have been observed within continental

basalts and attributed to mixing between components in subcontinental lithospheric mantle elsewhere (e.g. Zhang et al., 2009).

The restricted and mantle-like range in $\delta^{18}\text{O}$ (5.0-5.4‰) of the BA rocks suggests a source within the sub-continental lithospheric mantle. Its enriched end member may be the EM1-type mantle identified by Varekamp et al. (2010) in the Loncopue graben (37.5°-39°S, Neuquén, Argentina) that they also attributed to the subcontinental lithospheric mantle. The difference in Nb/Yb ratios between BA and VA could reflect trenchward advection and depletion of asthenospheric mantle but could also reflect a contrast between VA melts primarily derived from the asthenosphere versus BA melts that are in part from subcontinental lithospheric mantle beneath the BA. The latter may exist as delaminated old heterogeneities with lower solidi that melt out as mantle advects trenchward (Hochstaedter et al., 2001).

We also note the inconsistent correlation between trace element and isotope ratio measures of mantle enrichment and depletion. Nb/Yb and Nb/Zr ratios form crude positive correlations with $^{176}\text{Hf}/^{177}\text{Hf}$ and $^{143}\text{Nd}/^{144}\text{Nd}$ in the BA basalts (not shown), opposite to what is generally observed for the mantle (e.g. Douglass, 2002, Andres et al., 2002, Kingsley, 2002, Kingsley et al., 2007). Therefore, melting effects are superimposed on source effects within the BA basalts. The SBA basalts are farthest from the VA and reflect the lowest percent melting, because the amount of slab component fluxing is least.

Kay et al. (2004, 2005, 2006a,b) and Kay and Copeland (2006) (and references therein) proposed that magmatism in the southern Mendoza and Neuquén provinces (which overlap and extend further south than our BA area) resulted from melting of hydrated mantle after two temporary flat subduction episodes in the late Miocene that moved the volcanic front eastward and produced large stratovolcanoes like Tromen and Cerro Diamante. The NBA and Tromen groups exhibit more arc affinities than the rest of our BA samples by: 1) having greater positive anomalies in fluid-mobile elements (Pb, K) and negative anomalies in HFSEs (Nb, Ta), 2) plotting closest to the VA in the Ce/Pb versus Nb/U diagram (Figure 10), 3) plotting above the mantle array and close to the VA on the Nb/Yb versus Th/Yb diagram (Figure 11), 4) having higher La/Ta, Ba/Ta and Th/Hf ratios than the other BA rocks which are most similar to the VA, and 5) having Pb isotope ratios most similar to the VA rocks. This could reflect residual slab

components in the lithospheric mantle and/or crust beneath this part of the BA left over from when it was near the VA in the late Miocene/Early Pliocene, or more current input of slab components beneath these parts of the BA. The addition of Paleozoic crust to the mantle wedge as a result of forearc erosion in the late Miocene (Kay et al., 2005) cannot explain the more arc-like composition of the NBA because the addition of Paleozoic metamorphic or igneous crust would increase $^{207}\text{Pb}/^{204}\text{Pb}$ ratios in the NBA, yet they tend to be lower (not higher) at a given $^{206}\text{Pb}/^{204}\text{Pb}$ compared to the VA and other BA basalts (Figure 6a).

2.5.3 The slab component

In general, fluids and/or melts can be produced by dehydration and/or melting of the slab during subduction beneath the VA and BA. Possible slab sources include the sediments, AOC, and the underlying lithospheric mantle that may have been serpentinized at bend faults and/or fracture zones. In this section we will attribute features that cannot otherwise be accounted for by crustal assimilation or mantle heterogeneity to a slab-derived component, and explore the nature of that component.

2.5.3.1 Sources of the slab component

The incompatible element ratios of trench sediments almost completely overlap those of VA volcanic rocks in part because the former are almost entirely derived from the latter. Nonetheless, their similarity in Figure 4a means that the currently subducting sediments may be responsible for the trace element pattern of the currently erupting magmas. Pb isotopes confirm this observation because most of the Pb in the volcanic rocks is from the slab component. On both the uranogenic and thorogenic Pb isotope diagrams (Figures 6a,b), the TSVZ data form excellent positive correlations ($r^2 = 0.94$ and $r^2 = 0.97$ respectively if the Buta Ranquil sample is excluded), with the VA samples falling at the radiogenic end of the Pb isotope arrays and covering most of the sediment range in $^{206}\text{Pb}/^{204}\text{Pb}$. Therefore, most of the fluid-

mobile Pb must come from the sediment. This is confirmed by the overlap between VA and sediment in Figure 7.

However, there is permissive evidence that some of the Pb also comes from the AOC slab component. The most radiogenic VA samples plot at the base of or just below the sediment field, suggesting that some of the Pb comes from an AOC component with lower $^{207}\text{Pb}/^{204}\text{Pb}$ and $^{208}\text{Pb}/^{204}\text{Pb}$ at a given $^{206}\text{Pb}/^{204}\text{Pb}$. We cannot constrain this tightly because of uncertainty in the Pb isotopic composition of all components and the circularity of argument about whether the sediments control the VA magmas or vice versa. However, the subducting crust is from the East Pacific Rise and should have a composition similar to Pacific MORB. Therefore more oceanic crust in the slab component will decrease its $^{207}\text{Pb}/^{204}\text{Pb}$ and $^{208}\text{Pb}/^{204}\text{Pb}$ relative to $^{206}\text{Pb}/^{204}\text{Pb}$ ratios. This argument takes advantage of the difference in Pb isotopes between the subducting altered oceanic crust (Pacific-type) versus mantle wedge (South Atlantic-type) sources. The NBA samples have lower $^{207}\text{Pb}/^{204}\text{Pb}$ ratios than VA samples with similar $^{206}\text{Pb}/^{204}\text{Pb}$, suggesting a greater AOC slab component in these lavas than in the VA. The Buta Ranquil sample near Tromen may have the most AOC slab component which could explain the high $^{143}\text{Nd}/^{144}\text{Nd}$ isotope ratio on Figure 5 and why this sample has the lowest $^{207}\text{Pb}/^{204}\text{Pb}$ and $^{208}\text{Pb}/^{204}\text{Pb}$ at a given $^{206}\text{Pb}/^{204}\text{Pb}$. This sample also plots closer to the AOC end member on Figure 7, 10 and 11 than do the other NBA and Tromen samples.

Other isotopes are more ambiguous because of the extensive overlap between the mantle and trench sediments. Although Sr and Nd isotopes for a few samples from the northern VA lie within the field defined by BA samples with the least evidence of a slab component (SBA and Pampas Negras), most are displaced to higher Sr but not lower Nd ratios (Figure 5, 12a). This kind of offset is consistent with both elements being derived in part from AOC as well as sediment, and a higher mass fraction of slab component at the VA (Figure 12b). $\delta^{18}\text{O}_{\text{olivine}}$ is virtually constant across the range of Sr and Pb isotopes (e.g., Figures 6c, 13), indicating that variation in Sr and Pb isotope ratios in rocks as mafic as ours reflects source mixing between depleted upper mantle and an enriched component, such as sedimentary material or fluids/melts from subducted sediments, rather than crustal assimilation

Hf-Nd isotopes are not helpful in this regard, because there is so much variation within the mantle and the general immobility of Hf and to a lesser extent Nd in most slab components. However, all analyses of Chilean trench sediments from 35°-40°S have $^{143}\text{Nd}/^{144}\text{Nd}$ ratios overlapping those of the arc, none of the arc rocks are offset toward a more pelagic sediment composition, and a mixture of sediment and AOC may lie within the Hf-Nd VA array. Neither VA nor BA samples define the steep positive correlation between $^{176}\text{Hf}/^{177}\text{Hf}$ and LREE/Hf ratios that is common in oceanic arcs and can be attributed to addition of LREE > Hf in the slab component (e.g. Todd et al., 2011).

In conclusion, Pb, Sr, and Nd isotopes are most easily explained by mixing with a slab component that includes a significant mass fraction of AOC as well sediment.

2.5.3.2 Nature of the slab component: solid, fluid, or melt?

The slab component could be added to the overlying mantle wedge via subduction erosion, a fluid derived from the dehydration of the slab (e.g. Elliot et al., 1997), or a melt if the slab temperature exceeds the solidus of sediment (e.g. van Keken et al., 2011) and/or AOC (e.g. Tollstrup et al., 2010). In the previous section, we argued that the Pb isotope data rule out subduction erosion of Paleozoic or older crust. Therefore, fluids and/or melts from the subducting slab, or from a solid diaper carrying sediments and possibly some AOC from the subducting slab (e.g. Hall and Kincaid, 2001; Behn et al., 2011), probably carry the slab component into the mantle wedge beneath the TSVZ. The VA and BA volcanic rocks display an excellent positive correlation between Nb/U and Ce/Pb ($r^2 = 0.93$), extending from average MORB and OIB values of 45 for Nb/U and 25 for Ce/Pb (Hofmann et al., 1986) in the BA to values of 1 for Nb/U and 2 for Ce/Pb in the VA, which overlap values for trench sediments (Figure 10). The correlation suggests that two components dominate the geochemistry of the TSVZ rocks: a homogeneous slab component rich in fluid-mobile elements, such as Pb and U, and a decompressive partial melt of the mantle wedge that has the usual mantle values for these ratios.

The slab component must also contain Th and LREE, because all VA and NBA samples are displaced above the usual MORB-OIB array in Nb/Yb versus Th/Yb (Figure 11) and La/Yb diagrams (not shown). This rules out a fluid slab component, because Th and LREE partition strongly into the liquid component only at temperatures above the AOC or sediment solidus (Johnson and Plank, 1999; Kessel et al., 2005). Partial melts, on the other hand, can fractionate and transport Th and LREE (Kessel et al., 2005). Moreover, the VA samples overlap the trench sediment in Nb/Yb and extend to higher Th/Yb and La/Yb ratios, which means that the slab component is preferentially enriched in Th and La relative to Yb. Therefore, melting involving equilibrium with minerals such as garnet is required.

Pb isotope ratios (e.g. $^{206}\text{Pb}/^{204}\text{Pb}$) form good inverse correlations with Nb/Zr ($r^2 = 0.70$), Nb/U ($r^2 = 0.84$), Ce/Pb ($r^2 = 0.81$), and Nb/Ba ($r^2 = 0.75$) (Figure 7, not all ratios shown). Although the latter correlations could be explained by adding a slab-derived fluid to the mantle, it is unlikely that fluid can transport enough Zr to explain the correlation. Instead, we attribute the variation to mixing with a slab-derived melt.

We noted earlier that the Mocha Fracture Zone may project under Longaví. We looked for evidence of greater than usual slab component at Longaví that might result from greater slab hydration at the fracture zone, as proposed by Sellés et al. (2004). However, we found no such evidence. Typical fluid-mobile to fluid-immobile trace elements ratios (e.g. U/Th, Pb/Ce, Ba/Nb, not shown) are relatively constant along this portion of the arc.

In summary, we conclude that the slab component is a melt of both trench sediment and AOC that it is homogenous throughout the TSVZ, and that it is ubiquitous at the VA but less and variable in the BA – most in the NBA and Tromen and least at the SBA. The slab surface temperature beneath the TSVZ VA has been inferred to be $\sim 830^\circ\text{C}$ (van Keken et al., 2011), which is only hot enough to melt AOC and sediment at the depth of the slab beneath the VA under water saturated conditions (Hermann and Spandler, 2008; Klimm et al., 2008). This conclusion is true for most subduction zones and requires a ubiquitous source of water external to any remaining hydrous minerals in the sediment or AOC themselves. Serpentinite in the underlying subducting mantle, possibly produced during bend-faulting at the outer rise (e.g. Contreras Reyes et al., 2007; Grevemeyer et al., 2007; Ranero et al., 2003; Rüpke et al., 2002,

2004), is an obvious candidate for the water source. Bend-faults, which provide deep reaching pathways, can be observed in the seafloor bathymetry in the incoming plate outboard of the TSVZ (Ranero et al., 2005; Ranero et al., 2006).

2.5.4 Quantitative flux melting model

We quantified some of our arguments by using the Arc Basalt Simulator version 3.10 of Kimura et al. (2009, 2010) to which the reader is referred for full details of the method. Briefly, ABS calculates forward mass balance models for the trace element and isotopic composition of arc basalts using assumed values for input parameters (AOC, sediment, mantle), the local P-T conditions of the slab from Syracuse et al. (2010), temperature-dependent trace element partitioning from Kessel et al. (2005), the integrated dehydration history of the slab from van Keken et al. (2011), and PMELTS-based flux mantle melting from Katz et al. (2003). As in most papers, successful models are subjective judgments about the fit between model prediction and representative basalts for extended trace element patterns and isotope ratios (e.g. Figure 12).

Table 2.3 Sediment (SED), altered oceanic crust (AOC) and depleted MORB Mantle (DMM) compositions used for the Arc Basalt Simulator 3 calculations. South Atlantic MORB – depleted (SAM-D) – enriched (SAM-E). (*) See Table 4 for values used in calculation of the slab melt composition.

	AOC	SED	Slab melt <i>60SED:40AOC(*)</i>	SAM-D <i>DMM</i>	SAM-E <i>E-DMM</i>
Rb	13.7	44.7	16.7	0.050	0.108
Ba	15.6	1238	1286	0.563	1.22
Th	0.173	5.70	5.64	0.008	0.016
U	0.390	3.21	3.48	0.003	0.005
Nb	2.89	4.63	1.01	0.149	0.246
Ta	0.210	0.350	0.081	0.010	0.016
K	5147	17483	6476	80.0	120
La	3.40	13.5	11.0	0.192	0.253
Ce	11.4	32.4	31.7	0.550	0.726
Pb	0.437	17.5	18.7	0.018	0.024
Pr	2.06	3.93	4.15	0.107	0.132
Sr	109	257	311	7.66	9.72
Nd	11.3	16.3	16.8	0.581	0.703
Sm	3.95	3.65	2.72	0.239	0.273
Zr	112	123	84.4	5.08	6.09
Hf	3.00	3.40	2.36	0.157	0.186
Eu	1.34	0.905	0.614	0.096	0.108
Gd	5.55	3.51	1.58	0.358	0.397
Tb	1.01	0.547	0.164	0.070	0.076
Dy	6.56	3.32	0.750	0.505	0.543
Y	40.7	18.1	3.15	2.66	3.55
Ho	1.43	0.674	0.112	0.115	0.123
Er	4.09	1.88	0.290	0.348	0.369
Tm	4.02	0.290	0.141	0.055	0.055
Yb	0.636	1.97	0.110	0.365	0.382
Lu	3.07	0.298	0.081	0.058	0.060
⁸⁷ Sr/ ⁸⁶ Sr	0.704769	0.705637	0.705480	0.703300	0.704200
¹⁴³ Nd/ ¹⁴⁴ Nd	0.513153	0.512673	0.512946	0.512940	0.512690
²⁰⁶ Pb/ ²⁰⁴ Pb	18.54	18.71	18.71	18.15	18.25
²⁰⁷ Pb/ ²⁰⁴ Pb	15.45	15.63	15.63	15.54	15.55
²⁰⁸ Pb/ ²⁰⁴ Pb	37.70	38.65	38.64	38.00	38.10
δ ¹⁸ O (‰)	2	9	6.2	5.25	5.25

Table 2.4 Mixing and results parameters from the Arc Basalt Simulator 3. AOC = Altered Oceanic Crust, SED = Sediment.

			Sr	Nd	Pb
Slab	P (Gpa)	4			
	T (°C)	827			
AOC	Melting (%)	18			
	Xgar	45.8			
	Xcpx	42.8			
	Xphen	1.04			
	Xrut	1.28			
	Bulk D		0.034	0.404	0.029
	Melting (%)	18			
SED	Xgar	24.7			
	Xcpx	15.8			
	Xphen	28.9			
	Xrut	0.80			
	Bulk D		0.404	1.63	0.297
	P (Gpa)	2.1			
	T (°C)	1270			
Mantle	Slab component added (%)	0.5-1			
	Mantle melting (%)	1-1.2			
	Bulk D		0.022	0.028	0.017

Table 3 and 4 contain: 1) our assumed compositions for the mantle, AOC and sediment; 2) the pressure of the slab surface beneath the volcanic front (4 GPa) from Syracuse and Abers (2009); 3) the temperature of the slab surface at this depth for Central Chile (830°C) from Syracuse et al. (2010); 4) the modal mineralogy of basalt and sediment at these P-T conditions as calculated within ABS using *Perple_X*, following van Keken et al. (2011); and 5) the percent of water-saturated melting at this P-T (18%) from Hermann and Spandler (2008). Table 4 also gives the bulk partition coefficients for these modal mineralogies for Sr, Nd, and Pb at 830°C that are used for the mixing model in Figure 12. They are based on Kessel et al. (2005) for garnet and clinopyroxene, and Green and Adam (2003) for phengite. D's are assumed to be zero for the

SiO₂ phase and rutile except for rutile $D_{Nd} = 0.7$ (from Ayers and Watson, 1993). Table 4 also gives the P-T-F conditions of melting in the mantle wedge that results in the best match of the shape of the REE pattern of a representative volcanic arc basalt (CL575 from San Pedro), and the corresponding bulk partition coefficients based on Green et al. (2000). At these P-T conditions, each percent of slab melt added to the mantle results in about one percent of mantle melting based on Katz et al. (2003). Between 0.5-1.5% slab melt yields the best match for most trace elements and isotopes (Figure 12), and the resulting primitive basalts contain about 3 wt. % water. ABS version 3 does not include the sequential effects of dehydration in all layers of the slab or residual accessory minerals besides rutile. Although our model is only heuristic, predicted and observed isotope ratios agree well, and trace element concentrations agree to within 10-20% for most elements except for Ba and U that are over-predicted, perhaps because of the sediment values assumed.

Although this approach is easier for a homogeneous mantle, we adapted it for the heterogeneity that we infer for the TSVZ VA by using two South Atlantic MORB type mantle compositions -- Depleted (SAM-D) and Enriched (SAM-E) -- that bracket the VA samples in Sr, Nd, and Pb isotopes. We assume that SAM-D and SAM-E have the trace element concentrations of the DMM and E-DMM of Workman and Hart (2005), respectively. However, the difference in concentrations between N-MORB and E-MORB sources has no effect on the mixing model because the slab melts are so much more enriched than the mantle wedge.

We also assumed a uniform slab component derived from both sediment and AOC for reasons given earlier. A sediment:AOC ratio of 60:40 gave the most satisfactory results but we have little independent control for this parameter. The isotopic composition of the sediment in Table 3 is from Lucassen et al. (2010) and the trace element composition is from our sample SO210-#5-B as explained earlier. The AOC composition is from ODP Site 1149 in the western Pacific (Kelley et al., 2003; Hauff et al., 2003) as compiled by Tollstrup et al. (2010).

Figure 12 shows the Sr-Nd-Pb isotope ratios for the resulting mixtures. They bracket all the Sr-Nd-Pb isotope data for the TSVZ when 0.5-1% of slab component is added to the depleted to enriched mantles except for two northern VA samples requiring 2-3% slab component. The separation between VA and BA is greater for Pb than Sr-Nd isotopes. A mixed-

source slab component, slab melting, and a heterogeneous mantle all are required. Little or no slab component is needed for Sr and Nd in the SBA and Pampas Negras BA and Resolana/Los Hornitos VA basalts, but some slab-derived Pb is necessary for Resolana/Los Hornitos. Assuming an average $\delta^{18}\text{O}$ value of 9‰ for sediment (Table 2) plus 2‰ (for hydrothermally-altered lower AOC) and 5.25‰ (for mantle wedge) (see Bindeman et al., 2005, and references therein), the model shown in Figure 13 predicts little if any change in O isotopes from the slab contribution to the VA mantle source.

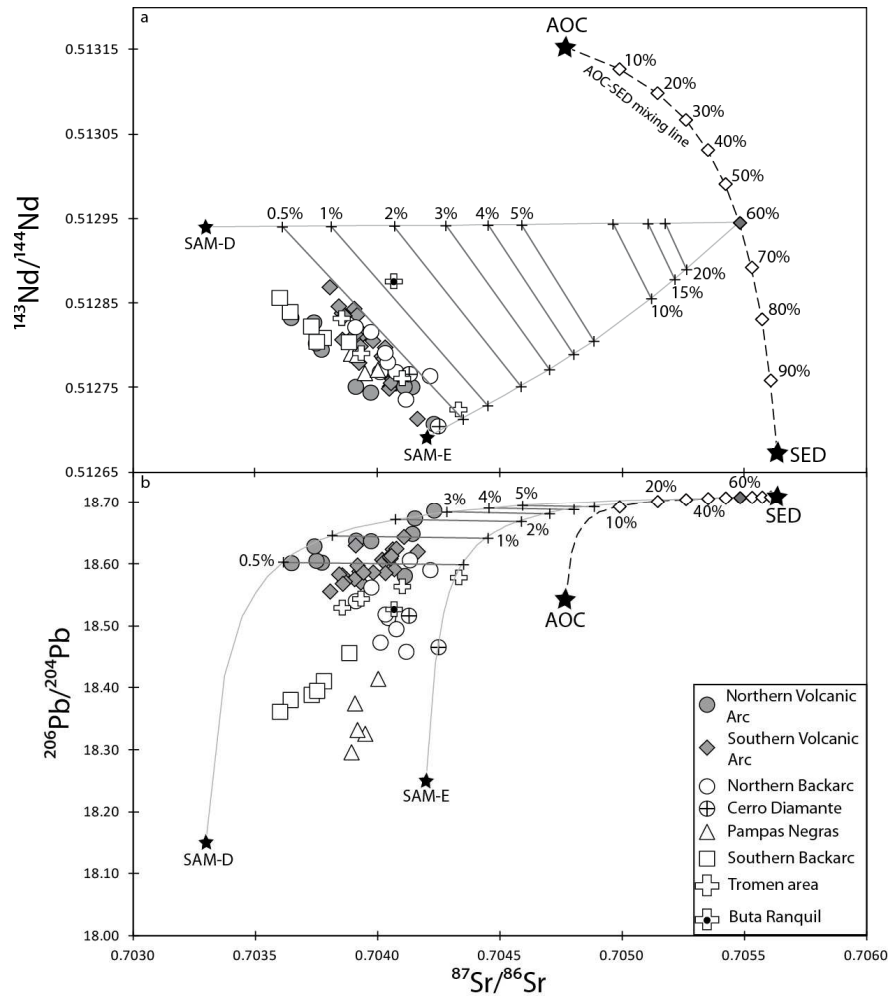


Figure 2.12 (a) $^{87}\text{Sr}/^{86}\text{Sr}$ versus $^{143}\text{Nd}/^{144}\text{Nd}$ and (b) $^{206}\text{Pb}/^{204}\text{Pb}$. The mixing lines are from the Arc Basalt Simulator 3.10 models for the VA. The dashed line represents mixing between altered oceanic crust (AOC) and sediment (SED). The thin lines represent mixing between a melt of a 60:40 SED:AOC source with South Atlantic MORB, and depleted (SAM-D) or enriched (SAM-E) mantle (the two stars). The labeled tick marks show the amount of slab component added to the mantle. Source compositions are in Table 3. Slab and mantle melting conditions are described in the text and summarized in Table 4. For partition coefficients and melting modes for the slab and mantle see Kimura et al. (2010). AOC is from Tollstrup et al. (2010).

Although some volcanic centers and regions define slopes that are shallower than the mixing lines, we attribute this to the heuristic generality of our model. All mixing components are likely to be heterogeneous in an area as large as this. Local variations in the isotopic composition of the mantle or subducted sediment or both, and in the P-T conditions of the slab component, all will affect the slope of mixing lines in Figure 12. For example, two samples (CL 323/CL 325) plot close to SAM-E on the Sr versus Nd isotope diagram (Figure 12a) but seem to mix to SAM-D on the Sr versus Pb isotope diagram (Figure 12b). More generally, our model predicts slightly more slab component when using Pb isotopes than when using Nd isotopes. This may reflect a more fluid-like slab component with higher Pb/Nd than the melt calculated using ABS3.10. Our model could be fine-tuned to any subset of samples but our goal is to create a framework with which such tuning can start.

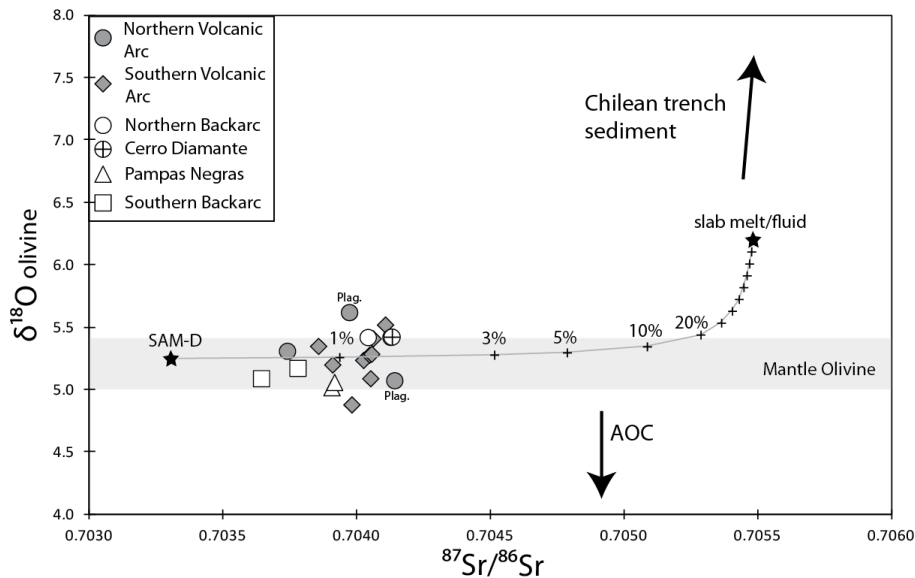


Figure 2.13 $\delta^{18}\text{O}_{\text{olivine}}$ versus $^{87}\text{Sr}/^{86}\text{Sr}$. The mixing lines are from the Arc Basalt Simulator 3.10 models for the VA. The thin line represents the mixing between a slab component of 60:40 SED:AOC source on one hand and depleted (SAM-D) mantle (stars) on the other. The labeled tick marks show the amount of slab component added to the mantle. Source compositions are in Table 3. The isotope ratios of the slab component (60% SED and 40% AOC) are calculated from the data in Table 3.

2.5.5 Regional and global comparisons

Although lying on relatively thick continental crust (ca. 40 km), the TSVZ differs from the CVZ in Peru and northern Chile (14-27°S) where the crust is ca. 70 km thick. There, crustal contamination plays a fundamental role in the magma genesis (e.g. Davidson et al., 1991, Francis and Hawkesworth, 1994, Lindsay et al., 2001b, Schmitt et al., 2001, 2002). In the CVZ, Sr, Nd and O isotopes correlate with increasing SiO₂ content, and Pb isotopes show correlations with the local Andean basement (e.g. Francis et al., 1984; Feeley and Davidson, 1994, Wörner et al., 1992b, 1994; Aitcheson et al., 1995). The TSVZ also differs from the NSVZ where the crust is also thick but where enriched Sr-Nd isotopic compositions have been observed and interpreted as the result of either crustal assimilation (Hildreth and Moorbath, 1988) or subduction erosion (Kay et al., 2005). Our TSVZ study reaches different conclusions about the crustal influence than previous large-scale studies (e.g. Hildreth and Moorbath, 1988, Tormey et al., 1991) or single-volcano studies (e.g. Dungan et al., 2001, Tormey et al., 1995) because we found no correlations between isotopes and differentiation indices and no mixing of Pb isotopes toward the local basement. Our O isotope data also show a typical subduction zone signature within and slightly above the mantle range.

Instead, the sediment-dominated slab component in the TSVZ is a feature more similar to the CSVZ to the south. There, previous studies have shown that basalts were formed by melting of the subarc mantle contaminated by fluids derived from the dehydration of the subducting oceanic lithosphere including sediments (e.g. Morris et al., 1990, Sigmarsson et al., 1990, 2002, Hickey-Vargas et al., 1984, 1986, 1989, 2003). However, we conclude that both the subducting oceanic crust and the sediments melt. Our conclusion that the mass fraction of slab component and the degree of mantle melting both decrease eastward into the back arc agrees with previous studies (e.g. Futa and Stern, 1988, Hickey-Vargas et al., 1986, 1989).

While most previous studies of the TSVZ showed a transition between a slab component in the CSVZ and a crustal component in the NSVZ, we show rather than the TSVZ segment can be interpreted as a “baseline” of subduction input, and that the mantle wedge is heterogeneous in its trace element and isotope ratios.

2.6 Conclusions:

We use new major and trace element and Sr-Nd-Hf-Pb-O isotope data for basalts from the volcanic arc and backarc of the Transitional Southern Volcanic Zone (34.4°S-38°S) of Chile, and adjacent trench sediments, to evaluate the origin of the arc magmas. We conclude the following.

- (1) Major assimilation of pre-Cenozoic sialic crust is inconsistent with our isotopic data for basalts to andesites despite their ascent through 35-45 km thick crust.
- (2) The mantle is heterogeneous within and between the volcanic arc and backarc. The range is similar to the South Atlantic MORB field in Sr and Nd, but not in Pb and Hf isotopes. Mixing between a slab component and South Atlantic MORB can explain the Pb isotope data. Pb isotopes in the VA, NBA, and Tromen are dominated by subducting sediments. We attribute the difference between VA and BA in Hf isotopes to the presence of subcontinental lithosphere beneath the backarc, but cannot constrain if it is presently located within the lithospheric mantle or has been delaminated and is presently in the asthenospheric mantle wedge.
- (3) All samples from the volcanic arc, and most from the backarc, contain a slab-derived component. The mass fraction of this component is less in the backarc and negligible in the SBA basalts farthest from the volcanic arc.
- (4) The slab component is homogeneous and drawn from subequal amounts of subducted sediment and altered oceanic crust. It must be a melt in order to transport Th, Zr and LREE, and to fractionate them so much from HREE. For melting to occur at the depth of the slab beneath the volcanic arc, the slab must be water-saturated at least locally, which requires an external source of water such as from dehydrating underlying serpentinite within the subducting plate, possibly formed through the access of water into the uppermost lithospheric mantle as a result of bend-faulting preceding subduction.
- (5) Trace element patterns and Sr-Nd-Pb isotope ratios are best modelled by adding 0.5-1% of a slab melt (except for two rear arc samples which require 2-3% slab melt)

- derived from a 60:40 sediment:AOC source to slightly depleted and isotopically heterogeneous mantle.
- (6) Addition of a few percent of this slab component causes an equivalent amount of melting of the mantle at about 2 GPa beneath the VA, with more melting beneath the volcanic arc than backarc. This is consistent with the larger magma flux observed at the volcanic arc.

Acknowledgements:

We thank U. Westernströer and S. Hauff for their analytical help. We thank the Federal Ministry of Education and Research (BMBF) for funding the R/V SONNE during the SO210 cruise. Ilya N. Bindeman acknowledges NSF grants EAR-0844772 and EAR-0948455. We thank three anonymous reviewers who helped to increase the quality of this paper. This paper is contribution No. 259 of Collaborative Research Center (Sonderforschungsbereich) SFB574 “Volatiles and Fluids in subduction Zones” at Kiel University, funded by the German Research Foundation

Chapter 3

Geochemical variations in the Central Southern Volcanic Zone, Chile (38-43°S): The role of fluids in generating arc magmas

This chapter was submitted to *Chemical Geology* in September 2013

Co-authors: Kaj Hoernle, James Gill, Heidi Wehrmann, Ilya Bindeman

Chapter overview

We present new Sr-Nd-Pb-Hf-O isotope data from the volcanic arc (VA, volcanic front and rear arc) in Chile and the backarc (BA) in Argentina of the Central Southern Volcanic Zone in Chile (CSVZ; 38-43°S). Compared to the Transitional (T) SVZ (34.5-38°S; Jacques et al., 2013), the CSVZ VA has erupted greater volumes over shorter time intervals (Völker et al., 2011) and produced more tholeiitic melts. Although the CSVZ VA monogenetic cones are similar to the TSVZ VA samples, the CSVZ VA stratovolcanoes have greater highly fluid-mobile to less fluid-mobile element ratios (e.g. U/Th, Pb/Ce, Ba/Nb) and lower more- to less-incompatible fluid-immobile element ratios (e.g. La/Yb, La/Sm, Th/Yb, Nb/Yb), consistent with an overall higher fluid flux and greater degrees of flux melting beneath the CSVZ stratovolcanoes compared to the CSVZ monogenetic centers and the TSVZ VA. The CSVZ monogenetic centers overlap the TSVZ in Sr and Nd isotopes, but the stratovolcanoes are shifted to higher Sr and/or Nd isotope ratios. The Pb isotopic composition of the CSVZ overlaps the TSVZ, which is clearly dominated by the composition of the trench sediments, but the CSVZ monogenetic samples extend to less radiogenic Pb. $\delta^{18}\text{O}(\text{melt})$ from the CSVZ stratovolcano samples are below the MORB range, whereas the CSVZ monogenetic and the TSVZ samples fall within and slightly above the MORB range. $\delta^{18}\text{O}(\text{melt})$ correlates negatively with U/Th and Nd isotopes. The Nd and Hf isotopic ratios of the CSVZ VA extend to more radiogenic compositions than found in the TSVZ VA, indicating a greater contribution from a more depleted source. These correlations are interpreted to reflect derivation of fluids from hydrothermally altered oceanic crust and/or serpentinized upper mantle of the subducting plate. CSVZ backarc (BA) basalts largely overlap TSVZ BA basalts, displaying less or no subduction influence compared to the VA, but some CSVZ BA basalts tap more enriched mantle, possibly subcontinental lithosphere, with distinctively lower Hf isotope ratios.

3.1 Introduction

Along-arc variation in the composition of magma is typical for many subduction zones, and can be related to many factors. For example, there can be a change in the composition of subducting sediment or oceanic crust or both. Erosion can vary as a function of rainfall and relief, resulting in a variable thickness and proportion of continentally-derived trench sediment. The subducting oceanic crust can vary in age and therefore slab surface temperature and degree of alteration, and in composition depending on the ocean ridge at which it formed. The mantle wedge can be heterogeneous in trace element and isotope ratios.

The tectonic setting can also change along strike, and can influence the ascending magmas. Thicker crust potentially increases assimilation of upper crustal material to the melts, and affect the depth and extent of crystal fractionation. The presence of large fracture zones or bend-faults on the subducting plate may increase the potential for hydration of the lower oceanic crust and/or serpentinization of the underlying lithospheric mantle. The geometry of the slab (depth, dip) can also vary. If the slab beneath the volcanoes is deeper, it will be hotter and is therefore more likely to melt rather than dehydrate, increasing the potential for recycling incompatible elements such as Th, Nb, Ta, Hf and Zr. Finally, there can be differences in the role of sediment accretion versus erosion in the forearc, which affects the amount of sediment and upper and lower continental crust being subducted.

All of the above variables vary along the Chilean margin. In order to evaluate these variables, this study focuses on the volcanic arc of a portion of the Southern Volcanic Zone (SVZ) of Chile and the backarc in Argentina between 38°S and 43°S. Together with major and trace element data from Wehrmann et al. (2013a, and in rev b), our new Sr-Nd-Hf-Pb-O isotope data provide a comprehensive new geochemical data set for this area. Combining geochemical, morphological and geophysical data, we compare and contrast cinder cone and stratovolcano samples from the Central SVZ (CSVZ: 38-43°S) and then compare and contrast the CSVZ with the Transitional SVZ (TSVZ: 34.5-38°S, Jacques et al., 2013) segment in order to identify the source of the main along-strike variations in magma composition.

3.2 Geological setting and previous geochemical studies

3.2.1 Geological background

The Andean cordillera is more than 7,500 km long, extending from Colombia to Southern Chile. Volcanism results from the subduction of the Nazca (7-9 cm/year) and the Antarctic (2 cm/year) Plates below the South American Plate (Norabuena et al., 1998; Angermann et al., 1999). The Andes volcanic arc has four active volcanic segments, divided by volcanic gaps. Volcanism occurs when the slab dip angle is greater than 25° (Stern, 2004). The segments have been named the Northern Volcanic Zone (NVZ; 5°N-2°S) in Colombia and Ecuador, the Central Volcanic Zone (CVZ; 16-28°S) in Peru and northern Chile, the Southern Volcanic Zone (SVZ, 33-46°S) in Central Chile, and the Austral Volcanic Zone (AVZ; 49-54°S) in southern Chile.

The SVZ in Chile consists of more than 60 Quaternary volcanoes, three silicic caldera systems, and numerous minor eruptive centers (Stern, 2004, Figure 1a). The SVZ has been divided into the Northern Southern Volcanic Zone (NSVZ; 33°-34.5°S; e.g. Hildreth and Moorbath, 1988), the Transitional Southern Volcanic Zone (TSVZ; 34.5-37°S; e.g. Tormey et al., 1991), the Central Southern Volcanic Zone (CSVZ; 37.0-41.5°S; e.g. Hickey et al., 1984, 1986, Hickey-Vargas et al., 1989) and the Southern Southern Volcanic Zone (SSVZ; 41.5-46°S; e.g. Naranjo and Stern, 2004), based on the geochemical characteristics of the erupted rocks (see also López-Escobar et al., 1995). Other authors, e.g. Dungan et al. (2001), suggested to divide the SVZ differently: the Tupungato-Maipo Segment (TMS, 33°-34.2°S), the Palomo-Tatara Segment (PTS, 34.7°-36°S), and the Longaví-Osorno Segment (LOS, 36.2°-42°S) (see also Sellés et al., 2004).

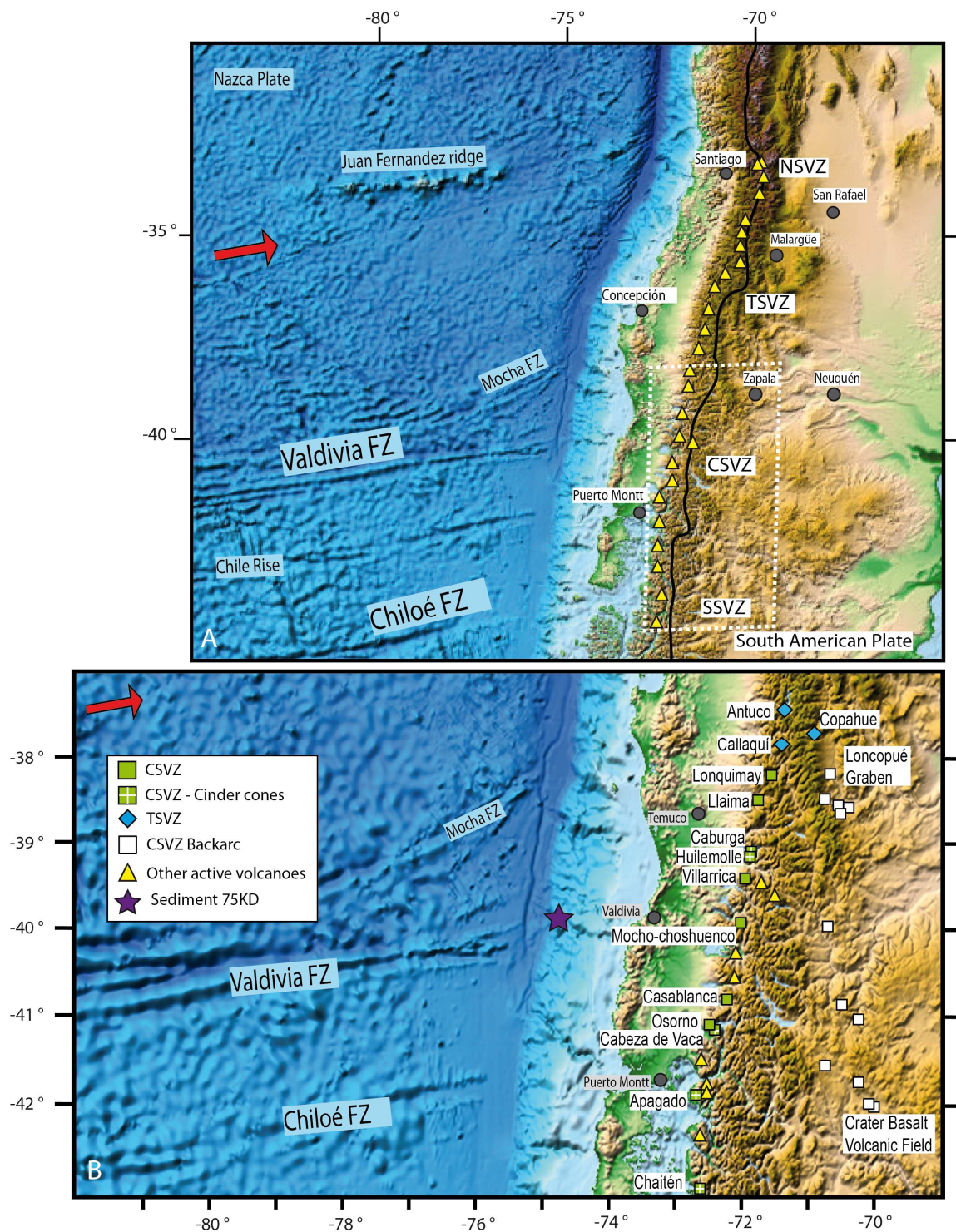


Figure 3.1. (A) Map of the Southern Volcanic Zone (SVZ) with volcanic front volcanoes denoted with yellow triangles. The black thick line represents the boundary between Chile and Argentina. (B) Map of the Central SVZ and the northern part of the Southern SVZ, from 38°S to 43°S. Green squares = CSVZ stratovolcanoes. Green squares with white cross = monogenetic cinder cones. Blue diamonds stand for the Transitional SVZ. Open squares = Backarc lavas. Yellow triangles = other Quaternary volcanoes. In (A) and (B): Grey filled circles = major cities. The red arrows show the relative movement of the Nazca plate beneath the South American plate. FZ = fracture zone. The ETOPO1 map source is from NOAA, modified (Amante and Eakins, 2009).

This study focuses on the SVZ volcanoes between 38-43°S, which we collectively refer to as the CSVZ (Figure 1b). CSVZ volcanic arc (VA, volcanic front and rear arc) volcanoes are Lonquimay, Llaima, Villarrica and two nearby cinder cones (Huilemolle and Caburga), Mocho-Choshuenco, Casablanca, Osorno and the monogenetic cones of Cabeza de Vaca. Apagado and Minchinmávida-Chaitén, sometimes included in the SSVZ, are here included in the CSVZ.

We separate the stratovolcanoes from the monogenetic cones, because they differ in geochemistry as well as morphology (see Section 5.2). The southernmost samples come from small cinder cones in the area of Minchinmávida-Chaitén. Apagado is also a small cinder cone near two stratovolcanoes (Yate and Hornopirén).

The CSVZ segment includes some of South America's most active volcanoes (e.g. Llaima erupted last in 2008, Puyehue in 2011, Chaitén in 2008-2010), including Villarrica considered to be amongst the most active volcano in South America (with annually recurrent activity since 2008). The CSVZ has also had the highest magma extrusion rate of the SVZ (NSVZ (33-34.5°S) = 3.8 km³/km/Ma, TSVZ (34.5-37°S) = 4.2 km³/km/Ma, CSVZ (37-42°S) = 14.9 km³/km/Ma, SSVZ (42-43°S) = 2.6 km³/km/Ma) (Völker et al., 2011).

The CSVZ backarc (BA) extends from 70 km to 230 km in Argentina behind the CSVZ VA. These samples are part of the large Patagonian province, which was active from Tertiary to Recent (Kay et al., 2004). From two different regions, a number of cinder cones have been sampled. Moreover, we obtained samples from isolated lava plateaux, possibly Pliocene to Recent in age (Kay et al., 2004, 2007). Our northernmost BA samples come from the southern part of the Loncopué Graben near Copahue volcano (ca 38-39°S) (Varekamp et al., 2010). Our southernmost BA samples come from the Crater Basalt Volcanic Field (700km²) which produced Quaternary (600-340 ka; Pécskay et al., 2007) lavas and tephras.

The Nazca Plate currently subducting north of the Valdivia fracture zone (40°S) formed at the East Pacific Rise (EPR) whereas the plate further south formed at the Chile Ridge (Herron et al., 1981; Tebbens and Cande, 1997; Tebbens et al., 1997). The age of the incoming plate ranges from 14 Ma south of the Chiloé fracture zone at 42°S, to 25 Ma south of the Mocha Fracture Zone at 38°S. More fracture zones with more pronounced morphology and multiple splays are present in the slab subducting beneath the CSVZ compared to the TSVZ (Figure 1),

where only the rather minor Mocha fracture zone subducts. There are also more numerous bend-faults on the trench outer-rise offshore the CSVZ (Contreras-Reyes et al., 2007). Consequently the potential for hydration of the lower oceanic crust and serpentinization of the upper mantle of the subducting slab is greater offshore the CSVZ than the TSVZ. Offshore of the CSVZ, the trench is flooded by ca. 2.2 km of sediments (Contreras-Reyes et al., 2008) that consist of 100 m of pelagic clays overlain by turbidites and silty clay derived from the continental basement and the arc (Völker et al., 2008; Lucassen et al., 2010; see also Plank, 2011 for sediment description compilation).

The thickness of the overriding crust is relatively uniform (ca. 30 km) beneath the CSVZ and is thinner than beneath the TSVZ (ca. 35-45 km) (Cembrano and Lara, 2009, Völker et al., 2011). The depth to the surface of the subducting slab beneath the CSVZ is also relatively constant, being located at ca. 130 km beneath the volcanic front north of 41°S and decreasing to ca. 110 km at 43°S (Tassara et al., 2006). The thickness of the overlying mantle wedge and asthenospheric portion of the wedge beneath the CSVZ range from 80-100 km and 60 to 80 km, respectively (Tassara et al., 2006; Völker et al., 2011). Throughout the area of this study (38-43°S), the VA eruptive centers lie directly on the Meso-Cenozoic plutonic rocks of the Patagonian batholiths (Stern, 2004, Lucassen et al., 2004, Cembrano and Lara, 2009 and references therein).

3.2.2 Previous geochemical studies

In the CSVZ VA, both stratovolcanoes and cinder cones produce mainly tholeiitic and high-Al basalts and basaltic andesites. Their Sr-Nd-Pb-O and U series isotopes preclude significant assimilation of old sialic crust (e.g. Hickey et al., 1984, 1986, Hickey-Vargas et al., 1989, 2002; Futa and Stern, 1988; Sigmarsson et al., 1990, 2002). Andesites, dacites and rhyolites in the CSVZ have the same isotopic composition as basalts, indicating that they form by fractionation without significant assimilation (Gerlach et al., 1988) or that they assimilated only isotopically similar crust such as Miocene plutonic rocks (e.g. Reubi et al., 2011). The aforementioned studies concluded that the magmas south of 34.5°S were produced by melting

of the subarc mantle wedge contaminated by fluids derived from the dehydration of the subducted oceanic basalts and sediments. Based on correlations between U-series disequilibria and $^{10}\text{Be}/^9\text{Be}$ isotope ratios, Morris et al. (1990) and Sigmarsson et al. (2002) argued that the largest slab signature is observed in the CSVZ, at Villarrica volcano. Finally, Hickey-Vargas et al. (2002) found that the small eruptive centers near Villarrica were depleted in fluid-mobile elements compared to the main edifice.

Varekamp et al. (2010) identified an EM-1-like signature in the young, olivine-rich basalts from the Loncopué Graben in the BA, possibly reflecting subcontinental lithospheric mantle. In the Crater Basalt Volcanic Field (BA), the lavas flows and scoria cones from monogenetic centers were produced as a result of decompression melting (Massaferro et al., 2006). Petrographic studies suggested rapid magma ascent from a garnet-bearing lherzolite mantle source with asthenospheric characteristics, precluding crustal assimilation (Massaferro et al., 2006, Pécskay et al., 2007).

3.3 Material and analytical methods

The youngest and freshest, generally olivine-bearing volcanic rocks (lava and tephra) were sampled from each volcanic area. During our sampling campaigns, we avoided units containing xenolithic or xenocrystic material in order to obtain material of low crustal contamination. Samples were later handpicked under a binocular microscope to select only the freshest part of the rock and to avoid xenolithic or xenocrystic material and tephra or lava pieces with vesicle fill. Details of the sample preparation, XRF and ICP-MS analyses can be found in Jacques et al. (2013). Samples preparation and isotope analyses were performed with the same instruments and instruments settings as by Jacques et al. (2013), with the following details.

We analyzed Sr, Nd and Pb isotope ratios on ThermoFinnigan TRITON (Sr, Nd) and Finnigan MAT 262-RPQ2+ (Pb) thermal ionization mass spectrometers at GEOMAR. To ensure high precision Pb isotope analyses, we used a double spike method. For a detailed description of the chemical and TIMS analytical procedures, refer to Hoernle et al. (2008, 2011). In order to

remove possible surface contamination, 100-150 mg of 0.5-2 mm sized, fresh rock chips were first leached in 2N HCl at 70°C for 1-2 hours and then triple-rinsed with ELGA water. Mass-bias correction for Sr and Nd isotope ratios were done within run to $^{86}\text{Sr}/^{88}\text{Sr} = 0.1194$ and $^{146}\text{Nd}/^{144}\text{Nd} = 0.7219$. All errors are reported at the 2σ confidence level. To obtain a normalization value, NBS987 and our in-house Nd SPEX standard were measured every 4th to 5th sample for each turret relative to our preferred values of $^{87}\text{Sr}/^{86}\text{Sr} = 0.710250$ for NBS987 and $^{143}\text{Nd}/^{144}\text{Nd} = 0.511715$ for SPEX (corresponding to $^{143}\text{Nd}/^{144}\text{Nd} = 0.511850$ for La Jolla, Krolikowska-Ciaglo et al., 2005). We applied the normalization value to the sample data for each turret. Thereby, possible machine drift over the course of the project (2009-2012) was compensated achieving maximum data comparability. External 2σ uncertainties did not exceed ± 0.000011 for NBS987 and ± 0.000005 for SPEX (n= 25). The reference material NBS981 was included in each analytical run and the double spike corrected values are $^{206}\text{Pb}/^{204}\text{Pb} = 16.9413 \pm 21$, $^{207}\text{Pb}/^{204}\text{Pb} = 15.4994 \pm 20$, $^{208}\text{Pb}/^{204}\text{Pb} = 36.7241 \pm 56$, $^{207}\text{Pb}/^{206}\text{Pb} = 0.914889 \pm 37$, $^{208}\text{Pb}/^{206}\text{Pb} = 2.16773 \pm 13$ (n=38). Our data are in good agreement with published double and triple spike data for NBS981 (see Hoernle et al., 2011). Each sample batch was accompanied by a blank measurement. Total Pb chemistry blanks were below 25 pg (with the exception of a single Pb blank of 200 pg), Sr-Nd chemistry blanks were usually less than 100 pg and 50 pg, respectively. All these blank levels are insignificant with regard to the samples' Pb, Sr, and Nd contents. Replicate analyses proved to be within the external 2σ reproducibility of the Sr-Nd-Pb reference materials.

For Hf isotopes, we used a NU Plasma HR MC-ICPMS at GEOMAR. 200-500 mg of 0.5-2 mm sized fresh rock chips were processed according to the protocol reported in Blichert-Toft and Albarède (1997) and Geldmacher and Hoernle (2006). Samples were diluted prior to analysis to 80-100 ppb Hf to obtain a total Hf beam of 12-14 V. Hf isotope ratios were determined through static multi-collection. Mass-bias correction was performed assuming exponential mass fractionation to $^{179}\text{Hf}/^{177}\text{Hf} = 0.7325$. A normalization value for each sample sequence was generated for our in-house Hf standard solution SPEX, which was analyzed every 3 to 5 samples. During the entire project period (2010-2012), the solution yielded $^{176}\text{Hf}/^{177}\text{Hf} = 0.282170 \pm 6$ (2σ , n = 45), corresponding to JMC-145 $^{176}\text{Hf}/^{177}\text{Hf} = 0.282163$.

We determined Oxygen isotopes using a CO₂-laser fluorination (e.g. Bindeman, 2008) and a Newwave 35W CO₂ laser at the University of Oregon. 0.6 to 2 mg of single and bulk phenocryst grains and bulk groundmass were reacted with BrF₅ to release oxygen gas, which was then purified in the laser chamber by several cryogenic traps (at liquid nitrogen temperature). Possible traces of fluorine gas were eliminated with a mercury diffusion pump. To react oxygen to CO₂, a small platinum graphite converter was employed. We analyzed the CO₂ gas on a MAT 253 mass spectrometer. For data quality control, several reference materials were included in each analytical run: four to seven aliquots of internal garnet standard, UOG1, $\delta^{18}\text{O} = 6.56\text{‰}$, corresponding to the Gore Mt. Garnet ($\delta^{18}\text{O}_{\text{olivine}} = 5.8\text{‰}$ VSMOW, Valley et al., 1995), and a San Carlos olivine with $\delta^{18}\text{O}_{\text{olivine}} = 5.25\text{‰}$. Repeatability of the measured $\delta^{18}\text{O}_{\text{olivine}}$ values on a day-to-day basis is within 0.1 to 0.25‰ less than the standards' accepted value, and the samples values were corrected to this variability. Replicate measurements of single grains and bulk analyses ranged within ± 0.02 to $\pm 0.08\text{‰}$ (1σ).

3.4 Results and descriptive comparison with the TSVZ

We provide new Sr-Nd-Pb isotope data for 37 samples and Hf isotope data for 20 samples (Table 1). 17 samples were newly characterized for O isotopes from mineral and groundmass (Table 2). Major and trace element and volatile analyses for the samples for which we present isotope data in this study and are published in Wehrmann et al. (2013a) and in Wehrmann et al. (in rev b), complemented by two VA analyses for samples CL 166 (Villarrica) and CL 701 (Casablanca), and the BA samples. These data are summarized in Supplementary Table 1 for the 37 samples in this study.

3.4.1 Major elements

Our CSVZ VA samples range from basalts to basaltic andesites to basaltic trachyandesites (SiO₂ = 49-61 wt. %) (Figure 2a), and most have 4-7 wt. % MgO, as compared to the TSVZ VA samples with 3-6 wt. % MgO, with one sample from the Los Hornitos cinder cones

having 8.5 wt. % MgO (Jacques et al., 2013). The two samples from Lonquimay are the most evolved, being the two trachyandesite samples. All CSVZ samples plot in the medium-K and tholeiitic fields of Gill (1981). The CSVZ VA samples extend to lower K₂O but higher FeO_{total}/MgO relative to SiO₂ compared to the TSVZ samples (Figure 2b, c).

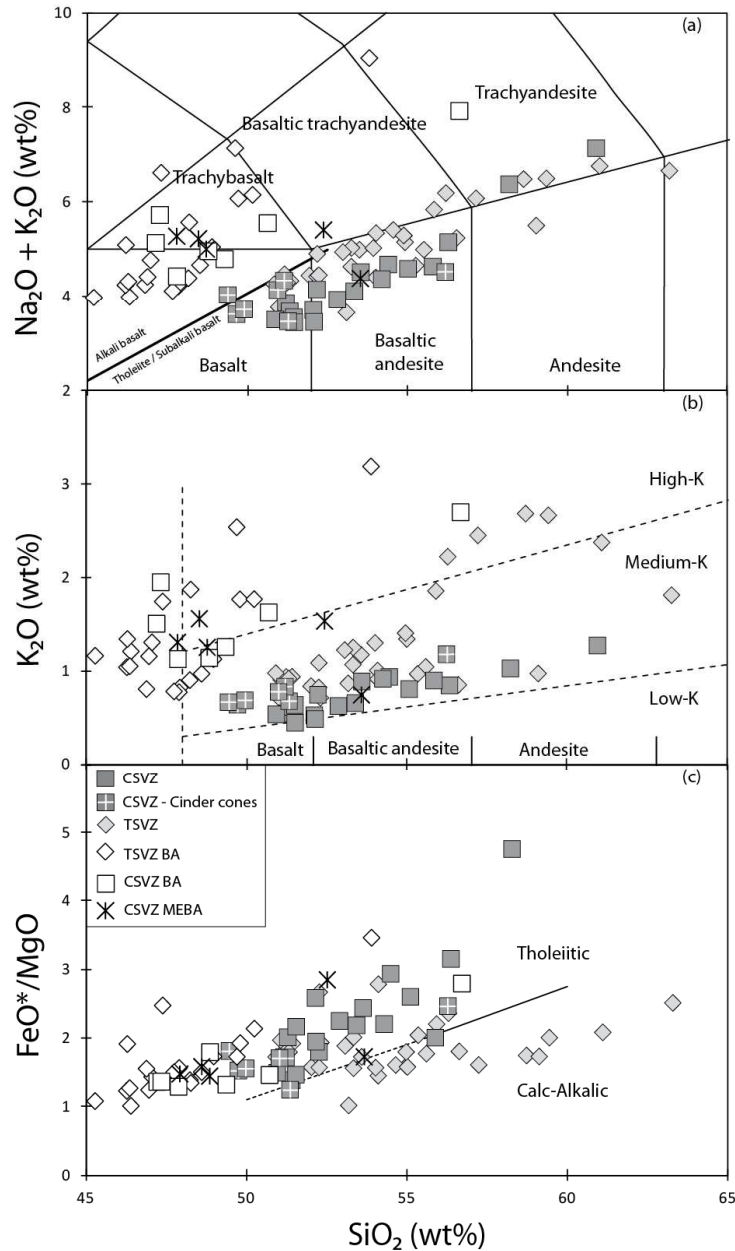


Figure 3.2 (a) Total Alkali versus Silica [TAS] after Le Maitre et al. (1989). CSVZ samples range from basalt to trachyandesite. The cinder cones are basaltic. (b) SiO₂ versus K₂O after Gill (1981), (c) SiO₂ versus FeO_{total}/MgO. The VA samples are medium-K and tholeiitic. Most BA samples are alkali basalts to trachybasalts. CSVZ data are from Wehrmann et al. (2013) and (in revision) and this study. TSVZ data are from Jacques et al. (2013).

Table 3.1

New Sr-Nd-Hf-Pb isotope data for the samples in the supplementary Table 1.
See the text for results for reference materials.

Sample number	Sample Location	$^{87}\text{Sr}/^{86}\text{Sr}$	2 σ	$^{143}\text{Nd}/^{144}\text{Nd}$	2 σ	ϵNd	$^{176}\text{Hf}/^{177}\text{Hf}$	2 σ
Volcanic Arc								
CL 045	Lonquimay	0.703952	3	0.512880	2	4.88	0.283065	4
CL 049	Lonquimay	0.703952	3	0.512884	2	4.96		
CL 029	Llaima	0.703972	3	0.512879	2	4.86	0.283076	10
CL 032	Llaima	0.703986	3	0.512878	3	4.84	0.283068	8
CL 034	Llaima	0.703980	4	0.512887	2	5.02		
CL 035	Llaima	0.703982	3	0.512886	2	4.99		
CL 036	Llaima	0.703999	3	0.512873	3	4.74		
CL 001	Villarrica	0.704005	3	0.512881	3	4.89		
CL 006	Villarrica	0.703993	3	0.512882	2	4.92	0.283073	5
CL 010	Villarrica	0.704019	3	0.512884	3	4.96	0.283074	6
CL 166	Villarrica	0.703932	3	0.512862	2	4.52	0.283068	8
CL 170	Villarrica	0.704022	3	0.512894	2	5.16		
CL 017*	Huilemolle*	0.703892	3	0.512834	3	3.99		
CL 022*	Caburga*	0.703739	2	0.512854	3	4.36	0.283038	5
CL159	Mocho	0.704067	3	0.512833	1	3.96	0.283032	5
CL161	Mocho	0.704102	3	0.512828	2	3.86		
CL 109	Casablanca	0.704049	3	0.512843	3	4.15	0.283037	6
<i>CL109_rep</i>		<i>0.704054</i>	<i>3</i>	<i>0.512842</i>	<i>2</i>	<i>4.14</i>		
CL 701	Casablanca	0.703941	3	0.512832	3	3.93	0.283020	6
CL 088*	Cabeza de Vaca*	0.703780	3	0.512839	2	4.08		
CL 098	Osorno	0.704300	2	0.512806	3	3.43	0.283014	4
CL 102	Osorno	0.704335	3	0.512796	3	3.24		
CL 713*	Apagado*	0.703531	3	0.512896	2	5.20	0.283050	4
<i>CL 713_rep</i>		<i>0.703523</i>	<i>3</i>	<i>0.512901</i>	<i>2</i>	<i>5.29</i>		
CL 443*	Chaiten*	0.703932	3	0.512807	2	3.46		
CL 486*	Chaiten*	0.704144	3	0.512787	3	3.07	0.282975	6
CL 490*	Chaiten*	0.704163	3	0.512784	3	3.00	0.282974	6
Backarc								
CL 425	old plateau basalt	0.703887	3	0.512794	2	3.20	0.282938	4
CL 426	Rd to Pino Hachado	0.703951	3	0.512778	2	2.89		
CL 430	old plateau basalt	0.703940	3	0.512792	2	3.17		
CL 475 b	around Laguna Blanca	0.703991	3	0.512774	3	2.81	0.282923	7
CL 481	Cerro Horqueta	0.704297	3	0.512725	2	1.85		
CL 482	older plateau	0.703822	3	0.512836	2	4.02		
CL 433	plateau basalt / Jacobacci Volc field	0.704048	3	0.512787	3	3.06	0.282936	5
<i>CL 433_rep</i>		<i>0.704078</i>	<i>3</i>	<i>0.512782</i>	<i>3</i>			
more-enriched Backarc								
CL 424	old plateau at meterite impact site	0.704868	3	0.512643	2	0.25	0.282712	4
CL 431	Jacobacci Volc field	0.704351	3	0.512753	3	2.40		
CL 432	Jacobacci Volc field	0.704550	3	0.512618	3	-0.24	0.282753	6
CL 434	Crater Basalt Volcanic Field	0.704879	3	0.512640	2	0.19		
CL 437	Crater Basalt Volcanic Field	0.704371	3	0.512722	3	1.80	0.282866	5

* cinder cones

Table 3.1 (continued)

Sample number	$^{206}\text{Pb}/^{204}\text{Pb}$	2σ	$^{207}\text{Pb}/^{204}\text{Pb}$	2σ	$^{208}\text{Pb}/^{204}\text{Pb}$	2σ
Volcanic Arc						
CL 045	18.6061	7	15.6083	9	38.5061	28
CL 049	18.6062	30	15.6087	27	38.5121	69
CL 029	18.5750	12	15.6051	15	38.4765	48
CL 032	18.5779	10	15.6057	11	38.4811	34
CL 034	18.5786	13	15.6053	15	38.4807	48
CL 035	18.5789	7	15.6051	9	38.4801	28
CL 036	18.5795	7	15.6058	9	38.4839	28
CL 001	18.5908	8	15.6091	9	38.5010	30
CL 006	18.5897	13	15.6074	15	38.4966	46
CL 010	18.5882	9	15.6077	9	38.4963	29
CL 166	18.6145	10	15.6094	10	38.5165	32
CL 170	18.5896	8	15.6078	9	38.4960	29
CL 017*	18.5662	17	15.6033	21	38.4635	68
CL 022*	18.5873	12	15.6028	12	38.4712	36
CL159	18.5913	4	15.6084	4	38.4999	11
CL161	18.5908	11	15.6079	11	38.5007	32
CL 109	18.5836	12	15.6072	15	38.4792	47
<i>CL109_rep</i>	<i>18.5873</i>	<i>12</i>	<i>15.6133</i>	<i>10</i>	<i>38.5018</i>	<i>26</i>
CL 701	18.5786	21	15.6043	26	38.4686	86
CL 088*	18.5461	10	15.5958	11	38.4015	35
CL 098	18.6107	9	15.6112	8	38.5195	23
CL 102	18.6148	8	15.6147	9	38.5330	26
CL 713*	18.4935	7	15.5786	6	38.2728	14
<i>CL 713_rep</i>	<i>18.4916</i>	<i>13</i>	<i>15.5777</i>	<i>16</i>	<i>38.2688</i>	<i>50</i>
CL 443*	18.5973	8	15.6074	10	38.4968	32
CL 486*	18.6123	8	15.6094	10	38.5105	31
CL 490*	18.6118	11	15.6073	12	38.5040	39
Backarc						
CL 425	18.5344	19	15.5980	23	38.4089	75
CL 426	18.5427	6	15.5997	6	38.4268	16
CL 430	18.5160	20	15.5869	25	38.3514	82
CL 475 b	18.5688	10	15.6004	11	38.4476	30
CL 481	18.4951	10	15.5907	12	38.4105	38
CL 482	18.4426	10	15.5748	12	38.2996	39
CL 433	18.4791	10	15.5907	13	38.4276	41
<i>CL 433_rep</i>	<i>18.4802</i>	<i>16</i>	<i>15.5909</i>	<i>19</i>	<i>38.4304</i>	<i>65</i>
more-enriched Backarc						
CL 424	18.5508	8	15.6360	8	38.5330	21
CL 431	18.3922	15	15.5923	18	38.3765	58
CL 432	18.4645	7	15.6258	7	38.5156	17
CL 434	18.3198	14	15.5898	16	38.4946	53
CL 437	18.3046	9	15.5790	9	38.4444	30

* cinder cones

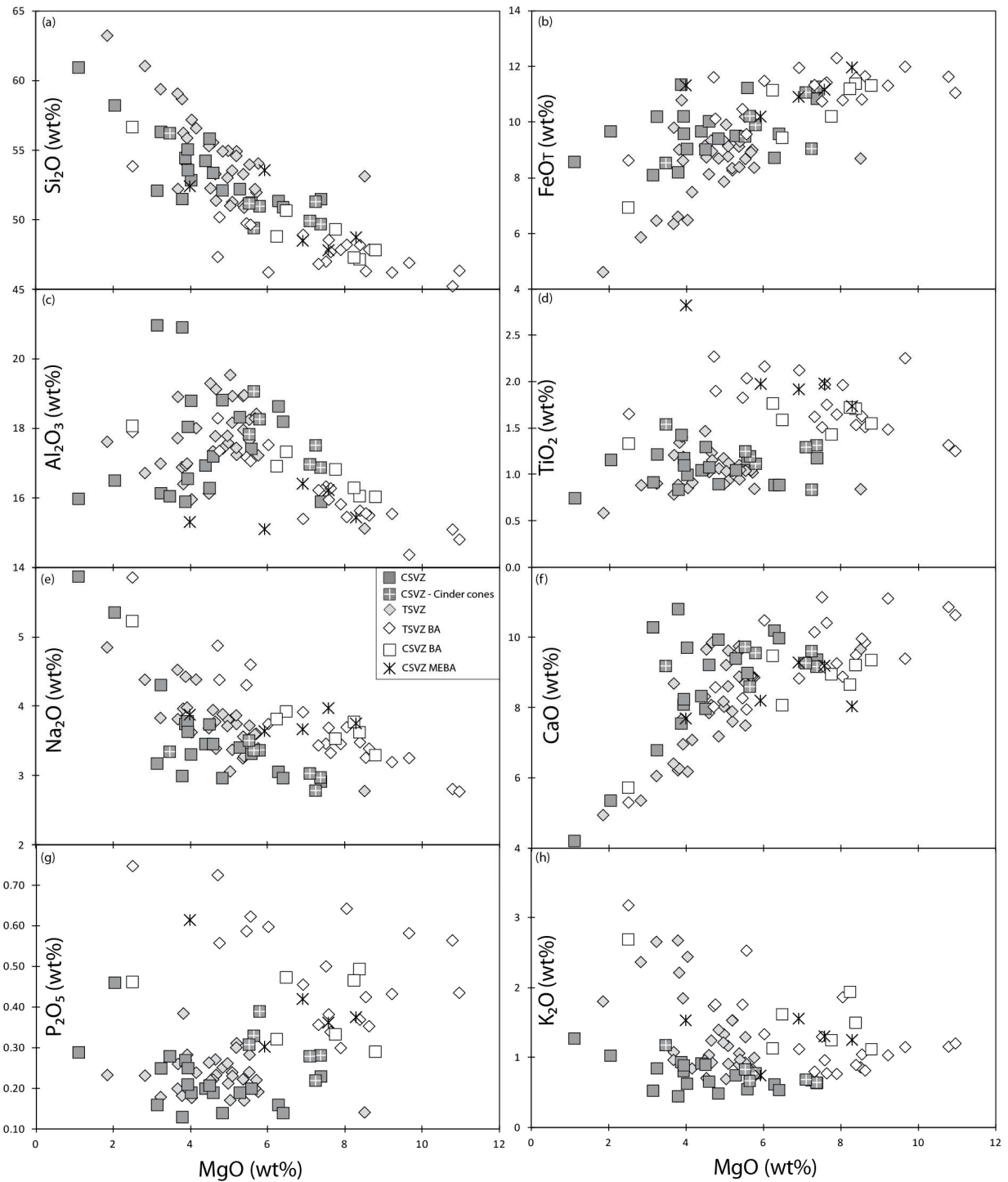


Figure 3.3 MgO versus major element oxides. The CSVZ VA trends overlap the TSVZ VA and have lower Na₂O and K₂O at a given MgO content. The cinder cones are least differentiated of the VA. BA samples extend to higher MgO, CaO and to lower SiO₂, Al₂O₃ compared to the VA. BA samples generally have lower SiO₂ and higher incompatible minor oxide abundances (Na₂O, TiO₂, K₂O and P₂O₅) at a given MgO content than VA samples. Data source are the same as in Figure 2.

The monogenetic cinder cone samples are basalts, except for one basaltic andesite sample from Apagado, and are characterized by lower SiO₂ (50-52 wt. %) and higher MgO contents (5.6-7.2 wt. %), forming the least differentiated end of the CSVZ trends in Figure 3. Otherwise there is substantial overlap between the CSVZ and TSVZ in major elements, especially at MgO > 4 wt. % (Figure 3). The BA samples are alkali basalts to trachybasalts, with SiO₂ = 47-56 wt. % and MgO = 2-9 wt. % (Figure 2a). Relative to the VA samples, the BA samples are in general shifted to lower SiO₂ but higher FeO_{total}, TiO₂, Na₂O, K₂O and P₂O₅ content at a given MgO content (Figure 3).

3.4.2 Trace elements

CSVZ VA samples show a pronounced subduction zone trace element signature on a multi-element diagram (Figure 4). This is characterized by enrichment relative to REE in the fluid-mobile Large Ion Lithophile Elements (LILEs), such as Cs, Rb, K, Ba, U, Pb and Sr, by relative depletion in the High Field Strength Elements (HFSEs) Nb and Ta compared to fluid mobile elements (Wehrmann et al., 2013), and by enrichment in melt-mobile elements such as LREE and Th relative to the HREE. Whereas the fluid mobile elements are similar or slightly enriched in the stratovolcanoes, the HFSE and LREE are more depleted and the HREE similar compared to the cinder cones. Consequently, the stratovolcano samples have greater highly fluid-mobile to less fluid-mobile trace element ratios (e.g. Ba/Nb, U/Th, Pb/Ce) and lower more-incompatible to less-incompatible trace element ratios (e.g. Nb/Yb, La/Yb, La/Sm) than the cinder cone samples (e.g. Figure 4, 5 and 6). The basaltic andesite from the Apagado cinder cone is least enriched in incompatible elements, except Nb, K, Sr and Ti, and has a relative Ti peak compared to all other CSVZ samples with Ti troughs (Figure 4) and have significantly higher La/Yb and lower U/Th than the other cinder cone samples (Figure 5). The BA basalts are characterized by greater enrichment in most incompatible elements between Cs and Y with the exception of Pb and have lower contents of the heaviest HREE (Tm, Yb and Lu) (Figure 4b).

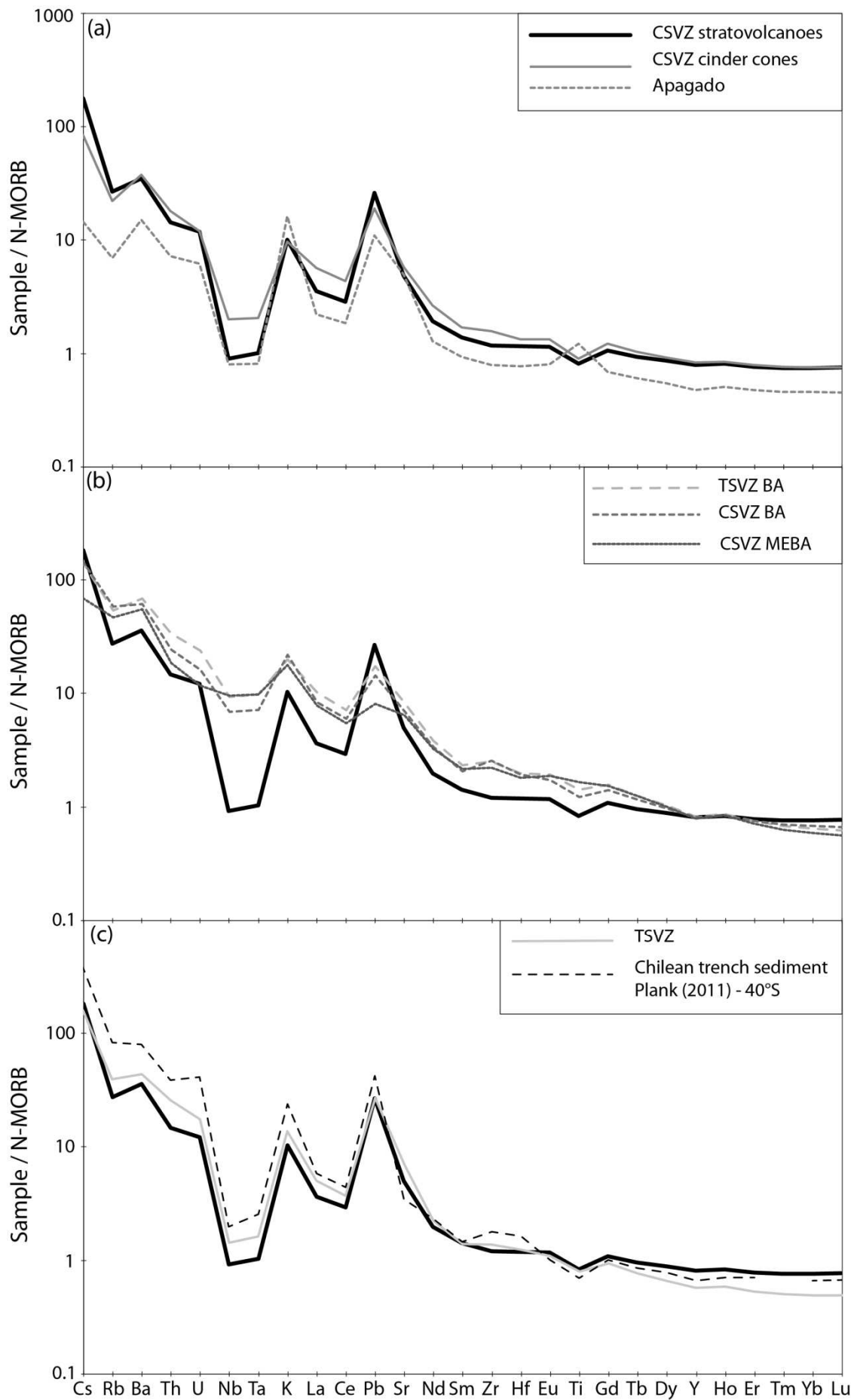


Figure 3.4 (Previous page) Multi-element diagram normalized to normal mid-ocean-ridge basalt (N-MORB) of Sun and McDonough (1989), showing the differences between: (a) the average CSVZ stratovolcanoes and cinder cones, (b) the average CSVZ BA, CSVZ MEBA, and TSVZ BA, and (c) the average CSVZ VA and TSVZ VA and the average Chilean trench sediment at 40°S from Plank (2011). All VA samples show typical subduction zone trace element signatures with e.g. K and Pb peaks and Nb and Ta troughs. Cinder cones overall have a less pronounced subduction signature than the stratovolcanoes. The Apagado cinder cone sample has the least enriched pattern in all elements, except Nb, K, Sr and Ti. The BA shows a similar pattern but with the least subduction signature, especially in the more-enriched backarc (MEBA) group. Data sources are the same as in Figure 2. The CSVZ has higher contents of all incompatible elements between Cs and Pb but lower HREE and Y abundances than the TSVZ. All samples follow the trench sediment pattern closely except for Zr and Hf, which show greater relative enrichment compared to Sm and Eu.

The BA basalts referred to based on isotopic composition as more-enriched (ME) have the least arc-like enrichment in Th or Pb and lie on the MORB (Mid-Ocean Ridge Basalt)-OIB (Oceanic Island Basalt) array of Pearce (2008) in Nb/Yb versus Th/Yb or La/Yb ratios (Figure 6) and have the highest, most MORB+OIB-like Nb/U and Ce/Pb (Hofmann et al., 1986) of the CSVZ BA samples (Figure 7). In respect to Nb/Yb, Th/Yb, Nb/U and Ce/Pb, they overlap the BA basalts of the southernmost TSVZ (Jacques et al., 2013). The CSVZ “more-enriched BA” (MEBA) and the TSVZ southern BA basalts display some Th and LREE enrichments. Finally, the CSVZ has higher contents of all incompatible elements between Cs and Pb but lower HREE and Y abundances than the TSVZ (Figure 4c). All samples follow the trench sediment pattern closely except for Zr and Hf, which show greater relative enrichment compared to Sm and Eu.

3.4.3 Isotopes

The CSVZ VA samples define a steep inverse correlation between $^{87}\text{Sr}/^{86}\text{Sr}$ and $^{143}\text{Nd}/^{144}\text{Nd}$ (Figure 8), with those from Llaima and Villarrica having the highest $^{143}\text{Nd}/^{144}\text{Nd}$ and the most offset to higher $^{87}\text{Sr}/^{86}\text{Sr}$ relative to $^{143}\text{Nd}/^{144}\text{Nd}$. The CSVZ stratovolcano samples are offset to higher $^{87}\text{Sr}/^{86}\text{Sr}$ at a given $^{143}\text{Nd}/^{144}\text{Nd}$ compared to the cinder cone samples, with no overlap between the two groups of volcanic edifices. Our Sr and Nd isotope data are similar to those in previous studies (e.g. Harmon et al., 1984, Hickey et al., 1986, Hickey-Vargas et al., 1989, Gerlach et al., 1988, Sigmarsson et al., 1990). The Apagado cinder cone basaltic andesite, with significantly lower abundances of most incompatible elements compared to the other

CSVZ samples, also has the most depleted Sr and Nd isotopic composition. All VA samples fall in the high $^{87}\text{Sr}/^{86}\text{Sr}$ half of the South Atlantic MORB field. The BA samples are shifted to lower Sr and Nd isotope ratios relative to the stratovolcano samples but most overlap the cinder cone samples. The five MEBA samples are shifted to higher $^{87}\text{Sr}/^{86}\text{Sr}$ and lower $^{143}\text{Nd}/^{144}\text{Nd}$ than all but one of the other BA samples.

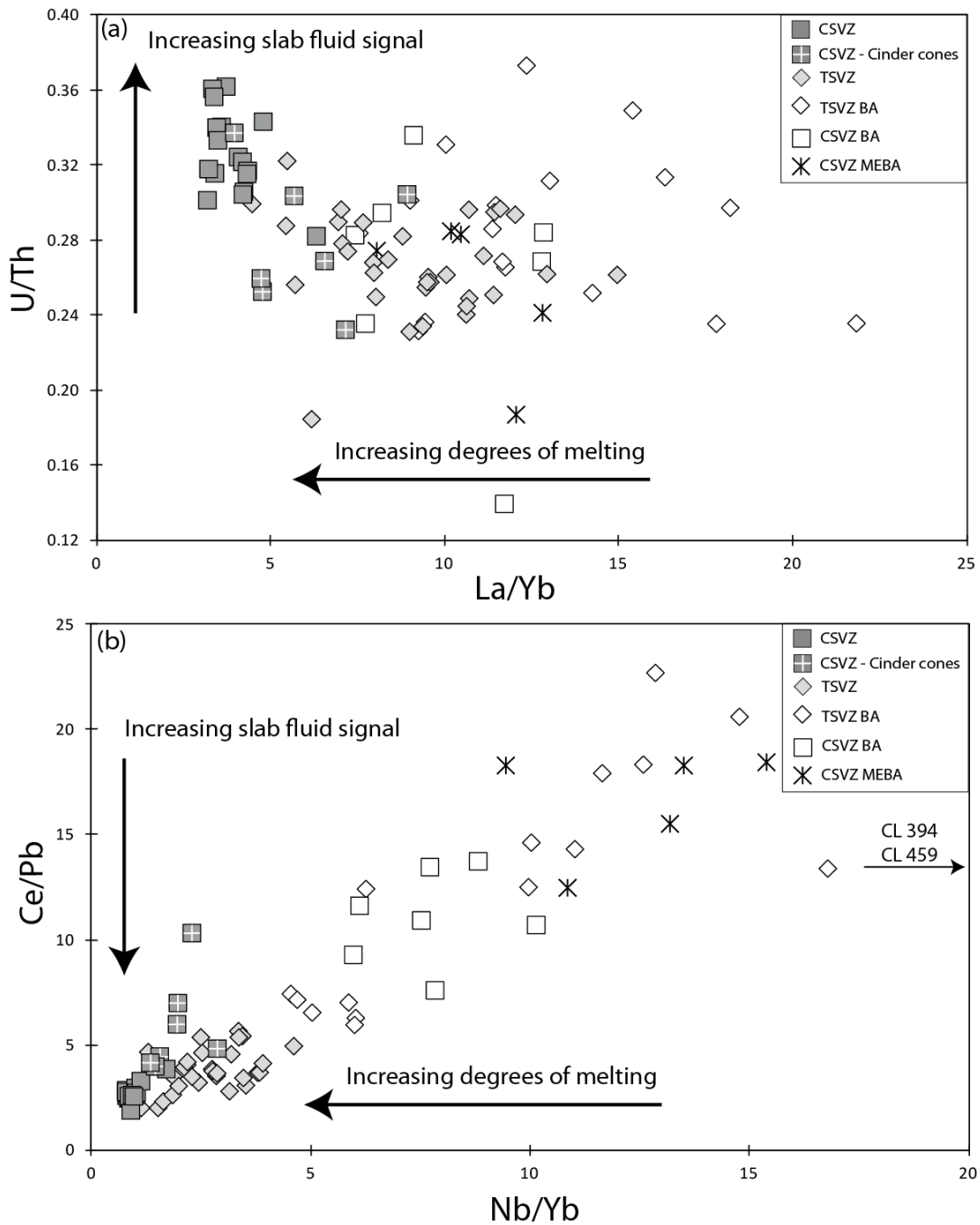


Figure 3.5 (Previous page) (a) La/Yb versus U/Th and. The SVZ samples form a negative correlation. The CSVZ stratovolcanoes have the highest slab fluid signal associated and the highest degrees of melting (see also Dzierma et al., 2012). The cinder cones are more similar in composition to the TSVZ. BA samples are offset to lower percent melting relative to U/Th. (B) Nb/Yb versus Ce/Pb. The SVZ samples form a positive correlation with the BA, consistent with more slab component and higher degrees of melting in the SVZ in general, and in the CSVZ in particular. Data sources are the same as in Figure 2.

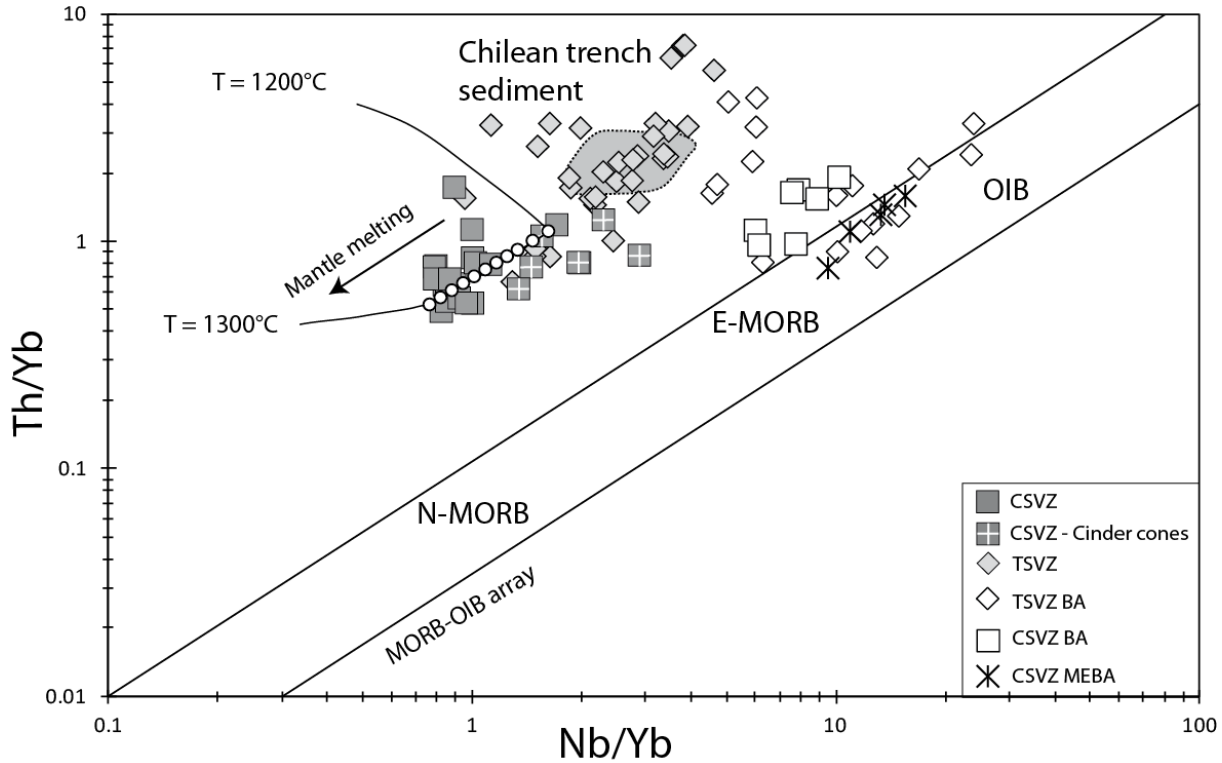


Figure 3.6 Nb/Yb versus Th/Yb, after Pearce (2008). MORB and OIB define the positive trend labeled MORB-OIB array, reflecting greater mantle enrichment at higher ratios along the array. All SVZ VA and some BA samples plot above the line indicating Th enrichment primarily through addition of a slab component to the source since evidence for crustal assimilation is minimal in these samples. The CSVZ BA samples lie slightly above the MORB-OIB array, indicating less slab component in their source. The MEBA samples lie within the MORB-OIB array, indicating no slab component in them, as is also the case for some of the TSVZ BA samples. The decreasing Nb/Yb ratios from the BA samples to the TSVZ VA to the CSVZ VA cinder cones to CSVZ VA stratovolcanoes could reflect derivation through increasing degrees of melting and/or from increasingly more depleted sources. The white dots shows the result of the ABS melting model in Section 5.7 as a function solely of temperature, starting at 1200°C and increasing to 1300°C in 10°C increments, which corresponds to percent melting increasing from 3 to 9%. Data source are the same as in Figure 2. The Chilean trench sediment field is from Jacques et al. (2013) and Lucassen et al. (2010).

On Pb isotope correlation diagrams (Figure 9), the CSVZ cinder cone samples almost completely overlap the TSVZ and CSVZ but two samples extend to significantly less radiogenic $^{206}\text{Pb}/^{204}\text{Pb}$, $^{207}\text{Pb}/^{204}\text{Pb}$ and $^{208}\text{Pb}/^{204}\text{Pb}$ ratios. As with Sr and Nd isotope ratios, the Apagado sample has the most depleted Pb isotope ratios also. All samples plot in the lower part of the Chilean trench sediment field. Anchored by the Apagado sample with the least radiogenic Pb, the cinder cones form a steeper slope than the stratovolcano samples with the Apagado sample even plotting beneath the BA array on both Pb isotope diagrams (Figure 9). Excluding the MEBA samples, the BA samples overlap the CSVZ and extend to less radiogenic Pb isotope ratios, overlapping the positive array formed by the TSVZ BA samples. The MEBA samples have distinctly higher $^{207}\text{Pb}/^{204}\text{Pb}$ and $^{208}\text{Pb}/^{204}\text{Pb}$ at a given $^{206}\text{Pb}/^{204}\text{Pb}$ (i.e. higher $\Delta 7/4\text{Pb}$ and $\Delta 8/4\text{Pb}$) than the other CSVZ and TSVZ BA samples.

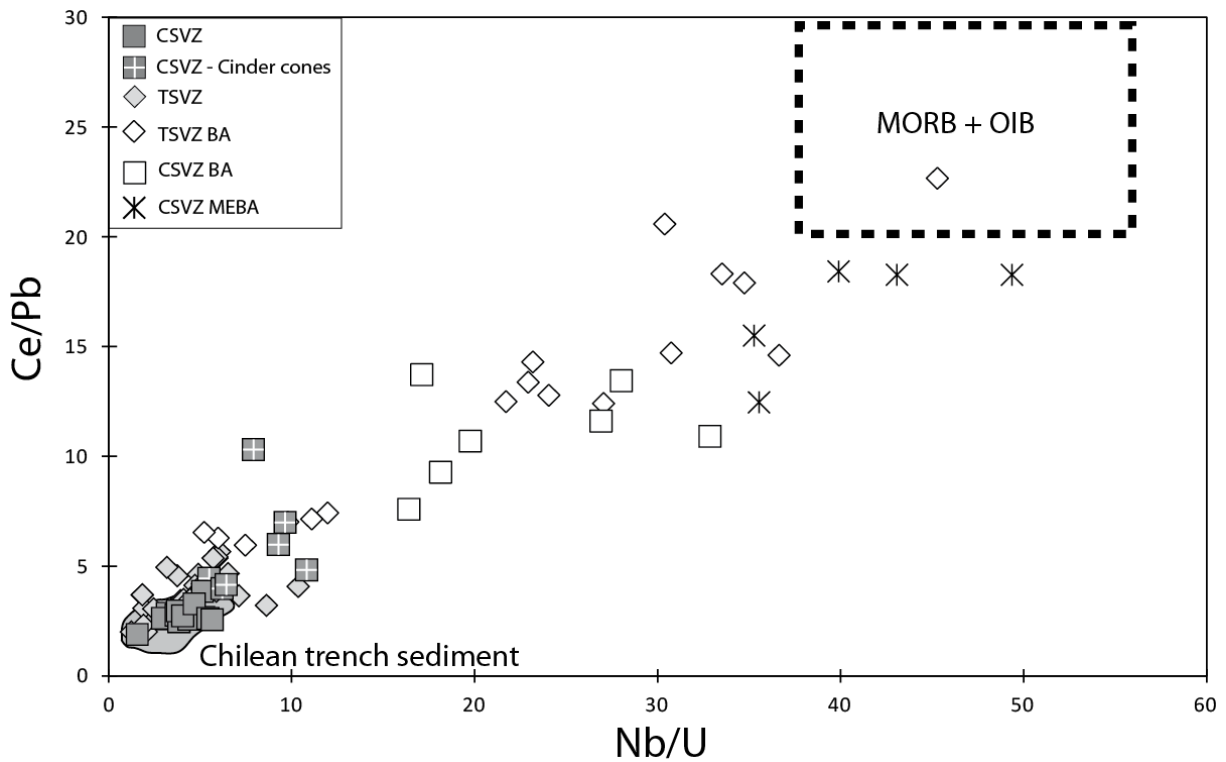


Figure 3.7 Nb/U versus Ce/Pb. The CSVZ stratovolcano samples overlap the TSVZ VA, while the monogenetic cinder cone samples have more mantle-like Ce/Pb and Nb/U ratios, with the typical mantle range (dashed box) represented by the typical MORB and OIB range (after Hofmann et al., 1986). The CSVZ BA samples extend to still more mantle-like values with the more-enriched BA samples having the most mantle-like values. Data source are the same as in Figure 6.

On ϵNd versus ϵHf isotope diagram, the stratovolcano and cinder cone samples overlap almost completely (Figure 10), in contrast to the Sr versus Nd and Pb versus Pb isotope diagrams. The CSVZ samples extend to the highest ratios of all SVZ samples. The BA samples are displaced to lower Hf isotope ratios than the arc trend, as was observed in the TSVZ BA samples (Jacques et al., 2013). The CSVZ MEBA samples extend the BA array to lower ratios.

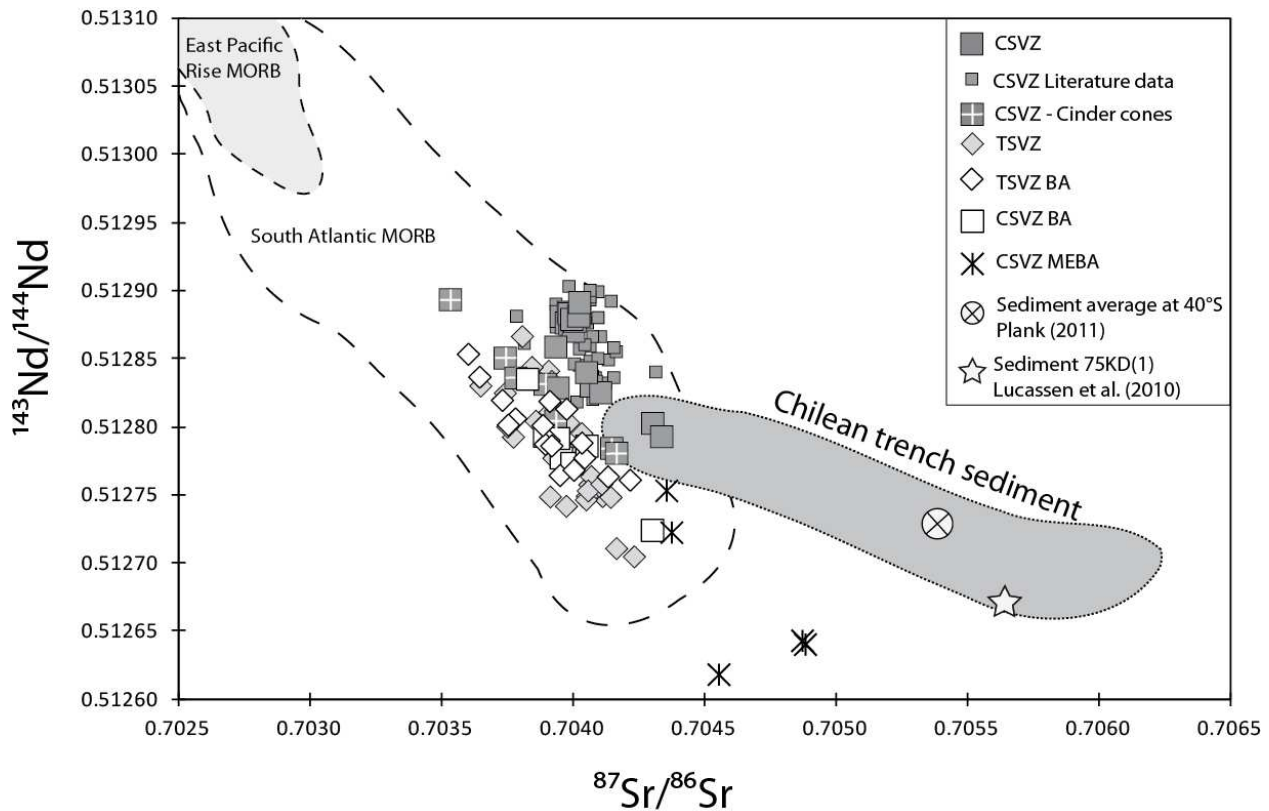


Figure 3.8 $^{87}\text{Sr}/^{86}\text{Sr}$ versus $^{143}\text{Nd}/^{144}\text{Nd}$. The CSVZ and TSVZ samples form a rough negative array but most of the CSVZ stratovolcano data form a cluster with elevated $^{87}\text{Sr}/^{86}\text{Sr}$ and/or $^{143}\text{Nd}/^{144}\text{Nd}$ compared to the CSVZ cinder cones and the TSVZ which overlap. CSVZ BA and TSVZ BA overlap, but the MEBA samples are shifted to more radiogenic compositions. All samples except the MEBA plot within the South Atlantic MORB field. The star denotes the “typical” sediment used in modeling (see Figure 13), while the circle shows the average Chilean trench sediment at 40°S of Plank (2011). CSVZ literature data are from Harmon et al., 1984, Hickey et al., 1986, Hickey-Vargas et al., 1989, Gerlach et al., 1988, Sigmarrsson et al., 1990. Trench sediment data are from Lucassen et al. (2010) and Jacques et al. (2013). Basement data are from Lucassen et al. (2004). TSVZ data are from Jacques et al. (2013). East Pacific Rise (20-34°S) MORB data are from Fontignie and Schilling (1991), Haase (2002), Hamelin et al. (1984), Hanan and Schilling (1989), Ito et al. (1980), Ito et al. (1987), Kingsley et al. (2007), MacDougall and Lugmair (1986), Mahoney et al. (1994), Newsom et al. (1986) and White et al. (1987). South Atlantic (30-50°S) MORB data are from Andres et al. (2002), Douglas et al. (1999), Fontignie and Schilling (1996), Hanan et al. (1986) and Roy-Barman et al. (1998).

Oxygen isotopes from olivine phenocrysts have values ranging from 4.43‰ to 5.50‰ (Table 2), which extend below and above the mantle range for olivine (5.2‰ ± 0.3; Matthey et al., 1994). All CSVZ VA stratovolcano samples have values lower than the mantle range, whereas the VA cinder cone samples straddle the mantle range. The BA samples range from 5.17‰ to 5.72‰. We also measured glass/groundmass (representing the melt composition) from some of the same CSVZ and TSVZ samples that we analyzed for mineral composition (TSVZ mineral data reported in Jacques et al., 2013). We compared the mineral and melt compositions in order to evaluate the validity of the analytical results (Table 2).

Table 3.2 O isotope data from olivine, plagioclase, groundmass (glass or matrix) and $\delta^{18}\text{O}(\text{melt})$ converted from mineral $\delta^{18}\text{O}$. Mineral $\delta^{18}\text{O}$ was converted to melt $\delta^{18}\text{O}$ by adding 0.6‰ to the olivine value.

Sample number	Sample Location	$\delta^{18}\text{O}$ olivine	1 σ	mineral	groundn	$\delta^{18}\text{O}(\text{melt})$ corrected	$\Delta(\text{measurements} - \text{correction})$
TSVZ Volcanic Arc							
CL 725	Tinguiririca#	5.07	0.10	pl	6.35	5.67	0.68
CL 726	Tinguiririca#	5.62	0.10	pl		6.22	
CL 196	Los Hornitos (small cone near Cerro Azul)	5.31	0.10	ol	5.88	5.91	-0.03
CL 571	San Pedro	5.24	0.05	ol		5.84	
CL 572	San Pedro (Satellite cones)	5.09	0.10	ol	5.81	5.69	0.12
CL 575b	San Pedro (Satellite cones)	5.28	0.05	ol		5.88	
CL 576	San Pedro (Satellite cones)	5.29	0.02	ol	5.96	5.89	0.07
<i>CL 576_rep</i>					6.20		
CL 449	Longaví	5.52	0.03	ol		6.12	
CL 531	Longaví	4.88	0.10	ol	5.42	5.48	-0.06
<i>CL 531_rep</i>					5.55		
CL 559	Callaqui (Satellite cones)	5.35	0.14	ol		5.95	
CL 560	Callaqui (Satellite cones)	5.20	0.10	ol		5.80	
CSVZ Volcanic Arc							
CL 029	Llaima	4.81	0.07	ol		5.41	
CL 032	Llaima	4.53	0.07	ol	5.44	5.13	0.31
CL 006	Villarrica	4.76	0.12	ol	5.39	5.36	0.03
CL 010	Villarrica	4.70	0.05	ol		5.30	
CL 166	Villarrica	4.93	0.09	ol	5.37	5.53	-0.16
CL 022*	Caburga*	4.90	0.23	ol		5.50	
CL 109	Casablanca	4.96	0.15	ol		5.56	
CL 088*	Cabeza de Vaca*	5.34	0.10	ol		5.94	
CL 098	Osorno	4.92	0.13	ol		5.52	
CL 486*	Chaiten*	5.50	0.04	ol		6.10	
CL 490*	Chaiten*	5.48	0.07	ol	6.24	6.08	0.16
CSVZ Backarc							
CL 425	old plateau basalt	5.31	0.01	ol	5.77	5.91	-0.14
CL 475 b	around Laguna Blanca	5.34	0.10	ol		5.94	
CL 433	plateau basalt / Jacobacci Volc field	5.17	0.12	ol		5.77	
More-enriched Backarc							
CL 424	old plateau at meterite impact site	5.72	0.10	ol	6.74	6.32	0.42
CL 432	Jacobacci Volc field	5.25	0.10	ol		5.85	
CL 437	Crater Basalt Volcanic Field	5.37	0.10	ol		5.97	

* cinder cones

Olivine corrected values, by subtracting 0.7 to the plagioclase value

The $\delta^{18}\text{O}$ in the glass/groundmass samples ranged from 5.37‰ to 6.35‰ (6.74‰ including the BA sample CL 424). We converted our VA phenocryst $\delta^{18}\text{O}$ to $\delta^{18}\text{O}(\text{melt})$ by adding 0.6‰ to $\delta^{18}\text{O}(\text{Olivine})$, which corresponds to the difference between the $\delta^{18}\text{O}$ in MORBs (e.g. 5.8‰ within the range of 5.5-5.9‰; e.g. Bindeman (2008) and references therein) and mantle peridotite ($5.2\text{‰} \pm 0.3$; e.g. Matthey et al., 1994). Comparison of the converted olivine $\delta^{18}\text{O}$ values with the $\delta^{18}\text{O}(\text{melt})$ (based on the measured glass and groundmass samples) shows overall very good agreement between phenocryst and glass/groundmass analyses. The converted $\delta^{18}\text{O}(\text{melt})$ ranges from 5.13‰ to 6.10‰ in the CSVZ VA (6.32‰ including BA sample CL 424). This simple approach is more appropriate for our samples than using the linear equation from Bindeman et al. (2004), which calculates the $\Delta(\text{min.-melt})$ based on the SiO_2 content of the whole rock and is based on the experimental determination of the liquid line of descent of Kamchatka magmas. The Kamchatka equation probably overestimates the $\delta^{18}\text{O}(\text{melt})$, because the liquid line of descent of the Andean magmas may be shifted to higher temperatures than for the Kamchatka magmas, consistent with higher slab surface temperature beneath central Chile than Kamchatka (Van Keken et al., 2011). All CSVZ stratovolcano samples have $\delta^{18}\text{O}(\text{melt})$ below the MORB range (Figure 11). In this regard, the $\delta^{18}\text{O}(\text{melt})$ correlates inversely with Nd isotopes, U/Th, Ba/Nb and Pb/Ce, and positively with La/Yb (Figure 11). The stratovolcano samples have the greatest highly fluid-mobile to less fluid-mobile trace element ratios and the lowest $\delta^{18}\text{O}(\text{melt})$, whereas the monogenetic CSVZ VA and TSVZ VA show the opposite. For the BA samples, they have $\delta^{18}\text{O}(\text{melt})$ within the MORB range, except CL 424 which extends largely above.

3.5 Discussion

To ensure the comparability of the arc rocks composition, we will first evaluate the data for crustal assimilation. Then, to identify the slab component and mantle wedge composition, we will discuss differences between the CSVZ VA stratovolcanoes versus CSVZ VA cinder cones and the TSVZ VA (using data from Jacques et al., 2013) and between the CSVZ and TSVZ BA samples. We will end with a quantitative flux melting model for generating the CSVZ melts.

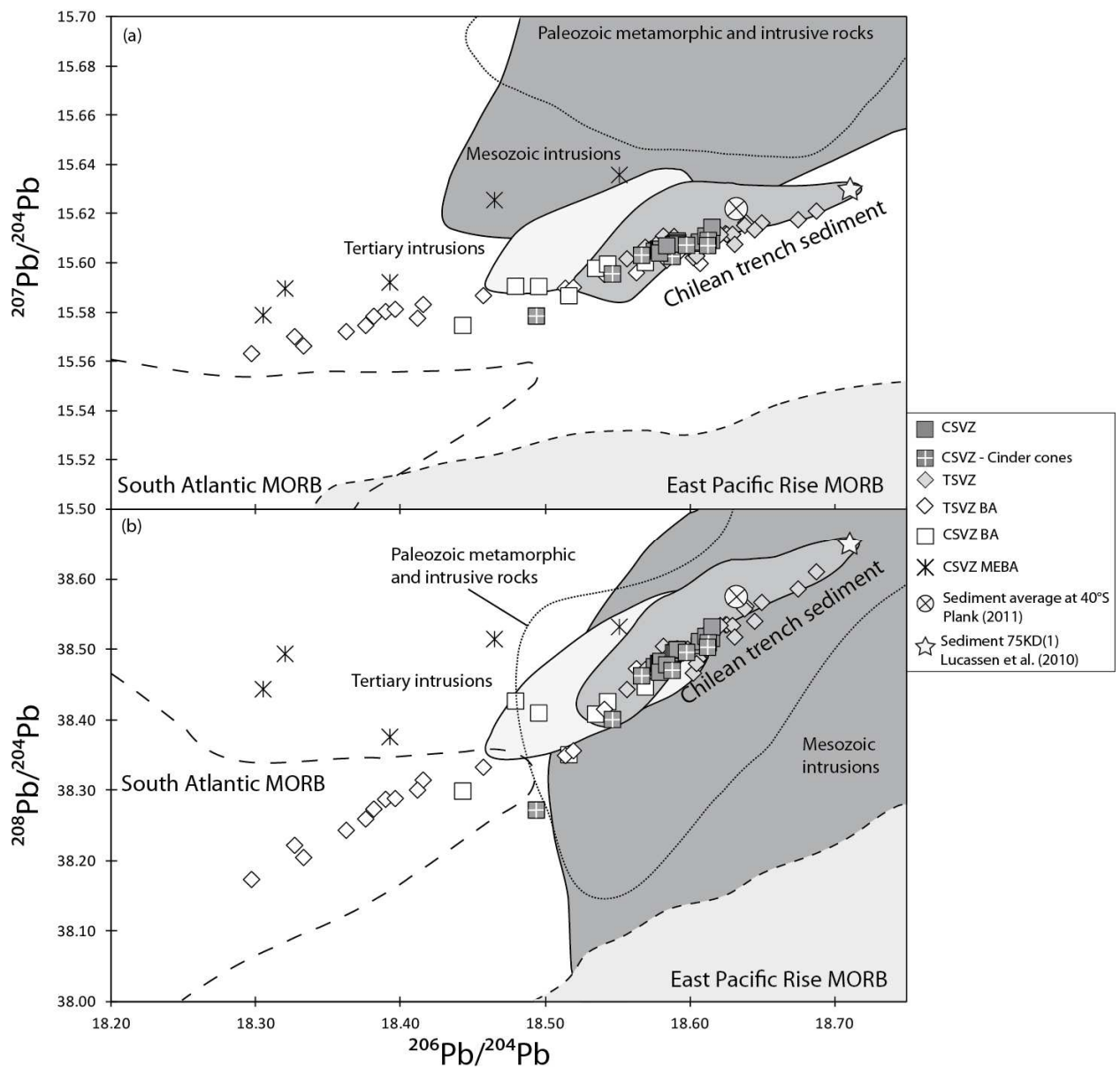


Figure 3.9 $^{206}\text{Pb}/^{204}\text{Pb}$ versus (a) $^{207}\text{Pb}/^{204}\text{Pb}$ and (b) $^{208}\text{Pb}/^{204}\text{Pb}$. The CSVZ samples form a tight positive array similar to the TSVZ samples. All samples plot at the base of the trench sediment field. The monogenetic cinder cones samples extend to less radiogenic Pb isotopic compositions with the Apagado sample having the least radiogenic Pb of all SVZ VA samples. Excluding the five MEBA samples, the CSVZ BA samples overlap the radiogenic end of the TSVZ BA array. The star shows the “typical” sediment used in modeling (see Figure 13), while the circle shows the average Chilean trench sediment at 40°S of Plank (2011). Data sources for TSVZ, sediment and MORBs are the same as for Figure 8. Basement data are from Lucassen et al. (2004). The trench sediment field includes river mouth sediments from Hildreth and Moorbath (1988).

3.5.1 Is crustal assimilation occurring during fractional crystallization in the CSVZ VA?

Crustal assimilation is possible throughout the SVZ VA because crustal thicknesses vary from 30-60 km decreasing from north to south (e.g. Cembrano and Lara, 2009). The crust

beneath the TSVZ VA diminishes from 45 to 30 km towards the south and then remains at ~30 km beneath the CSVZ VA. If crustal assimilation occurred, a clear correlation between geochemical indicators for magma differentiation and isotopic compositions would be expected. Our isotope data, however, are not consistent with significant crustal assimilation during differentiation in either the TSVZ or CSVZ. As shown in figure 12, there is no substantial variation with decreasing MgO (or increasing SiO₂).

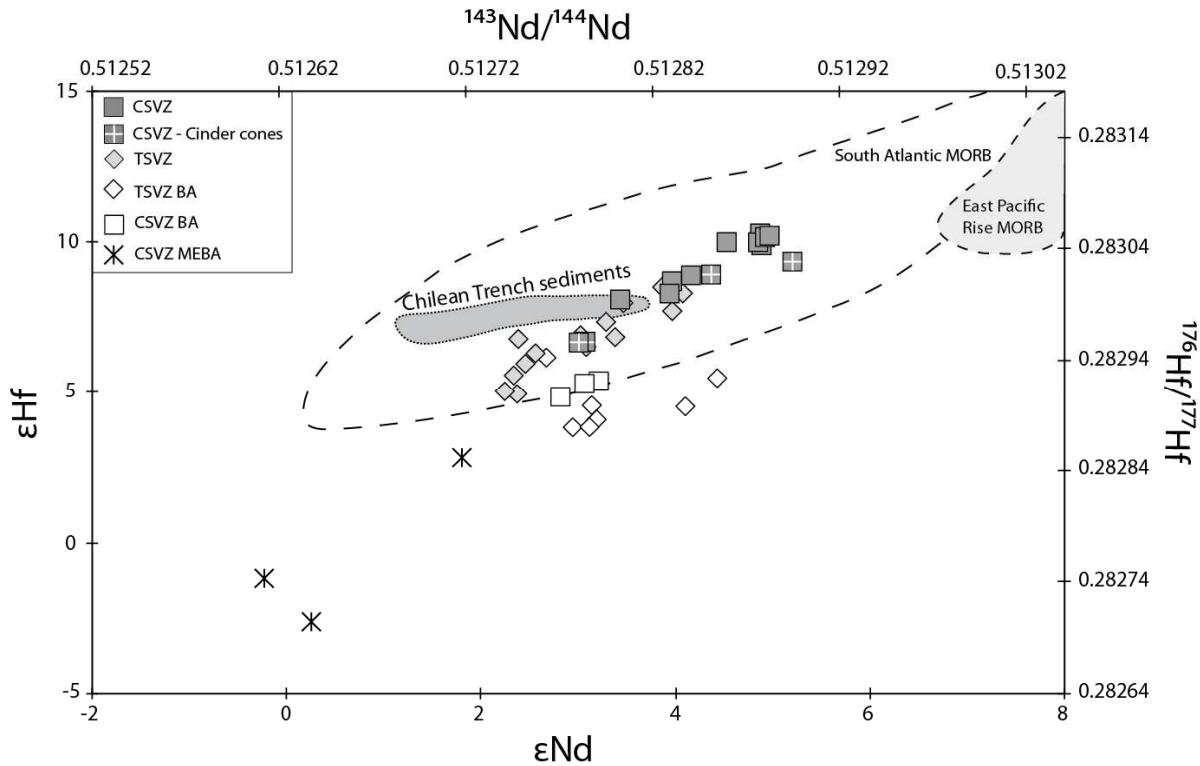


Figure 3.10 ϵ_{Nd} versus ϵ_{Hf} . The CSVZ VA samples plot on the same positive array defined by the TSVZ VA samples but the CSVZ extend to more radiogenic compositions. In both segments, the VA and BA samples form two subparallel trends, the BA having lower ϵ_{Hf} at a given ϵ_{Nd} . The offset is generally less than for the CSVZ BA samples, while the ME BA samples have the lowest ϵ_{Hf} and ϵ_{Nd} of all the BA samples. Data source for MORBs are the same as in Figure 8. TSVZ data and sediments are from Jacques et al. (2013).

The radiogenic isotope data are also not consistent with assimilation of Paleozoic and Mesozoic basement in our samples from both arc segments. These basement rocks, especially the Paleozoic ones, are characterized by higher $^{87}Sr/^{86}Sr$, $^{207}Pb/^{204}Pb$ and $^{208}Pb/^{204}Pb$ ratios at a given $^{206}Pb/^{204}Pb$ ratio, and lower $^{143}Nd/^{144}Nd$ than in the volcanic rocks (e.g. Figure 9; see also Lucassen et al., 2004). None of the VA samples from either segment are shifted in this direction.

Instead, the CSVZ cinder cones and TSVZ VA largely overlap in all isotopes, and the isotopic differences between the CSVZ and TSVZ stratovolcanoes cannot be explained by less assimilation of Paleozoic and Mesozoic basement in the CSVZ. We test this conclusion further in Figure 12, which shows that Sr and Nd isotopes from this study and others do not vary with differentiation within specific CSVZ volcanoes down to at least 3 wt. % MgO. The same lack of correlation is true for all differentiation indices (not shown). Osorno may be an exception but the difference in Nd isotopes is in only one sample from a different study and is not accompanied by a difference in Sr isotopes.

The Tertiary intrusive rocks, which lie beneath the CSVZ volcanoes, have similar Sr-Nd-Pb isotopes to the Quaternary volcanic rocks (Table 1) (e.g. Figure 9; see also Lucassen et al., 2004). Assimilation of these crustal rocks would not significantly affect the radiogenic isotopes. Indeed, Jicha et al. (2007) and Reubi et al. (2011) proposed that the hydrothermally-altered young plutonic roots of the CSVZ arc are variably assimilated at Puyehue and Llaima, respectively, based on U-series disequilibria. Unfortunately, by their arguments, differentiation increases U-series disequilibria at Puyehue but decreases it at Llaima, which makes it difficult to use differentiation to monitor assimilation. Assimilation of plutonic roots also has been inferred at San Pedro volcano in the TSVZ (Dungan et al., 2001; Dungan and Davidson, 2004). Reubi et al. (2011) argued that such assimilation affects the most incompatible trace elements, such as U and Th. However, there is no evidence for enrichment in U or Th in some San Pedro samples from Jacques et al. (2013) and there is no correlation between U/Th or Ba/Th and MgO or SiO₂ in our CSVZ samples (not shown). Dungan et al. (2001) and Dungan and Davidson (2004) used Rb/SiO₂ ratios to monitor assimilation in San Pedro. There is no clear correlation between Rb/SiO₂ and isotopes (e.g. ¹⁴³Nd/¹⁴⁴Nd) although the Villarrica and Llaima samples with high ¹⁴³Nd/¹⁴⁴Nd (and thus most likely to be contaminated by the Tertiary intrusive rocks) have *in general* high Rb/SiO₂. However, Rb is an incompatible, fluid-mobile element and could come from the slab.

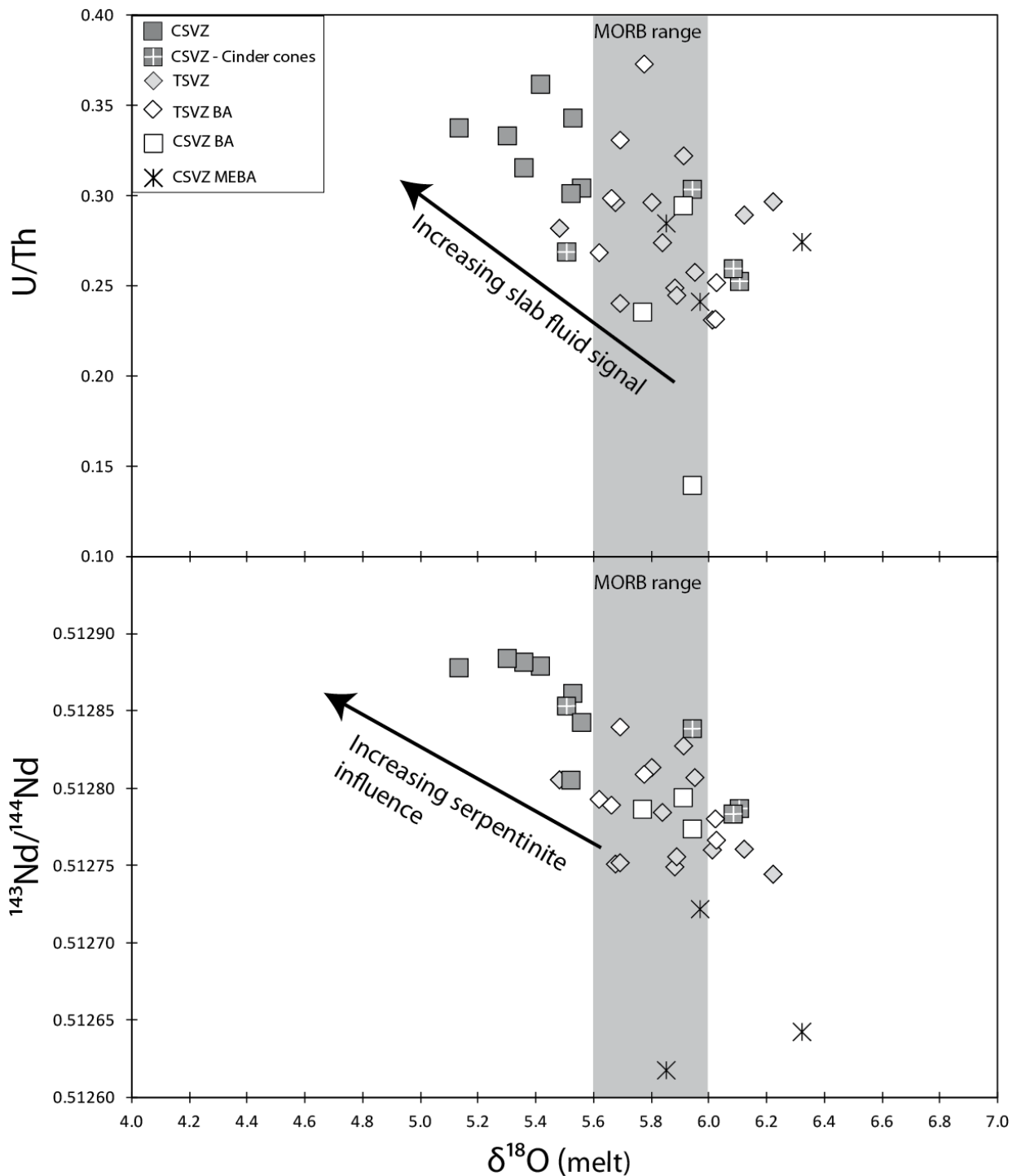


Figure 3.11 $\delta^{18}\text{O}(\text{melt})$ versus (a) U/Th and (b) $^{143}\text{Nd}/^{144}\text{Nd}$. CSVZ stratovolcano samples have lower $\delta^{18}\text{O}(\text{melt})$ values than CSVZ cinder cone and TSVZ VA samples. $\delta^{18}\text{O}(\text{melt})$ correlates negatively with Nd isotopes and U/Th , indicating that the higher fluid flux beneath the CSVZ is associated with a more depleted source such as lower oceanic crust or serpentinites. MORB range after Bindeman (2008) and references therein. Data sources are the same as in Figure 2.

In summary, the differences in trace elements and isotopes between 1) the monogenetic cinder cones and the stratovolcanoes, and 2) the CSVZ and the TSVZ VAs are not

consistent with assimilation of older crust (with different Sr-Nd-Pb isotopes) and do not show clear evidence of assimilation of Tertiary intrusive rocks with similar Sr-Nd-Pb isotopes. Assimilation of hydrothermally-altered plutonic roots could lower the $\delta^{18}\text{O}$ of VA melts, but this would require all CSVZ stratovolcanoes to have assimilated significant amounts of exclusively hydrothermally-altered plutonics. We believe this is unlikely considering the wide range in $\delta^{18}\text{O}$ of the plutonic rocks (-1.73‰ to 6.29‰; G. Jacques unpublished data) that we analyzed with values both substantially lower and higher than mantle rocks. We argue below that these differences reflect subcrustal processes that occur in the mantle and come from the slab.

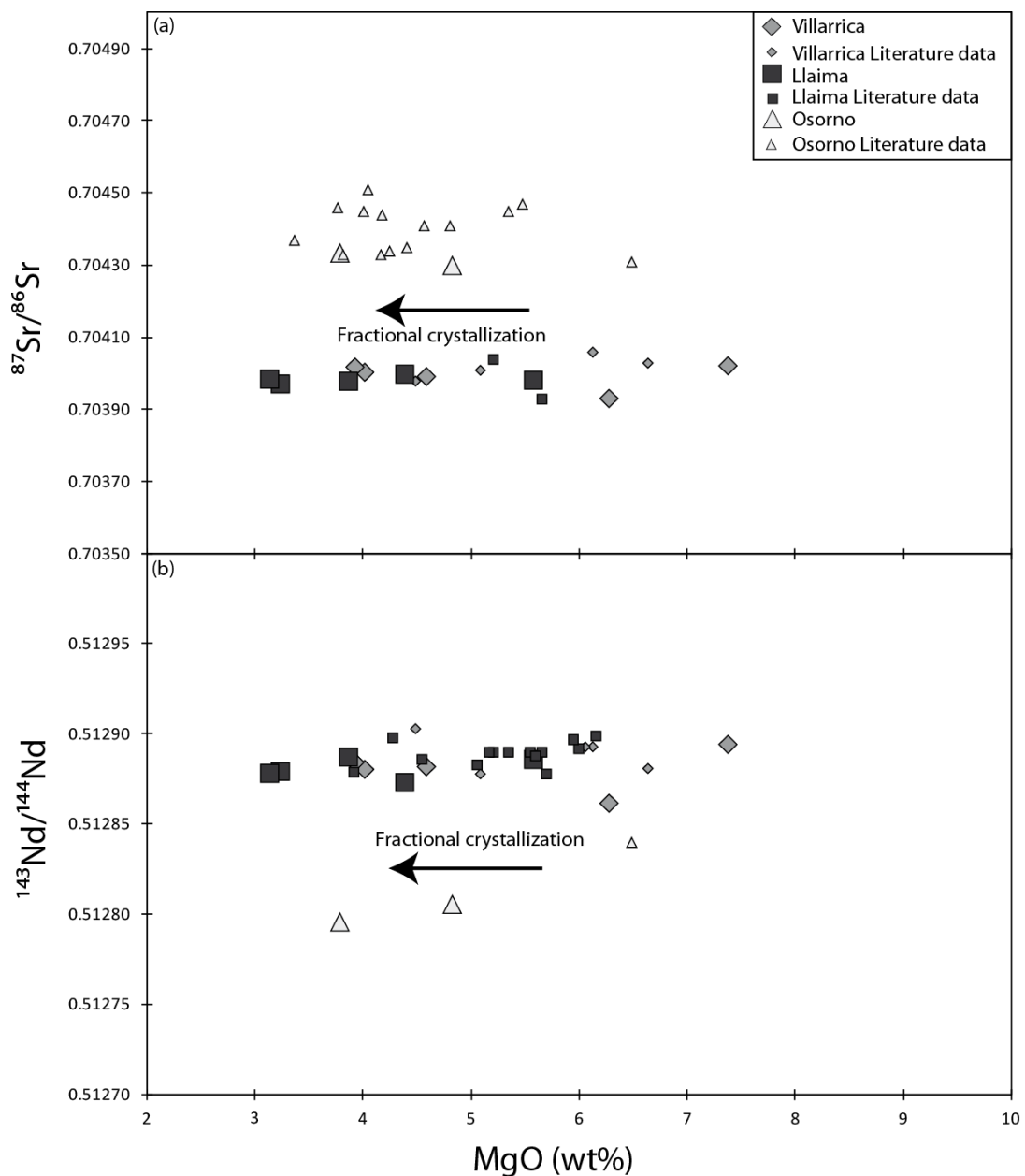


Figure 3.12 (Previous page) MgO versus (a) $^{87}\text{Sr}/^{86}\text{Sr}$, (b) $^{143}\text{Nd}/^{144}\text{Nd}$ for Llaima, Villarrica and Osorno. The data for the individual volcanoes and for the CSVZ on the whole can be explained by crystal fraction (indicated by horizontal black arrows) without the need to invoke concomitant assimilation (AFC). MgO from our samples from Wehrmann et al. (2013a) and (in rev b). Data source for Villarrica:; Hickey-Vargas et al., 1989, 2002, Llaima: Hickey et al., 1986, Hickey-Vargas et al., 1989, Reubi et al., 2011, Osorno: Hickey et al., 1986, Tagiri et al., 1993.

3.5.2 CSVZ VA stratovolcanoes compared to CSVZ VA cinder cones and TSVZ VA: Differences in the mass fraction of the slab component

The CSVZ VA stratovolcano and monogenetic cinder cone samples show systematic differences in geochemistry with the cinder cones often overlapping the TSVZ VA samples. Compared to the CSVZ VA cinder cone and the TSVZ VA samples, the CSVZ VA stratovolcano samples have higher ratios of highly fluid-mobile to less fluid-mobile trace elements (e.g. U/Th, U/Nb and Pb/Ce), reflecting a greater addition of slab component to the source of the CSVZ stratovolcanoes, and lower ratios of more-incompatible to less-incompatible trace elements (e.g. La/Yb, Nb/Yb), reflecting higher degrees of melting and/or derivation from a more depleted source (e.g. Figure 5, 6 and 7). The CSVZ VA stratovolcanoes also have higher Sr isotope ratios at a given Nd isotope ratio than the CSVZ VA cinder cone and TSVZ VA samples with the range in Nd isotope ratios being nearly identical in both types of CSVZ VA volcanic edifices, which is again consistent with greater addition of a slab component to the source of the CSVZ stratovolcanoes. The more radiogenic Pb isotopic compositions of the CSVZ stratovolcanoes, plotting in the field for trench sediments, are also consistent with a greater addition of slab component to the stratovolcano source. The simplest explanation for these combined differences is that a higher flux of hydrous fluids/melts from the slab (altered ocean crust (AOC) and sediment) beneath the CSVZ stratovolcanoes caused greater amounts of flux melting and depletion of the mantle wedge. Greater amounts of melting resulted in greater volumes of magma being produced that formed larger volcanic edifices (stratovolcanoes compared to monogenetic vents).

The CSVZ stratovolcano samples have $\delta^{18}\text{O}(\text{melt})$ lower than the MORB range (e.g. 5.8‰ within the range of 5.5-5.9‰; e.g. Bindeman (2008) and references therein), whereas the CSVZ cinder cone and TSVZ samples overlap the MORB range or extend to slightly higher values. The

trench sediments in Chile have high $\delta^{18}\text{O}$ (8-14‰, Jacques et al., 2013). Therefore the slightly elevated $\delta^{18}\text{O}$ in these samples could reflect the addition of sediment melts to the mantle wedge source, consistent with our ABS model calculations (see below and Jacques et al., 2013). In order to explain the lower values found in the CSVZ stratovolcano samples, a component with low $\delta^{18}\text{O}$ (e.g. serpentine, 0-6‰, Bindeman et al., 2005 and references therein) is needed to compensate the high $\delta^{18}\text{O}$ in the sediments. The trace element and radiogenic isotope data support a higher fluid/hydrous melt flux from the slab, causing greater degrees of melting beneath the CSVZ stratovolcanoes (Figure 5, 6, 11). Samples having the highest ϵHf and ϵNd isotopes have the lowest $\delta^{18}\text{O}$ (Figure 10, 11), consistent with low $\delta^{18}\text{O}(\text{melt})$ reflecting derivation of fluids from a depleted reservoir such as hydrothermally-altered lower crust and/or serpentinized upper mantle of the incoming slab to the source of the CSVZ stratovolcanoes (Figure 11). A similar observation in Central America led Eiler et al. (2005) and Heydolph et al. (2012), to propose that aqueous fluids from serpentinites or altered gabbros were the cause of the lower than typical mantle $\delta^{18}\text{O}$ in olivine.

3.5.3 Comparison of CSVZ and TSVZ BA lavas: Differences in mantle source composition

The CSVZ VA samples have higher fluid mobile (LILE) and lower fluid immobile element (HFSE and heavy REE) contents than the CSVZ BA samples and lower ratios of more to less incompatible HFSE and REE (e.g. La/Yb, Nb/Yb) (Figures 4, 5 and 6). These ratios can be fractionated by differing degrees of mantle melting due to differences in bulk distribution coefficients (e.g. Green et al., 2000). On the opposite, ratios of highly fluid-mobile (e.g. LILE) to less fluid-mobile (e.g. HFSE and REE) elements (e.g. U/Th, Ba/Nb, Pb/Ce) (e.g. Figure 5, not all ratios shown) are higher in CSVZ VA lavas. These ratios are not easily fractionated by mantle melting, but can be fractionated by fluids or hydrous melts from the subducting slab. These variations are consistent with a higher fluid flux beneath the VA than the BA, resulting in higher degrees of melting beneath the VA (e.g. Elliot et al., 1997; Kelley et al., 2006).

The CSVZ VA samples overlap the CSVZ BA in Sr isotopes but are shifted to higher Nd isotope ratios (Figure 8). They also extend to higher Pb isotope ratios which overlap the trench

sediment field, whereas the BA samples have less radiogenic Pb, intersecting the South Atlantic MORB field (Figure 9). Similar to the TSVZ, the CSVZ VA and BA form distinct positive sub-parallel trends on the Nd versus Hf isotope diagram (Figure 10). Although sample CL 424 with elevated $\delta^{18}\text{O}(\text{melt}) = 6.32\text{‰}$ may have assimilated some crust, the two CSVZ MEBA samples with the lowest $^{206}\text{Pb}/^{204}\text{Pb}$ and highest $\Delta 8/4$ have mantle-like $\delta^{18}\text{O}(\text{melt})$, favoring a mantle origin for the isotopic enrichment. The CSVZ MEBA samples have less pronounced Nb-Ta troughs and thus higher Nb/U ratios (within the mantle range of 47 ± 10 as defined by Hofmann et al., 1986; Figure 7) and less pronounced Pb peaks and thus higher Ce/Pb and Nd/Pb ratios than the other CSVZ BA samples, reflecting less of a slab-derived component in these samples (Figure 7). Most CSVZ BA basalts overlap the TSVZ BA basalts on all isotope plots (Figure 8, 9, 10). The CSVZ MEBA samples and the southernmost TSVZ BA samples are free from slab-derived Th and LREE (Figure 6), but they differ isotopically. Compared to the other BA samples from the CSVZ and TSVZ, the CSVZ MEBA samples have more radiogenic $^{87}\text{Sr}/^{86}\text{Sr}$, $^{207}\text{Pb}/^{204}\text{Pb}$ and $^{208}\text{Pb}/^{204}\text{Pb}$, less radiogenic $^{143}\text{Nd}/^{144}\text{Nd}$ and $^{176}\text{Hf}/^{177}\text{Hf}$, yet a similar range in $^{206}\text{Pb}/^{204}\text{Pb}$. Both BA compositions could reflect subcontinental lithosphere or enriched plums in the asthenospheric mantle. Neither is observed in the CSVZ or TSVZ volcanic arc samples as indicated by the near-complete separation of the BA and VF samples on the Nd versus Hf isotope diagram (Figure 10).

3.5.4 Differences in the composition of the mantle wedge, subducting oceanic crust, and subducting sediment

3.5.4.1 *The mantle wedge*

The CSVZ VA samples have lower highly incompatible to less incompatible trace element ratios (e.g. Nb/Yb, La/Yb, Th/Yb; Figure 5 and 6) than the TSVZ VA samples. The lower Nb/Yb indicates a more depleted mantle wedge and/or higher degree of melting beneath the CSVZ VA. Although the range of ϵNd and ϵHf is small within the CSVZ (e.g., 2 ϵNd units; Figure 10), there is a rough negative correlation with Nb/Yb for the CSVZ stratovolcanoes that define the

depleted end of an array that includes the entire SVZ VA (not shown). Therefore, the variations in trace element ratios reflect differences in source composition and not just in the degree of mantle melting. Because Hf is the least likely isotopic tracer to be modified by a slab-derived component, we conclude that the mantle wedge beneath the CSVZ VA is more depleted (more N-MORB-like) than beneath the TSVZ VA segment (more E-MORB-like or reflects a mixture between MORB and ocean-island basalt type component).

In the TSVZ, Jacques et al. (2013) concluded that the mantle wedge beneath the arc can be best represented by two end-members: depleted South Atlantic mantle (SAM-D with lower Sr and Pb and higher Nd isotope ratios), and enriched South Atlantic mantle (SAM-E with slightly higher Sr and Pb and lower Nd isotope ratios). These end-members were constrained using BA basalts largely free of slab influence, but Hf isotope ratios in the TSVZ BA are systematically lower relative to Nd isotopes than in the VA. The same traits also characterize the CSVZ. We conclude that the mantle wedge beneath the CSVZ VA is also heterogeneous isotopically and similar to the TSVZ VA, despite being primarily more depleted in the most incompatible trace elements. In addition to having lower Hf isotope ratios than in the VA, the mantle beneath the CSVZ BA also includes a component with higher $\Delta 7/4\text{Pb}$ and $\Delta 8/4\text{Pb}$ than seen further north, as discussed in Section 5.3.

3.5.4.2 Subducting altered oceanic crust (AOC)

The oceanic crust currently subducting beneath both the TSVZ and CSVZ probably formed at the EPR. However, the age of subducting crust is ambiguous south of the Valdiva fracture zone and might have formed at the Chile Ridge (Herron et al., 1981; Tebbens and Cande, 1997; Tebbens et al., 1997).

MORB forming now at the northern Chile Ridge is similar to EPR MORB but with higher $\Delta 7/4\text{Pb}$ (Bach et al., 1996). However, crust of this type is not yet subducting. In contrast, MORB forming now at the southern Chile Ridge is isotopically enriched (Klein and Karsten, 1995; Sturm et al., 1999), is part of the global DUPAL anomaly, and is similar to Southern Atlantic enriched mantle (SAM-E). It may reflect flow of such mantle through the slab window associated with

the subduction of the Chile Ridge. This enriched crust may be subducting beneath the southernmost part of the CSVZ, i.e. Apagado and Chaitén.

Subduction of isotopically enriched AOC cannot explain the differences between the TSVZ and CSVZ because the CSVZ is characterized by more depleted Nd isotopes, not more enriched. Indeed, the southernmost CSVZ volcanoes, beneath which enriched AOC is most likely to be subducting, are characterized by the most depleted isotopes (i.e. Apagado).

3.5.4.3 Subducting sediment

The trench sediments are generally similar in composition along strike, but there is a slight increase in average $^{87}\text{Sr}/^{86}\text{Sr}$ and Ce/Pb, and decrease in average $^{143}\text{Nd}/^{144}\text{Nd}$ and Ba/La southward due to more continent-derived material supplied by greater erosion in this region of the Andes (Lucassen et al., 2010; Plank, 2011). Although the $^{87}\text{Sr}/^{86}\text{Sr}$ of the CSVZ stratovolcanoes is slightly higher than in the TSVZ stratovolcanoes, the $^{143}\text{Nd}/^{144}\text{Nd}$ is similar and Ba/La is higher, not lower. Moreover, a difference in sediment composition cannot explain the shift to lower $\delta^{18}\text{O}(\text{melt})$ of the CSVZ samples compared to the TSVZ samples, because the trench sediments have high $\delta^{18}\text{O}$ (Jacques et al., 2013).

3.5.5 Difference in slab surface temperature beneath the Volcanic Front

The slab surface temperature beneath the CSVZ should be slightly hotter than beneath the TSVZ because the slab is younger to the south yet the depth to the slab beneath the VA is similar (van Keken et al., 2011). A hotter slab would be more likely to melt, and melts could more readily transport fluid-immobile elements such as Nb, Ta, Hf and Zr. However, the CSVZ samples have lower ratios of these elements to HREE (e.g. Figure 6) than in the TSVZ, which can either indicate higher degrees of mantle melting, greater source depletion through melt extraction or a lower slab-melt flux. The inverse correlation of Nb/Yb with Nd isotopes, mentioned above, suggests that differences in degree of melting alone do not govern the variations in HFSE/HREE ratios. The numerical model presented in Section 5.7 evaluated the

effects of different slab surface temperatures and found them to be insignificant. Therefore, the difference in slab surface temperature does not explain the differences between the TSVZ and CSVZ.

3.5.6 Differences in the amount of slab serpentinization

There are numerous fracture zones, including the large Valdivia and Chiloé fracture zones, on the incoming Nazca Plate outboard of the CSVZ (Figure 1). These two major fracture zones, if projected beneath the CSVZ, are located beneath Villarrica (believed to be one of South America's most active volcano) at $\sim 39^{\circ}\text{S}$ and Puyehue and Casablanca at $\sim 41^{\circ}\text{S}$ (e.g. Dzierma et al., 2012). There are also numerous bend-faults on the outer rise of the Nazca Plate, although largely buried by sediments outboard of the CSVZ (Ranero et al., 2005; Ranero et al., 2006, Contreras-Reyes et al., 2007). These fracture zones and bend-faults provide pathways for water to enter and hydrothermally alter the lower crust and to serpentinize the upper mantle (e.g. Ranero et al., 2003; Rüpke et al., 2002, 2004; Grevemeyer et al., 2007; Contreras Reyes et al., 2007). The abundance and extent of both fracture zones and bend-faults (which can be identified west of the trench in Figure 1 despite greater sediment cover) are greater outboard of the CSVZ than the TSVZ and therefore it is likely that the plate outboard of the CSVZ has been more extensively hydrated (Dzierma et al., 2012). In consequence of the greater hydration, larger amounts of water are available for being released and added to the mantle wedge beneath the CSVZ compared to the TSVZ.

Local earthquake tomography shows a low velocity anomaly and high V_p/V_s values beneath the CSVZ forearc between 39° - 40°S (Dzierma et al., 2012). These features are consistent with serpentinization and/or underthrusting of forearc material such as sediments. The same velocity anomaly and V_p/V_s values were observed along the projected Valdivia fracture zone further east, extending beneath the VA at Villarrica. These observations are evidence of high fluid flux at Villarrica in particular, and other CSVZ stratovolcanoes in general, and it seems likely to be related to the subduction of more fracture zones and bend-faults beneath the CSVZ than the TSVZ.

In summary, based on geophysical, morphological and geochemical data, we attribute the differences between the TSVZ versus CSVZ VA to higher slab-derived fluid flux in the CSVZ that coincides with the presence of large fractures zones and more extensive bend-faulting on the incoming plate that can hydrate the subducting lower crust and underlying upper mantle. Highly serpentinized mafic and ultramafic portions of the slab may form a larger water reservoir that can be released to the mantle wedge beneath the volcanic front resulting in higher degrees of mantle melting. The higher magma flux, higher ratios of fluid-mobile to other trace elements, $^{87}\text{Sr}/^{86}\text{Sr}$, $^{143}\text{Nd}/^{144}\text{Nd}$ and $^{177}\text{Hf}/^{176}\text{Hf}$ ratios in the CSVZ relative to the TSVZ are consistent with this simple tectonic difference along strike of the incoming plate outboard the arc.

3.5.7 Quantitative flux melting model

We quantified our arguments by using the Arc Basalt Simulator version 3.10 of Kimura et al. (2009, 2010). This approach was successfully applied to the TSVZ segment (Jacques et al., 2013) to which we make comparison. The model predicts that TSVZ basalts are produced by a slab melt derived from 60% trench sediments and 40 % AOC. Addition of a few percent of this slab component to an enriched heterogeneous mantle wedge causes ca. 1% melting of the mantle.

We assumed the same sediment composition (sample 75Kd(1) from Lucassen et al., 2010; Table 3) for the CSVZ as for the TSVZ, because this sample was taken offshore of the CSVZ (Figure 1b). Its composition is close to the average of Plank (2011) at 40°S, and it has the most radiogenic Pb. Choosing sediment with even more radiogenic Sr has little effect on our results. We also assumed the same AOC values that are from ODP site 1149 in the western Pacific (Tollstrup et al., 2010; Table 3), even though the AOC beneath the CSVZ is younger and probably less altered than for the TSVZ. Using southern Chile Ridge instead of EPR basalt for AOC does not affect our results, because 30% sediment swamps the AOC trace element composition.

Table 3.2 Sediment (SED), altered oceanic crust (AOC) and depleted MORB Mantle (DMM) compositions used for the Arc Basalt Simulator 3 calculations. (*) See Table 3 for values used in calculation of the slab melt composition.

	AOC	SED	Slab melt <i>30SED:70AOC(*)</i>	DMM
Rb	13.7	44.7	26.4	0.050
Ba	15.6	1238	525	0.563
Th	0.173	5.70	2.87	0.008
U	0.390	3.21	2.21	0.003
Nb	2.89	4.63	0.879	0.149
Ta	0.210	0.350	0.067	0.010
K	5147	17483	10267	80.0
La	3.40	13.5	9.18	0.192
Ce	11.4	32.4	27.8	0.550
Pb	0.437	17.5	8.44	0.018
Pr	2.06	3.93	4.62	0.107
Sr	109	257	187	7.66
Nd	11.3	16.3	21.4	0.581
Sm	3.95	3.65	3.72	0.239
Zr	112	123	90.1	5.08
Hf	3.00	3.40	2.50	0.157
Eu	1.34	0.905	0.892	0.096
Gd	5.55	3.51	2.23	0.358
Tb	1.01	0.547	0.228	0.070
Dy	6.56	3.32	1.03	0.505
Y	40.7	18.1	4.31	2.66
Ho	1.43	0.674	0.152	0.115
Er	4.09	1.88	0.418	0.348
Tm	4.02	0.290	0.268	0.055
Yb	0.636	1.97	0.087	0.365
Lu	3.07	0.298	0.145	0.058
$^{87}\text{Sr}/^{86}\text{Sr}$	0.704769	0.705637	0.705318	0.703700
$^{143}\text{Nd}/^{144}\text{Nd}$	0.513153	0.512673	0.513066	0.512820
$^{206}\text{Pb}/^{204}\text{Pb}$	18.54	18.71	18.71	18.15
$^{207}\text{Pb}/^{204}\text{Pb}$	15.45	15.63	15.63	15.54
$^{208}\text{Pb}/^{204}\text{Pb}$	37.70	38.65	38.63	38.00

For the mantle wedge, we again used the DMM trace element composition from Workman and Hart (2005) and the isotopic compositions of Jacques et al. (2013) (SAM-D and SAM-E) plus one in between that is close to the cinder cone values (Table 3). We assume that these compositions represent the least slab-contaminated mantle wedge beneath the CSVZ. Even though we argued above that the mantle wedge beneath the CSVZ may be more depleted in trace elements than the TSVZ (Section 5.4.1), the model does not require more depleted DMM concentrations. Likewise, the model does not require mantle sources more enriched than SAM-E, such as found in the TSVZ and CSVZ BA. We infer that such components are melted out in the backarc prior to advection beneath the arc itself.

We modeled sample CL 170 from Villarrica which is our most mafic sample from the CSVZ with MgO = 7.4 wt. %. The most satisfactory results were obtained when adding a slab melt to DMM from a source that is 30% sediment and 70% AOC. We assumed formation of the slab component directly beneath the CSVZ stratovolcanoes (130 km; ~3.9 GPa) at the slab surface temperature calculated for the CSVZ by van Keken et al. (2011). We then adjusted the P-T conditions of mantle melting to best match the trace element pattern and isotopic composition of basalt produced by addition of the slab-derived melt. The best match is obtained for mantle melting at 1.9 GPa and 1230°C. For trace element concentrations, the best match requires addition of 2 to 6% slab component, whereas for isotopes less than 2% slab component is needed. This inconsistency probably reflects limitations of ABS3.10 (e.g., the assumption that sediment and AOC melt equally), uncertainties in trace element partition coefficients, and especially the role of accessory phases. Adding < 2 to 6% slab component causes < 1-5% mantle melting under these conditions, and the resulting primitive basalts contain about 3-4 wt. % water. The amount of slab component added to the mantle beneath the CSVZ is higher than beneath the TSVZ where only up to 2-3% slab component is needed to explain the TSVZ basalts.

We also modeled the monogenetic cinder cones (samples CL 017 and CL 088) with MgO = 5-7 wt. %. Unlike the stratovolcano samples, the P-T conditions of mantle melting to match the trace elements differ significantly. Mantle melting occurs at 1.9-2.0 GPa and 1270-1280°C, which is similar to the P-T conditions at the TSVZ (Jacques et al., 2013). For CL 017, only 1% of

slab component is needed to best match the trace element concentrations, while 3% slab component are needed for CL 088. Therefore, the degree of mantle melting under these conditions varies from 1% to 3.5%, and the resulting basalts contain only ca. 2 wt. % water, respectively. The monogenetic cinder cones require the least amount of slab component. This is consistent with their inferred lower degree of melting (e.g. higher La/Yb), lower fluid flux (e.g. lower U/Th) and lower amount of slab component (lower Sr and Nd isotope ratios), which produce smaller magma volumes than in the surrounding stratovolcanoes. However, we note inconsistent results to match La, Ce, Sr, Zr and Hf, and to lesser extent, U and Y, where the resulting basalts have lower concentrations than the target basalts. Yet, the overall modelling is robust and clearly supports the geochemical observations made in the previous sections.

Figure 13 shows the model results for Sr-Nd and Sr-Pb isotopes. The central mixing line goes through the Llama and Villarrica samples. The Osorno, Mocho and Minchinmávida-Chaitén samples, which have higher Sr isotopes, and the Apagado sample, which is the most depleted, are bracketed by the mixing lines to the SAM-E and SAM-D mantle wedge components, respectively. The Apagado sample is the closest sample to the SAM-D component, which agrees with its depleted trace element and isotope ratios.

We will now compare our model results for the CSVZ to the results for the TSVZ using the same approach (Jacques et al., 2013). The pressure and temperature of the slab surface beneath the CSVZ (3.9 GPa, 845°C) differs only slightly from the TSVZ (4 GPa, 830°C). The modal mineralogy of AOC and sediment at these P-T conditions (van Keken et al., 2011) is relatively similar for both segments, but no phengite is left in the AOC beneath the CSVZ (Table 4) which increases trace element bulk partition coefficients and decreases Pb/Nd fractionation. This indicates that dehydration of the mafic part of the slab is more complete beneath the CSVZ volcanic front even though the slab reaches higher P (but lower T) beneath the TSVZ. The ABS model predicts that most fluid is lost from the sediment and AOC beneath the CSVZ forearc, and that serpentine dehydration is the primary source of fluid beneath the CSVZ volcanic front. Unfortunately, ABS3.10 does not include the sequential effects of dehydration in all layers of the slab or residual accessory minerals besides rutile.

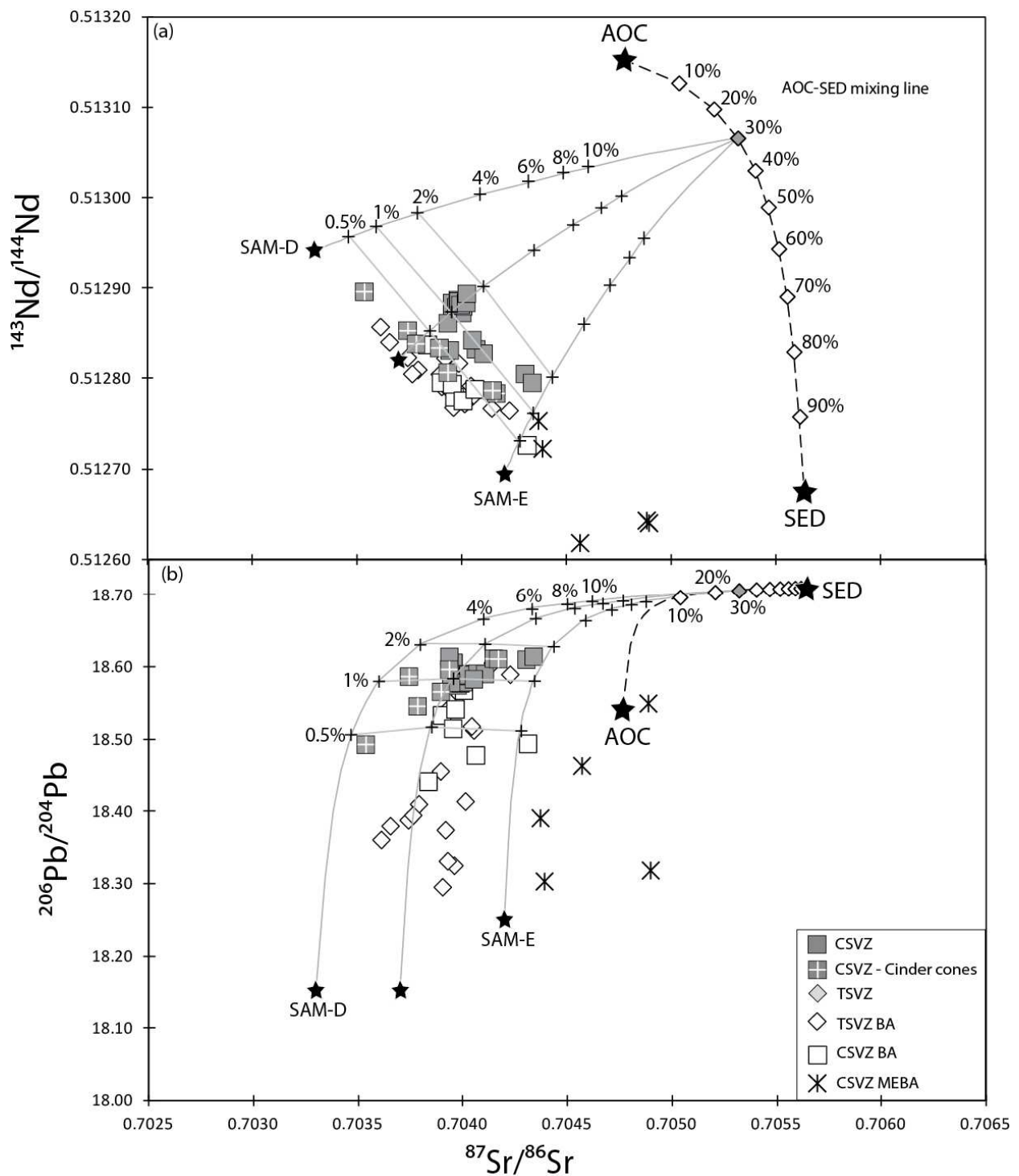


Figure 3.13 $^{87}\text{Sr}/^{86}\text{Sr}$ versus (a) $^{143}\text{Nd}/^{144}\text{Nd}$ and (b) $^{206}\text{Pb}/^{204}\text{Pb}$. The mixing lines show results from a forward mass balance model using the Arc Basalt Simulator 3.10 as explained in the text using the values summarized in Table 2. The dashed line represents mixing between altered oceanic crust (AOC) and sediment (SED). The thin lines represent mixing between an 22% melt of a 30:70 SED:AOC source on the one hand, and depleted (SAM-D) or enriched (SAM-E) mantle (the two stars) on the other. An intermediate mantle close to value for the cinder cones was also used (the unlabeled star). The labeled tick marks show the amount of slab component added to the mantle. Slab and mantle melting conditions are described in the text. Partition coefficients and melting modes for the slab and mantle are from Kimura et al. (2010) and given in Table 3.

The phase diagrams used by ABS for AOC and sediment (from Hermann and Spandler, 2008) predict 22% water-saturated slab melting beneath the CSVZ versus 18% in the TSVZ (Jacques et al., 2013). Our conclusion that both sediment and AOC melt beneath the CSVZ volcanic front is consistent with the thermal model of van Keken et al. (2011) in which the temperature in the top several km of the slab exceeds the water-saturated solidi of both sediment and basalt. The slightly higher degree of slab melting beneath the CSVZ might also be caused by more serpentine-derived fluid, which increases slab melting. Our model differs slightly from the conclusion of Watt et al. (2013) that slab melting only occurs behind the volcanic front at Apagado, but the small mass fraction of slab component that we infer for Apagado renders the distinction moot. The elevated Th/Yb ratios in all volcanic arc samples (Figure 6) are consistent with the slab component being a melt. Moreover, slab melting increases the potential to carry relatively fluid-immobile elements such as Nd and Hf. This, plus the higher %AOC in our CSVZ slab component, is consistent with the CSVZ stratovolcanoes having higher Nd and Hf isotope ratios compared to the TSVZ. The serpentine-derived fluid is also probably the source of excess U over Th observed in most CSVZ stratovolcanoes.

Our models predict 1.6-5.5% mantle melting at 2.1 GPa and 1270°C for the TSVZ (Jacques et al., 2013), versus 1.0-1.2% melting at 1.9 GPa and 1240°C for the CSVZ. The lower degree of melting beneath the CSVZ contradicts our conclusion based on Figure 6. CSVZ stratovolcanoes have lower Nb/Yb and Th/Yb which indicate higher degrees of mantle melting if the source is homogeneous. However, if the slab component in the CSVZ has more fluid (e.g., water from serpentine dehydration), then we predict more mantle melting beneath the CSVZ even at lower depth and temperature. The line in Figure 6 merely shows the isobaric effect of increasing temperature and not also increasing the percent of slab component or X_{H_2O} in that component.

Table 3.3 Mixing and results parameters from the Arc Basalt Simulator 3. AOC = Altered Oceanic Crust, SED = Sediment.

			Sr	Nd	Pb	
Slab	P (Gpa)	3.9				
	T (°C)	844				
AOC	Melting (%)	22				
	Xgar	46.7				
	Xcpx	43.8				
	Xphen	0.00				
	Xrut	1.31				
	Bulk D		0.020	0.326	0.019	
	Melting (%)	22				
SED	Xgar	26.1				
	Xcpx	16.7				
	Xphen	27.8				
	Xrut	0.84				
	Bulk D		0.389	1.57	0.287	
	Mantle	P (Gpa)	1.9			
	T (°C)	1240				
Slab component added (%)	2.0-6.0					
Mantle melting (%)	1.6-5.5					
	Bulk D		0.020	0.026	0.015	

3.6 Conclusions

We used trace element and Sr-Nd-Hf-Pb-O isotope data to compare and contrast monogenetic cinder cones and stratovolcanoes from the CSVZ (38-43°S), the CSVZ VA and BA, and the CSVZ and the TSVZ (34.5-38°S) segments. The CSVZ BA is similar to that of the TSVZ but contains an additional enriched component in some areas, either in the lithosphere or in the asthenospheric mantle wedge. Compared to the CSVZ cinder cones and TSVZ, the CSVZ stratovolcanoes have greater highly fluid-mobile to less fluid-mobile trace element ratios (such as U/Th, Pb/Ce, Ba/Nb), lower incompatible to less incompatible trace element ratios (such as La/Yb), lower $\delta^{18}\text{O}(\text{melt})$, and higher Nd and Hf isotopes. The cinder cones differ from the stratovolcanoes by having less of a slab-derived component in their source resulting in smaller degrees of melting. The combined morphological, geophysical and geochemical data suggest an enhanced fluid flux beneath the CSVZ stratovolcanoes, as compared to the TSVZ volcanoes,

resulting in greater magma production, reflected in increased eruption rates in the past and the present in the CSVZ.

No clear evidence for assimilation, fractionation and crystallisation (AFC) processes was found in our samples, as was proposed by Jicha et al. (2007) and Reubi et al. (2011) in Puyehue and Llaima volcano, respectively. Our geochemical data indicate that the processes are subcrustal and come primarily from the slab. However, the along-strike variations are not related to changes in the subducting AOC or sediments.

Instead, we favor a fluid enrichment of the CSVZ mantle wedge by fluids from the incoming Nazca plate. It is likely that the lower oceanic crust has been hydrothermally altered and the underlying upper mantle has been serpentinized due to the deep introduction of seawater via large and abundant fracture zones and faults related to the bending of the plate outboard the trench. This scenario is in agreement with geophysical observations of a low velocity zone along fracture zones (Dzierma et al., 2012), which is interpreted to reflect more abundant serpentine in the mantle wedge beneath the CSVZ forearc extending beneath Villarrica Volcano. The quantitative mass balance model we provided here also supports the geochemical observations. Trace element patterns and Sr-Nd-Pb isotopes are best modelled by adding < 2 to 6% of a slab melt derived from a 30:70 sediment:AOC source. Addition of a few percent of this slab component causes 1.0-1.2% melting of the mantle at about 1.9 GPa and 1240°C.

Acknowledgment

F. and S. Hauff are greatly thanked for their help with the isotopic analyses. We would like to thank P. van den Bogaard, L. Lara, J. Clavero and SERNAGEOMIN for their support with the field studies. This paper is contribution No. 268 of Collaborative Research Center (Sonderforschungsbereich) SFB574 "Volatiles and Fluids in subduction Zones" at Kiel University, funded by the German Research Foundation. JG's contribution to this paper was supported by an Alexander von Humboldt Research Prize. Ilya N. Bindeman acknowledges NSF grants EAR-0844772 and EAR-0948455.

Appendix

Supplementary Table 3.1 Major (wt. %) and trace elements ($\mu\text{g/g}$) for the Central Southern Volcanic Zone Volcanic Arc of Chile and the Backarc in Argentina. (a) and (b) data are from Wehrmann et al. (accepted, 2013a) and (in revision b), respectively, and are included here to give readers complete analyses. N.d. = not determined. Total Fe expressed as FeO. (#) Original sum retained

Sample number	Sample Location	Country	Sample type	Lat (S)	Long (W)	Age (estimate)	reference
Volcanic Arc							
CL 045(a)	Lonquimay	Chile	Lava	-38.36	-71.53	Holocene	Stern (2004)
CL 049(a)	Lonquimay	Chile	Lava	-38.34	-71.51	Holocene	Stern (2004)
CL 029(a)	Llaima	Chile	Tephra	-38.75	-71.62	Holocene	Stern (2004)
CL 032(a)	Llaima	Chile	Tephra	-38.75	-71.62	Holocene	Stern (2004)
CL 034(a)	Llaima	Chile	Tephra	-38.75	-71.62	Holocene	Stern (2004)
CL 035(b)	Llaima	Chile	Tephra	-38.75	-71.62	Holocene	Stern (2004)
CL 036(b)	Llaima	Chile	Tephra	-38.75	-71.62	Holocene	Stern (2004)
CL 001(b)	Villarrica	Chile	Tephra	-39.35	-71.97	Holocene	Stern (2004)
CL 006(a)	Villarrica	Chile	Tephra	-39.38	-71.97	Holocene	Stern (2004)
CL 010(a)	Villarrica	Chile	Tephra	-39.31	-71.98	Holocene	Stern (2004)
CL 166	Villarrica	Chile	Lava	-39.39	-71.95	Holocene	Stern (2004)
CL 170(b)	Villarrica	Chile	Tephra	-39.40	-71.95	Holocene	Stern (2004)
CL 017(a)*	Huillemolle	Chile	Lava	-39.27	-71.81	Holocene	Stern (2004)
CL 022(a)*	Caburga	Chile	Tephra	-39.20	-71.82	Holocene	Stern (2004)
CL 159(a)	Mocho	Chile	Lava	-39.93	-72.00	Holocene	Stern (2004)
CL 161(b)	Mocho	Chile	Tephra	-39.93	-72.00	Holocene	Stern (2004)
CL 109(a)	Casablanca	Chile	Lava	-40.78	-72.19	Holocene	Stern (2004)
CL 701	Casablanca	Chile	Tephra	-40.71	-72.95	Holocene	Stern (2004)
CL 088(a)*	Cabeza de Vaca	Chile	Bomb	-41.30	-72.27	Holocene	Stern (2004)
CL 098(a)	Osorno	Chile	Tephra	-41.14	-72.53	Holocene	Stern (2004)
CL 102(a)	Osorno	Chile	Tephra	-41.15	-72.52	Holocene	Stern (2004)
CL 714*	Apagado	Chile	Tephra	-41.87	-72.95	Holocene	Stern (2004)
CL 443(a)*	Chaiten	Chile	Bomb	-42.93	-72.60	Holocene	Stern (2004)
CL 486(a)*	Chaiten	Chile	Lava	-42.72	-72.60	Holocene	Stern (2004)
CL 490(a)*	Chaiten	Chile	Lava	-42.73	-72.60	Holocene	Stern (2004)
Backarc							
CL 425	old plateau basalt	Argentina	Lava	-38.30	-70.61	Holocene to Pliocene	Kay et al. (2004)
CL 426	Rd to Pino Hachado	Argentina	Lava	-38.65	-70.78	Holocene to Pliocene	Kay et al. (2004)
CL 430	old plateau basalt	Argentina	Lava	-39.98	-70.78	Holocene to Pliocene	Kay et al. (2004)
CL 475 b	around Laguna Blanca	Argentina	Lava	-39.11	-70.31	Holocene to Pliocene	Kay et al. (2004)
CL 481	Cerro Horqueta	Argentina	Lava	-39.99	-70.75	Holocene to Pliocene	Kay et al. (2004)
CL 482	older plateau	Argentina	Lava	-41.45	-70.67	Holocene to Pliocene	Kay et al. (2004)
CL 433	Jacobacci Volcanic Field	Argentina	Lava	-41.77	-70.14	Holocene to Pliocene	Kay et al. (2004, 2007)
More-enriched Backarc							
CL 424	old plateau	Argentina	Lava float	-39.16	-69.87	Holocene to Pliocene	Kay et al. (2004)
CL 431	Jacobacci Volcanic Field	Argentina	Lava	-41.04	-70.22	Holocene to Pliocene	Kay et al. (2004, 2007)
CL 432	Jacobacci Volcanic Field	Argentina	Lava	-41.37	-69.80	Holocene to Pliocene	Kay et al. (2004, 2007)
CL 434	Crater Basalt Volcanic Field	Argentina	Lava	-42.14	-70.05	300-600 ka	Pécskay et al. (2007)
CL 437	Crater Basalt Volcanic Field	Argentina	Lava	-42.07	-70.21	300-600 ka	Pécskay et al. (2007)

* cinder cones

Supplementary Table 3.1 (Continued)

Sample number	Method	SiO ₂ (wt. %)	TiO ₂ (wt. %)	Al ₂ O ₃ (wt. %)	FeO _t (wt. %)	MnO (wt. %)	MgO (wt. %)	CaO (wt. %)	Na ₂ O (wt. %)	K ₂ O (wt. %)	P ₂ O ₅ (wt. %)	L.O.I	Sum(#)
Volcanic Arc													
CL 045(a)	XRF	61.42	0.75	16.10	8.65	0.23	1.10	4.25	5.92	2.19	0.29	0.17	99.55
CL 049(a)	XRF	58.21	1.16	16.50	6.67	0.22	2.03	5.36	5.35	1.03	0.46	0.15	99.95
CL 029(a)	XRF	56.61	1.23	16.22	10.26	0.18	3.25	6.80	4.33	0.85	0.25	0.44	99.53
CL 032(a)	XRF	52.36	0.92	21.06	8.15	0.13	3.14	10.35	3.19	0.53	0.16	0.64	99.55
CL 034(a)	XRF	54.62	1.43	15.95	11.39	0.18	3.87	7.58	3.76	0.94	0.27	0.44	99.71
CL 035(b)	XRF	51.31	1.17	17.44	11.25	0.17	5.58	9.01	3.32	0.55	0.20	0.88	99.90
CL 036(b)	XRF	54.60	1.06	17.05	9.74	0.15	4.41	8.39	3.48	0.93	0.20	0.52	99.38
CL 001(b)	XRF	53.01	1.00	18.85	9.07	0.15	4.02	9.75	3.32	0.63	0.19	0.39	99.73
CL 006(a)	XRF	53.39	1.08	17.20	10.04	0.18	4.58	9.23	3.46	0.66	0.19	0.42	100.20
CL 010(a)	XRF	55.06	1.18	16.56	10.22	0.16	3.92	8.10	3.79	0.81	0.21	0.42	100.30
CL 166	XRF	51.38	0.89	18.64	8.73	0.13	6.27	10.21	3.06	0.62	0.16	0.25	100.29
CL 170(b)	XRF	51.44	1.18	15.90	10.83	0.16	7.36	9.37	2.92	0.64	0.23	0.25	100.14
CL 017(a)*	XRF	50.82	1.12	18.21	9.88	0.16	5.76	9.54	3.36	0.78	0.39	0.53	100.35
CL 022(a)*	XRF	50.09	1.22	19.32	10.36	0.16	5.70	8.72	3.41	0.68	0.33	1.68	98.71
CL 159(a)	XRF	52.07	1.05	18.27	9.49	0.15	5.25	9.38	3.10	0.75	0.19	0.29	100.31
CL 161(b)	XRF	55.85	1.30	16.29	9.03	0.15	4.49	7.98	3.74	0.90	0.21	n.d	100.10
CL 109(a)	XRF	51.04	0.89	18.24	9.61	0.15	6.40	10.01	2.98	0.54	0.14	0.22	99.79
CL 701	XRF	53.60	1.10	18.05	9.60	0.16	3.93	8.25	3.64	0.89	0.25	0.82	100.17
CL 088(a)*	XRF	51.62	0.84	17.62	9.11	0.15	7.27	9.67	2.81	0.68	0.22	0.32	99.44
CL 098(a)	XRF	52.24	0.90	18.86	9.44	0.15	4.83	9.97	2.98	0.49	0.14	n.d	99.80
CL 102(a)	XRF	51.63	0.84	20.95	8.23	0.13	3.79	10.84	3.01	0.45	0.13	n.d	99.79
CL 714*	EMP	56.24	1.54	16.06	8.55	0.14	3.46	9.20	3.35	1.18	0.28		
CL 443(a)*	XRF	51.28	1.25	17.84	9.51	0.15	5.52	9.76	3.52	0.84	0.31	0.20	99.85
CL 486(a)*	XRF	49.81	1.32	16.91	11.30	0.17	7.37	9.20	2.99	0.65	0.28	0.34	98.82
CL 490(a)*	XRF	50.03	1.30	17.00	11.10	0.17	7.09	9.30	3.04	0.69	0.28	0.17	99.85
Backarc													
CL 425	XRF	49.35	1.44	16.83	10.22	0.16	7.74	8.97	3.54	1.25	0.33	0.02	98.94
CL 426	XRF	56.68	1.34	18.08	6.95	0.14	2.49	5.74	5.23	2.69	0.46	1.69	97.29
CL 430	XRF	47.19	1.71	16.06	11.39	0.18	8.37	9.22	3.63	1.50	0.49	0.00	99.19
CL 475 b	XRF	50.69	1.59	17.33	9.45	0.15	6.47	8.08	3.93	1.62	0.47	0.00	99.23
CL 481	XRF	48.84	1.77	16.92	11.16	0.16	6.22	9.49	3.82	1.14	0.32	0.00	99.47
CL 482	XRF	47.32	1.73	16.30	11.21	0.16	8.22	8.67	3.78	1.94	0.47	0.22	100.63
CL 433	XRF	47.86	1.55	16.04	11.33	0.16	8.78	9.37	3.30	1.12	0.29	0.30	98.96
More-enriched Backarc													
CL 424	XRF	53.59	1.98	15.11	10.21	0.13	5.91	8.21	3.65	0.75	0.30	0.25	98.99
CL 431	XRF	47.85	1.98	16.23	11.18	0.15	7.56	9.20	3.98	1.31	0.36	0.00	99.30
CL 432	XRF	52.44	2.83	15.32	11.33	0.17	3.98	7.70	3.88	1.54	0.61	1.27	97.60
CL 434	XRF	48.77	1.74	15.45	11.98	0.15	8.28	8.05	3.76	1.26	0.38	0.18	100.32
CL 437	XRF	48.53	1.92	16.42	10.92	0.14	6.90	9.30	3.67	1.56	0.42	0.33	99.04
Standards													
BHVO	XRF	49.95	2.76	13.63	12.25	0.17	7.41	11.46	2.31	0.51	0.26		100.71
JA-2	XRF	56.23	0.67	15.47	6.39	0.11	8.00	6.27	3.12	1.76	0.15		98.17

* cinder cones

Supplementary Table 3.1 (Continued)

Sample number	Li	Sc	V	Cr	Co	Ni	Cu	Zn	Ga	Rb	Sr	Y	Zr	Nb	Cs	Ba	La	Ce	Pr	Nd	Sm	Eu	Gd	Tb	Dy	Ho	Er	Tm	Yb	Lu	Hf	Ta	Ti	Pb	Th	U		
	µg/g	µg/g	µg/g	µg/g	µg/g	µg/g	µg/g	µg/g	µg/g	µg/g	µg/g	µg/g	µg/g	µg/g	µg/g	µg/g	µg/g	µg/g	µg/g	µg/g	µg/g	µg/g	µg/g	µg/g	µg/g	µg/g	µg/g	µg/g	µg/g	µg/g	µg/g	µg/g	µg/g	µg/g	µg/g	µg/g	µg/g	
Volcanic Arc																																						
CL 045(a)	22.1	26.1	n.d.	n.d.	n.d.	n.d.	20.3	n.d.	n.d.	27.6	40.3	39.3	155	3.28	2.83	402	16.9	40.9	5.83	26.9	6.84	2.07	7.12	1.14	7.14	1.47	4.08	0.619	4.17	0.629	4.27	0.201	n.d.	15.6	3.26	1.06		
CL 049(a)	18.9	27.5	n.d.	n.d.	n.d.	19.4	n.d.	n.d.	n.d.	22.1	47.6	35.4	125	2.82	2.26	349	15.1	36.9	5.35	25.2	6.48	2.04	6.79	1.07	6.58	1.34	3.67	0.542	3.61	0.542	3.46	0.175	n.d.	12.8	2.79	0.900		
CL 029(b)	14.4	39.2	241	16.5	23.1	82.6	93.4	99.0	22.6	17.3	42.5	29.0	107	2.78	1.50	259	10.3	24.6	3.55	16.3	4.22	1.36	4.61	0.748	4.75	0.989	2.79	0.416	2.79	0.428	2.79	0.170	0.102	9.14	1.50	0.542		
CL 032(a)	8.63	32.7	207	46.8	20.4	14.7	77.9	66.3	21.8	10.1	51.2	18.6	64.0	1.59	0.614	166	6.31	15.2	2.23	10.3	2.75	0.962	3.02	0.450	3.08	0.644	1.80	0.269	1.80	0.273	1.75	0.106	0.072	5.80	0.995	0.336		
CL 034(a)	13.34	35.7	306	32.3	26.2	11.8	117	102	193	20.0	414	29.0	115	2.76	1.62	269	11.1	27.0	3.89	18.1	4.75	1.41	5.16	0.844	5.31	1.11	3.10	0.464	3.12	0.473	3.21	0.181	0.132	10.0	2.04	0.693		
CL 035(b)	9.48	34.5	281	83.5	33.4	37.9	106	88.5	183	10.5	449	20.7	75.6	1.80	0.924	183	7.35	17.9	2.63	12.6	3.38	1.12	3.69	0.604	3.84	0.799	2.23	0.332	2.21	0.333	2.10	0.119	0.073	6.59	1.09	0.394		
CL 036(b)	11.7	31.8	241	65.0	26.8	19.8	95.8	81.1	178	22.2	453	21.0	87.8	2.24	1.31	256	9.54	22.0	3.38	35.1	11.1	3.11	3.78	0.614	3.83	0.803	2.23	0.337	2.26	0.345	2.50	0.160	0.133	8.31	2.56	0.782		
CL 001(b)	10.2	37.8	242	50.1	26.3	22.9	103	79.5	21.6	15.1	466	21.8	81.7	1.72	1.44	186	7.11	17.2	2.52	11.8	3.11	0.989	3.41	0.556	3.55	0.742	2.07	0.314	2.07	0.314	2.20	0.107	0.075	6.91	1.33	0.454		
CL 006(a)	9.88	33.9	282	55.6	30.5	22.3	105	85.2	182	15.0	450	21.2	82.4	1.78	1.40	196	7.72	19.8	2.74	12.9	3.38	1.08	3.70	0.614	3.88	0.811	2.28	0.342	2.28	0.346	2.36	0.117	0.106	7.10	1.56	0.494		
CL 010(a)	13.2	39.9	276	30.7	26.2	13.8	62.6	91.1	21.7	19.5	428	26.0	102	2.17	1.88	229	8.75	21.2	3.08	14.3	3.74	1.16	4.14	0.674	4.27	0.897	2.48	0.382	2.52	0.385	2.76	0.145	0.067	8.49	1.73	0.577		
CL 166	5.80	32.8	248	231	32.1	83.1	94.3	67.2	20.3	10.0	618	16.0	59.3	1.33	0.820	186	7.18	16.6	2.38	10.8	2.75	0.927	2.85	0.443	2.73	0.559	1.54	0.228	1.50	0.225	1.55	0.091	0.055	8.65	2.61	0.896		
CL 170(b)	11.3	43.2	281	380	38.7	112	133	85.6	19.6	15.4	397	25.0	93.2	2.00	1.65	190	7.99	19.6	2.91	13.7	3.65	1.11	3.99	0.655	4.14	0.869	2.48	0.360	2.38	0.356	2.54	0.129	0.044	7.54	1.30	0.464		
CL 017(a)*	9.85	34.5	210	97.6	33.5	43.2	80.4	82.7	21.2	12.8	635	23.8	139	5.11	0.665	291	19.1	42.2	5.55	23.0	4.82	1.43	4.64	0.665	3.98	0.802	2.18	0.321	2.14	0.317	2.98	0.327	0.064	8.69	1.87	0.568		
CL 022(a)*	8.81	27.5	242	34.6	30.6	26.6	61.5	84.3	18.6	8.37	698	20.0	92.9	3.14	0.444	232	13.3	30.0	4.32	19.2	4.33	1.37	4.15	0.622	3.74	0.762	2.08	0.307	2.04	0.309	2.43	0.186	0.061	6.70	2.16	0.580		
CL 159(b)	7.28	27.4	253	79.2	30.8	39.0	79.0	76.9	18.8	11.7	455	19.4	84.8	2.03	0.601	234	8.84	21.3	2.97	13.7	3.53	1.08	3.76	0.596	3.72	0.763	2.09	0.310	2.04	0.303	2.42	0.126	n.d.	7.15	1.74	0.551		
CL 109(a)	7.05	28.2	243	108	35.4	59.7	82.9	74.2	17.0	8.61	423	13.9	59.4	1.68	0.361	154	6.34	15.3	2.07	9.43	2.43	0.852	2.62	0.422	2.66	0.548	1.51	0.228	1.51	0.227	1.65	0.109	n.d.	4.62	1.20	0.366		
CL 701	9.80	30.5	247	26.2	24.0	12.5	90.0	80.3	20.1	18.0	559	22.0	111	3.57	0.969	286	13.3	29.9	4.03	17.9	4.12	1.31	3.99	0.618	3.78	0.773	2.14	0.316	2.11	0.329	2.54	0.177	0.056	7.70	2.50	0.707		
CL 088(a)*	7.59	29.6	228	173	31.2	64.0	69.2	70.3	17.0	9.42	562	17.4	81.9	2.61	0.480	179	10.2	24.0	3.31	14.7	3.52	1.12	3.49	0.542	3.30	0.674	1.85	0.273	1.81	0.273	2.18	0.159	0.058	5.99	1.40	0.426		
CL 098(b)	10.1	31.5	250	74.9	26.8	25.2	80.8	77.5	18.4	12.1	360	16.8	57.4	1.62	1.04	141	5.63	13.7	2.00	9.54	2.64	0.919	2.91	0.483	3.07	0.637	1.79	0.267	1.78	0.268	1.73	0.107	0.073	5.17	1.01	0.303		
CL 402(a)	9.25	27.2	223	66.0	21.5	79.4	81.6	68.2	19.2	10.5	387	15.5	55.8	1.57	0.882	128	5.27	12.9	1.89	8.99	2.49	0.879	2.74	0.454	2.89	0.599	1.65	0.247	1.64	0.248	1.66	0.103	0.060	4.98	0.884	0.281		
CL 714*	6.22	31.0	251	444	43.6	195	68.8	73.2	16.1	3.89	450	13.3	58.5	1.86	0.101	95.3	5.21	13.8	2.00	9.33	2.44	0.819	2.52	0.404	2.50	0.513	1.42	0.209	1.42	0.206	1.59	0.107	0.029	3.31	0.857	0.293		
CL 443(a)*	9.81	32.3	250	130	30.8	36.1	44.5	77.7	18.4	17.6	512	28.1	151	5.28	0.727	323	19.7	44.1	5.71	24.39	5.44	1.61	5.43	0.836	5.08	1.03	2.82	0.419	2.76	0.412	3.34	0.372	0.032	4.27	3.45	0.802		
CL 482	9.83	36.5	304	281	40.3	104	38.2	91.0	18.2	12.6	417	27.1	126	5.27	0.608	220	12.8	31.0	4.27	19.26	4.75	1.43	4.96	0.787	4.89	0.996	2.74	0.406	2.69	0.402	2.90	0.309	0.035	4.41	2.18	0.550		
CL 490(a)*	10.24	36.0	294	257	39.2	95.1	55.7	91.6	18.2	15.4	407	26.7	125	5.16	0.689	216	12.5	30.1	4.17	18.62	4.63	1.40	4.83	0.771	4.78	0.982	2.70	0.400	2.66	0.392	2.89	0.306	0.052	5.00	2.16	0.561		
Backarc																																						
CL 425	6.77	29.8	251	300	40.9	129.9	53.7	84.2	19.3	26.2	620	23.0	139	12.93	0.902	269	17.8	39.2	5.20	22.52	5.19	1.65	5.10	0.767	4.44	0.865	2.30	0.335	2.17	0.321	3.17	0.784	0.081	4.21	2.43	0.715		
CL 426	11.72	16.8	152	16	13.7	6.3	25.5	125.7	20.1	37.4	592	23.6	360	18.42	1.179	781	30.2	64.2	8.02	32.17	6.30	2.11	5.63	0.816	4.50	0.875	2.38	0.350	2.36	0.353	5.63	1.045	0.215	8.42	3.96	1.127		
CL 430	7.36	25.0	239	301	45.0	159.1	47.5	116.3	21.7	40.6	822	23.9	182	20.21	1.602	387	25.5	54.5	7.08	30.10	6.58	2.08	6.21	0.897	4.92	0.906	2.32	0.312	2.00	0.288	4.04	1.232	0.197	5.08	3.81	1.026		
CL 475 b	8.92	25.0	227	181	33.5	84.0	32.1	75.1	19.2	28.9	752	24.1	196	16.87	0.494	458	26.3	55.6	7.07	29.32	6.09	1.86	5.67	0.825	4.65	0.894	2.40	0.343	2.25	0.329	4.19	0.940	0.045	5.08	3.68	0.514		
CL 481	7.04	30.3	259	188	41.3	75.0	48.6	96.3	21.5	23.0	552	24.6	155	7.06	0.896	301	16.4	34.7	4.58	20.44	4.87	1.66	5.16	0.806	4.74	0.924	2.44	0.340	2.22	0.322	3.36	0.995	0.098	2.57	2.16	0.610		
CL 482	6.27	24.8	213	277	41.4	144.9	49.4	80.0	18.0	54.9	605	21.8	171	17.02	1.688	274	17.6	38.9	5.12	22.29	5.01	1.63	4.87	0.733	4.22	0.808	2.11	0.299	1.93	0.281	3.75	1.025	0.204	2.82	2.97	0.998		
CL 433	6.19	28.1	223	371	49.1	134.2	51.9	116.9	19.2	22.8	546	21.5	155	11.60	0.330	291	14.7	32.8	4.33	19.04	4.49	1.52	4.61	0.709	4.19	0.805	2.11	0.298	1.90	0.278	3.29	0.691	0.022	1.83	2.89	0.432		
More-enriched Backarc																																						
CL 424	6.74	19.9	219	238	39.2	88.9	33.9	115.6	22.1	20.9	487	19.3	117	15.88	0.398	296	11.8	25.0	3.50	16.91	4.87	1.74	5.05	0.753	4.12	0.733	1.80	0.238	1.46	0.206	2.84	0.890	0.071	2.00	1.63	0.447		
CL 431	7.15	25.0	233	236	47.0	112.7	47.8																															

Chapter 4

Origin of the enriched isotopic signature in the Northern Southern Volcanic Zone (33-34.5°S), Chile

This chapter is in preparation to be submitted to *Earth and Planetary Science Letters*

Co-authors: Kaj Hoernle, James Gill, Heidi Wehrmann, Ilya Bindeman

Chapter overview

The origin of the enriched Sr and Nd isotopic signature in volcanic rocks from the Northern Southern Volcanic Zone (NSVZ; 33-34.5°S) in Chile is controversial. Because the crust beneath the NSVZ is thick (ca. 60 km), Hildreth and Moorbath (1988) argued for crustal assimilation, while Stern (1991) and recently Kay et al. (2005) proposed that subduction erosion of the continental forearc can best explain the progressive increase in isotopic enrichment of the magmas from Miocene to Present. Together with additional major and trace element data (Wehrmann et al., 2013), we present a new and comprehensive geochemical data set (major and trace elements, and Sr-Nd-Hf-Pb-O isotopes) from young volcanic rocks from the three volcanic centers of Tupungatito, San José and Maipo and from the local Andean basement. The volcanic rocks consist of basaltic trachyandesites, trachyandesites and andesites. All NSVZ samples show typical subduction zone trace element enrichment and depletion patterns. Compared to the Transitional (T) SVZ of Jacques et al. (2013), the NSVZ samples have higher Sr but lower Nd and Hf isotope ratios. They overlap but are shifted to less radiogenic $^{206}\text{Pb}/^{204}\text{Pb}$ and $^{207}\text{Pb}/^{204}\text{Pb}$ ratios compared to the TSVZ, and are shifted to higher $^{208}\text{Pb}/^{204}\text{Pb}$ at a given $^{206}\text{Pb}/^{204}\text{Pb}$ ratio (or to higher $\Delta 8/4$). The shift in Pb isotopes from the SVZ array cannot be explained by a greater upper crustal component in the NSVZ magmas, since the Andean basement have both higher $\Delta 7/4$ and $\Delta 8/4$. The $\delta^{18}\text{O}(\text{melt})$ ranges from 5.64 to 6.36‰, and shows no correlation with indices of differentiation or radiogenic isotope ratios. These geochemical observations preclude contamination with the Andean upper crustal basement. The mantle-like $\delta^{18}\text{O}(\text{melt})$ of most of the NSVZ samples may suggest that the source of the enrichment is from the mantle. Lower crust from Arizona has the appropriate composition and assuming that the lower crust in Chile is similar in composition than in Arizona, subduction erosion of the lower crust and therefore source mixing can be responsible for the progressive isotopic enrichment observed by Kay et al. (2005) since the Miocene. Alternatively, the geochemical variations in the NSVZ may reflect the involvement of old enriched subcontinental lithospheric mantle that stagnated beneath South America since the Mesoproterozoic, or possibly enriched asthenospheric mantle with a Gough-type composition.

4.1 Introduction

The Andean Cordillera is often considered a continental endmember for subduction zones. With a crustal thickness reaching 70 km beneath the Central Volcanic Zone (CVZ; 16°-28°S) in Peru/Northern Chile, incorporation of continental crust by assimilation or subduction erosion may play an important role in generating isotopically enriched arc lavas there (Stern 2004, references therein). The crust is almost as thick in the Northern Southern Volcanic Zone volcanic arc of Chile (NSVZ; 33-34.5°S) (e.g. Hildreth and Moorbath, 1988). There, most volcanic rocks are quite differentiated and have more enriched Sr and Nd isotopes than in the Transitional SVZ volcanic arc (TSVZ; 34.5-38°S) or the Central SVZ volcanic arc (CSVZ; 38-43°S) further south. The origin of this enriched isotopic signature is controversial. Hildreth and Moorbath (1988) argued for crustal assimilation with their MASH (Melting, Assimilation, Storage and Hybridization) model. On the other hand, Stern (1991) and Kay et al. (2005) proposed that subduction erosion of the continental forearc crust can better explain the temporal pattern of isotopic enrichment in this area.

Significant assimilation of pre-Tertiary sialic crust is precluded in the TSVZ based on trace elements and isotopes (Jacques et al., 2013), even though most of the TSVZ volcanoes lie on relatively thick crust (Hildreth and Moorbath, 1988, Völker et al., 2011). In order to evaluate the potential influence of the continental crust in the NSVZ magmas, we present new Sr-Nd-Pb-Hf-O isotopes from Holocene volcanic rocks and crustal basement rocks. This paper will mainly compare and contrast the NSVZ with the TSVZ (Jacques et al., 2013) in order to identify the origin of the enriched isotopic signature.

4.2 Geological setting

From Colombia (5°N) to Southern Chile (54°S), the Andean cordillera is a 7,500 km long volcanic arc. The subduction of the Nazca (7-9 cm/year) and the Antarctic Plates (2 cm/year) below the South American Plate (Norabuena et al., 1998; Angermann et al., 1999) triggers arc volcanism where the slab dip angle is higher than 25°. The Andes consist of four active volcanic

segments: the Northern Volcanic Zone (NVZ; 5N-2°S) in Colombia and Ecuador; the Central Volcanic Zone (CVZ; 16-28°S) in Peru and northern Chile; the Southern Volcanic Zone (SVZ, 33-46°S) in central Chile; and the Austral Volcanic Zone (AVZ; 49-54°S) in southern Chile. Volcanic gaps occur where dip angles are less than 10° (Stern, 2004). The transition between the low and steep subduction angle can be either gradual or abrupt. The latter occurs between the SVZ and the Pampean Flat slab segment where the Juan Fernández ridge subducts, whereas the former occurs between the Pampean Flat slab segment and the southern part of the CVZ (Bevis and Isacks, 1984; Cahill and Isacks, 1992).

More than 60 active Cenozoic to Quaternary volcanoes compose the SVZ in central Chile (Stern, 2004, Figure 1A). Based on the geochemistry of the erupted rocks, the SVZ has been divided into the Northern Southern Volcanic Zone (NSVZ; 33-34.5°S; e.g. Hildreth and Moorbath, 1988), the Transitional Southern Volcanic Zone (TSVZ; 34.5-37°S; e.g. Tormey et al., 1991), the Central Southern Volcanic Zone (CSVZ; 37.0-41.5°S; e.g. Hickey et al., 1984, 1986, Hickey-Vargas et al., 1989) and the Southern Southern Volcanic Zone (SSVZ; 41.5-46°S; e.g. Naranjo and Stern, 2004) (see also López-Escobar et al., 1995). Dungan et al. (2001), however, proposed the following divisions: the Tupungato-Maipo Segment (TMS, 33-34.2°S), the Palomo-Tatara Segment (PTS, 34.7-36°S), and the Longaví-Osorno Segment (LOS, 36.2-42°S) (see also Sellés et al., 2004 for additional discussion).

Our samples come from three Quaternary volcanic arc centers in the NSVZ and TMS: Tupungatito, San José and Maipo (Figure 1B). Hildreth and Moorbath (1988) studied several andesitic to dacitic samples from the NSVZ centers. They sampled Tupungatito and the extinct vent of Tupungato, the Marmolejo-San José volcanic complex and Maipo (for which they do not provide isotope data). Futa and Stern (1988) analyzed two samples from Maipo, one from Marmolejo and one from Tupungato. Kay et al. (2005) analyzed a suite of rocks from the El Teniente copper district at ca. 34°S, close to San José and Maipo. Their samples are from the Coya-Machalí/Old Plutonic Complex (20 Ma), the Farellones Formation, the Teniente Volcanic-Plutonic Complexes (15-7 Ma) and the Young Plutonic Complex (7-3 Ma).

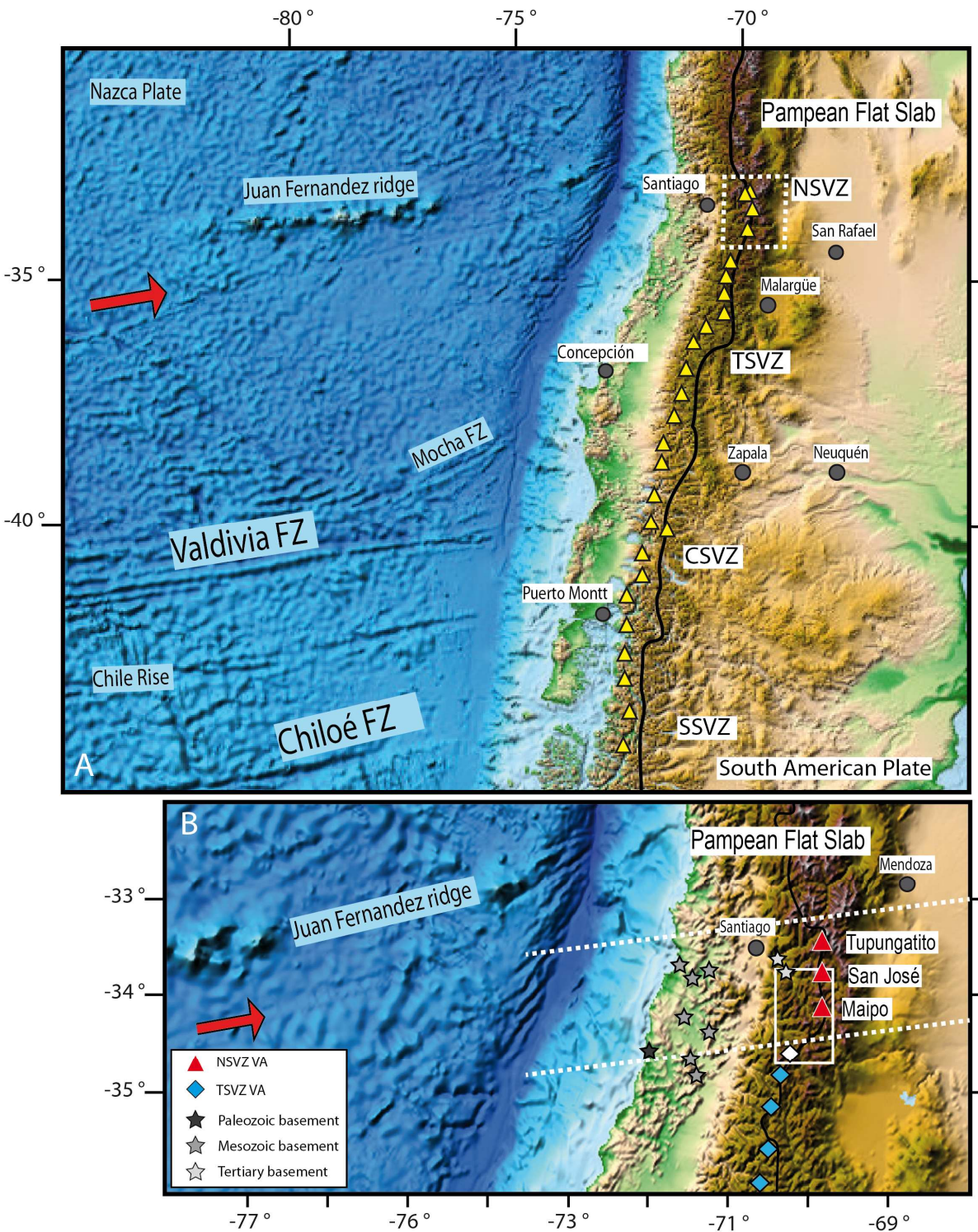


Figure 4.1 (A) Map of the Southern Volcanic Zone (SVZ) in Chile and Argentina between 30° and 45°S. Yellow triangles = Quaternary active volcanic front volcanoes. (B) Map of the Northern Southern Volcanic Zone volcanic arc (NSVZ) between 33°S and 34.5°S. Red triangles = studied NSVZ centers. Blue diamonds = Transitional SVZ volcanic arc (TSVZ) centers. White diamond = not-studied volcano. Shaded stars = sampling sites of basement rocks: light shade for the Tertiary, medium shade for the Mesozoic, and dark shade for metasediments. The white box in panel B indicates the El Teniente region from Kay et al. (2005). For both panels: Grey filled circles = major cities. The red arrows show the relative movement of the Nazca Plate to the South American Plate. The white dashed lines bracket the NSVZ transect. The thick black line represents the Chile/Argentina border. The ETOPO1 map source is from NOAA, modified (Amante and Eakins, 2009).

In the last 25 Ma, the northern part of the SVZ (33-36°S) has seen different episodes of eastward arc migration, linked to sudden chemical changes in magmatic rocks. These changes are associated with crustal shortening, back arc thrusting and peaks of subduction erosion of forearc crust (e.g. Kay et al., 2005, 2006ab, Kay and Copeland, 2006). Based on Sr-Nd-Pb isotopes, subduction erosion of continental crust has been proposed to explain the temporal magmatic trends and progressive isotopic enrichment of Early to Late Miocene and Pliocene volcanic rocks from the El Teniente copper district (ca. 34°S).

Offshore of the NSVZ, the subducting oceanic crust formed at the East Pacific Rise (EPR) (Herron et al., 1981; Tebbens and Cande, 1997; Tebbens et al., 1997). The age of the Nazca plate increases northward, and is about 34-36 Ma old between 33°-34.5°S. The Chilean trench is filled with mostly continent-derived turbidites (Völker et al., 2008; Contreras-Reyes et al., 2008; Lucassen et al., 2010; Plank, 2011). The pelagic sediment layer is 150 m thick offshore of the TSVZ and probably is slightly thicker offshore of the NSVZ because the plate is older. Plank (2011) considered the composition of trench sediment to be the same for both NSVZ and the TSVZ. The slab depth decreases from 120-140 km beneath the TSVZ volcanic front to 100 km beneath the NSVZ volcanic front (Tassara et al., 2006). The thickness of the asthenospheric mantle wedge beneath the NSVZ is about 40 km (Tassara et al., 2006, Völker et al., 2011).

The crust beneath the NSVZ is thick based on interpretations of regional gravity data (~50-65 km, Hildreth and Moorbath, 1988; Völker et al., 2011). The Andean basement in the NSVZ segment consists primarily of Mesozoic and Cenozoic volcanic and sedimentary rocks intruded by Miocene to Pliocene plutons. The central valley is filled with the same Mesozoic and Cenozoic volcano-sedimentary units, intruded by Mesozoic plutons. On the coast, metamorphic meta-sedimentary rocks are intruded by Carboniferous to Permian granitic batholiths (e.g. Stern, 2004; Lucassen et al., 2004; Cembrano and Lara, 2009). The Meso-Cenozoic volcano-sedimentary cover may be underlain by the same Paleozoic metamorphic rocks that crop out east of the volcanic arc in the Cordillera Frontal (Hildreth and Moorbath, 1988). Some of this eastern metamorphic basement probably is part of the Chilenia terrane (Ramos, 2010) that contains 1069-1081 Ma zircons (Ramos and Basei, 1997a,b).

Lucassen et al. (2004) provided major and trace element and Sr-Nd-Pb isotope data for the Andean basement, including Paleozoic to Tertiary magmatic rocks and Paleozoic silicic metamorphic rocks from 36°S to 41°S in Chile and Argentina, covering most of the units described above.

4.3 Sampling and analytical methods

We collected and analyzed the youngest, most mafic, and freshest samples we could find from the three volcanoes, including samples from young vents (some still degassing sulfur). As also noted by Hildreth and Moorbath (1988), we observed crustal xenoliths in some sequences of the Tupungatito lavas. However, we avoided these sequences in order to minimize crustal contamination effects. All samples contain large plagioclases as the main phenocryst phase. Pyroxenes are also present in most of the samples, while amphiboles are limited to the San José samples (and one Tupungatito sample, CL 246). The Tupungatito samples contain small olivines.

We also collected basement samples between 33.5-34.5°S (Figure 1B). We used the geological map of Chile (Mapa Geológico de Chile, SERNAGEOMIN) to target the different crustal units present in the NSVZ forearc, in order to provide a similar dataset for the forearc of the NSVZ as Lucassen et al. (2004) did further south (36-41°S). On the coast, the Paleozoic meta-sediment samples are quartzitic and pelitic schists. The Mesozoic and Tertiary samples are plutons that have intruded the Tertiary to Recent volcano-sedimentary cover. Those samples are felsic syenites, diorites, granodiorites, and granites. All samples contain quartz, plagioclase and alkali feldspar, and sometimes biotite and amphibole. Table 1 includes the GSP-based location and age estimate for the volcanic and crustal rocks.

Samples were crushed, sieved, and washed in distilled water in an ultrasonic bath. In order to minimize the effects of alteration and crustal contamination, 5 to 10 g of 1-2 mm size chips were carefully handpicked under a binocular microscope to ensure selection of the freshest part of the rock and to avoid xenolithic material. Handpicked chips were powdered in an agate mill to obtain homogenous powders for XRF and ICPMS analysis. Chips were used for

isotope analysis, including bulk groundmass oxygen isotopes. Fresh olivine, plagioclase and orthopyroxene phenocrysts were carefully selected for mineral oxygen isotope analysis to avoid inclusions and attached matrix.

Details of XRF and ICP-MS analyses can be found in Jacques et al. (2013). The basement samples were digested in PARR bombs in an oven in order to maximize zircon digestion. The relative difference between XRF and ICPMS results for Zr is better than 7% for all crustal samples, indicating that they were completely in solution for ICPMS analysis.

We determined Sr, Nd and Pb isotope ratios at GEOMAR using a ThermoFinnigan TRITON (Sr, Nd) and Finnigan MAT 262-RPQ2+ (Pb) thermal ionization mass spectrometers. In order to provide high precision analyses, Pb isotope ratios were measured using a double spike method. Hoernle et al. (2008, 2011) give detailed description of the chemical and TIMS analytical procedures. Fresh rock chips (100-150 mg of 0.5-2 mm size) were leached in 2N HCl at 70°C for 1-2 hours and then triple-rinsed with ELGA water prior to acid-digestion, in order to remove possible surface alteration/contamination. All errors are given at the 2σ confidence level. Sr and Nd isotope ratios were mass-bias corrected to $^{86}\text{Sr}/^{88}\text{Sr} = 0.1194$ and $^{146}\text{Nd}/^{144}\text{Nd} = 0.7219$. We measured NBS987 and our in-house Nd SPEX reference materials every 4th to 5th sample to obtain a normalization value for each turret relative to our preferred values of $^{87}\text{Sr}/^{86}\text{Sr} = 0.710250$ for NBS987 and $^{143}\text{Nd}/^{144}\text{Nd} = 0.511715$ for SPEX (corresponding to $^{143}\text{Nd}/^{144}\text{Nd} = 0.511850$ for La Jolla). This normalization value was applied for each turret, which compensates for machine drift over the course of the project (2009-2012). External 2σ uncertainties are ± 0.000011 (n= 25) for NBS987 and ± 0.000005 for SPEX. We also measured the reference material NBS981 along with the samples and the double spike corrected values are $^{206}\text{Pb}/^{204}\text{Pb} = 16.9413 \pm 21$, $^{207}\text{Pb}/^{204}\text{Pb} = 15.4994 \pm 20$, $^{208}\text{Pb}/^{204}\text{Pb} = 36.7241 \pm 56$, $^{207}\text{Pb}/^{206}\text{Pb} = 0.914889 \pm 37$, $^{208}\text{Pb}/^{206}\text{Pb} = 2.16773 \pm 13$ (n=38). It compares well with published double and triple spike data for NBS981 (see Hoernle et al., 2011). Chemistry blanks were monitored for each batch of samples. Total Pb blanks were below 25 pg (except for one blank of 200 pg), and Sr-Nd blanks are typically below 100 pg and 50 pg, respectively. These amounts are negligible compared to the amount of Pb, Sr and Nd in the samples. Replicate analyses of

separate digestions are within the external 2σ reproducibility of the Sr-Nd-Pb standards stated above.

Hf isotopes were analyzed using a NU Plasma HR MC-ICPMS at GEOMAR, following the chemical and analytical procedures reported in Blichert-Toft and Albarède (1997) and Geldmacher and Hoernle (2006). Briefly, 200-500 mg of fresh rock chips (0.5-2 mm size) were digested for 60 hours at 130°C in a HF-HNO₃ mixture. Samples were diluted to 80-100 ppb Hf to obtain a total Hf beam of 12-14 V. Hf isotope ratios were analyzed using static multi-collection. Mass-bias correction assumed $^{179}\text{Hf}/^{177}\text{Hf} = 0.7325$ and exponential mass fractionation. We measured our in-house Hf reference material solution SPEX every 3 to 5 samples to obtain a normalization value for each sample sequence. Over the course of the project (2010-2012), the standard solution had $^{176}\text{Hf}/^{177}\text{Hf} = 0.282170 \pm 6$ (2σ , $n = 45$) which corresponds to $^{176}\text{Hf}/^{177}\text{Hf} = 0.282163$ for JMC-145.

Oxygen isotope analyses were determined at the University of Oregon using CO₂-laser fluorination (e.g. Bindeman, 2008) and a Newwave 35W CO₂ laser. Single or bulk phenocryst grains, bulk basement samples, and bulk groundmass (0.6-2 mg), were reacted in the presence of BrF₅ to release oxygen gas, which was purified through a series of cryogenic traps held at liquid nitrogen temperature. A mercury diffusion pump was used to remove traces of fluorine gas. We converted the Oxygen to CO₂ gas in a small platinum graphite converter. The CO₂ gas was then analyzed on a MAT 253 mass spectrometer. During each analytical session, reference materials were measured along with the samples: four to seven aliquots of internal garnet standard UOG1 ($\delta^{18}\text{O} = 6.56\text{‰}$), calibrated against the Gore Mt. Garnet ($\delta^{18}\text{O}_{\text{olivine}} = 5.8\text{‰}$ VSMOW, Valley et al., 1995), as well as San Carlos olivine with $\delta^{18}\text{O}_{\text{olivine}} = 5.25\text{‰}$. The measured $\delta^{18}\text{O}_{\text{olivine}}$ values of the reference materials ranged from 0.1 to 0.25‰ less than the accepted values. Samples were corrected for this day-to-day variability. Replicate measurements ranged within ± 0.02 to $\pm 0.08\text{‰}$ (1σ).

Table 4.1Major (wt. %) and trace elements ($\mu\text{g/g}$) for the NSVZ volcanic arc and basement samples.

Major element compositions recalculated to 100% (# original sum retain), Total Fe expressed as FeO.

* data after Wehrmann et al. (accepted, 2013) and are included here to give readers complete analyses.

Sample number	Sample Location	Country	Sample type	Lat (S)	Long (W)	Age (estimate)	reference
Volcanic Arc							
CL 225 A*	Tupungatito	Chile	bomb	-33.39	-69.83	Holocene	Stern (2004)
CL 235*	Tupungatito	Chile	tephra	-33.41	-69.84	Holocene	Stern (2004)
CL 238*	Tupungatito	Chile	lava	-33.40	-69.96	Holocene	Stern (2004)
CL 242*	Tupungatito	Chile	lava	-33.39	-69.83	Holocene	Stern (2004)
CL 246*	Tupungatito	Chile	lava	-33.35	-69.86	Holocene	Stern (2004)
CL 293	Tupungatito	Chile	lava	-33.35	-69.86	Holocene	Stern (2004)
CL 251*	San José	Chile	lava	-33.74	-69.92	Holocene	Stern (2004)
CL 255*	San José	Chile	lava	-33.77	-69.91	Holocene	Stern (2004)
CL 257*	San José	Chile	lava	-33.77	-69.91	Holocene	Stern (2004)
CL 262*	San José	Chile	lava	-33.78	-69.94	Holocene	Stern (2004)
CL 289*	San José	Chile	bomb	-33.78	-69.90	Holocene	Stern (2004)
CL 290*	San José	Chile	bomb	-33.78	-69.90	Holocene	Stern (2004)
CL 211	Maipo	Chile	lava	-34.16	-69.76	Holocene	Stern (2004)
CL 213	Maipo	Chile	bomb	-34.15	-69.78	Holocene	Stern (2004)
CL 214	Maipo	Chile	lava	-34.15	-69.78	Holocene	Stern (2004)
Basement							
CL 601	Santa Cruz	Chile	Syenite	-34.75	-71.44	Mesozoic	Geological map
CL 603	Santa Cruz	Chile	Granite	-34.53	-71.41	Mesozoic	Geological map
CL 605	Pichidegua	Chile	Granodiorite	-34.38	-71.32	Mesozoic	Geological map
CL 606	Pichidegua	Chile	Granodiorite	-34.35	-71.33	Mesozoic	Geological map
CL 607	Pichidegua	Chile	Granite	-34.35	-71.33	Mesozoic	Geological map
CL 610	Litueche	Chile	Granite	-34.09	-71.68	Mesozoic	Geological map
CL 611	Ruta 66	Chile	Diorite	-33.75	-71.31	Mesozoic	Geological map
CL 612	Ruta 66	Chile	Syenite	-33.80	-71.48	Mesozoic	Geological map
CL 615	San Antonio	Chile	Diorite	-33.63	-71.60	Mesozoic	Geological map
CL 616	El Teniente	Chile	Syeno-diorite	-33.82	-70.22	Tertiary	Geological map
CL 617	El Teniente	Chile	Syeno-diorite	-33.84	-70.21	Tertiary	Geological map
CL 618	Maipo Canyon	Chile	Granodiorite	-33.58	-70.46	Tertiary	Geological map
CL 619	Maipo Canyon	Chile	Diorite	-33.58	-70.46	Tertiary	Geological map
CH 1-9	Pichilemu	Chile	Metasediment	-34.39	-72.02	Paleozoic	Geological map
CH 1-44	Pichilemu	Chile	Metasediment	-34.39	-72.02	Paleozoic	Geological map

Table 4.1 (Continued)

Sample number	Method	SiO2 (wt. %)	TiO2 (wt. %)	Al2O3 (wt. %)	Fe2O3 (wt. %)	MnO (wt. %)	MgO (wt. %)	CaO (wt. %)	Na2O (wt. %)	K2O (wt. %)	P2O5 (wt. %)	L.O.I	Sum(#)
Volcanic Arc													
CL 225 A*	XRF	56.37	0.96	17.55	7.82	0.11	4.24	6.47	4.26	1.95	0.27	0.11	99.82
CL 235*	XRF	58.58	0.91	16.79	6.95	0.10	3.87	5.79	4.08	2.59	0.23	0.34	99.83
CL 238*	XRF	58.90	0.91	17.06	6.65	0.09	3.65	5.65	4.24	2.60	0.25	0.39	99.81
CL 242*	XRF	56.58	0.97	17.50	7.70	0.11	4.13	6.42	4.27	2.02	0.28	0.08	99.80
CL 246*	XRF	59.56	0.88	15.95	6.69	0.10	4.15	5.52	4.03	2.88	0.23	0.21	99.81
CL 293	XRF	58.77	0.89	17.49	6.45	0.10	4.08	5.82	4.33	2.36	0.22	0.00	100.26
CL 251*	XRF	61.23	0.82	16.70	6.10	0.10	2.97	5.22	4.13	2.52	0.20	0.10	99.84
CL 255*	XRF	60.51	0.87	16.98	6.42	0.09	3.02	5.56	4.16	2.16	0.21	0.12	99.83
CL 257*	XRF	60.30	0.87	17.10	6.47	0.09	3.02	5.61	4.18	2.14	0.21	0.22	99.83
CL 262*	XRF	60.76	0.82	17.02	6.40	0.10	2.83	5.33	4.09	2.45	0.19	0.31	99.86
CL 289*	XRF	62.52	0.76	16.57	5.75	0.10	2.42	4.64	4.24	2.80	0.20	0.11	99.83
CL 290*	XRF	60.31	0.87	17.44	6.43	0.10	2.71	5.29	4.18	2.42	0.24	0.21	99.85
CL 211	XRF	62.22	0.81	16.42	5.63	0.09	2.69	4.98	4.07	2.71	0.22	0.00	100.27
CL 213	XRF	58.86	0.93	19.31	5.55	0.09	1.85	6.64	4.15	2.24	0.24	0.00	98.65
CL 214	XRF	61.85	0.81	16.73	5.48	0.09	2.74	5.21	4.07	2.66	0.22	0.03	99.61
Basement													
CL 601	XRF	54.18	0.67	20.61	5.93	0.14	1.75	5.94	3.70	4.70	0.52	1.97	100.20
CL 603	XRF	71.83	0.38	14.26	2.47	0.01	0.28	0.49	3.23	5.26	0.05	1.16	99.81
CL 605	XRF	66.20	0.65	15.65	3.93	0.06	1.30	3.20	4.02	3.90	0.14	0.75	99.96
CL 606	XRF	67.72	0.57	16.02	3.68	0.06	1.54	3.86	4.17	1.84	0.15	0.70	100.16
CL 607	XRF	70.21	0.32	15.06	2.51	0.04	0.75	3.13	3.89	2.16	0.12	0.89	99.61
CL 610	XRF	77.90	0.10	11.83	1.25	0.01	0.03	0.08	4.27	4.46	0.01	0.30	100.16
CL 611	XRF	58.98	0.80	16.71	7.45	0.14	3.25	6.59	3.23	2.04	0.14	0.36	99.89
CL 612	XRF	66.31	0.49	17.54	2.66	0.06	0.51	2.03	5.86	3.71	0.10	0.31	99.82
CL 615	XRF	64.13	0.56	17.94	4.11	0.07	1.69	4.50	4.45	2.16	0.17	0.39	100.12
CL 616	XRF	57.60	0.92	17.59	6.90	0.11	3.65	5.90	4.30	2.95	0.18	0.53	100.40
CL 617	XRF	57.92	0.96	18.07	6.84	0.11	2.97	5.94	4.45	2.73	0.23	0.68	100.52
CL 618	XRF	66.25	0.83	14.92	5.94	0.12	1.09	3.34	4.61	2.27	0.24	0.80	100.28
CL 619	XRF	60.37	0.95	16.75	7.86	0.14	2.45	6.65	4.25	0.86	0.29	0.75	100.71
CH 1-9	XRF	78.41	0.53	10.75	3.09	0.04	1.13	0.45	4.49	1.01	0.10	1.41	98.60
CH 1-44	XRF	61.04	0.75	18.37	7.05	0.07	3.16	0.78	8.56	0.03	0.17	2.66	96.90
Standards													
BHVO	XRF	49.95	2.76	13.63	12.25	0.17	7.41	11.46	2.31	0.51	0.26		100.71
JA-2	XRF	56.23	0.67	15.47	6.39	0.11	8.00	6.27	3.12	1.76	0.15		98.17

Table 4.1 (Continued)

Sample number	Li	Sc	V	Cr	Co	Ni	Cu	Zn	Ga	Rb	Sr	Y	Zr	Nb	Sn	Cs	Ba	La	Ce	Pr	Nd	Sm	Eu	Gd	Tb	Dy	Ho	Er	Tm	Yb	Lu	Hf	Ta	Ti	Pb	Th	U
	$\mu\text{g/g}$	$\mu\text{g/g}$	$\mu\text{g/g}$	$\mu\text{g/g}$	$\mu\text{g/g}$	$\mu\text{g/g}$	$\mu\text{g/g}$	$\mu\text{g/g}$	$\mu\text{g/g}$	$\mu\text{g/g}$	$\mu\text{g/g}$	$\mu\text{g/g}$	$\mu\text{g/g}$	$\mu\text{g/g}$	$\mu\text{g/g}$	$\mu\text{g/g}$	$\mu\text{g/g}$	$\mu\text{g/g}$	$\mu\text{g/g}$	$\mu\text{g/g}$	$\mu\text{g/g}$	$\mu\text{g/g}$	$\mu\text{g/g}$	$\mu\text{g/g}$	$\mu\text{g/g}$	$\mu\text{g/g}$	$\mu\text{g/g}$	$\mu\text{g/g}$	$\mu\text{g/g}$	$\mu\text{g/g}$	$\mu\text{g/g}$	$\mu\text{g/g}$	$\mu\text{g/g}$	$\mu\text{g/g}$	$\mu\text{g/g}$	$\mu\text{g/g}$	$\mu\text{g/g}$
Volcanic Arc																																					
CL 225 A*	15.4	17.8	162	48.8	24.9	25.7	9.43	83.7	21.1	61.4	650	19.0	199	7.56	1.52	2.49	497	24.1	52.0	6.37	25.5	5.08	1.31	4.47	0.651	3.66	0.696	1.84	0.266	1.74	0.257	4.63	0.522	0.044	11.7	6.77	2.01
CL 235*	20.4	18.1	168	59.2	22.0	29.6	44.5	78.8	21.2	92.2	613	19.5	228	8.71	1.58	4.27	530	27.2	57.8	6.96	27.0	5.21	1.19	4.47	0.643	3.65	0.703	1.92	0.282	1.87	0.277	5.45	0.652	0.311	16.2	10.7	3.42
CL 238*	20.0	16.1	156	46.9	20.3	28.5	51.7	75.9	21.5	91.4	645	18.8	220	8.85	1.58	4.16	536	28.1	59.3	7.15	27.7	5.29	1.20	4.48	0.635	3.53	0.672	1.82	0.266	1.78	0.265	5.32	0.661	0.341	15.9	10.5	3.32
CL 242*	16.3	18.9	171	46.6	25.1	24.4	36.5	82.5	21.4	64.8	676	19.7	207	7.70	1.45	2.70	522	24.9	53.7	6.59	26.3	5.17	1.34	4.56	0.659	3.70	0.715	1.90	0.272	1.79	0.262	4.79	0.518	0.196	11.7	7.02	2.06
CL 246*	22.0	17.1	161	112	22.4	44.9	50.6	76.8	20.8	112	555	20.3	239	9.46	1.69	5.22	524	29.2	62.6	7.49	28.7	5.54	1.17	4.66	0.672	3.76	0.721	1.95	0.290	1.92	0.284	5.76	0.743	0.418	17.0	12.9	4.20
CL 293	15.2	14.2	150	68.3	20.2	31.3	42.3	76.8	22.7	75.7	696	17.3	183	7.55	1.22	2.36	532	25.4	53.9	5.57	25.6	4.98	1.20	4.21	0.601	3.34	0.635	1.72	0.249	1.64	0.241	4.80	0.575	0.316	13.7	8.69	2.65
CL 251*	18.5	15.0	132	27.7	16.5	11.2	18.6	73.8	20.3	93.7	445	22.4	163	9.47	1.80	3.33	455	26.5	55.9	6.65	25.5	5.05	1.12	4.56	0.687	4.00	0.783	2.16	0.326	2.21	0.329	4.19	0.744	0.424	15.3	10.1	3.07
CL 255*	20.7	11.7	132	38.5	17.9	15.3	15.9	82.9	21.4	73.8	501	17.0	175	8.71	1.49	3.20	489	25.9	54.8	6.59	25.6	5.00	1.22	4.31	0.611	3.29	0.607	1.58	0.228	1.50	0.221	4.38	0.679	0.340	13.6	8.04	2.65
CL 257*	20.7	12.3	135	38.4	18.3	14.1	31.0	87.7	21.7	73.4	512	17.3	183	8.73	1.49	3.20	489	26.0	55.1	6.57	25.8	5.05	1.24	4.38	0.618	3.34	0.614	1.60	0.227	1.51	0.221	4.48	0.674	0.356	13.5	7.99	2.61
CL 262*	18.9	14.8	139	23.2	16.9	9.28	13.4	75.0	20.7	88.4	434	23.3	171	9.52	1.80	3.23	438	26.1	54.6	6.50	25.2	5.05	1.12	4.60	0.704	4.14	0.819	2.28	0.347	2.33	0.353	4.47	0.764	0.380	15.3	9.86	3.15
CL 289*	21.0	11.2	114	16.6	14.5	7.20	12.9	74.3	20.4	103	447	21.7	140	10.7	1.66	3.78	548	30.3	63.1	7.37	27.8	5.37	1.12	4.73	0.690	3.94	0.763	2.09	0.311	2.09	0.306	3.79	0.865	0.441	15.6	11.6	3.57
CL 290*	15.6	12.8	135	12.3	16.7	7.88	13.3	80.7	21.1	80.0	511	21.2	173	9.80	1.56	2.81	544	28.9	60.2	7.10	27.6	5.32	1.25	4.69	0.680	3.91	0.750	2.03	0.299	2.00	0.295	4.36	0.736	0.282	13.1	9.20	2.71
CL 211	18.7	15.3	150	62.4	16.9	24.7	27.5	95.2	22.0	109	474	19.8	222	10.1	1.71	3.22	629	33.0	66.0	7.61	28.4	5.27	1.19	4.42	0.620	3.49	0.663	1.81	0.267	1.79	0.269	5.10	0.688	0.454	15.5	12.0	3.19
CL 213	17.6	14.2	168	6.62	14.7	7.80	43.8	84.6	24.1	86.5	631	18.7	208	9.27	1.53	3.16	557	28.8	58.7	5.90	26.5	5.08	1.30	4.34	0.607	3.36	0.632	1.59	0.247	1.61	0.240	4.66	0.604	0.415	15.0	9.56	2.65
CL 214	16.6	15.6	152	58.6	16.9	24.1	70.8	77.7	22.2	106	494	19.8	218	9.93	1.65	2.35	627	32.3	64.5	7.51	28.1	5.20	1.20	4.39	0.619	3.46	0.663	1.80	0.268	1.79	0.268	4.99	0.659	0.418	17.1	11.5	3.06
Basement																																					
CL 601	16.5	8.26	109	9.27	11.3	2.52	2.65	56.4	19.0	64.4	540	22.6	149	6.27	1.59	6.23	709	35.6	49.9	9.17	36.2	7.26	1.75	5.95	0.791	4.26	0.822	2.27	0.337	2.29	0.344	3.69	0.320	0.201	6.14	10.9	2.22
CL 603	4.46	1.86	32.9	8.51	1.73	0.544	4.89	5.88	14.4	130	34.1	8.17	276	7.20	2.68	4.39	414	7.43	17.3	2.26	8.85	1.86	0.224	1.51	0.225	1.34	0.284	0.872	0.145	1.08	0.172	8.12	0.589	0.401	3.92	9.44	2.91
CL 605	31.9	6.21	56.2	28.4	8.73	12.0	5.37	66.7	19.5	27.9	253	12.9	150	5.42	1.65	3.09	448	15.7	25.6	4.16	16.5	3.31	0.869	2.94	0.431	2.43	0.466	1.26	0.184	1.21	0.180	3.89	0.417	0.296	9.53	3.02	1.02
CL 607	23.0	3.15	22.7	13.8	3.15	0.714	12.0	36.2	20.8	26.0	279	9.88	169	7.67	1.02	1.53	572	22.9	35.8	5.45	20.1	3.50	0.906	2.71	0.364	1.89	0.346	0.918	0.136	0.91	0.136	4.42	0.618	0.251	16.8	6.22	0.958
CL 610	28.1	0.377	1.48	14.8	0.262	0.174	5.72	62.4	26.1	161	335	25.3	328	17.2	8.09	1.36	725	13.9	22.9	3.42	13.1	2.91	0.241	3.21	0.608	4.24	0.937	2.84	0.462	3.10	0.440	10.7	0.554	0.793	13.3	5.75	2.35
CL 611	15.1	23.0	193	19.9	18.2	6.66	46.9	76.8	19.3	73.7	355	25.3	147	4.03	1.37	4.05	405	15.3	35.5	4.65	19.6	4.59	1.04	4.53	0.731	4.58	0.949	2.70	0.413	2.83	0.430	4.14	0.306	0.371	10.9	6.74	1.44
CL 612	7.66	2.51	8.59	10.8	1.20	0.813	3.83	27.0	23.8	36.9	161	17.9	514	11.7	1.65	1.09	1297	62.2	104	14.2	52.9	8.15	1.66	6.23	0.727	3.48	0.637	1.74	0.256	1.81	0.294	12.1	0.624	0.349	14.4	15.8	1.35
CL 615	45.3	5.69	59.5	13.4	9.23	6.86	4.64	62.8	22.6	38.1	413	7.74	150	4.75	0.900	2.57	607	19.6	28.2	3.95	14.0	2.31	0.888	1.94	0.262	1.44	0.277	0.770	0.112	0.76	0.120	3.73	0.279	0.414	13.0	4.02	0.670
CL 616	26.2	16.4	159	78.7	19.9	38.5	55.9	77.5	21.8	115	497	20.5	191	8.03	2.02	6.50	499	19.7	44.8	5.81	23.7	5.06	1.17	4.38	0.652	3.79	0.744	2.08	0.311	2.10	0.315	5.05	0.539	0.318	15.2	13.7	3.92
CL 617	7.62	13.9	157	27.0	16.6	16.8	77.1	58.6	21.6	67.6	435	20.0	169	7.80	1.55	4.02	455	17.2	39.7	5.34	22.3	4.82	1.22	4.23	0.630	3.65	0.729	2.01	0.300	2.03	0.301	4.55	0.515	0.252	10.8	10.0	2.10
CL 618	5.67	10.1	43.3	7.62	7.91	1.26	27.9	77.5	17.8	14.7	173	35.9	237	5.72	1.65	1.11	459	15.8	30.6	5.32	23.5	5.88	1.36	6.01	0.983	6.21	1.27	3.59	0.542	3.68	0.553	6.62	0.393	0.270	5.84	4.70	1.37
CL 619	5.62	22.9	129	22.7	16.7	5.69	79.1	81.2	19.5	15.1	344	30.5	148	3.68	1.25	0.533	303	13.7	32.8	4.51	20.4	5.13	1.37	5.36	0.889	5.47	1.12	3.12	0.472	3.16	0.471	4.17	0.259	0.097	4.51	3.13	0.912
CH 1-9	7.81	8.39	58.4	40.7	7.49	14.8	8.87	51.6	12.2	29.3	22.7	23.8	156	9.28	1.77	1.84	298	28.9	60.7	7.22	27.1	5.40	1.15	4.86	0.762	4.59	0.912	2.57	0.385	2.59	0.373	4.19	0.648	0.132	11.6	9.24	2.10
CH 1-44	22.5	18.1	137	88.6	17.5	40.1	40.9	104	20.3	0.430	26.6	30.6	122	14.9	3.65	0.030	11.4	49.6	106	11.8	44.5	8.64	1.63	7.55	1.11	6.29	1.22	3.32	0.486	3.21	0.459	3.39	1.04	0.002	16.0	17.9	2.47
Standards																																					
BHVO	4																																				

Table 4.2 Sr-Nd-Hf-Pb isotope data for the NSVZ volcanic arc and basement sample for the samples in Table 1. See text for reference material results.

Sample number	Sample Location	$^{87}\text{Sr}/^{86}\text{Sr}$	2σ	$^{143}\text{Nd}/^{144}\text{Nd}$	2σ	ϵNd	$^{176}\text{Hf}/^{177}\text{Hf}$	2σ	ϵHf
Volcanic Arc									
CL 225 A	Tupungatito	0.704864	4	0.512569	3	-1.19			
CL 235	Tupungatito	0.704765	3	0.512576	3	-1.06	0.282782	0.000006	-0.09
CL 238	Tupungatito	0.704776	3	0.512570	3	-1.18	0.282774	0.000005	-0.39
CL 242	Tupungatito	0.704870	3	0.512561	2	-1.35	0.282767	0.000007	-0.63
<i>CL 242_rep</i>		<i>0.704870</i>	<i>3</i>						
CL 246	Tupungatito	0.704773	3	0.512570	3	-1.17	0.282771	0.000006	-0.51
CL 293	Tupungatito	0.704808	3	0.512564	3	-1.29			
CL 251	San José	0.705277	3	0.512543	3	-1.69			
CL 255	San José	0.705328	3	0.512525	3	-2.04	0.282738	0.000005	-1.68
CL 257	San José	0.705311	3	0.512534	2	-1.88			
CL 262	San José	0.705416	3	0.512531	3	-1.93	0.282741	0.000008	-1.57
CL 289	San José	0.705183	3	0.512541	2	-1.73			
CL 290	San José	0.705091	3	0.512556	3	-1.45			
CL 211	Maipo	0.705093	3	0.512548	2	-1.60	0.282780	0.000004	-0.19
CL 213	Maipo	0.704836	4	0.512591	2	-0.76			
CL 214	Maipo	0.705080	3	0.512563	3	-1.31	0.282782	0.000003	-0.09
Basement									
CL 601	Santa Cruz	0.704912	2	0.512668	3	0.73			
CL 603	Santa Cruz	0.715076	3	0.512680	3	0.97			
<i>CL 603_rep</i>		<i>0.715113</i>	<i>3</i>	<i>0.512685</i>	<i>2</i>				
CL 605	Pichidegua	0.705802	2	0.512798	2	3.28			
CL 606	Pichidegua	0.707265	3	0.512393	2	-4.62			
CL 607	Pichidegua	0.708281	3	0.512254	1	-7.33			
CL 610	Litueche	0.708281	3	0.512670	2	0.78	0.282867	0.000004	2.90
CL 611	Ruta 66	0.705834	3	0.512672	2	0.82	0.283084	0.000005	10.56
CL 612	Ruta 66	0.708449	3	0.512383	2	-4.82			
CL 615	San Antonio	0.707334	3	0.512374	2	-5.00			
CL 616	El Teniente	0.703910	3	0.512824	3	3.78	0.283021	0.000006	8.35
CL 617	El Teniente	0.703984	3	0.512824	2	3.79			
CL 618	Maipo Canyon	0.703901	3	0.512926	2	5.78	0.283084	0.000005	10.56
CL 619	Maipo Canyon	0.703735	3	0.512929	1	5.82			
CH 1-9	Pichilemu	0.722264	4	0.512218	3	-7.13	0.282518	0.000004	-9.5474
<i>CH 1-9_rep</i>		<i>0.722245</i>	<i>3</i>	<i>0.512224</i>	<i>3</i>				
CH 1-44	Pichilemu	0.709943	3	0.512736	3	2.063	0.282602	0.000006	-6.4285

Table 4.2 (Continued)

Sample number	$^{206}\text{Pb}/^{204}\text{Pb}$	2σ	$^{207}\text{Pb}/^{204}\text{Pb}$	2σ	$^{208}\text{Pb}/^{204}\text{Pb}$	2σ
Volcanic Arc						
CL 225 A	18.6023	23	15.6073	28	38.5322	92
CL 235	18.5802	12	15.6070	14	38.5120	43
CL 238	18.5834	12	15.6041	13	38.5037	43
CL 242	18.6010	12	15.6058	12	38.5273	32
<i>CL 242_rep</i>	<i>18.6001</i>	<i>5</i>	<i>15.6051</i>	<i>4</i>	<i>38.5262</i>	<i>11</i>
CL 246	18.5788	13	15.6054	16	38.5049	52
CL 293	18.5811	10	15.6033	10	38.5027	31
CL 251	18.5721	13	15.6008	15	38.5109	47
CL 255	18.6087	17	15.6097	20	38.5670	64
CL 257	18.6067	16	15.6069	18	38.5616	55
CL 262	18.5319	14	15.5943	14	38.4653	44
CL 289	18.5636	9	15.5984	10	38.5138	32
CL 290	18.5551	14	15.5995	16	38.5183	51
CL 211	18.5809	8	15.6076	8	38.5296	25
<i>CL 211_rep</i>	<i>18.5764</i>	<i>7</i>	<i>15.6041</i>	<i>8</i>	<i>38.5202</i>	<i>24</i>
CL 213	18.5763	15	15.6042	15	38.5162	47
<i>CL 213_rep</i>	<i>18.5782</i>	<i>6</i>	<i>15.6065</i>	<i>6</i>	<i>38.5218</i>	<i>15</i>
CL 214	18.5791	13	15.6043	12	38.5222	33
Basement						
CL 601	18.8031	13	15.6056	14	38.9577	42
CL 603	20.6507	16	15.7246	16	41.1387	54
<i>CL 603_rep</i>	<i>20.6737</i>	<i>13</i>	<i>15.7246</i>	<i>13</i>	<i>41.1563</i>	<i>43</i>
CL 605	18.9147	12	15.6181	10	38.7846	27
CL 606	18.7536	9	15.6465	9	38.6729	25
CL 607	18.6901	31	15.6466	28	38.7165	73
CL 610	18.8434	15	15.6454	16	38.7778	50
CL 611	18.7051	12	15.6222	13	38.6494	41
CL 612	18.7252	32	15.6510	27	39.2959	65
CL 615	18.6561	25	15.6404	24	38.6930	71
CL 616	18.5701	18	15.6026	21	38.4563	69
CL 617	18.5985	20	15.6051	24	38.4927	79
CL 618	18.4808	11	15.5905	10	38.3778	25
CL 619	18.4831	10	15.5909	11	38.3735	34
CH 1-9	19.0567	11	15.6696	10	39.0272	32
<i>CH 1-9_rep</i>	<i>19.0567</i>	<i>14</i>	<i>15.6702</i>	<i>16</i>	<i>39.0268</i>	<i>52</i>
CH 1-44	18.8418	23	15.6618	19	39.1769	49

4.4 Results

Results are given in Tables 1 (major and trace elements), 2 (Sr-Nd-Pb isotopes), and 3 (oxygen isotopes). The major and trace element data for the three Maipo samples and Tupungatito sample CL 293 are new; the rest are from Wehrmann et al. (2013). Fifteen volcanic samples were analyzed for Sr-Nd-Pb isotope compositions and eight for Hf isotopes. O isotopes were measured for thirteen minerals and twelve groundmasses.

Fifteen representative basement plutonic and metamorphic rocks were analyzed for major and trace elements and Sr-Nd-Pb isotopes. Six of them were analyzed for Hf isotopes, and eight for O isotopes.

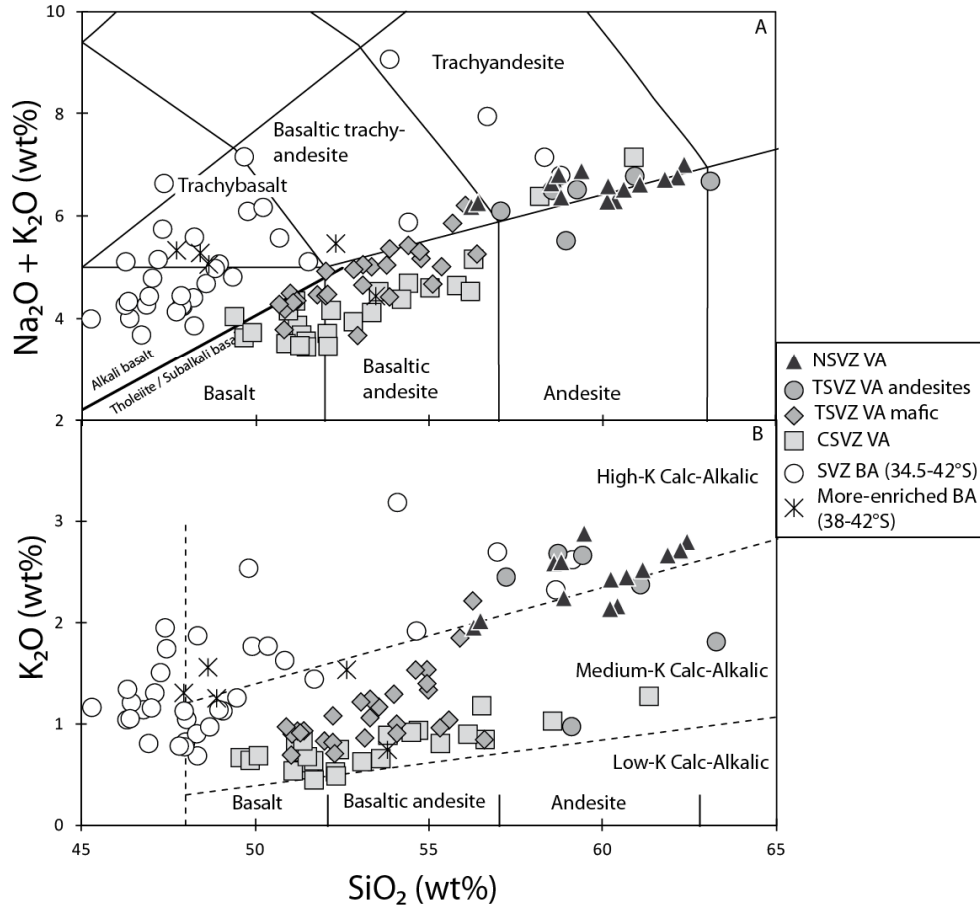


Figure 4.2 (A) Total Alkali versus Silica [TAS] after Le Maitre et al. (1989). NSVZ samples range from basaltic trachandesites to trachyandesites/andesites. (B) SiO_2 versus K_2O after Gill (1981). Most NSVZ samples plot on the High-K field. Data for Tupungatito and San José from Wehrmann et al. (2013). Data source for TSVZ, CSVZ and backarc samples from Jacques et al. (2013, and in prep) and Wehrmann et al. (2013).

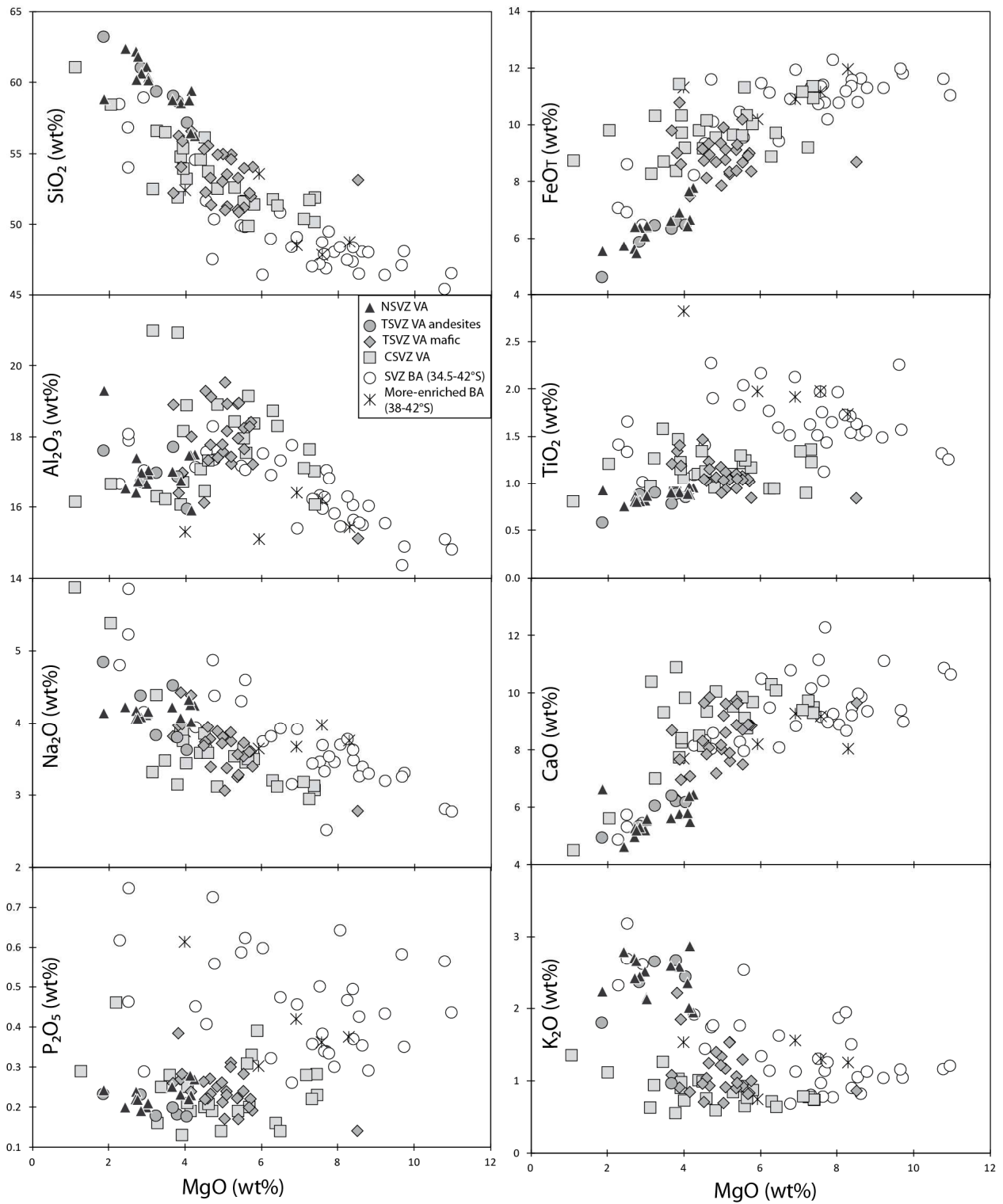


Figure 4.3 MgO versus major element oxides. The NSVZ samples overall are more differentiated than the TSVZ samples, but overlap the TSVZ andesites on all plots and form similar differentiation trends. Data source are the same as in Figure 2.

4.4.1 Major Elements

The NSVZ samples consist of basaltic trachyandesites, trachyandesites, and andesites with $\text{SiO}_2 = 56\text{-}62$ wt. % (Figure 2A) and $\text{MgO} = 1.9\text{-}4.2$ wt. %. Most of the samples plot near the medium-K to high-K boundary of Gill (1981) (Figure 2B). The data form positive correlations on diagrams of MgO versus $\text{FeO}_{\text{total}}$, TiO_2 , CaO, and P_2O_5 , and negative correlations versus SiO_2 (Figure 3). No systematic trends are observed between MgO and Al_2O_3 , MnO, Na_2O and K_2O .

4.4.2 Trace elements

The NSVZ samples show typical subduction zone trace element patterns (Figure 4A), characterized by enrichment in fluid-mobile Large Ion Lithophile Elements (LILE) such as Cs, Rb, Ba, U, K, and Pb, and depletion in some High Field Strength Elements (HFSE) Ti, Nb, and Ta but enrichment in Zr and Hf. They are similar to TSVZ andesites. The andesites in both segments are more enriched in incompatible elements than TSVZ mafic rocks but display the same flat Heavy (H) REE patterns.

4.4.3 Isotopes

Our $^{87}\text{Sr}/^{86}\text{Sr}$ and $^{143}\text{Nd}/^{144}\text{Nd}$ isotope data are similar to those of previous studies from the NSVZ (Hildreth and Moorbath, 1988, Futa and Stern, 1988) (Figure 5). The NSVZ samples form a good negative correlation and extend to more enriched Sr and Nd isotope ratios than the TSVZ. The samples from San José have the most radiogenic Sr values in the NSVZ. The samples from the El Teniente copper district show a progressive increase in Sr and decrease in Nd isotope ratios with decreasing age (Kay et al., 2005).

Our high-precision double spike Pb isotope data form a much narrower array than the unspiked data of Hildreth and Moorbath (1988) and thus their data are not shown in figure 6 and 7. Our NSVZ data overlap those for the TSVZ volcanic arc on the uraniumogenic Pb isotope diagram (Figure 6) but are shifted to less radiogenic values, and completely overlap the CSVZ.

The NSVZ literature data extend to both lower and higher $\Delta 7/4$ values over a larger range in $^{206}\text{Pb}/^{204}\text{Pb}$ (not shown). The NSVZ overlap the lower bound of the Chilean trench sediment field. They also lie at the radiogenic end of the array for the TSVZ backarc close to the northernmost backarc samples. On the $^{208}\text{Pb}/^{204}\text{Pb}$ versus $^{206}\text{Pb}/^{204}\text{Pb}$ diagram (Figure 7), our NSVZ samples have higher $\Delta 8/4$ than the rest of the SVZ volcanic arc samples and overlap the literature results (not shown).

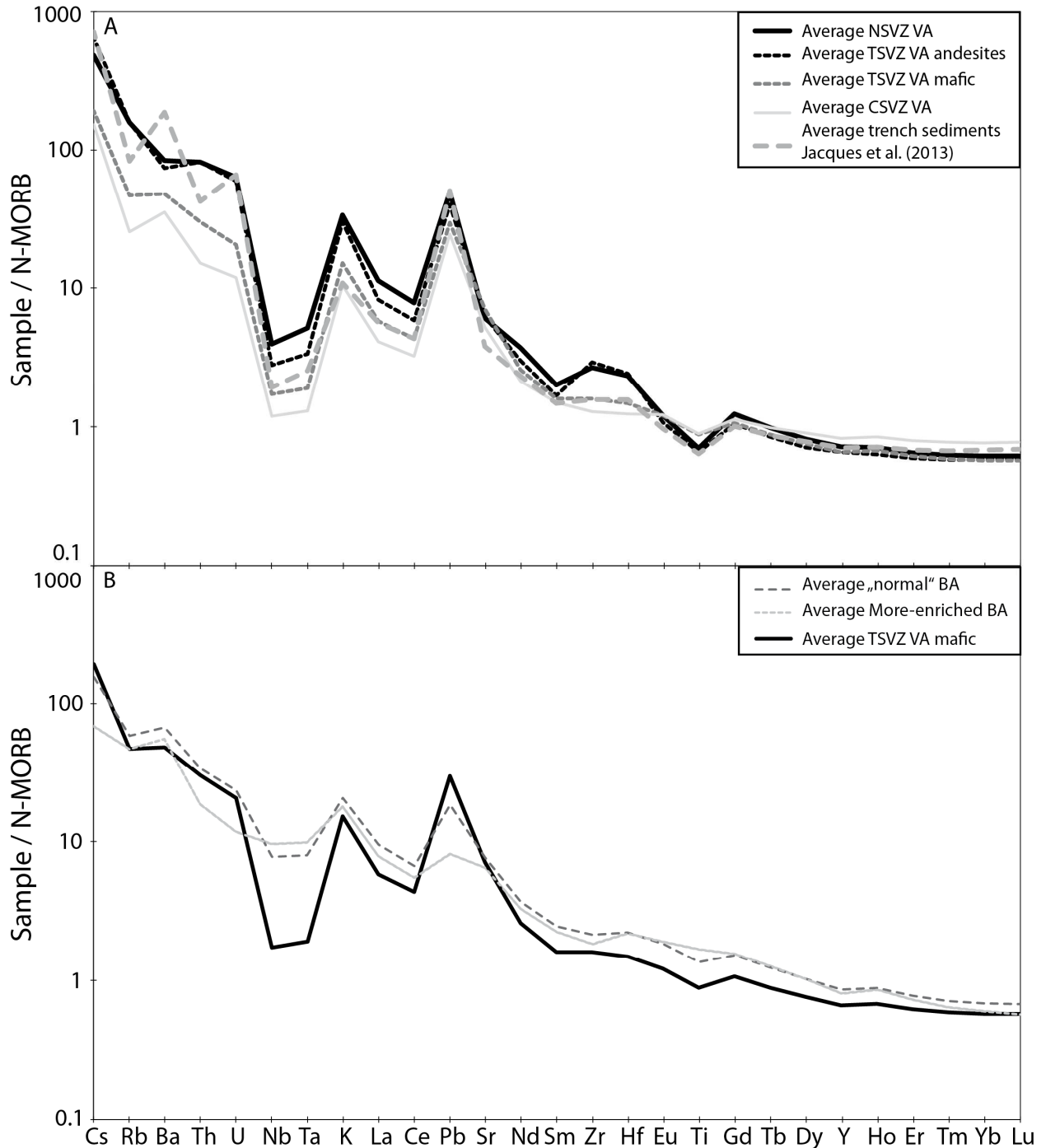


Figure 4.4 (Previous page) Multi-element diagram normalized to N-MORB after Sun and McDonough (1989) showing (A) average of all SVZ volcanic arc segments and average trench sediments between 34.5-38°S (Jacques et al., 2013) and (B) average of the “normal” backarc (34.5-42°S) and the “More-enriched” backarc (38-42°S) groups and compared with average of TSVZ VA mafic samples. NSVZ samples show typical subduction zone trace element signatures highlighted by Pb and K peaks and Nb and Ta troughs. The NSVZ samples have positive Zr-Hf anomalies and overlap the TSVZ andesites samples. The TSVZ mafic and CSVZ samples have lower abundances of moderately to highly incompatible elements. Data source are the same as in Figure 2.

The NSVZ samples define a good positive correlation between $^{176}\text{Hf}/^{177}\text{Hf}$ and $^{143}\text{Nd}/^{144}\text{Nd}$ ($r^2 = 0.98$) and extend the trend defined by other SVZ volcanic front samples to lower values (Figure 8), slightly below the mantle array defined by Vervoort et al. (1999). Taken together, the SVZ volcanic front samples form an excellent linear correlation ($r^2 = 0.99$). The BA samples also form a sub-parallel linear array ($r^2 = 0.82$) that is shifted to lower eHf values.

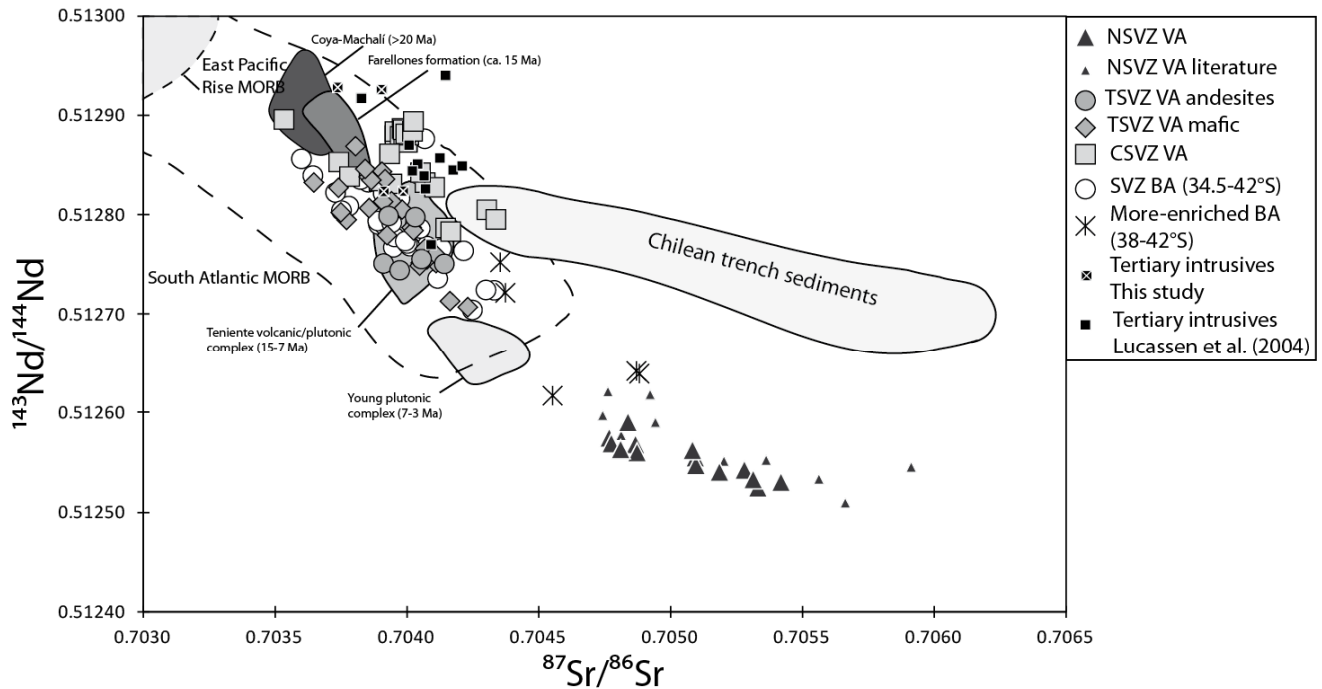


Figure 4.5 $^{87}\text{Sr}/^{86}\text{Sr}$ versus $^{143}\text{Nd}/^{144}\text{Nd}$ showing data for the NSVZ, TSVZ, CSVZ, backarc (BA), trench sediments, Tertiary intrusive and MORBs. The error bars are within the size of the symbols. The NSVZ samples are displaced toward higher Sr and lower Nd isotope ratios relative to the TSVZ. They overlap the trench sediments in Sr isotopes but have lower Nd isotopes. The data from El Teniente show a progressive enrichment in Sr and Nd isotope ratios with decreasing age. SVZ and BA data after Jacques et al. (2013, and Submitted, Chemical Geology). NSVZ Literature data from Hildreth and Moorbath (1988) and Futa and Stern (1988). El Teniente data after Kay et al. (2005) (initial ratios plotted). Tertiary basement from this study and Lucassen et al. (2004). Chilean trench sediments data after Jacques et al. (2013) and Lucassen et al. (2010). Southern East Pacific Rise (20-34°S) MORB data after Fontignie and Schilling (1991), Haase (2002), Hamelin et al. (1984), Hanan and Schilling (1989), Ito et al. (1980), Ito et al. (1987), Kingsley et al. (2007), MacDougall and Lugmair (1986), Mahoney et al. (1994), Newsom et al. (1986) and White et al. (1987). South Atlantic (30-50°S) MORB data after Andres et al. (2002), Douglas et al. (1999), Fontignie and Schilling (1996), Hanan et al. (1986) and Roy-Barman et al. (1998).

Oxygen isotope ratios are commonly measured for minerals (olivine and plagioclase) in order to reduce effects of alteration. However, it is then necessary to calculate $\delta^{18}\text{O}$ for co-existing melts and this is not simple for rocks as differentiated as in this study. For the TSVZ, Jacques et al. (2013) used the mineral-melt equilibrium equation from Bindeman et al. (2004) that adjusts mostly for the silica content of the melt and temperature. For the CSVZ, Jacques et al. (submitted, Chemical Geology) analyzed the $\delta^{18}\text{O}$ in the groundmass as well as minerals and found discrepancies of 0.5-1‰ between the measured groundmass and calculated melt values. The average ‰ difference between measured groundmass and olivine was +0.6‰ which is also the difference between MORB (e.g. 5.8‰; e.g. Bindeman (2008) and references therein) and mantle peridotite (5.2‰ \pm 0.3; e.g. Matthey et al., 1994). Table 3 reports the mineral, whole rock, and calculated melt (olivine equivalent plus 0.6‰) $\delta^{18}\text{O}$ data for the NSVZ samples. Measured and calculated results agree \pm 0.3‰ on average except for three samples from San José and one from Maipo. Plagioclase separates from the three discrepant San José samples have the lowest and the highest $\delta^{18}\text{O}$, that we measured yet their whole rock $\delta^{18}\text{O}$ are very similar. Lacking more detailed information about mineral compositions and histories in samples such as these, we will use our whole rock data as melt values in this paper.

The $\delta^{18}\text{O}(\text{melt})$ ranges from 5.64‰ to 6.36‰. This extends from the MORB mantle range (5.5-5.9‰, Bindeman, 2008 and references therein) to slightly higher values, but remain within the range of oceanic island arcs (5.5-6.8‰; e.g. Ewart and Hawkesworth, 1987, Turner et al., 2009, Vallier et al., 1991, Wade et al., 2005) (Figure 9). $\delta^{18}\text{O}(\text{melt})$ from the NSVZ samples do not correlate with parameters of differentiation (e.g. SiO_2 , $r^2 = 0.05$; MgO , $r^2 = 0.004$) (Figure 9) or with other isotopes (e.g. $^{87}\text{Sr}/^{86}\text{Sr}$, $r^2 = 0.04$). There is, however, a crude positive correlation with $\Delta 7/4$ ($r^2 = 0.67$) (Figure 10).

4.4.4 Basement samples

We compare our results to those by Kay et al. (2005) for Tertiary plutonic rocks from the El Teniente region in the forearc of the NSVZ and to those by Lucassen et al. (2004) for Tertiary to Paleozoic plutonic and metamorphic rocks between 36-41°S. Isotopic comparison between

the recent NSVZ volcanic rocks versus basement samples is complicated by the diversity of basement rocks and by the greater scatter of unspiked Pb isotope analyses.

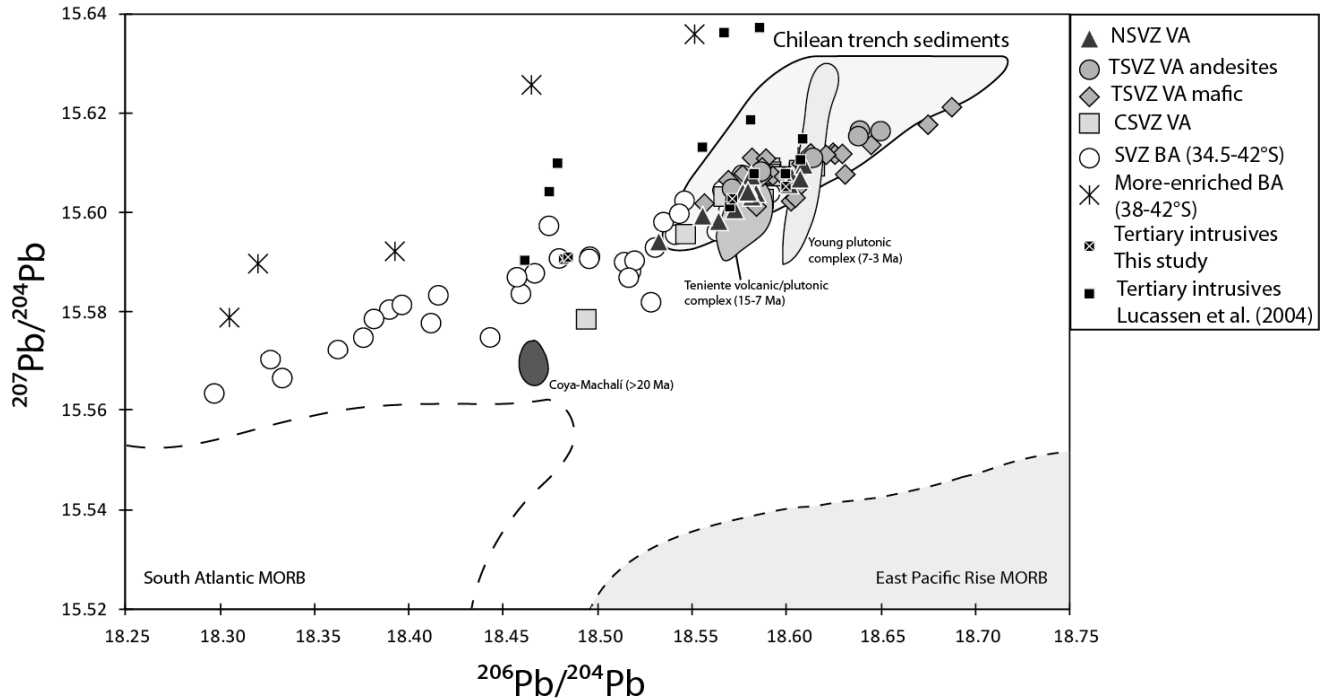


Figure 4.6 $^{206}\text{Pb}/^{204}\text{Pb}$ versus $^{207}\text{Pb}/^{204}\text{Pb}$ showing data for the NSVZ, TSVZ, CSVZ, backarc, trench sediments, Tertiary intrusive and MORBs. The errors are smaller than the symbol size. The NSVZ samples overlap with but extend to less radiogenic uraniumogenic Pb isotope ratios than the TSVZ, and overlap the radiogenic end of the BA array (Jacques et al. 2013, and Submitted, Chemical Geology). The NSVZ samples overlap the unradiogenic end of the trench sediment field. The data from El Teniente show a progressive enrichment in $^{206}\text{Pb}/^{204}\text{Pb}$ and $^{207}\text{Pb}/^{204}\text{Pb}$ with decreasing age. Data sources are the same as in Figure 5. El Teniente data are renormalized to our preferred values for NBS981 (see text).

Our samples from Tertiary plutons in the El Teniente region in the forearc of the NSVZ have Sr and Nd isotopic compositions similar to the samples from Kay et al. (2005). However, the plutonic and volcanic rocks from Kay et al. (2005) are progressively more enriched in Sr and Nd through time. Consequently, the Tertiary intrusives analyzed by Lucassen et al. (2004) between 36-41°S and our Teniente samples only overlap the Early Miocene samples from Kay et al. (2005). On both Pb isotope diagrams, our Tertiary samples overlap those of Lucassen et al. (2004) but our samples form a much tighter array, whereas Lucassen et al. (2004)'s data extend to slightly higher $^{207}\text{Pb}/^{204}\text{Pb}$ and $^{208}\text{Pb}/^{204}\text{Pb}$ at a given $^{206}\text{Pb}/^{204}\text{Pb}$. The Early Miocene Teniente samples analyzed by Kay et al. (2005) have lower $\Delta 7/4$ and $\Delta 8/4$ than the other Tertiary units.

The Early Miocene units overlap the other Tertiary data in $^{207}\text{Pb}/^{204}\text{Pb}$ and $^{208}\text{Pb}/^{204}\text{Pb}$ but have slightly higher $^{206}\text{Pb}/^{204}\text{Pb}$.

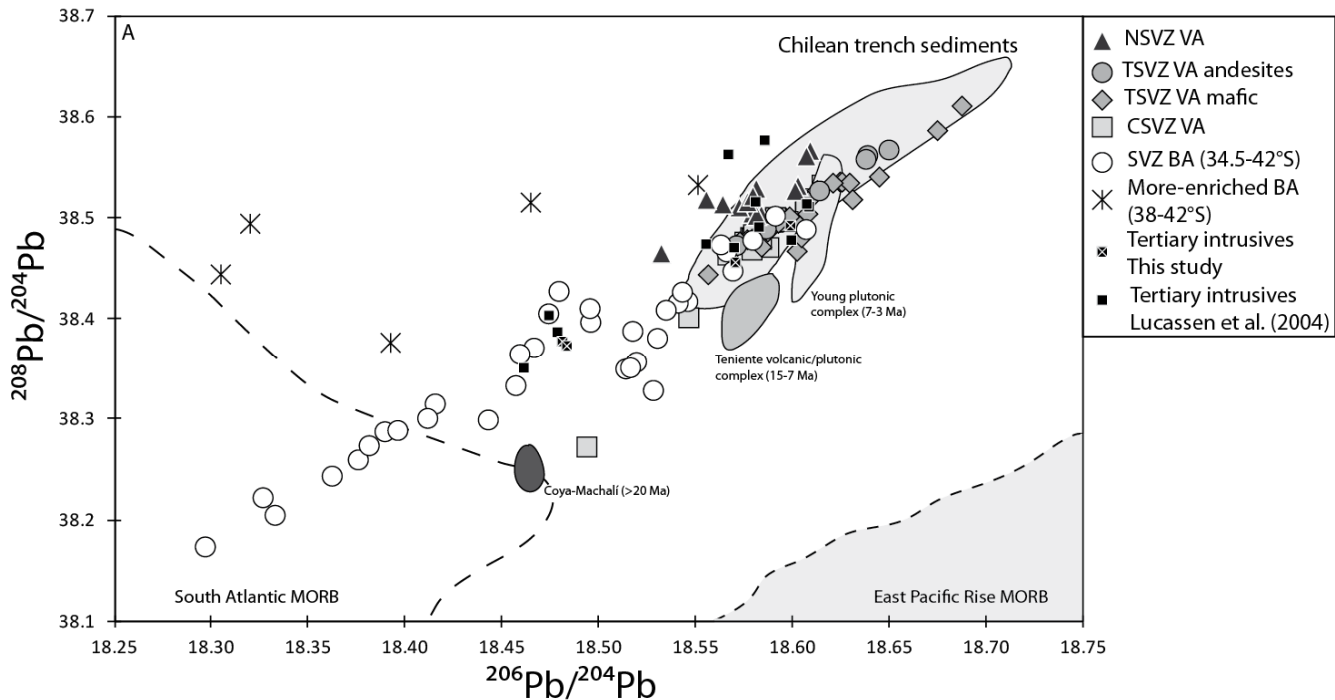


Figure 4.7 $^{206}\text{Pb}/^{204}\text{Pb}$ versus $^{208}\text{Pb}/^{204}\text{Pb}$ showing the NSVZ, TSVZ, CSVZ, backarc, trench sediments, Tertiary intrusive and MORBs. The NSVZ form a positive array that is sub-parallel to the array formed by the TSVZ and CSVZ but shifted to higher $^{208}\text{Pb}/^{204}\text{Pb}$ at similar $^{206}\text{Pb}/^{204}\text{Pb}$ ratios (i.e. have higher $\Delta 8/4$). The BA samples overlap but form two distinct arrays on the thorogenic Pb isotope diagram: one for samples with $^{206}\text{Pb}/^{204}\text{Pb} < 18.5$ and one with $^{206}\text{Pb}/^{204}\text{Pb} > 18.5$. The NSVZ array also lies above backarc samples with similar $^{206}\text{Pb}/^{204}\text{Pb}$ ratios, but on an extension of the array formed by samples with $^{206}\text{Pb}/^{204}\text{Pb} < 18.5$. The errors are smaller than the symbols. Data sources are the same as in Figure 5. El Teniente data renormalized to our preferred values for NBS981 (see text).

Our Mesozoic samples (in the NSVZ forearc, ca. 34°S) are also similar in Sr-Nd-Pb isotopic compositions than those from Lucassen et al. (2004) (between 36-41°S). In the Sr versus Nd isotope diagram, the Mesozoic rocks have higher Sr but lower Nd isotope ratios than the Tertiary units, although their Nd isotope ratios are slightly higher than the late Miocene samples from Kay et al. (2005). In the Pb isotopes diagrams, our data form a much tighter array than those of Lucassen et al. (2004). CL 603 exhibits very radiogenic Pb compositions, and two samples (CL 601 and CL 605) have higher $^{206}\text{Pb}/^{204}\text{Pb}$ at similar $^{207}\text{Pb}/^{204}\text{Pb}$ than the other samples. The Mesozoic samples from Lucassen et al. (2004) also extend to lower $^{208}\text{Pb}/^{204}\text{Pb}$

than our samples. Sample CL 603 has the most radiogenic Sr and Pb, and the highest $\delta^{18}\text{O}$ (9.1‰), of any Mesozoic plutonic sample, but similar Nd isotopes.

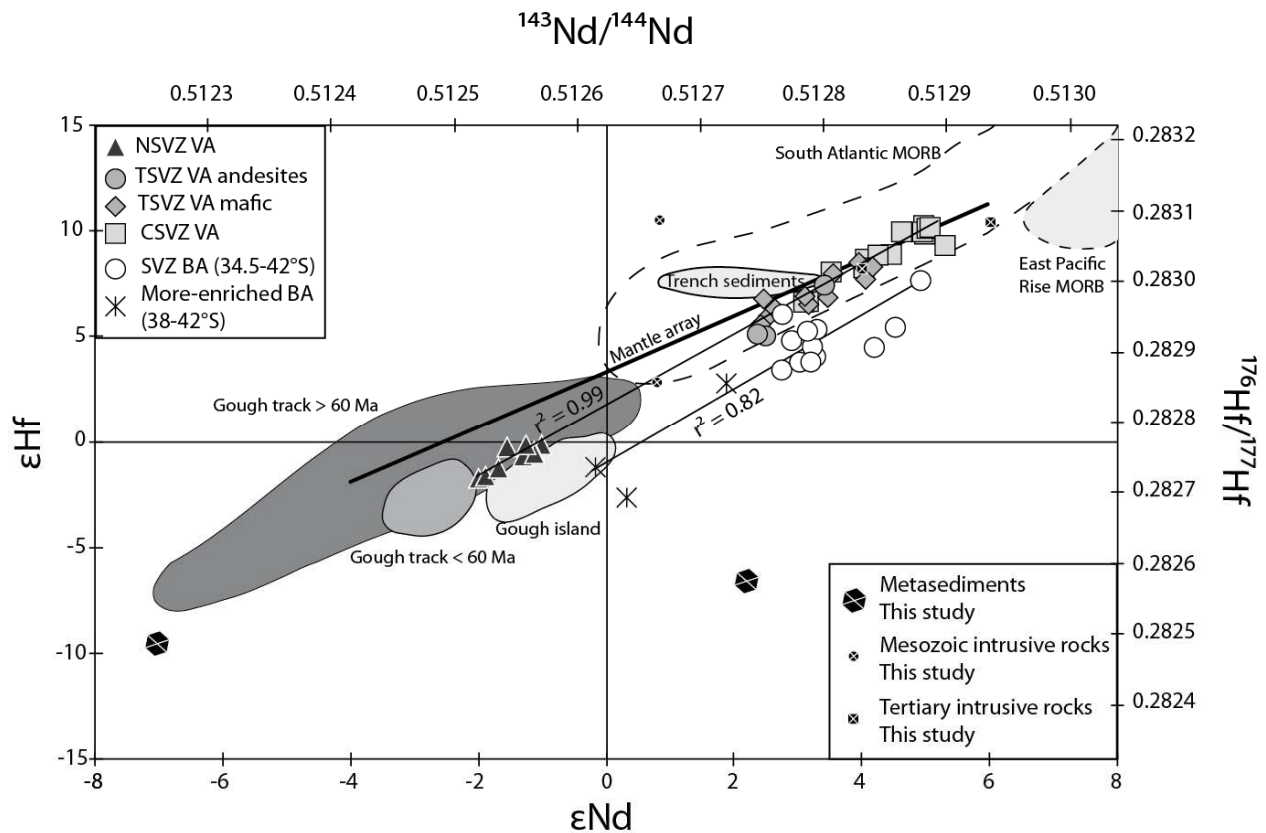


Figure 4.8 ϵNd versus ϵHf . The NSVZ samples plot on the same array defined by the other SVZ samples, slightly below the mantle array of Vervoort et al. (1999). The SVZ volcanic arc and backarc form two subparallel trends. Data sources are the same as in Figure 5. Gough Island, Gough track < 70 Ma and Gough track > 70 Ma from Rohde et al. (2013) and references therein.

Our two meta-sediment samples have comparable Sr, Nd, and Pb isotopes to the metamorphic rocks of Lucassen et al. (2004) that are as, or more, enriched than their Paleozoic intrusives (Figure 11A, 12A, 13A). In particular, our spiked analyses confirm the distinctively high $\Delta 7/4$ of all metamorphic rocks and Paleozoic intrusives in the area. Our meta-sediments have much higher O isotopes values than the plutonic rocks (> 15‰, Ralf Halama unpublished data) (Figure 10). One of our samples, CH 1-44, a pelitic schist, has anomalously high $^{143}\text{Nd}/^{144}\text{Nd}$ relative to other isotopes whereas the other lies on the enriched end of a trend in Hf-Nd isotopes that extends from Tertiary to Mesozoic intrusives (Figure 8).

The Tertiary intrusives are consistently more isotopically depleted than the Mesozoic intrusives in both studies, and the Paleozoic intrusives are more enriched, especially in ^{207}Pb . $\delta^{18}\text{O}$ in our plutonic rocks display a wide range from -1.73 to 9.08‰ (Figure 10). Duplicate analyses show that their O isotopic compositions are also variable between different aliquots of the same sample (Table 2).

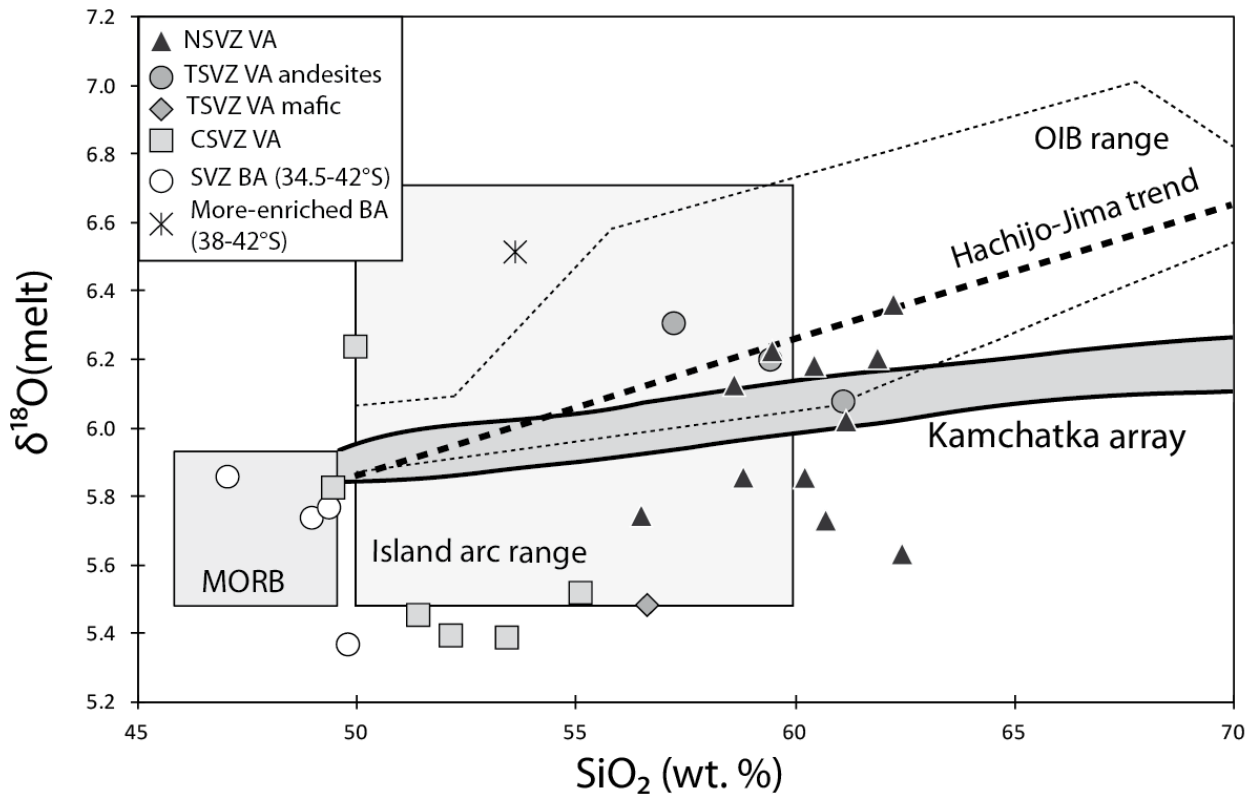


Figure 4.9 SiO_2 (wt. %) versus $\delta^{18}\text{O}$ (melt). The NSVZ samples overlap the MORB range (5.5-5.9‰) and extend to slightly higher values, but remain within the range of Island arc (5.5-6.8‰). There is no correlation between $\delta^{18}\text{O}$ (melt) and SiO_2 . MORB range and Kamchatka array after Bindeman et al. (2004); Hachijo-jima trend after Matsuhisa (1979); OIB range after Harris et al. (2000), Muehlenbachs and Byerly (1982), Sheppard and Harris (1985); Island arc range after Ewart and Hawkesworth, 1987, Turner et al., 2009, Vallier et al., 1991, Wade et al., 2005.

The Tertiary samples have lower Sr and higher Nd isotope ratios than our NSVZ volcanic samples, but they overlap in Pb isotopes. However, half of Lucassen et al. (2004)'s data have slightly higher $\Delta 7/4$ than the NSVZ volcanic rocks.

The Mesozoic samples have overall higher $^{143}\text{Nd}/^{144}\text{Nd}$ but four of our samples (CL 606, CL 607, CL 6012 and CL 615) plot at the lower end of the NSVZ array. In the Pb isotope space, the Mesozoic samples overlap the NSVZ volcanic samples, but extend to higher $^{206}\text{Pb}/^{204}\text{Pb}$

whereas the NSVZ samples extend rather to lower $^{206}\text{Pb}/^{204}\text{Pb}$ compared to the TSVZ volcanic rocks. Moreover, the four aforementioned samples are more radiogenic than the NSVZ volcanic samples.

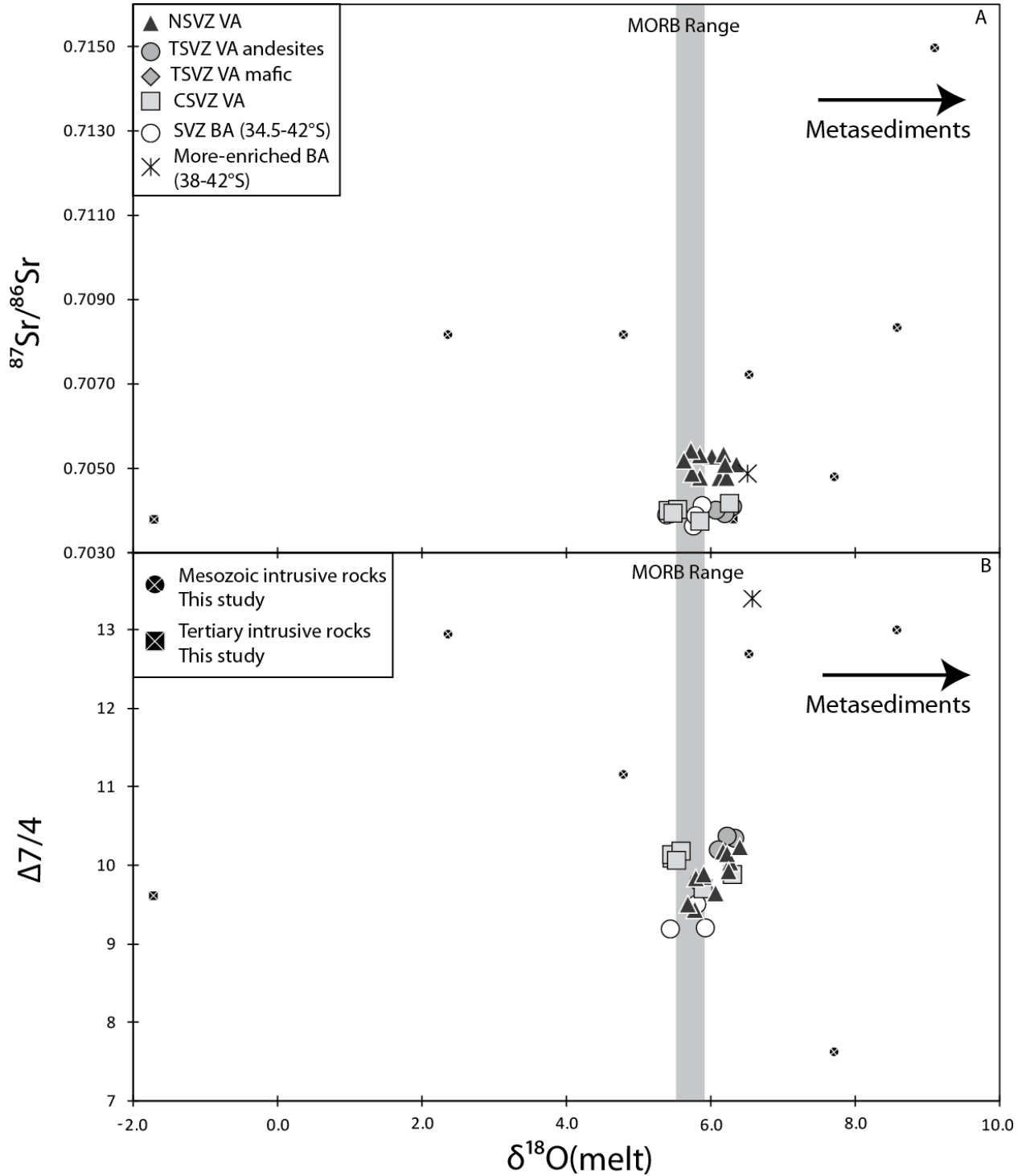


Figure 4.10 (Previous page) $\delta^{18}\text{O}(\text{melt})$ versus (A) $^{87}\text{Sr}/^{86}\text{Sr}$ and (B) $\Delta 7/4$. There is no clear correlation between $\delta^{18}\text{O}$ and Sr isotope ratio for the NSVZ. $\delta^{18}\text{O}(\text{melt})$ forms a very crude positive correlation with $\Delta 7/4$. Data source are the same as in Figure 2. $\Delta 7/4$ calculated after Hart (1984).

Although the Paleozoic plutonic and metamorphic rocks have higher Sr and lower Nd isotope ratios than the NSVZ volcanic rocks and overlap them in $^{208}\text{Pb}/^{204}\text{Pb}$, they extend to higher $^{207}\text{Pb}/^{204}\text{Pb}$.

4.5 Discussion

4.5.1 Variations of the slab input compositions and mantle wedge

Variations in the slab inputs and mantle wedge best explain the diversity of Quaternary magma compositions elsewhere in the SVZ (Jacques et al., 2013, in review) so we will first examine whether they can explain the more enriched isotope signature in the NSVZ despite the thicker continental crust.

4.5.1.1 *The oceanic crust*

The subducted oceanic crust has an EPR composition offshore of the NSVZ, as is also the case for the adjacent TSVZ, although it is slightly older and therefore might be more altered. Consequently, it might have more radiogenic Sr and perhaps Pb. However, Nd and Hf isotope ratios in NSVZ samples are much lower than in EPR MORB and TSVZ samples (Figure 8), and these elements are insensitive to seawater alteration. The subducting crust and the lithospheric mantle might be more serpentized, but this would lead to higher Nd isotope ratios as in the CSVZ (Jacques et al., submitted, Chemical Geology), not lower. More EPR-type oceanic crust cannot explain the higher $\Delta 8/4$ in NSVZ samples relative to TSVZ samples (Figure 7).

The enriched isotopic composition may also come from seamounts from the Juan Fernández Ridge subducting just north of the NSVZ. The subduction of seamounts can contaminate the mantle wedge in trace elements and isotopes, e.g. the subduction of the

Galapagos hotspot track in Central America (Hoernle et al., 2008; Gazel et al., 2011). However, the NSVZ do not resemble the HIMU-type Juan Fernández Ridge (Baker et al., 1987; Devey et al., 2000; Farley et al., 1993; Gerlach et al., 1986). They are characterized by low Sr and high Nd isotope ratios, and radiogenic Pb isotopic composition (Figure 11B, 12B, 13B) and cannot explain the shift to higher $^{87}\text{Sr}/^{86}\text{Sr}$ and $\Delta 8/4$, and lower $^{143}\text{Nd}/^{144}\text{Nd}$, $^{176}\text{Hf}/^{177}\text{Hf}$, $^{206}\text{Pb}/^{204}\text{Pb}$ and $^{207}\text{Pb}/^{204}\text{Pb}$ isotope ratios of NSVZ lavas relative to the TSVZ.

Table 4.3 O isotope data from olivine, plagioclase, groundmass and $\delta^{18}\text{O}(\text{melt})$ converted from mineral $\delta^{18}\text{O}$ (by adding 0.6‰ to the olivine value). $\delta^{18}\text{O}$ determined from: o = olivine, pl = plagioclase, px = orthopyroxene, br = bulk rock, gm = groundmass. # unpublished data (R. Halama).

Sample number	Sample Location	$\delta^{18}\text{O}(\text{olivine})$	1σ	Mineral	$\delta^{18}\text{O}(\text{melt})$ (gm values)	$\delta^{18}\text{O}(\text{melt})$ (+0.6)	$\Delta(\text{measurements-corrected})$
Volcanic Arc							
CL 235	Tupungatito	5.58	0.07	o	6.13	6.18	0.05
CL 238	Tupungatito	4.99	0.10	o	5.86	5.59	0.27
CL 242	Tupungatito	5.52	0.21	o	5.75	6.12	0.37
CL 246	Tupungatito	5.68	0.05	o	6.23	6.28	0.05
CL 293	Tupungatito	5.76	0.10	pl		6.36	
CL 251	San José	4.60	0.10	pl	6.02	5.20	0.82
CL 255	San José	6.53	0.10	pl	6.19	7.13	0.94
CL 257	San José	5.25	0.10	pl	5.86	5.85	0.01
CL 262	San José	4.83	0.10	pl	5.73	5.43	0.30
CL 289	San José	5.28	0.14	pl	5.64	5.88	0.25
CL 290	San José	4.58	0.10	pl	6.31	5.18	1.13
CL 211	Maipo	5.06	0.10	px	6.36	5.66	0.70
CL 214	Maipo	5.21	0.10	px	6.21	5.81	0.40
Basement							
CL 601	Santa Cruz	7.69	0.15	pl			
		6.65	0.15	pl			
		5.94	0.15	pl			
CL 603	Santa Cruz	9.08	0.15	br			
CL 607	Pichidegua	2.34	0.15	pl			
		1.29	0.15	pl			
		2.77	0.15	pl			
CL 610	Litueche	4.77	0.15	br			
CL 612	Ruta 66	8.56	0.15	pl			
		8.09	0.15	pl			
		7.57	0.15	pl			
CL 615	San Antonio	6.51	0.15	pl			
		7.65	0.15	pl			
		8.58	0.15	pl			
CL 616	El Teniente	6.29	0.15	pl			
		6.84	0.15	pl			
		7.13	0.15	pl			
CL 618	Maipo Canyon	-1.73	0.15	br			
CH 1-9#	Pichilemu	16.55					
CH 1-44#	Pichilemu	14.3					

4.5.1.2 The sediments

No difference in composition is expected for sediment being subducted between the NSVZ versus TSVZ (Plank, 2011) but NSVZ parental magmas might have a larger mass fraction of melts of subducted sediment. The sediment trace element pattern on the multi-element diagram (Figure 4A) overlaps the NSVZ, TSVZ andesites, and TSVZ mafic samples. The NSVZ samples also overlap the Chilean trench sediment field in Sr and Pb isotopes, but their Nd and Hf isotopes are much more enriched (Figure 5, 6, 7 and 8). The NSVZ lavas also have similar Ce/Pb and Nb/U trace element ratios than the TSVZ lavas (not shown). Therefore, although there is a component in NSVZ volcanic arc that apparently comes from trench sediment, the distinctively low Nd and Hf isotopes in the volcanic rocks cannot be explained by such sediments.

4.5.1.3 The mantle wedge

The SVZ mantle wedge has been sampled by backarc basalts behind the TSVZ and CSVZ (Jacques et al., 2013 and submitted, *Chemical Geology*). However, these centers only extend to the southernmost part of the NSVZ behind Maipo. Therefore, we use our data for backarc basalts behind the TSVZ and CSVZ segments plus the northernmost backarc center that is 30 km south of Maipo. The backarc samples overlap the TSVZ samples (including the TSVZ andesites, see section 5.2 below) in Sr and Nd isotopes, and extend to less radiogenic Pb isotope ratios (Figure 5, 6, 7; Jacques et al., 2013 and submitted, *Chemical Geology*) with the exception of five more-enriched backarc samples with higher $^{207}\text{Pb}/^{204}\text{Pb}$. Their trace element patterns show less prominent peaks and troughs than the volcanic front (Figure 4B) consistent with less of a slab-derived component in their source.

Based on backarc basalts free of slab influence (36-42°S), the mantle wedge beneath the TSVZ and the CSVZ has two end-member components: 1) depleted South Atlantic mantle (SAM-D) with lower Sr and Pb and higher Nd isotope ratios; and 2) enriched South Atlantic mantle (SAM-E) with higher Sr and Pb and lower Nd isotope ratios (Jacques et al., 2013, and submitted,

Chemical Geology). Although the NSVZ samples lie somewhat below an extension of the TSVZ and CSVZ Hf-Nd arc data (Figure 8), their lower Hf and Nd isotopes do not converge toward the more-enriched component present in the CSVZ backarc (38-42°S). Instead, both backarc and volcanic arc form two sub-parallel trends even at low Nd isotope ratios (Figure 8).

4.5.1.4 Summary

In summary, inputs from subducting oceanic crust and trench sediments are similar in chemical composition between the NSVZ and the TSVZ, as foreseen by Hildreth and Moorbath (1988). Therefore, the geochemical differences between NSVZ versus TSVZ segments must come from the mantle wedge or continental crust. This is most evident in the ϵNd versus ϵHf diagram where the NSVZ volcanic arc andesites and regional backarc basalts form two sub-parallel trends, indicating that one or both of the more-enriched components in the NSVZ is either from the crust or from a somewhat different mantle.

The slab input into the backarc-type mantle wedge produces TSVZ-type volcanic arc magmas (Jacques et al., 2013). Either additional processes (crustal assimilation, subduction erosion of upper and/or lower continental crust, or lithospheric interaction) are needed to enrich TSVZ-type magmas into NSVZ magmas, or a different type of subarc mantle is needed beneath the NSVZ. This component must have higher $^{87}\text{Sr}/^{86}\text{Sr}$ and $\Delta 8/4$, and lower $^{206}\text{Pb}/^{204}\text{Pb}$, $^{207}\text{Pb}/^{204}\text{Pb}$, $^{143}\text{Nd}/^{144}\text{Nd}$ and $^{176}\text{Hf}/^{177}\text{Hf}$ than the TSVZ magmas.

4.5.2 Crustal effects: crystal fractionation, assimilation, and subduction erosion

The increased thickness of continental crust north of 37°S may play a prominent role in the differences between NSVZ magmas versus those farther south (e.g. Hildreth and Moorbath, 1988, Tormey et al., 1991) through some combination of more or different crystal fractionation, or more assimilation during magma ascent, or more subduction of the continental margin. It is inherently difficult to distinguish between these alternatives on purely geochemical grounds.

The evolved character and restricted range of composition of our samples from NSVZ volcanoes exacerbates the problem by making it hard to evaluate differentiation processes.

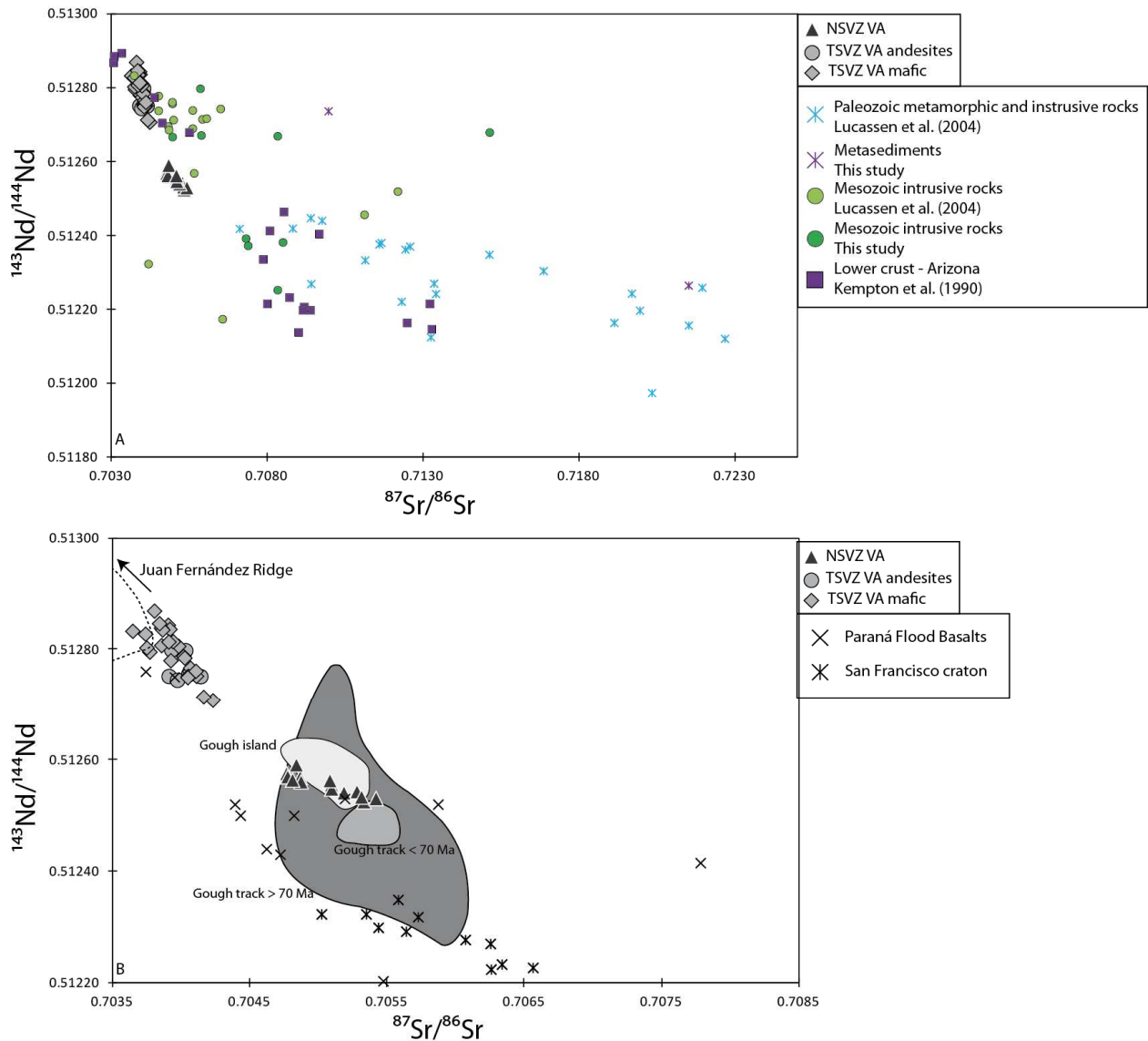


Figure 4.11 $^{87}\text{Sr}/^{86}\text{Sr}$ versus $^{143}\text{Nd}/^{144}\text{Nd}$ showing (A) the different crustal units and (B) the OIB Gough, the Juan Fernández Ridge, the Paraná Flood Basalts and the San Francisco craton. Paleozoic metamorphic and intrusive rocks may be required to explain this shift, but subcontinental lithosphere cannot be excluded. The Gough data overlap the NSVZ samples. Andean basement data after this study and Lucassen et al. (2004). Gough Island, Gough track < 70 Ma and Gough track > 70 Ma from Rohde et al. (2013) and references therein. Data for the Juan Fernández Ridge after Baker et al. (1987), Devey et al. (2000), Farley et al. (1993), Gerlach et al. (1986). Data for the San Francisco craton after Carlson et al. (1996). Filtered data ($\text{MgO} > 7 \text{ wt. } \%$) for the Paraná Flood Basalts after Gibson et al. (1997, 1999 and 2005), Marques et al. (1999), Rocha-Júnior et al. (2012, 2013). Lower crust data Kempton et al. (1990).

4.5.2.1 The effect of fractional crystallization (FC)

Our Tupungatito lavas are slightly more mafic (MgO = 3.6-4.2 wt. %) than those from San José and Maipo (MgO = 1.9-3.0 wt. %) but the difference is small, and parental magmas may differ between and within the volcanoes. Feineman et al. (2012) present evidence for crustal assimilation within Maipo from basaltic andesites to andesites. Our Maipo samples may also show some within-volcano enrichment in Sr-Nd-Pb isotopes with increased differentiation (Tables 1 and 2), but the apparent differentiation may simply reflect plagioclase accumulation because the Maipo sample that is most depleted in Sr-Nd isotopes (CL 213) also has anomalously high CaO, Al₂O₃, and Sr contents (Table 1 and 2). Therefore, the isotopic differences between our samples cannot be related to differentiation.

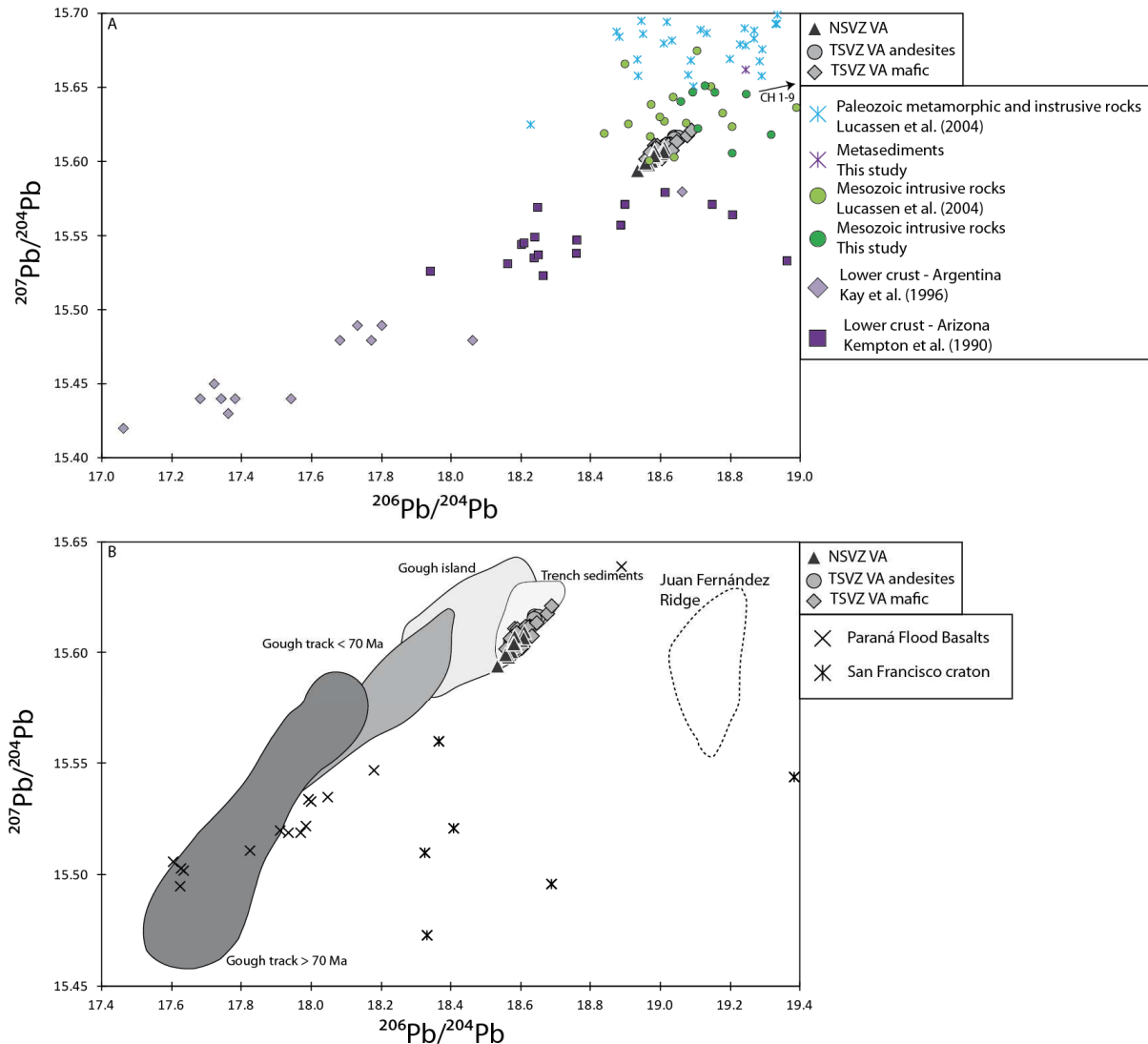


Figure 4.12 (Previous page) $^{206}\text{Pb}/^{204}\text{Pb}$ versus $^{207}\text{Pb}/^{204}\text{Pb}$ showing (A) the different crustal units and (B) the OIB Gough, the Juan Fernández Ridge, the trench sediments, the Paraná Flood Basalts and the San Francisco craton. While most of the crustal units have higher $^{206}\text{Pb}/^{204}\text{Pb}$ than the TSVZ and NSVZ, the Gough data may have the right composition. The lower crust cannot be excluded. Data sources are the same as in Figure 11. Lower crust data after Kay et al. (1996) and Kempton et al. (1990).

However, the differences between all of our samples and those from the adjacent TSVZ segment might be related to greater crystal fractionation in the NSVZ. Because basalts are generally absent in the NSVZ, our samples are mainly andesites (i.e. SiO_2 57-63 wt. %; Figure 2A) whereas most of our TSVZ samples are basalts to basaltic andesites (i.e. $\text{SiO}_2 < 56$ wt. %; Figure 2A). Nevertheless, because Jacques et al. (2013) also analyzed some TSVZ andesites and trachyandesites, we can directly compare andesites from both segments.

The major and trace element patterns for NSVZ andesites almost completely overlap those for TSVZ andesites (Figures 3 and 4A). Most andesites from both segments fall within the High-K field of Gill (1981) or at the Medium-K/High-K boundary (Figure 2B). They show the same enrichment in highly incompatible elements such as Rb, Cs, Zr, and Hf, and depletion in Ti, Nb, and Ta, relative to the TSVZ mafic samples. However, the NSVZ andesites have higher Nb, Ta, La and Ce abundances and therefore higher (Nb, Ta, La, Ce)/(Y, Yb) and La/Sm ratios relative to the TSVZ andesites, and the NSVZ samples have lower Eu^* . Therefore, either the NSVZ andesitic samples are derived from basalts that are more enriched in incompatible elements, or the differentiation processes caused more enrichment in incompatible elements relative to SiO_2 and MgO. And of course fractional crystallization alone cannot cause the differences in Nd and Hf isotopes between the segments.

4.5.2.2 Assimilation plus Fractional Crystallisation (AFC) of the upper crust

Hildreth and Moorbath (1988) proposed that the isotopic enrichment in the NSVZ comes from assimilating Paleozoic to Mesozoic upper crustal rocks. Our four enriched Mesozoic plutonics are examples of possible assimilants. They indeed have more enriched Sr and Nd isotopes than the NSVZ samples so mixing them into TSVZ-type magmas offers an explanation for those isotopes. Our Hf isotope data also are consistent with this proposal except for samples CL 611 and CH 1-44.

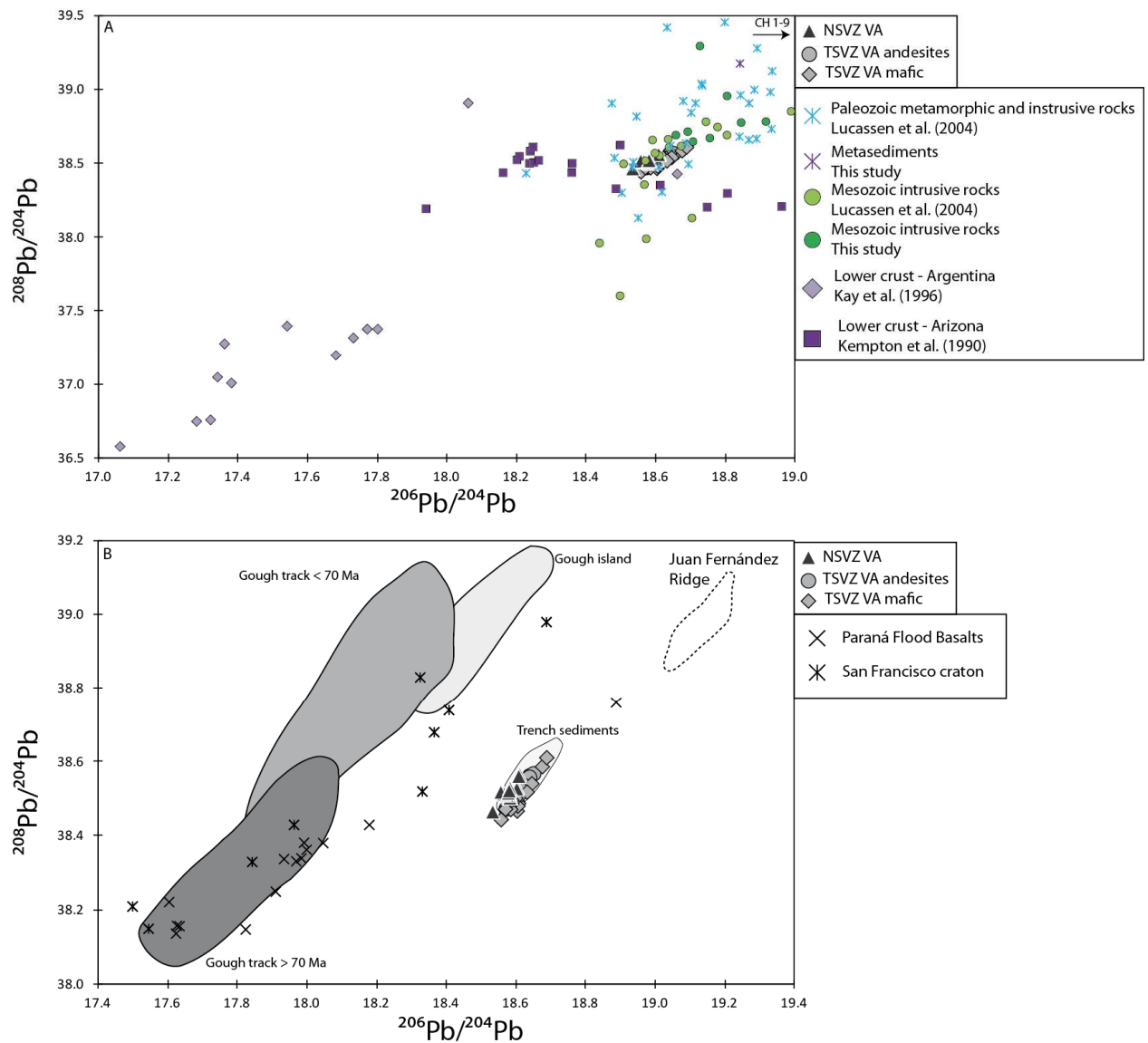


Figure 4.13 $^{206}\text{Pb}/^{204}\text{Pb}$ versus $^{208}\text{Pb}/^{204}\text{Pb}$ showing (A) the different crustal units and (B) the OIB Gough, the Juan Fernández Ridge, the trench sediments, the Paraná Flood Basalts and the San Francisco craton. The lower crust from Arizona works as an endmember, but not the one from Argentina. The Gough data provide a good alternative solution to explain the shift to higher $\Delta 8/4$ and lower $^{206}\text{Pb}/^{204}\text{Pb}$ for the NSVZ compared to the TSVZ. Data sources are the same as in Figure 12.

However, as previously pointed out by Stern (1991), within or between NSVZ volcanoes, correlations between SiO_2 and isotope ratios are absent or weak in volcanic rocks with $\text{SiO}_2 < 63$ wt. % (e.g. $^{87}\text{Sr}/^{86}\text{Sr}$, $r^2 = 0.39$; $^{143}\text{Nd}/^{144}\text{Nd}$, $r^2 = 0.27$; $^{206}\text{Pb}/^{204}\text{Pb}$, $r^2 = 0.19$) (Figure 14), even when including previous literature data (Hildreth and Moorbath, 1988, Futa and Stern, 1988). The same is true relative to MgO (e.g. $^{87}\text{Sr}/^{86}\text{Sr}$, $r^2 = 0.25$; $^{143}\text{Nd}/^{144}\text{Nd}$, $r^2 = 0.04$; $^{206}\text{Pb}/^{204}\text{Pb}$, $r^2 = 0.17$) (not shown). Furthermore, the Pb isotopes of all analyzed Paleozoic and Mesozoic basement rocks preclude them as assimilants because their Pb is more radiogenic than in TSVZ volcanics. Our spiked Pb isotope analyses show that NSVZ samples have lower $^{207}\text{Pb}/^{204}\text{Pb}$ ratios

than all Paleozoic and most Mesozoic basement rocks at similar $^{206}\text{Pb}/^{204}\text{Pb}$ (Lucassen et al., 2004, and this study; Figure 12A). In addition, most of our NSVZ samples have mantle-like $\delta^{18}\text{O}(\text{melt})$ (Figure 9). The few samples with $\delta^{18}\text{O}(\text{melt})$ higher than the MORB mantle range still have $\delta^{18}\text{O}(\text{melt}) < 6.4\text{‰}$. These values overlap those from the TSVZ mafic and andesitic samples, and Jacques et al. (2013) attributed the slight enrichment in TSVZ magmas to fluxing the mantle wedge by a melt of Chilean trench sediments with $\delta^{18}\text{O} = 8\text{-}14\text{‰}$. Finally, despite the wide isotopic diversity of upper basement rocks studied, none has isotopic traits that can explain the differences between NSVZ and TSVZ volcanic rocks.

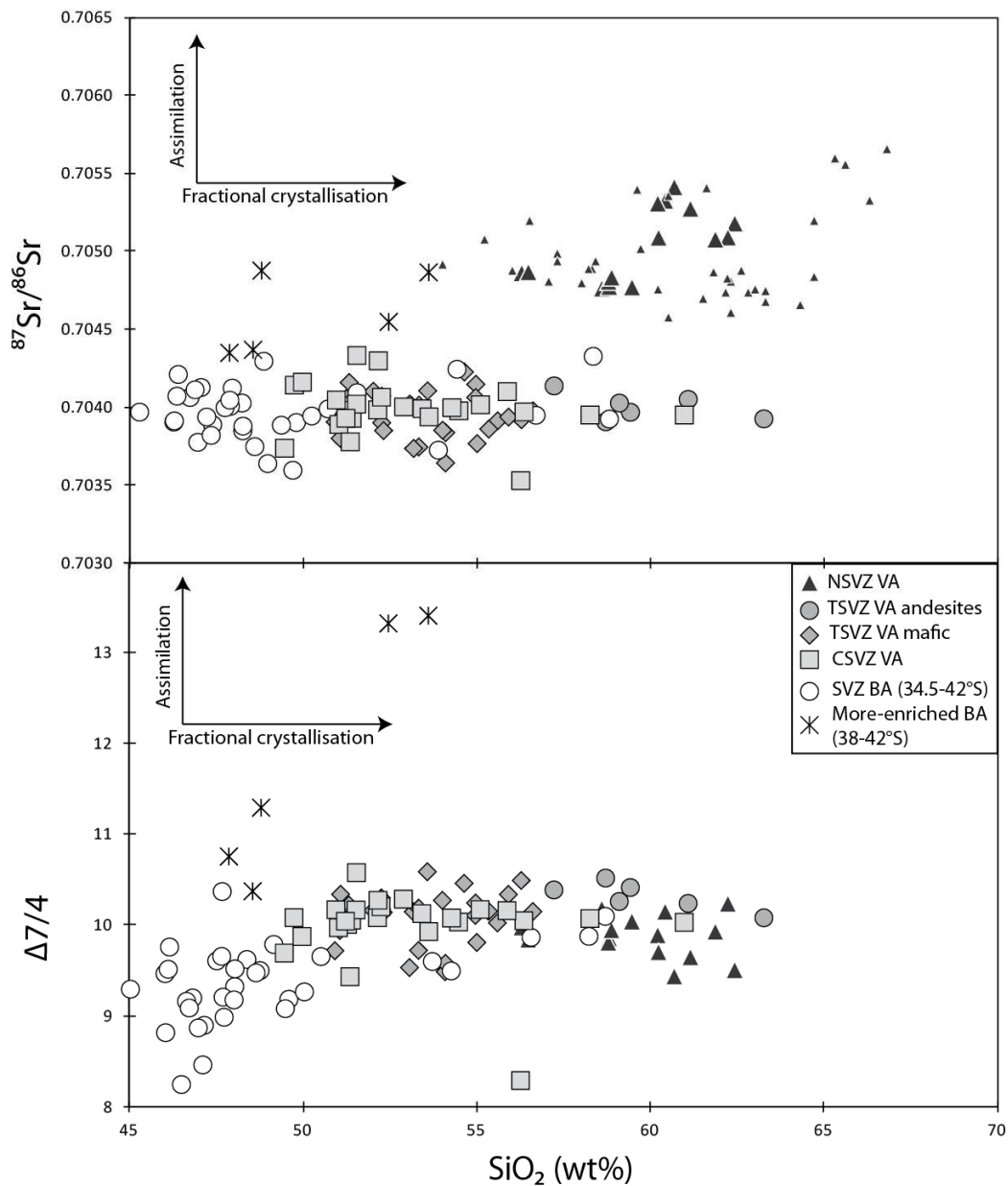


Figure 4.14 (Previous page) SiO₂ (wt. %) versus (A) ⁸⁷Sr/⁸⁶Sr, (B) Δ7/4. There is no correlation between SiO₂ content and isotopes. The isotopic shifts, especially in Δ7/4 cannot be explained by either differentiation or assimilation of the Andean basement. Data source are the same as in Figure 2. Δ7/4 calculated after Hart (1984).

Assimilation of young Tertiary plutonic rocks rather than upper crust has been proposed in the CSVZ at Llama volcano (Reubi et al., 2011) and at Puyehue volcano (Jicha et al., 2007). Tertiary plutons (El Teniente region) are the closest basement rocks to our NSVZ volcanoes (Figure 1B), and they overlap our NSVZ samples in Pb isotopes (Figure 12A, 13A). However, they have much lower ⁸⁷Sr/⁸⁶Sr and higher ¹⁴³Nd/¹⁴⁴Nd than the NSVZ samples (Figure 11A). Although one of the Tertiary plutons has similar δ¹⁸O to our NSVZ samples, the other has very low values probably due to hydrothermal alteration (Bindeman et al., 2004) (Figure 10). Within our volcanic rocks, we observe poor correlations between δ¹⁸O(melt) and other parameters of differentiation (e.g. SiO₂, r² = 0.05; MgO, r² = 0.004) or with other isotopes (e.g. ⁸⁷Sr/⁸⁶Sr, r² = 0.04) (Figure 9 and 10). Even if δ¹⁸O(melt) correlates positively with Δ7/4 (r² = 0.67), assimilation of Tertiary plutonic rocks does not explain the relative enrichment of Sr-Nd-Pb isotopes in our NSVZ samples.

4.5.2.3 Subduction erosion of the upper crust

Stern et al. (1991) concluded that addition of 1-2 % upper crust to the mantle wedge by subduction erosion could explain the isotopic enrichment NSVZ lavas. Kay et al. (2005) observed a decrease of Nd isotope ratios and an increase of ²⁰⁶Pb/²⁰⁴Pb from 27 to 3 Ma through time in volcanic and plutonic rocks from close to San José and Maipo. They concluded that the isotopic enrichment was triggered by two episodes of crustal shortening and arc migration that led to subduction erosion of Paleozoic rocks from the forearc crust. They attributed the reduced width of the metamorphic belt in the northern most part of the NSVZ forearc (north of 34°S, see Kay et al., 2005) and in the Pampean Flat Slab segment (27-33°S) to subduction erosion.

However, δ¹⁸O in Chilean metamorphic rocks (34.5°S) is much higher (above 15‰, Halama, unpublished data) (Figure 10, Table 3) than in the NSVZ samples. These metamorphic rocks (i.e., our metasediments and/or the Paleozoic metamorphic and intrusive rocks of

Lucassen et al., 2004) also have *more* radiogenic Pb isotope ratios. Incorporation of such material into the mantle wedge will make the Pb isotope ratios more radiogenic, but the NSVZ is instead shifted towards less radiogenic uraniumogenic Pb isotope ratios (Figure 12).

4.5.2.4 Lower crust influence

The previous sections have ruled out, on isotopic grounds, the involvement of upper crustal plutonic and metamorphic rocks, either assimilated during magma ascent or underthrust by subduction erosion.

However, it is possible that the isotopic characteristics of our NSVZ samples, in particular their low $^{206}\text{Pb}/^{204}\text{Pb}$ and $^{207}\text{Pb}/^{204}\text{Pb}$, reflects addition of lower crustal material. There is evidence of Proterozoic (Grenville age) lower crust beneath the NSVZ (Chilenia terrane: see Ramos, 2010). Kay et al. (1996) analyzed lower crustal samples from the Precordillera in Argentina, which come most probably from the Cuyenia terrane. The Cuyenia and Chilenia blocks were part of Laurentia that were accreted to Gondwana during the Paleozoic (see section 5.3.1). These two blocks share a tight history since the Proterozoic and some of the Chilenia terrane may be derived from the Cuyenia terrane (Ramos, 2010). Therefore, the samples analyzed by Kay et al. (1996) may be representative of the Chilenia terrane beneath the NSVZ. Although they have the necessary lower $^{206}\text{Pb}/^{204}\text{Pb}$ and $\Delta 7/4$ than the TSVZ, they also have lower $\Delta 8/4$ whereas the NSVZ has higher $\Delta 8/4$ (Figure 12A, 13A). Therefore they are not suitable assimilants either.

Because the North American and South American plates shared a common history during the Proterozoic, the lower crust in the Andes may have the same isotopic compositions as the lower crust that outcrops in the U.S.A. Kay et al. (1996) already mentioned that the Precordillera in Argentina has a connection with the Appalachian-Ouachita basement. Kempton et al. (1990) provides data from the Proterozoic lower crust in Arizona (which is close to the Appalachian-Ouachitan system) that we show in figures 11A, 12A and 13A. Although those samples cover a wide range in Sr, Nd and Pb isotopes, we will focus attention on the few samples that have the potential to be the required enriched component. They have relatively

high Sr and low Nd isotope ratios and $^{206}\text{Pb}/^{204}\text{Pb} < 18.5$, similar to the Argentinean lower crust, but most importantly they have the appropriate low $^{207}\text{Pb}/^{204}\text{Pb}$ and high $^{208}\text{Pb}/^{204}\text{Pb}$ isotope ratios.

We show these samples in Figure 15 where we use them to quantify the amount of lower crust necessary to add to TSVZ magma. For the latter we chose a typical depleted basalt (CL196 from Los Hornitos, Jacques et al., 2013). Between 10% and 30% of lower crust is required to explain the shift in $^{87}\text{Sr}/^{86}\text{Sr}$, $^{143}\text{Nd}/^{144}\text{Nd}$, and $\Delta 8/4$. Our data and mixing model cannot distinguish between assimilation (i.e. the lower crust is added into a TSVZ-type melt) versus subduction erosion (delaminating lower crust and mixing it into the mantle wedge) because of too many unknown parameters.

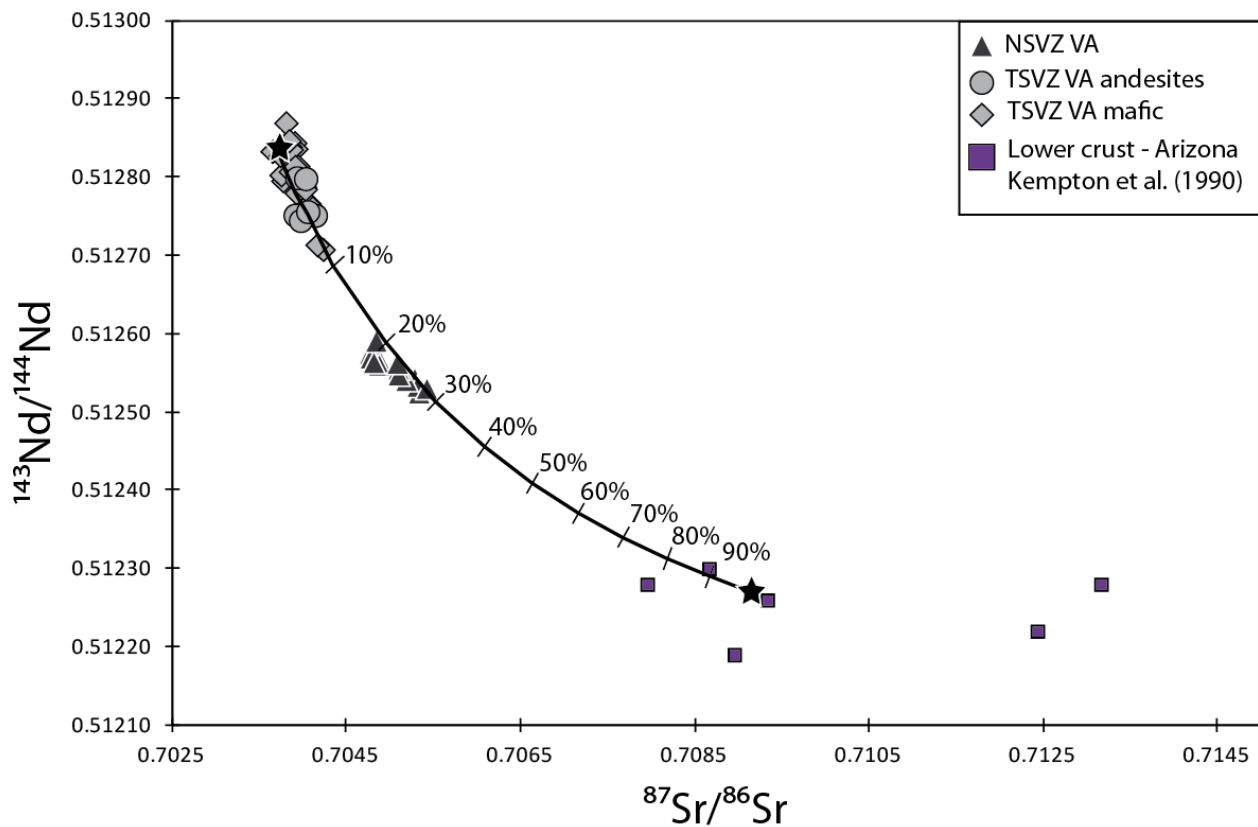


Figure 4.15 $^{87}\text{Sr}/^{86}\text{Sr}$ versus $^{143}\text{Nd}/^{144}\text{Nd}$ showing a binary mixing model between a depleted TSVZ component (CL 196 from Jacques et al., 2013; Sr = 482 ppm, $^{87}\text{Sr}/^{86}\text{Sr} = 0.7037$; Nd = 9.78 ppm, $^{143}\text{Nd}/^{144}\text{Nd} = 0.51283$) and an enriched lower crustal-type component (GN 22A from Kempton et al., 1990, Sr = 555 ppm, $^{87}\text{Sr}/^{86}\text{Sr} = 0.7091$; Nd = 29.4 ppm, $^{143}\text{Nd}/^{144}\text{Nd} = 0.51227$). The tick marks on the curve represent the amount of enriched component added, by 10% increment. The calculated curve passes through the NSVZ and ca. 20-30% lower crustal component are needed to explain the shift from the TSVZ to the NSVZ.

Nonetheless, we favor subduction erosion over assimilation. First, even though the lower crust samples from Arizona have high $\delta^{18}\text{O}$ (most have $> 6\text{‰}$), most of the $\delta^{18}\text{O}$ values from the NSVZ samples are within or slightly above the MORB range (5.5-5.9‰) which means that the primary O isotope signature is from the mantle. Assimilation would increase the $\delta^{18}\text{O}$ values in the NSVZ samples. Second, Kay et al. (2005) a temporal evolution of the isotopic enrichment in the El Teniente samples close to 34°S . Progressive enrichment of the mantle wedge can be better achieved via progressive erosion rather than progressive assimilation.

4.5.2.5 Summary

In summary, our isotope data rule out incorporation of upper crustal material, either by assimilation or subduction erosion. Assimilation of Paleozoic basement could explain the shift in Sr and Nd isotope ratios, but is not consistent with the mantle-like $\delta^{18}\text{O}(\text{melt})$ in most of the NSVZ samples. Pb isotope data also rule out both Paleozoic upper crust and Proterozoic lower crust from Argentina because the NSVZ has higher $\Delta 8/4$ and is shifted to lower $^{206}\text{Pb}/^{204}\text{Pb}$ and $^{207}\text{Pb}/^{204}\text{Pb}$ compared to the TSVZ. No known potential assimilant has such characteristics.

The Arizona lower crust, on the other hand, has an appropriate composition with low $\Delta 7/4$ and Nd isotopes, and high $\Delta 8/4$ and Sr isotopes. Our data do not let us distinguish between assimilation versus subduction erosion, but the mantle-like $\delta^{18}\text{O}(\text{melt})$ of our NSVZ samples and the geological evidence (see Kay et al., 2005) would favor subduction erosion over assimilation.

4.5.3 Mantle effects: enriched mantle in the NSVZ?

We demonstrated in the previous sections that none of the upper crustal rocks from the Andean basement can explain the distinctive isotopic composition of the Quaternary NSVZ lavas although lower crust from Arizona, which might also lie beneath NSVZ volcanoes, might possibly work. Therefore, we will also explore whether the enriched component might come from the lithospheric or asthenospheric mantle beneath the region. The Paraná Flood Basalt

Province in Brazil and Paraguay may have sampled an enriched component in the subcontinental lithosphere that results from terrane accretion during the Proterozoic to Paleozoic (Ramos et al., 2010). Alternatively, an enriched plume component may be present in the sub-South American asthenosphere (e.g. Carlson et al., 1996, Gibson et al., 1997, 1999, 2005). It would be from the Trindade plume that formed the Walvis Ridge and Rio Grande Rise and then separated into two separate tracks leading to Gough and Tristan da Cunha islands.

4.5.3.1 Enriched lithospheric mantle

The basement beneath the SVZ volcanic arc is primarily the Chilenia block; whereas the basement beneath the backarc is the Cuyenia block forms (see Ramos, 2010 for summary). These blocks were part of the Laurentian plate, located adjacent to what is now Texas (see Kay et al., 1996 and Ramos, 2010 for further discussion), and separated from Gondwana during the Mesoproterozoic. These blocks were later accreted to the Amazonian craton. During the Neoproterozoic and Paleozoic, they were amalgamated again to Gondwana. These displacements, detachments, and accretions indicate a complex system of paleo-subduction and terrane transfer between Laurentia and Gondwana during the Paleozoic (Ramos, 2010). Therefore, the presence of enriched subcontinental lithosphere beneath the NSVZ is possible, although there is no evidence of a tectonic boundary between the NSVZ and the TSVZ. Kay et al. (2005) noted that the geochemical enrichment occurred after different steps of arc migration during the Miocene, linked to sudden slab flattening. Arc migration could therefore result in progressively tapping different lithospheres, including lithospheric mantle that had not previously been stripped of its enrichment.

Lucassen et al. (2007) distinguished two different lithospheric mantle sources beneath the Cretaceous backarc of the Central Andes (18-34°S). One is more depleted and is the sub-arc mantle beneath the early Paleozoic arc. The other is more enriched and is the old subcontinental lithospheric mantle of the Proterozoic Brazilian Shield that was the source of Cretaceous intra-plate magmatic rocks. The latter was progressively thrust beneath the CVZ (McQuarrie et al., 2005). Delamination of the lithosphere could contaminate the underlying

asthenosphere. However, this component did not contribute to (or is not visible in) the Mesozoic to Cenozoic CVZ volcanic arc (Lucassen et al., 2007).

4.5.3.2 Enriched asthenosphere

Enriched Mantle type 1 (EM1) OIBs, such as the Gough domain of the Tristan-Gough hotspot track, has an isotopic composition (Rohde et al., 2013 and references therein) that in some respects matches what is needed as the enriched endmember of the NSVZ (Figure 11B, 12B and 13B). The Gough domain contains Gough Island, the southern “Gough” subtrack of the Guyot Province leading to the Walvis Ridge, and the > 70 Ma old portion of the Walvis Ridge and Rio Grande Rise. Although Sr-Nd-Hf largely overlap for the different areas (Figure 8 and 11B), there is a crude progression to more radiogenic Pb isotope ratios with decreasing age from the ≥ 70 Ma Walvis Ridge and Rio Grande Rise to the < 70 Ma Gough subtrack (Figure 12B and 13B). Most of the Gough domain samples have low $^{206}\text{Pb}/^{204}\text{Pb}$ and $^{207}\text{Pb}/^{204}\text{Pb}$ (in particular those from the older part of the hotspot track) and high $\Delta 8/4$ and overlap the NSVZ in Sr, Nd and Hf isotopes. Interestingly, this domain lies at the same latitude as the NSVZ. It has been proposed that the same plume component from Gough and Tristan da Cunha (the Trindade plume) was present beneath the San Francisco craton and the Paraná continental flood basalt field and contributed to Cenozoic intra-plate volcanism in southern Brazil and Paraguay (e.g. Carlson et al., 1996, Gibson et al., 1997, 1999, 2005) or at least heated the Brazilian subcontinental lithospheric mantle (Marques et al., 1999, Peate et al., 1999). In this scenario, some enriched plume material could have been left in the subcontinental lithospheric mantle when Gondwana broke up during late Mesozoic. The Brazilian subcontinental lithospheric mantle lies on the same array as the SVZ on the uraniumogenic Pb isotope diagram, has higher $\Delta 8/4$ than the NSVZ samples, and extends to more radiogenic Sr and Nd isotope ratios (Figure 11B, 12B and 13B). However, other authors (e.g. Comin-Chiaramonti et al., 1997, Rocha-Júnior et al., 2012, 2013) argued that the EM1 component is not present in Southern Brazil volcanism and that melting was triggered by a thermal anomaly unrelated to a plume (Ernesto et al., 2002). Instead, Rocha-Júnior et al. (2012, 2013) proposed that the

sublithospheric mantle beneath the Paraná flood province has been enriched by fluids or melts from Neoproterozoic subduction processes.

Husson et al. (2012) modeled the westward flow of South Atlantic mantle beneath South America as a counter-flow above the subducting Nazca plate. Therefore, this convection may bring enriched plume-derived asthenosphere from beneath the Parana province to beneath the Andes. Moreover, Wagner et al. (2006) observed the presence of low V_p/V_s ratios above the Pampean Flat Slab segment similar to cratonic lithosphere. They also observed high V_p/V_s ratios that indicate the presence of cold asthenosphere. They suggested that this material may be ancient Laurentian lithosphere while the cold asthenosphere was the result of the slab flattening during the Miocene which trapped and cooled the local asthenosphere. The Laurentian lithosphere metasomatized during the Parana flood basalt event, or asthenospheric mantle involved in the formation of the Tristan-Gough hotspot track, could have been pushed southward via trench-parallel flow, which occurs beneath the Andes (Russo and Silver, 1994), especially in northern Chile related to the flattening of the Pampean slab (Kneller and van Keken, 2007), possibly caused by the subduction of the Juan Fernandez Ridge (Figure 1).

4.5.4 General comparison: NSVZ – TSVZ – CSVZ

Upper crustal contamination has been proposed to explain the geochemical variations observed in the SVZ in Chile for more than two decades. This is especially true for arc segments north of 37°S where the crust gets thicker (e.g. Hildreth and Moorbath, 1988, Futa and Stern, 1988, Tormey et al., 1991, 1995). Others invoke subduction erosion of upper continental crust (Kay et al., 2005) ± small amounts of trench sediments (Stern, 1991) to explain the same data. Our results contradict both of these hypotheses.

South of 37°S, there is overall agreement that fluids derived from the dehydration of the subducting slab dominate the geochemistry of the volcanic rocks (e.g, Hickey et al., 1984, Hickey-Vargas et al., 1986, 1989, 2003; Futa and Stern, 1988; Sigmarsson et al., 1990, 2002). Assimilation of the hydrothermally-altered plutonic roots has also been invoked to explain

certain eruptive units from some volcanoes (San Pedro, Dungan and Davidson, 2004; Llaima, Reubi et al., 2011; Puyehue, Jicha et al., 2007).

Our studies have dealt with the most mafic volcanic rocks from volcanoes from 33°S to 43°S, extending 300 km into the backarc in Argentina (this paper; Jacques et al., 2013; Jacques et al., submitted, *Chemical Geology*) Surprisingly, upper crustal contamination cannot explain the geochemical variations observed in most of the SVZ. Instead, variations within TSVZ magmas result from variable slab input (largely dominated by the Chilean trench sediments) and variable South Atlantic-type mantle wedge. Further the south, CSVZ magmas require more fluid from the slab (possibly from serpentine).

We propose that the mantle wedge in the SVZ contains a minimum of two enriched mantle components: SAM-E, constrained by “normal” backarc basalts; and a more-enriched component, constrained from some CSVZ backarc basalts that has higher $^{87}\text{Sr}/^{86}\text{Sr}$, $\Delta 7/4$ and $\Delta 8/4$, and lower $^{143}\text{Nd}/^{144}\text{Nd}$ and $^{176}\text{Hf}/^{177}\text{Hf}$ than SAM-E. The latter may reflect enriched areas in the lithosphere.

If subduction erosion is not responsible for the isotopic enrichment seen in the NSVZ, then a third enriched mantle component might be present. It has higher $^{87}\text{Sr}/^{86}\text{Sr}$ and $\Delta 8/4$, lower Nd and $^{206}\text{Pb}/^{204}\text{Pb}$, and similar $\Delta 7/4$ than the SVZ samples. It may be from asthenospheric mantle beneath the NSVZ as a result of convection of plume material from beneath the Rio Grande Rise and South Atlantic Mid-Ocean Ridge (Husson et al., 2012) plus a southward push via trench-parallel flow from the flat-slab region (e.g. Russo and Silver, 1994, Kneller and van Keken, 2007). Alternatively it could be sub-continental lithosphere delaminated beneath the Paraná flood basalt region that was carried by asthenospheric flow.

4.6 Conclusions

We presented new Sr-Nd-Hf-Pb-O isotope data from the Northern Southern Volcanic Zone in Chile (33-34.5°S) from volcanic and crustal rocks. This comprehensive dataset provides new insights on the origin of the enriched signature observed in the northernmost segment of the SVZ.

Based on our new isotope data, we conclude that assimilation or subduction erosion of the continental upper crust cannot explain the enriched isotopic signature observed in the NSVZ samples. However, influence of local lower crust may not be excluded. The local lower crust in Argentina does not fit as an endmember, whereas the Arizona lower crust does. Assuming that the lower crust in Chile is similar to the one in Arizona because they share common history (see Kay et al., 1996 and Ramos, 2010 for more discussion about the South American tectonic history) and based on mantle-like $\delta^{18}\text{O}(\text{melt})$, subduction erosion of the lower crust may be a possibility. This scenario would be consistent with the geological observations made by Kay et al. (2005).

We also explore the possible involvement of enriched subcontinental lithospheric mantle similar to the Brazilian subcontinental lithospheric mantle or derived from enriched Proterozoic lithosphere, or enriched asthenospheric mantle derived from a plume with Gough-type composition. This component may have the appropriate composition in order to explain the enrichment in the NSVZ samples, and could have been transferred to the NSVZ from the Miocene as the arc migrates eastward and the slab flattens, capturing some enriched material that has then been pushed southward via trench-parallel flow.

References

- Aitchison S.J., Moorbath S., Soler P., Schneider A., Soria-Escalante E., Steele G., Swainbank I. and Wörner G. (1995) Pb isotopes define basement domains of the Altiplano, central Andes, *Geology* **23**, 555-558
- Amante C. and Eakins B.W. (2009) ETOPO1 1 Arc-Minute Global Relief Model: Procedures, Data sources and Analysis, NOAA Technical Memorandum NESDIS NGDC-24, 19pp
- Andres M., Blichert-Toft J. and Schilling J.G. (2002) Hafnium isotopes in basalts from the Southern Mid-Atlantic Ridge from 40° to 55°S: Discovery and Shona plume-Ridge interactions and the role of recycled sediments, *Geochemistry Geophysics Geosystems* **3**
- Auer S., Bindeman I.N., Wallace P., Ponomareva V. and Portnyagin M. (2009) The origin of hydrous, high- $\delta^{18}\text{O}$ voluminous volcanism: diverse oxygen isotope values and high magmatic water contents within the volcanic record of Klyuchevskoy volcano, Kamchatka, Russia, *Contributions to Mineralogy and Petrology* **157**, 209-230
- Angermann D., Klotz J. and Reigber C. (1999) Space geodetic estimation of the Nazca-South America Euler vector, *Earth and Planetary Science Letters* **171**, 329-334
- Ayers and Watson (1993) Rutile solubility and mobility in supercritical aqueous fluids, *Contributions to Mineralogy and Petrology* **114**, 321-330
- Bach W., Erzinger J., Dosso L., Bollinger C., Bougault H., Etoubleau J. And Sauerwin J. (1996) Unusually large Nb-Ta depletions in North Chile Ridge basalts at 36°50' to 38°56'; major element, trace element and isotopic data, *Earth and Planetary Science Letters* **142**, 223-240
- Baker P.E., Gledhill A.R., Harvey P.K. and Hawkesworth C.J. (1987) Geochemical evolution of the Juan Fernández islands, SE Pacific, *Journal of Geological Society of London* **144**, 933-944
- Behn M.D., Kelemen P.B., Hirth G., Hacker B.R. and Massonne H.-J. (2011) Diapirs as the source of the sediment signature in arc lavas, *Nature Geosciences* **4**, 641-646
- Bertotto G.W., Cingolani C.A. and Bjerg E.A. (2009) Geochemical variations in Cenozoic back-arc basalts at the border of La Pampa and Mendoza provinces, Argentina, *Journal of South American Earth Sciences* **28**, 360-373

- Bevis M. and Isacks B.L. (1984) Hypocentral trend surface analysis; probing the geometry of Benioff zones, *Journal of Geophysical Research* **89**, 6153-6170
- Bindeman I.N., Ponomareva V.V., Bailey J.C. and Valley J.W. (2004) Volcanic arc of Kamchatka: a province with high- $\delta^{18}\text{O}$ magma sources and large scale $^{18}\text{O}/^{16}\text{O}$ depletion of the upper crust, *Geochimica et Cosmochimica Acta* **68**, 841-865
- Bindeman I.N., Eiler J.M., Yogodzinski G.M., Tatsumi Y., Stern C.R., Grove T.L., Portnyagin M., Hoernle K. and Danyushevsky L.V. (2005) Oxygen isotope evidence for slab melting in modern and ancient subduction zones, *Earth and Planetary Science Letters* **235**, 480-496
- Bindeman I.N. (2008) Oxygen isotopes in mantle and crustal magmas as revealed by single crystal analysis, *Reviews in Mineralogy and Geochemistry* **69**, 445-478
- Blichert-Toft J. and Albarède F. (1997) The Lu-Hf isotope geochemistry of chondrites and the evolution of the mantle-crust system, *Earth and Planetary Science Letters* **148**, 243-258
- Burd A., Booker J.R., Pomposiello M.C., Favetto A., Larsen J., Giordanengo G. and Orozco Bernal L. (2008) Electrical conductivity beneath the Payún Matrú volcanic field in the Andean back-arc of Argentina near 36.5°S: insights into the magma source, 7th International symposium on Andean Geodynamics (Nice), Extended abstracts, 90-93
- Cahill T. and Isacks B. (1992) Seismicity and shape of the subducted Nazca plate, *Journal of Geophysical Research* **97**, 17503-17529
- Carlson R.W., Esperança S. and Svisero D.P. (1996) Chemical and Os isotopic study of Cretaceous potassic rocks from Southern Brazil, *Contributions to Mineralogy and Petrology* **125**, 393-405
- Cembrano J. and Lara L.E. (2009) The link between volcanism and tectonics in the southern volcanic zone of the Chilean Andes: a review, *Tectonophysics* **471**, 96-123
- Comin-Chiaramonti P., Cundari A., Piccirillo E.M., Gomes C.B., Castorina F., Censi P., De Min A., Marzoli A., Speziale S. and Velásquez V.F. (1997) Potassic and sodic igneous rocks from the eastern Paraguay: their origin from the lithospheric mantle and genetic relationships with the associated Paraná flood tholeiites, *Journal of Petrology* **38**, 495-528

- Contreras-Reyes E., Grevenmeyer I., Flueh E.R., Scherwath M. and Heesemann M. (2007) Alteration of the subducting oceanic lithosphere at the southern central Chile trench-outer rise, *Geochemistry Geophysics Geosystems* **8**
- Contreras-Reyes E., Grevenmeyer I., Flueh E.R. and Reichert C. (2008) Upper lithospheric structure of the subduction zone offshore of southern Arauco peninsula, Chile, at ~38°S, *Journal of Geophysical Research* **113**
- Davidson J.P., Dungan M.A., Ferguson K.M. and Colucci M.T. (1987) Crust-magma interactions and the evolution of arc magmas : The San Pedro-Pellado volcanic complex, southern Chilean Andes, *Geology* **15**, 443-446
- Davidson J.P., Harmon R.S. and Wörner G. (1991) The source of central Andean magmas: some considerations. In Andean Magmatism and Its tectonic Setting (Harmon R.S.; Rapela C.W.; editors) *Geological Society of America* special Publication **265**, 233-243
- Davidson J.P., Ferguson K.M., Colucci M.T. and Dungan M.A. (1988) The origin and evolution of magmas from the San Pedro-Pellado volcanic complex, S. Chile: multicomponent sources and open system evolution, *Contributions to Mineralogy and Petrology* **100**, 429-445
- Devey C.W., Hemond C and Stoffers P. (2000) Metasomatic reactions between carbonated plume melts and mantle harzburgite: The evidence from Friday and Domingo seamounts (Juan Fernández Chain, SE Pacific), *Contributions to Mineralogy and Petrology* **139**, 68-84
- Douglass J., Schilling J.G. and Fontignie D. (1999) Plume-ridge interactions of the Discovery and Shona mantle plumes with the Southern mid-Atlantic ridge (40-55 degree South), *Journal of Geophysical Research* **104**, 2941-2962
- Douglass J. (2002) Isotopic and trace element variations along the Southern Mid-Atlantic Ridge (40-50°S): An evaluation of regional plume-ridge interaction and large-scale mantle heterogeneities, Ph.D. thesis, Univ. of Rhode Island, Kingston, R.I.
- Dungan M.A., Wulff A. and Thompson R. (2001) Eruptive stratigraphy of the Tatara-San Pedro complex, 36°S, Southern Volcanic Zone, Chilean Andes: reconstruction method and implications for magma evolution at long-lived arc volcanic centers, *Journal of Petrology* **42**, 555-626

- Dungan M.A. and Davidson J.P. (2004) Partial assimilative recycling of the mafic plutonic roots of arc volcanoes: an example from the Chilean Andes, *Geology* **32**, 773-776
- Dzierma Y., Rabbel W., Thorwart M., Koulakov I., Wehrmann H., Hoernle K. And Comte D. (2012) Seismic velocity structure of the slab and continental plate in the region of the 1960 Valdivia (Chile) slip maximum – Insights into fluid release and plate coupling, *Earth and Planetary Science Letters* **331-332C**, 164-176
- Eiler J.M., Carr M.J., Reagan M. and Stolper E. (2005) Oxygen isotope constraints on the sources of Central American arc lavas, *Geochemistry Geophysics Geosystems* **6**
- Elliot T., Plank T., Zindler A., White W. and Bourdon B. (1997) Element transport from slab to volcanic front at the Mariana arc, *Journal of Geophysical Research* **102**, 14991-15019
- Ernesto M., Marques L.S., Piccirillo E.M., Molina E.C., Ussami N., Comin-Chiaramonti P. and Bellieni G. (2002) Paraná Magmatic Province-Tristan da Cunha plume system: fixed versus mobile plume, petrogenetic considerations and alternative heat sources, *Journal of Volcanology and Geothermal Research* **118**, 15-36
- Ewart A. and Hawkesworth C.J. (1987) The Pleistocene-Recent Tonga-Kermadec arc lavas: Interpretation of new isotopic and Rare Earth data in terms of Depleted Mantle source model, *Journal of Petrology* **28**, 495-530
- Farley K.A., Basu A.R. and Craig H. (1993) He, Sr, and Nd isotopic variations in lavas from the Juan Fernández archipelago, SE Pacific, *Contributions to Mineralogy and Petrology* **115**, 75-87
- Feeley T.C. and Davidson J.O. (1994) Petrology of calc-alkaline lavas at Volcán Ollagüe and the origin of compositional diversity at Central Andean stratovolcanoes, *Journal of Petrology* **35**, 1295-1340
- Feineman M., Murray T., Drew D. And Sruoga P. (2012) “Normal Southern Volcanic Zone basalts behind the arc at 34°15’-34°45’S, Goldschmidt Abstract
- Folguera A., Naranjo J.A., Orihashi Y., Sumino H., Nagao K., Polanco E. and Ramos V.A. (2009) Retroarc volcanism in the northern San Rafael Block (34°-35°30S), southern Central Andes: Occurrence, age, and tectonic setting, *Journal of Volcanology and Geothermal Research* **186**, 169-185

- Fontignie D. and Schilling J.G. (1991) $^{87}\text{Sr}/^{86}\text{Sr}$ and REE variations along the Easter microplate boundaries (South Pacific): application of multivariate statistical analyses to ridge segmentation, *Chemical Geology* **89**, 209-241
- Fontignie D. and Schilling J.G. (1996) Mantle heterogeneities beneath the South Atlantic : a Nd-Sr-Pb isotopes study along the mid-Atlantic ridge (3 degree South-46 degree South), *Earth and Planetary Science Letters* **142**, 209-221
- Francis P.W. and Hawkesworth C.J. (1994) Late Cenozoic rates of magmatic activity in the Central Andes and their relationships to continental crust formation and thickening, *Journal of the Geological Society of London* **151**, 845-854
- Francis P.W. Gardeweg M., Ramirez C.F. and Rothery D.A. (1985) Catastrophic debris avalanche deposit of Socompa volcano, northern Chile, *Geology* **13**, 600-603
- Futa K. and Stern C.R. (1988) Sr and Nd isotopic and trace element compositions of Quaternary volcanic centers of the Southern Andes, *Earth and Planetary Sciences Letters* **88**, 253-262
- Garbe-Schönberg C.-D. (1993) Simultaneous determination of thirty-seven trace elements in twenty-eight international rocks standards by ICP-MS, *Geostandards Newsletter* **17**, 81-97
- Gazel E., Hoernle K., Carr M.J., Herzberg C., Saginor I., van den Bogaard P., Hauff F., Feigenson M. and Swisher C. (2011) Plume-subduction interaction in southern Central America: Mantle upwelling and slab melting, *Lithos* **121**, 117-134
- Geldmacher J.R. and Hoernle K. (2006) Origin and geochemical evolution of the Madeira-Tore Rise (eastern North Atlantic), *Journal of Geophysical Research* **111**
- Gerlach D., Frey F.A., Moreno H. and López-Escobar L. (1988) Recent volcanism in the Puyehue-Cordón Caulle region, southern Andes, Chile (40.5°S): Petrogenesis of evolved lavas, *Journal of Petrology* **29**, 333-392
- Gibson S.A. Thompson R.N., Weska R.K., Dickin A.P. and Leonardos O.H. (1997) Late Cretaceous rift-related upwelling and melting of the Trindade starting mantle plume head beneath western Brazil, *Contributions to Mineralogy and Petrology* **126**, 303-314
- Gibson S.A., Thompson R.N., Leonardos O.H., Dickin A.P. and Mitchell J.G. (1999) The limited extent of plume-lithosphere interactions during continental flood-basalt genesis:

- geochemical evidence from Cretaceous magmatism in southern Brazil, *Contributions to Mineralogy and Petrology* **137**, 147-169
- Gibson S.A., Thompson R.N., Day J.A., Humphris S.E. and Dickin A.P. (2005) Melt-generation processes associated with the Tristan mantle plume: Constraints on the origin of EM-1, *Earth and Planetary Science Letters* **237**, 744-767
- Gilbert H., Beck S. and Zandt G. (2006) Lithospheric and upper mantle structure of central Chile and Argentina, *Geophysical Journal International* **165**
- Gill J.B. (1981) Orogenic andesites and plate tectonics, Berlin, Heidelberg, New York, Tokyo, Springer, 390p
- Govindaraju K. (1994) Compilation of working values and sample description for 383 geostandards, *Geostandards Newsletter* **18**, 1-158
- Green T.H., Blundy J.D., Adam J. and Yaxley G.M. (2000) SIMS determination of trace element partition coefficients between garnet, clinopyroxene, and hydrous basaltic liquids at 2-7.5 GPa and 1080-1200°C, *Lithos* **53**, 165-187
- Green T.H. and Adam J. (2003) Experimentally determined trace element characteristics of aqueous fluid from partially dehydrated mafic oceanic crust at 3.0 GPa, 650-700°C, *European Journal of Mineralogy*. **15**, 815-830
- Grevemeyer I., Ranero C.R., Flueh E.R., Kläschen D. and Bialas J. (2007) Passive and active seismological study of bending-related faulting and mantle serpentinization at the Middle America trench, *Earth and Planetary Science Letters* **258**, 528-542
- Gudnason J., Martin Holm P., Sjøager N. and Llambías E.J. (2012) Geochronology of the late Pliocene to recent volcanic activity in the Payenia back-arc volcanic province, Mendoza Argentina, *Journal of South American Earth Sciences* **37**, 191-201
- Haase K.M. (2002) Geochemical constraints on magma sources and mixing processes in Easter microplate MORB (SE Pacific); A case study of plume-ridge interaction, *Chemical Geology* **182**, 335-355
- Hall P.S. and Kincaid C. (2001) Diapiric flow at subduction zones: A recipe for rapid transport, *Science* **292**, 2472

- Hamelin B., Dupré B. and Allègre C.J. (1984) Lead-Strontium isotopic variations along the East Pacific Rise and the Mid-Atlantic Ridge: a comparative study, *Earth and Planetary Science Letters* **67**, 340-350
- Hanan B.B., Kingsley R.H. and Schilling J.G. (1986) Pb isotope evidence in the South Atlantic for migrating ridge-hot spots interactions, *Nature* **322**, 137-144
- Hanan B.B. and Schilling J.G. (1989) Easter microplate evolution: Pb isotope evidence, *Journal of Geophysical Research* **94**, 7432-7448
- Harmon R.S., Barreiro B.A., Moorbath S., Hoefs J., Francis P.W., Thorpe R.S., Deruelle B., McHugh J. and Viglino J.A. (1984) Regional O-, Sr-, and Pb-isotopes relationships in late Cenozoic calc-alkaline lavas of the Andean cordillera, *Journal of Geological Society London* **141**, 803
- Harris C., Smith H.S. and Le Roex A.P. (2000) Oxygen isotope composition of phenocrysts from Tristan da Cunha and Gough Island lavas: Variation with fractional crystallization and evidence for assimilation, *Contributions to Mineralogy and Petrology* **138**, 164-175
- Hart S.R. (1984) A large-scale isotope anomaly in the Southern Hemisphere mantle, *Nature* **309**, 753-757
- Hauff F., Hoernle K. and Schmidt A. (2003) Sr-Nd-Pb composition of Mesozoic Pacific oceanic crust (Site 1149 and 801, ODP Leg 185): Implications for alteration of ocean crust and the input into the Izu-Bonin-Mariana subduction system, *Geochemistry Geophysics Geosystems* **4**
- Hermann J. and Spandler C.J. (2008) Sediment melts at sub-arc depths: an experimental study, *Journal of Petrology* **49**, 717-740
- Herron E.M., Cande S.C. and Hall B.R. (1981) An active spreading center collides with a subduction zone – a geophysical survey of the Chile margin triple junction, *Geological Society of America Memoirs* **154**, 683-701
- Heydolph K., Hoernle K., Hauff F., van den Bogaard P., Portnyagin M., Bindeman I. and Garbe-Schönberg C.-D. (2012) Along- and across-arc geochemical variations in northwestern Central America: Increased contribution of enriched lithosphere to lavas along the

- volcanic from Nicaragua to Guatemala and behind the volcanic front, *Geochimica et Cosmochimica Acta* **84**, 459-491
- Hickey R.L., Gerlach D.C. and Frey F.A. (1984) Geochemical variations in volcanic rocks from central-south Chile (33°-42°S): Implications for their petrogenesis In *Andean magmatism: Chemical and isotopic constraints* (Harmon R. Barreiro B., editors). Shiva Publishing Limited p. 72-95 Nantwich, U.K.
- Hickey R.L., Frey F.A. and Gerlach D.C. (1986) Multiple sources for basaltic arc rocks from the Southern Volcanic Zone of the Andes (34°-41°S): Trace element and isotopic evidence for contributions from subducted oceanic crust, mantle, and continental crust, *Journal of Geophysical Research* **91**, 5963-5983
- Hickey-Vargas R.L., Moreno Roa H., Lopez-Escobar L. and Frey F.A. (1989) Geochemical variations in Andean basaltic and silicic lavas from the Villarrica-Lanin volcanic chain (39.5°S): an evaluation of source heterogeneity, fractional crystallization and crustal assimilation, *Contributions to Mineralogy and Petrology* **103**, 361-386
- Hickey-Vargas R.L., Sun M., Lopez-Escobar L., Moreno Roa H., Reagan M.K., Morris J.D. and Ryan J.G. (2003) Multiple subduction components in the mantle wedge: Evidence from eruptive centers in the Central Southern volcanic zone, Chile, *Geology* **30**, 3, 199-202
- Hildreth W. and Moorbath S. (1988) Crustal contributions to arc magmatism in the Andes of Central Chile, *Contributions to Mineralogy and Petrology* **98**, 455-489
- Hildreth W., Godoy E., Fierstein J. and Singer B. (2010) Laguna del Maule Volcanic Field: Eruptive history of a Quaternary basalt-to-rhyolite distributed field on the Andean rangecrest in central Chile, *Servicio Nacional de Geología y Minería Boletín* **63**, 145p
- Hochstaedter A., Gill J.B., Peters R., Broughton P., Holden P. and Taylor B. (2001) Across-arc geochemical trends in the Izu-Bonin arc: contributions from the subducting slab, *Geochemistry Geophysics Geosystems* **2**
- Hoernle K., Abt D.L., Fisher K.M., Nichols H., Hauff F., Abers G.A., van den Bogaard P., Heydolph K., Alvarado G., Protti M., Strauch W. (2008) Arc parallel flow in the mantle wedge beneath Costa Rica and Nicaragua, *Nature* **451**, 1094-1097

- Hoernle K., Hauff F., Kokfelt T.F., Haase K., Garbe-Schönberg C.-D. and Werner R. (2011) On- and off-axis chemical heterogeneities along the South Atlantic Mid-Ocean Ridge (5-11°S): Shallow or deep recycling of ocean crust and/or intraplate volcanism? *Earth and Planetary Science Letters* **306**, 86-97
- Hofmann A.W., Jochum K.P., Seufert M. and White W.M. (1986) Nb and Pb in oceanic basalts: new constraints on mantle evolution, *Earth and Planetary Sciences Letters* **79**, 33-45
- Hofmann A.W. (1997) Mantle geochemistry: The message from oceanic volcanism, *Nature* **385**, 219-229
- Husson L., Conrad C.P. and Faccenna C. (2012) Plate motions, Andean orogeny, and volcanism above the South Atlantic convection cell, *Earth and Planetary Sciences Letters* **317-318**, 126-135
- Ito E., White W.M., von Drach V., Hofmann A.W. and James D.E. (1980) Isotopic studies of ocean ridge basalts, Carnegie Institute, DTM, annual report director, 465-471
- Ito E., White W.M. and Goepel C. (1987) The O, Sr, Nd and Pb isotope geochemistry of mid-oceans ridge basalts, *Chemical Geology* **62**, 157-176
- Jacques G., Hoernle K., Gill J.B., Hauff F., Wehrmann H., Garbe-Schönber D., van den Bogaard P., Bindeman I. And Lara L.E. (2013) Across-arc geochemical variations in the Southern Volcanic Zone, Chile (34.5-38°S): Constraints on Mantle wedge and source input compositions, *Geochimica et Cosmochimica Acta* **123**, 218-243
- Jacques G., Hoernle K., Gill J., Wehrmann H. and Bindeman I. (Submitted) Geochemical variations in the Central Southern Volcanic Zone, Chile (38-43°S): The role of fluids in generating arc magmas, *Chemical Geology*
- Jicha B.R., Singer B.S., Beard B.L., Johnson C.M., Moreno-Roa H. and Naranjo J.A. (2007) Rapid magma ascent and generation of ²³⁰Th excesses om the lower crust at Puyehue-Cordón Caulle, Southern Voclanic Zone, Chile, *Earth and Planetary Science Letters* **255**, 229-242
- Johnson M.C. and Plank T. (1999) Dehydration and melting experiments constrain the fate of subducted sediments, *Geochemistry Geophysics Geosystems* **1**, 1007-1033

- Karsten J., Klein E.M. and Sherman C. (1996) subduction zone geochemical characteristics in ocean ridge basalts from the Southern Chile Ridge; implications of modern Ridge subduction systems for the archaean, *Lithos* **37**, 143-161
- Katz R.F., Spiegelman M. and Langmuir C.H. (2003) A new parameterization of hydrous mantle melting, *Geochemistry Geophysics Geosystems* **4**, 1073-1092
- Kay S.M., Orrel S. and Abbruzzi J.M. (1996) Zircon and whole rock Nd-Pb isotopic evidence for a Greenville age and a Laurentian origin for the basement of the Precordillera in Argentina, *The Journal of Geology* **104**, 637-648
- Kay S.M., Gorrington M. and Ramos V.A. (2004) Magmatic sources, setting and causes of Eocene to recent Patagonian plateau magmatism (36° to 52°S latitude), *Revista de la Asociación Geológica Argentina* **59**, 556-568, 2004
- Kay S.M., Godoy E. and Kurtz A. (2005) Episodic arc migration, crustal thickening, subduction erosion, and magmatism in the south-central Andes, *Geological Society of America* **117**, 67-88
- Kay S.M. and Copeland P. (2006) Early to middle Miocene backarc magmas of the Neuquén Basin: geochemical consequences of slab shallowing and westward drift of South America, *Geological Society of America Special Paper* **407**, 185-214, 2006b
- Kay S.M., Burns W.M., Copeland P. and Mancilla O. (2006a) Upper Cretaceous to Holocene magmatism and evidence for transient Miocene shallowing of the Andean subduction zone under the northern Neuquén Basin, *Geological Society of America Special Paper* **407**, 19-60
- Kay S.M., Mancilla O. and Copeland P. (2006b) Evolution of the late Miocene Chachahuén volcanic complex at 37°S over a transient shallow subduction zone under the Neuquén Andes, *Geological Society of America Special Paper* **407**, 215-246
- Kay S.M., Ardolino A.A., Gorrington M.L. and Ramos V.A. (2007) The Somuncura Large Igneous Province in Patagonia: Interaction of a transient mantle thermal anomaly with a subducting slab, *Journal of Petrology* **48**, 43-77

- Kempton P.D., Harmon R.S. Hawkesworth C.J. and Moorbath S. (1990) Petrology and geochemistry of lower crustal granulites from Geronimo Volcanic Field, southeastern Arizona, *Geochimica et Cosmochimica Acta* **54**, 3401-3426
- Kessel R., Schmidt M.W., Ulmer P. and Pettke T. (2005) Trace element signature of subduction-zone fluids, melts and supercritical liquids at 120-180 km depth, *Nature* **437**, 724-727
- Kelley K.A., Plank T., Ludden J. and Staudigel H. (2003) Composition of altered oceanic crust at ODP Sites 801 and 1149, *Geochemistry Geophysics Geosystems* **4**
- Kelley K.A., Plank T., Grove T.L., Stolper E.M., Newman S. and Hauri E. (2006) Mantle melting as a function of water content beneath back-arc basins, *Journal of Geophysical Research* **111**
- Kimura J.-I., van Keken P.E., Hacker B.R., Kawabata H., Yoshida T. and Stern R.J. (2009) Arc Basalt Simulator version 2, a simulation for slab dehydration and fluid-fluxed mantle melting for arc basalts: Modeling scheme and implication, *Geochemistry Geophysics Geosystems* **10**
- Kimura J.-I., Kent A.J.R., Rowe M.C., Katakuse M., Nakano F., Hacker B.R., van Keken P.E., Kawabata H. and Stern R.J. (2010) Origin of cross-chain geochemical variation in Quaternary lavas from the northern Izu arc: Using a quantitative mass balance approach to identify mantle sources and mantle wedge processes, *Geochemistry Geophysics Geosystems* **11**
- Kinglsey R.H. (2002) The geochemistry of basalts from the Easter Microplate boundaries and the western Easter-Salas y Gomez Seamount Chain: A comprehensive study of mantle plume-spreading center interaction, Ph.D. thesis, Univ. of Rhode Island, Kingston, R.I.
- Kingsley R.H., Blichert-Toft J., Fontignie D. and Schilling J.G. (2007) Hafnium, Neodymium and Strontium isotope and parent-daughter element systematic in basalts from the plume-ridge interaction system of the Salas y Gomes seamount chain and Easter microplate, *Geochemistry Geophysics Geosystems* **8**
- Klein E.M and Karsten J.L (1995) Ocean-ridge basalts with convergent margin geochemical affinities from the Chile Ridge, *Nature* **374**, 52-57

- Klimm K., Blundy J.D. and Green T.H. (2008) Trace element partitioning and accessory phase saturation during H₂O-saturated melting of basalt with implications for subduction zone chemical fluxes, *Journal of Petrology* **49**, 523-553
- Kneller E.A. and van Keken P.E. (2007) Trench-parallel flow and seismic anisotropy in the Mariana and Andean subduction systems, *Nature* **450**, 1222, 1226
- Krolikowska-Ciaglo S., Hauff F. and Hoernle K. (2005) Sr-Nd isotope systematics in 14–28 Ma low-temperature altered mid-ocean ridge basalt from the Australian Antarctic Discordance, Ocean Drilling Program Leg 187, *Geochemistry Geophysics Geosystems* **6**
- Le Maitre R.W., Bateman P., Dudek A., Keller J., Lameyre Le Bas M.J., Sabine P.A., Schmid R., Sorensen H., Streckeisen A., Woodley A.R. and Zanettin B. (1989) A classification of igneous rocks and glossary of terms, Blackwell, Oxford
- Lindsay J.M., Schmitt A.K., Trumbull R.B., de Silva S.L., Siebel W. and Emmermann R. (2001) Magmatic evolution of the La Pacana Caldera system, central Andes, Chile: compositional variation of two cogenetic large-volume ignimbrites and implications for contrasting eruption mechanisms, *Journal of Petrology* **42**, 459-486
- Linke P. and Shipboard Scientific Party (2011) CHIFLUX – Identification and investigation of fluid flux, mass wasting and sediments in the forearc of the central Chilean subduction zone, Cruise Report SO210, 103 pp., GEOMAR report, Kiel
- López-Escobar L., Cembrano J. and Moreno H. (1995) Geochemistry and tectonics of the Chilean Southern Andes basaltic Quaternary volcanism (37-46°S), *Revista Geológica de Chile* **22**, 219-234
- Lucassen F., Trumbull R., Franz G., Creixell C., Vázquez P., Romer R.L. and Figeroa O. (2004) Distinguishing crustal recycling and juvenile additions at active continental margins : the Paleozoic to recent compositional evolution of the Chilean Pacific margin (36-41°S), *Journal of South American Earth Sciences* **17**, 103-119
- Lucassen F., Franz G., Lomer R.L., Schultz F., Dulski P and Wemmer K. (2007) Pre-Cenozoic intra-plate magmatism along the Central Andes (17-37°S): Composition of the mantle at an active margin, *Lithos* **99**, 312-338

- Lucassen F., Wiedicke M. and Franz G. (2010) Complete recycling of a magmatic arc : evidence from chemical and isotopic composition of Quaternary trench sediments in Chile (36-40°S), *International Journal of Earth Sciences* **99**, 687-701
- MacDougall J.D. and Lugmair G.W. (1986) Sr and Nd isotopes in basalts from the East Pacific Rise: significance for mantle heterogeneity, *Earth and Planetary Science Letters* **77**, 273-284
- Mahoney J.J., Sinto J.M., Kurz M.D., MacDougall J.D., Spencer K.J. and Lugmair G.W. (1994) Isotope and trace element characteristics of a super-fast spreading ridge: East Pacific Rise 13-23°S, *Earth and Planetary Science Letters* **121**, 171-191
- Martin E., Bindeman I.N. and Grove T.L. (2011) The origin of high-Mg magmas in Mt Shasta and Medicine lake volcanoes, Cascade arc (California): higher and lower than mantle oxygen isotope signatures attributed to current and past subduction, *Contributions to Mineralogy and Petrology* **162**
- Marques L.S., Dupré B. and Piccirillo E.M. (1999) Mantle source compositions of the Paraná Magmatic Province (southern Brazil): evidence from trace element and Sr-Nd-Pb isotope geochemistry, *Journal of Geodynamics* **28**, 439-458
- Massaferro G.I., Haller M.J., D’Orazio M. and Alric V.I. (2006) Sub-recent volcanism in Northern Patagonia: A tectonomagmatic approach, *Journal of Volcanology and Geothermal Research* **155**, 227-243
- Mattey D., Lowry D. and Macpherson C. (1994) Oxygen isotope composition of mantle peridotite, *Earth and Planetary Science Letters* **128**, 231-241
- Matsuhisa Y. (1979) Oxygen isotopic compositions of volcanic rocks from the east Japan island arc and their bearing on petrogenesis, *Journal of Volcanology and Geothermal Research* **5**, 271-296
- McQuarrie N., Horton B.K., Zandt G., Beck S. and DeCelles P.G. Lithospheric evolution of the Andean fold-thrust belt, Bolivia, and the origin of the central Andean plateau, *Tectonophysics* **399**, 15-37
- Morris J.D., Leeman W.P. and Tera F. (1990) The subducted component in island arc lavas constraints from Be isotopes and B-Be systematics, *Nature* **344**, 31-36

- Mix A.C., Tiedemann R., Blum P. et al. (2003) Proceedings of the Ocean Drilling program, Initial Report **202**
- Muehlenbachs K. and Byerly G. (1982) ^{18}O enrichment of silicic magmas caused by crystal fractionation at the Galapagos spreading center, *Contributions to Mineralogy and Petrology* **79**, 76-79
- Munoz J. and Stern C.R. (1988) The Quaternary volcanic belt of the southern continental margin of South America: transverse structural and petrochemical variations across the segment between 38°S and 39°S, *Journal of South American Earth Sciences* **1**, 147-161
- Naranjo J.A. and Stern C.R. (2004) Holocene tephrochronology of the southernmost part (42°30'-45°S) of the Andean Southern Volcanic Zone, *Revista Geológica de Chile* **31**, 225-240
- Newsom H.E., White W.M., Jochum K.P. and Hofmann A.W. (1986) Siderophile and chalcophile element abundances in oceanic basalts, Pb isotopes evolution and growth of the Earth's core, *Earth and Planetary Science Letter* **80**, 299-313
- Norabuena E., Leffer-Griffin L., Mao A., Dixon T., Stein S., Sacks S., Ocola L. And Ellis M. (1998) Space geodetic observations of Nazca-South America convergence across the central Andes, *Science* **279**, 358-362
- Peacock S.M. (2001) Are the lower planes of double seismic zones caused by serpentine dehydration in subduction oceanic mantle? *Geology* **29**, 299-302
- Pearce J.A., Kempton P.D., Nowell G.M. and Noble S.R. (1999) Hf-Nd element and isotope perspective on the nature and provenance of mantle and subduction components in Western Pacific arc-basin systems, *Journal of Petrology* **40**, 1579-1611
- Pearce J.A. (2008) Geochemical fingerprinting of oceanic basalts with applications to Ophiolite classification and the search for Archean oceanic crust, *Lithos* **100**, 14-48
- Peate D.W., Hawkesworth C.J., Mantovani M.S.M., Rogers N.W. and Turner S.P. (1999) Petrogenesis and stratigraphy of the high-Ti/Y Urubici magma type in the Paraná flood basalt province and implications for the nature of "Dupal"-type mantle in the South Atlantic region, *Journal of Petrology* **40**, 451-473

- Pécskay Z., Haller M.J. and Németh K.(2007) Preliminary K/Ar Geochronology of the Crater basalt Volcanic Field (CBVF), northern Patagonia, *Revista de la Asociación Geológica Argentina* **62**, 25-29
- Plank T. (2005) Constraints from Thorium/Lanthanum on sediment recycling at subduction zones and the evolution of the continents, *Journal of Petrology* **46**, 921-944
- Plank T. (2011) The chemical composition of subducting sediments, Chapter for Treatise on Geochemistry
- Plank T. and Langmuir C.H. (1993) Tracing trace elements from sediment input to volcanic output at subduction zones, *Nature* **362**, 739-742
- Potts P.J. and Kane J.S. (2005) International association of geoanalysts – Certificate of analysis : Certified reference material OU-6 (penrhyn slate), *Geostandards and Geoanalytical Research* **29**, 233-236
- Ramos V.A. (2010) The Grenville-age basement of the Andes, *Journal of South American Earth Sciences* **29**, 77-91
- Ramos V.A. and Basei M.A. (1997a) Gondwanan, Perigondwanan, and exotic terranes of southern South America. In: South American Symposium on Isotope Geology, Sao Paulo, 250-252
- Ramos V.A. and Basei M.A. (1997b) The basement of Chilenia: an exotic continental terrane to Gondwana during the Early Paleozoic. In: Symposium on Terrane Dynamics, New Zealand, **97**, 140-143
- Ramos V.A. and Folguera A. (2011) Payenia volcanic province in the Southern Andes: an appraisal of an exceptional Quaternary tectonic setting, *Journal of Volcanology and Geothermal Research* **201**, 53-64
- Ranero C.R., Phipps Morgan J., McIntosh K. and Reichert C. (2003) Bending-related faulting and mantle serpentinization at the Middle America trench, *Nature* **425**, 367-373
- Ranero C.R., Villasenor A., Phipps Morgan J. and Weinrebe W. (2005) Relationship between bend-faulting at trenches and intermediate-depth seismicity, *Geochemistry Geophysics Geosystems* **6**

- Ranero C.R., Huene R.v., Weinrebe W. and Reichert C. (2006) Tectonic Processing along the Chile Convergent Margin, In: O. Oncken, G. Chong, G. Franz, P. Giese, H.-J. Götze, V. Ramos M. Strecker, and P. Wigger (Eds): The Andes Active Subduction Orogeny, *Frontiers in Earth Science*. Springer Verlag, Berlin, 91-121
- Reubi O., Bourdon B., Dungan M.A., Koornneef J.M., Sellés D., Langmuir C.H. and Aciego S., (2011) Assimilation of the plutonic roots of the Andean arc controls variations in U-series disequilibria at Volcan Llaima, Chile, *Earth and Planetary Science Letters* **303**, 37-47
- Rocha-Júnior E.R.V., Marques L.S., Babinski M., Nardy A.J.R., Figueiredo A.M.G. and Machado F.B. (2013) Sr-Nd-Pb isotopic constraints on the nature of the mantle sources involved in the genesis of the high-Ti tholeiites from Northern Paraná Continental Flood Basalts (Brazil), *Journal of South American Earth Sciences*, DOI: 10.1016/j.jsames.2013.04.004
- Rocha-Júnior E.R.V., Puchtel I.S., Marques L.S, Walker R.J., Machado F.B., Nardy A.J.R., Babinski M. And Figueiredo A.M.G. (2012) Re-Os isotope and highly siderophile element systematic of the Paraná Continental Flood Basalts (Brazil), *Earth and Planetary Science Letters* **337-338**, 164-173
- Rohde J., Hoernle K., Hauff F., Werner R., O'Connor J., Class C., Garbe-Schönberg D. and Jokat W. (2013) 70 Ma chemical zonation of the Tristan-Gough hotspot track, *Geology* **41**, 335-338
- Roy-Barman M., Wasserburg G.J., Papanastassiou D.A. and Chaussidon M. (1998) Osmium isotopic compositions and Re-Os concentrations in sulfide globules from basaltic glasses, *Earth and Planetary Science Letters* **154**, 331-347
- Rüpke L.H., Phipps Morgan J., Hort M. and Connolly J.A.D. (2002) Are the regional variations in Central American arc lavas due to differing basaltic versus peridotitic slab sources of fluids?, *Geology* **30**, 1035-1038
- Rüpke L.H., Phipps Morgan J., Hort M. and Connolly J.A.D. (2004) Serpentine and the subduction zone water cycle, *Earth and Planetary Science Letters* **223**, 17-37
- Russo R.M. and Silver P.G. (1994) Trench-parallel flow beneath the Nazca plate from seismic anisotropy, *Science* **263**, 1105-1111

- Sheppard S.M.F. and Harris C. (1985) Hydrogen and oxygen isotope geochemistry of Ascension Island lavas and granites: Variation with crystal crystallization and interaction with sea water, *Contributions to Mineralogy and Petrology* **91**, 74-81
- Schmidt M.W. and Poli S. (1998) Experimentally based water budgets for dehydrating slabs and consequences for arc magma generation, *Earth and Planetary Science Letters* **163**, 361-379
- Schmitt A.K., de Silva S.L., Trumbull R.B. and Emmermann R. (2001) Magma evolution in the Purico ignimbrite complex, Northern Chile: Evidence for zoning of a dacitic magma by injection of rhyolitic melts following mafic recharge, *Contributions to Mineralogy and Petrology* **140**, 680-700
- Schmitt A.K., Lindsay J.M., de Silva S.L. and Trumbull R.B. (2002) U-Pb zircon chronostratigraphy of early Pliocene ignimbrites from La Pacana, north Chile: implications for the formation of stratified magma chambers, *Journal of Volcanology and Geothermal Research* **120**, 43-53
- Sellés D., Ródriguez A.C., Dungan M.A, Naranjo J.A. and Gardeweg M. (2004) Geochemistry of Neva de Longaví volcano (36.2°S): a compositionally atypical arc volcano in the Southern Volcanic Zone of the Andes, *Revista Geológica de Chile* **31**, 293-315
- SERNAGEOMIN (2003) Mapa Geológico de Chile : versión digital, *Servicio Nacional de Geología y Minería, Publicación Geológica Digital* **4** (versión 1.0, 2003) Santiago
- Sigmarsson O., Condomines M., Morris J.D. and Harmon R.S. (1990) Uranium and ¹⁰Be enrichments by fluids in Andean arc magmas, *Nature* **346**, 163-165
- Sigmarsson O., Chmeleff J., Morris J. and López-Escobar L. (2002) Origin of ²²⁶Ra-²³⁰Th disequilibria in arc lavas from southern Chile and implications for magma transfer time, *Earth and Planetary Science Letters* **196**, 189-196
- Stern C.R. (1989) Pliocene to present migration of the volcanic front, Andean Southern Volcanic Front, *Revista Geológica de Chile* **16**, 145-162
- Stern C.R. (1991) Role of subduction erosion in the generation of andean magmas, *Geology* **19**, 78-81

- Stern C.R. (2004) Active Andean volcanism: its geologic and tectonic setting, *Revista Geológica de Chile* **31**, 161-206
- Stern R.J. (2002) Subduction zones, *Reviews of Geophysics* **40**, pp 1012
- Sturm M., Klein E.M., Graham D. And Karsten J.L. (1999) Age constraints on crustal recycling to the mantle beneath the Southern Chile Ridge: He-Pb-Sr-Nd isotopes systematic, *Journal of Geophysical Research* **104**, 5097-5114
- Sun S.-S. and McDonough W.F. (1989) Chemical and isotopic systematic of oceanic basalts : implications for mantle composition and processes, in Magmatism in ocean basins (Saunders A.D. and Norry M.J., editors) Geological Society, London special publication **42**, 313-345
- Syracuse E.M. and Abers G.A. (2009) Systematic biases in subduction zone hypocenters, *Geophysical Research Letters* **36**
- Syracuse E.M., van Keken P.E. and Abers G.A. (2010) The global range of subduction zone thermal models, *Physics of the Earth and Planetary Interiors* **183**(1-2), 73-90
- Tagiri M., Moreno H., López-Escobar L. and Notsu K. (1993) Two magma types of the high-alumina basalt series of Osorno Volcano, Southern Andes (41°06'S) – plagioclase dilution effect, *Journal of Mineralogy, Petrology and Economic Geology* **88**, 359-371
- Tassara A., Götze H.J., Schmidt S. and Hackney R. (2006) Three-dimensional density model of the Nazca plate and the Andean continent margin, *Journal of Geophysical Research* **111**
- Tebbens S.F. and Cande S.C. (1997a) Southeast Pacific tectonic evolution from early Oligocene to present, *Journal of Geophysical Research* **102**, 12,061-12,084
- Tebbens S.F., Cande S.C., Kovacs L., Parra Labrecque J.L. and Vergara H. (1997b) The Chile ridge: a tectonic framework, *Journal of Geophysical Research* **102**, 12,035-12,059
- Todd E., Gill J.B., Wysoczanski R.J., Hergt J., Wright I.C., Leybourne M.I. and Mortimer N. (2011) Hf isotopic evidence for small-scale heterogeneity in the mode of mantle wedge enrichment: Southern Havre Trough and South Fiji Basin back arcs, *Geochemistry Geophysics Geosystems* **12**, 34pp
- Tollstrup D. and Gill J.B. (2005) Hafnium systematics of the Mariana arc: Evidence for sediment melt and residual phases, *Geology* **33**, 737-740

- Tollstrup D., Gill J.B., Kent A., Prinkey D., Williams R., Tamura Y. and Ishizuka O. (2010) Across-arc geochemical trends in the Izu-Bonin arc: Contributions from the subducting slab, revisited, *Geochemistry Geophysics Geosystems* **11**
- Tormey D.R., Hickey-Vargas R., Frey F.A. and López-Escobar L. (1991) Recent lavas from the Andean volcanic front (33 to 42°S); Interpretations of along-arc compositional variations, *Geological Society of America special paper* **265**, 57-77
- Tormey D.R., Frey F.A. and Lopez-Escobar L. (1995) Geochemistry of the Active Azufre—Planchón—Peteroa Volcanic Complex, Chile (35°15'S): Evidence for Multiple Sources and Processes in a Cordilleran Arc Magmatic System, *Journal of Petrology* **36**, 265-298
- Turner S., Handler M., Bindeman I.N. and Katsuhiko S. (2009) New insights into the origin of O-Hf-Os signatures in arc lavas from Tonga-Kermadec, *Chemical Geology* **266**, 187-193
- Valley J. W., Kitchen N., Kohn M. J., C.R. N. and Spicuzza M. J. (1995) UWG-2, a garnet standard for oxygen isotope ratios: strategies for high precision and accuracy with laser heating, *Geochimica et Cosmochimica Acta* **59**, 5223-5231
- Vallier T.L., Jenner G.A., Frey F.A., Gill, J.B., Davis A.S., Volpe A.M., Hawkins J.W., Morris J.D., Cawood P.A., Morton J.L., Scholl D.W., Rautenschlein M., White W.M., Williams R.W., Stevenson A.J. and White L.D. (1991) Subalkaline andesite from Valu Fa Ridge, a back-arc spreading center in southern Lau Basin: petrogenesis, comparative chemistry, and tectonic implications, *Chemical Geology* **91**, 227-256
- Van Keken P.E., Hacker B.R., Syracuse E.M. and Abers G.A. (2011) Subduction factory: 4. Depth-dependent flux of H₂O from subducting slabs worldwide, *Journal of Geophysical Research* **116**
- Varekamp J.C., Hesse A. and Mandeville C.W. (2010) Back-arc basalts from the Loncopue graben (Province of Neuquén, Argentina), *Journal of Volcanology and Geothermal Research* **197**, 313-328
- Vervoort J.D., Patchett P.J., Blichert-Toft J. and Albarède F. (1999) Relationships between Lu-Hf and Sm-Nd isotopic systems in the global sedimentary system, *Earth and Planetary Science Letters* **168**, 79-99

- Vervoort J.D., Plank T. And Prytulak J. (2011) The Hf-Nd isotopic composition of marine sediments, *Geochimica et Cosmochimica Acta* **75**, 5903-5926
- Völker D., Reichel T., Wiedicke M. and Heubeck C. (2008) Turbidites deposited on Southern Central Chilean seamounts: Evidence for energetic turbidity currents, *Marine Geology* **251**, 15-31
- Völker D., Kutterolf S. and Wehrmann H. (2011) Comparative mass balance of volcanic edifices at the Southern Volcanic Zone of the Andes between 33°S and 46°S, *Journal of Volcanology and Geothermal Research* **205**, 114-129
- Wade J.A, Plank T., Stern R.J, Tollstrup D.L., Gill J.B., O’Leary J.C., Eiler J.M., Moore R.B., Woodhead J.D., Trusdell F., Fisher T.P. and Hilton D.R. (2005) The May 2003 eruption of Anatahan volcano, Mariana Islands: Geochemical evolution of a silicic island-arc volcano, *Journal of Volcanology and Geothermal Research* **146**, 139-170
- Wagner L.S., Beck S., Zandt G. And Ducea M.N. (2006) Depleted lithosphere, cold, trapped asthenosphere, and frozen melt puddles above the flat slab in central Chile and Argentina, *Earth and Planetary Science Letters* **245**, 289-301
- Watt S.F.L., Pyle D.M., Tamsin A.M. and Naranjo J.A. (accepted, 2013) Arc magma compositions controlled by linked thermal and chemical gradients above the subducting slab, *Geophysical Research Letters*, DOI: 10.1002/grl.50513
- Webb P.C., Thompson M., Potts P.J. and Enzweiler J. (2009) An international proficiency test for analytical geochemistry laboratories – report on round 25 (basalt, HTB-1), GeoPT25
- Wehrmann H., Hoernle K., Garbe-Schönberg C.-D., Jacques G., Mahlke J. and Schumann K. (accepted, 2013 a) Fluids in volcanic arc systems: Insights from trace element geochemistry of mafic to intermediate volcanic rocks, *International Journal of Earth Sciences*
- Wehrmann H., Hoernle K., Jacques G., Garbe-Schönberg D., Schumann K., Mahlke J. and Lara L. (in revision b) Sulphur and chlorine geochemistry of mafic to intermediate tephras from the Chilean Southern Volcanic Zone (33-43°S) compared with those from the Central American Volcanic Arc, *International Journal of Earth Sciences*

- Woodhead J.D., Hergt J.M., Davidson J.P. and Eggins S.M. (2001) Hafnium isotope evidence for “conservative” element mobility during subduction zone processes, *Earth and Planetary Science Letters* **192**, 331-346
- Woodhead J.D., Stern R.J., Pearce J., Hergt J. and Vervoort J. (2012) Hf-Nd isotope variation in Mariana Trough basalts: The importance of “ambient mantle” in the interpretation of subduction zone magmas, *Geology* **40**, 539-542
- White W.M., Hofmann A.W. and Puchelt H. (1987) Isotope geochemistry of Pacific Mid-Ocean Ridge basalts, *Journal of Geophysical Research* **92**, 4881-4893
- Workman R.K. and Hart S.R. (2005) Major and trace element composition of the depleted MORB mantle (DMM), *Earth and Planetary Science Letters* **231**, 53-42
- Wörner G., López-Escobar L., Moorbath S., Horn S., Entenmann J. And Davidson J.D. (1992a) Variaciones geoquímicas, locales y regionales, en el arco volcánico Andino del Norte de Chile (17°30'S-22°00'S), *Revista Geológica de Chile* **19**, 37-53
- Wörner G., Moorbath S. and Harmon R.S. (1992b) Andean Cenozoic volcanic centers reflect basement isotopic domains, *Geology* **20**, 1103-1106
- Yododzinski G.M., Vervoort J.D., Brown S.T. and Gersen M. (2010) Subduction controls Hf and Nd isotopes in lavas of the Aleutian island arc, *Earth and Planetary Science Letters* **300**, 226-238
- Yuan X., Ash G., Bataile K., Bohm M., Echtler H., Kind R., Oncken O. and Wölbern L. (2006) Deep seismic images of the Southern Andes, *Geological Society of America special paper* **407**, 61-72
- Zhang J-J, Zheng Y-F, and Zhao Z-F (2009) Geochemical evidence for interaction between oceanic crust and lithospheric mantle in the origin of Cenozoic continental basalts in east-central China. *Lithos* **110**, 305-326.

Acknowledgments

It all started when I was five year-old, when I first received a set of books about dinosaurs. From that moment, I knew I would be a scientist. More than twenty years later, I am presenting my dissertation about geochemical variations in magmatic rocks. Things changed, but the motivation of investigating and understanding our planet Earth remained intact.

Above all I would like to thank my parents and my brother who supported me in my studies and encouraged me to pursue in Science. Merci pour tout!

Then, I would like to thank Kaj Hoernle, my supervisor, who taught me the joy and the pain of magmatic geochemistry. We had very stimulating and passionate discussions about data interpretation and presentation. He showed me the way of transforming a list of numbers into stories, changing a piece of rock into an open book about the Earth's processes.

I am very grateful to Jim Gill, who spent a lot of time thinking, discussing, and reviewing the data. His thoughtful input is greatly appreciated.

I also would like to thank Heidi Wehrmann, who helped me in the daily tasks of a PhD student, and more. She was always available, for anything I could ask, and that was sometimes a relief. We shared good moments during the first fieldtrip in 2009, together with Kaj and Paul, drinking sweet Pisco Sour.

I will not forget Folkmar Hauff and Dieter Garbe-schönberg, who showed me the tricky ways of analytical work. Processing accurate and clean data is crucial for good interpretations, and I have been to the right place. I thank Silke Hauff and Ulrike Westernstöer who helped me during the analytical process.

I would like to thank all my co-workers from SFB-574 and from GEOMAR in general: Ken, Steffen, Armin, Thor, David G., David V., Kai, and my PhD fellows – Joana, Julia, Antje – and many more!

Special thanks to Maren and Dieter, who came with me in Chile for the second fieldtrip in 2010. Maren was a precious navigator and Dieter a safe driver! I won't forget the few days we spent at Lonquimay together with David G.

It happened sometimes that I was not in the lab or in my office, and the friendly support of Robert, Nico, Andrea and Elfi was essential for my sake. I will never forget our cooking evening, the Tarot games we played and all the moment we passed together all these years. Thanks guys!

Last but not least, my heart is thanking Maxi. Her support during the last months of finishing this PhD was precious; otherwise I would have become insane. Danke, danke, danke!

Name Guillaume JACQUES
Date of Birth 02nd March 1985

Sex: Male
Nationality: French
Age: 28

EDUCATION

2009-2013 GEOMAR Helmholtz Center for Ocean Research, Kiel (Germany), PhD on the Southern Volcanic Zone (Chile/Argentina)
2006-2008 Blaise Pascal University, Clermont-Ferrand (France), Master thesis on Li isotopes on basaltic samples from Rurutu Island (French Polynesia)
2003-2006 University of Poitiers (France)

QUALIFICATIONS

2008 Master's degree in geosciences
2006 Bachelor's degree in geosciences
2005 Two-year university degree in geosciences

LABORATORY EXPERIENCE

2009-2013 Clean-lab and chemical isolations of Sr-Nd-Hf-Pb - Use of TIMS (Thermo Triton and Thermo MAT262) – Pb double spike - ICP-MS.
2008 Clean-lab and chemical isolations of Li – standard bracketing to normalize Li isotope data – Use of MC-ICP-MS
2007 Short lab-work on Sr-Nd isotopes of Sal Island (Cape Verde) - Clean-lab and TIMS

FIELD WORK EXPERIENCE

06.11.10-16.11.10 Field work in Chile aiming at crustal samples
05.02.09-14.03.09 Field work in Chile and Argentina aiming at young mafic volcanic front and backarc samples
2003-2008 Many fieldtrip in France, mostly mapping, within university program